The Effect of Finite Ion Larmor Radius on the Stability of a Cylindrically Confined Plasma.

By

Richard John Wright.

Thesis submitted in partial satisfaction of
the requirements for the degree of
Doctor of Philosophy of
The University of London.

Imperial College of Science and Technology, 1976.

Abstract

Finite Larmor radius (FLR) effects, in Hall terms and the collisionless stress tensor, are thought to constitute an important stabilising agent in confined kilovolt plasmas. This thesis considers a cylindrical confined plasma subject to a sheared equilibrium magnetic field and investigates the associated macroscopic instabilities.

Collisionless instabilities are described by a general second order differential eigenvalue equation. Mode localisation near a resonant surface, where the pitches of a helical mode and the magnetic field match, is employed in a semi-analytic solution that yields a generalised sufficient stability criterion including the effects of pressure gradient, rotation, sheared axial velocity and heat flow. Numerical solution reveals the destabilising influence of any resonant surface present, considers FLR stabilisation of interchange (Suydam) modes and shows that its effect on rotational instabilities leads to the optimum rotation being non-zero. Displacement of the eigenfunction from the resonant surface by axial heat flow is also demonstrated.

A low-beta, resistive system yields a fourth order differential set of eigenvalue equations; to these, the application of the developed numerical method reveals that the plasma radius beyond which the standard treatment of resistive instabilities is valid increases as resistivity rises. FLR produces growth rate reduction, but no cut-off, and generates rapid spatial oscillations that caused the computations to fail. A new spatially oscillatory, resistive FLR dependent mode is discussed.

A resistive system with finite-beta and FLR is analysed

using traditional localisation assumptions and reduced to a form suited to numerical analysis. With FLR in excess of a critical value, there exists a cut-off value of the matching parameter independent of the pressure gradient sign and of the azimuthal magnetic field. The approach to FLR-free results is considered and additional, more questionable modes are discussed.

Contents.

		Page.
Abstract.		2
Contents.		4
List of Illustrations.		7
List of Tables.		13
Chapter I.	Background and Introduction.	14
1)	The System Studied.	14
2)	Finite Ion Larmor Radius Effects.	17
3)	FLR Ordering.	19
4)	The Dispersion Equation of the System in the Collisionless Limit.	22
Chapter II.	Solution of the Collisionless Eigenvalue Equation Using an Analytic Approach.	26
1)	Introduction.	26
2)	Method.	27
3)	Results I - Deductions from the Dispersion Equation.	35
4)	Results II - Computations.	38
5)	Conclusion.	47
Chapter III.	Numerical Solution of the Collisionless Eigenvalue Equation.	48
1)	Introduction.	48
2)	Numerical Method.	48
3)	Suydam Modes.	57
4)	Rotational Effects.	70
5)	Heat Flux Modes.	81
6)	Pressure Anisotropy.	84
7)	Some Comments on Singular, F=0, Instabilities.	87
8)	Conclusion.	88

Contents contd.

		Page.
Chapter IV.	A Numerical Approach to Resistive Instabilities.	90
1)	Introduction.	90
2)	The System of Equations.	92
3)	Numerical Procedure.	97
4)	Comparison of Results with Previous Theory.	104
5)	The Effect of FLR Terms.	114
6)	The Effect of Two Resonant Surfaces.	124
7)	Conclusion.	126
Chapter V.	Finite Larmor Radius Effects and the Resistive Tearing Mode at Non-zero Beta.	128
1)	Resistivity and Plasma Instability.	128
2)	Resistive Instability at Finite-Beta Including FLR.	131
3)	The Unperturbed State.	134
4)	Perturbation Analysis I - FLR Expansion.	135
5)	'Outer' Region Solution.	141
6)	The 'Inner' Region Solution - Discussion.	143
7)	Perturbation Analysis II - Tearing Mode Ordering and Expansion.	144
8)	The Calculation of Δ - The Mathematical Manipulation.	151
9)	The Numerical Problem.	158
10)	Checks on the Calculation.	161
11)	Nyquist Techniques - General Comments.	162
12)	Results of the Computations.	163
13)	Discussion and Conclusions.	192

Contents contd.

		Page.
Chapter VI.	Conclusion.	195
References.		197
Appendix A.	Pott's Derivation of the Collisionless Eigenvalue Equation.	200
Appendix B.	The Resistive Interchange Ordering.	205

List of Illustrations.

	Figure.		Page.
Chapter II	1	The sufficient stability criterion to Interchange modes.	38
	2	$m\zeta$ versus A2 with A1=-2.	40
	3	$m\zeta$ versus A2 with A1=0.	40
	4	$m\zeta$ versus A2 with A1=1.	41
	5	$m\zeta$ versus A2 with A1=2.	41
	6	$m\zeta$ versus A2 with $A4=-1$.	42
	7	$m\zeta$ versus $A4$.	43
	8	$m\zeta$ versus A1; A2=1.6	44
	9	$m\zeta$ versus A1; A2=3.	45
	10	A2 at marginal stability versus 1/A3.	46
	11	A2 at marginal stability versus 1/A3 with $A4=-1$.	46
Chapter III	1	Growth rate spectrum of Suydam modes.	57
	2	Growth rate spectrum of Suydam modes with flatter μ profile.	59
	3	Eigenfunctions in the absence of FLR.	60
	4	FLR dependence of growth rate.	61
	5	FLR dependence of oscillation frequency.	61
	6	Complex eigenfunctions related to figure III 4.	63

	Figure.		Page.
Chapter III	7	The Righi-Leduc effect.	66
	8	Suydam modes with two resonant surfaces.	68
	9	Eigenfunctions from figure III 8.	68
	10	m=1 eigenfunctions from figure III 8.	69
	11	Rotational modes with constant magnetic pitch.	72
	12	Growth rate of rotational modes as the width of the density profile is varied.	73
	13	Rotational modes, including profiled pitch.	74
	14	m=1 eigenfunctions from figure III 13.	75
	15	B_θ dependence of growth rate of k=0, m=1 mode.	76
	16	Rotational mode spectrum with steeper magnetic pitch profile.	77
	17	Rotational modes with FLR.	77
	18	Rotational modes at zero beta.	77
	19	FLR stabilisation of rotational instability.	78
	20	The effect of an ion temperature profile on figure III 19.	79
	21	The dependence of growth rate on $\underline{E}x\underline{B}$ rotation.	80
	22	Heat flux destabilisation.	82

	Figure.		Page.
Chapter III	23	Heat flux perturbation of m=2 eigenfunctions.	83
	24	Temperature anisotropy destabilisation.	85
	25	Temperature anisotropy perturbation of eigenfunctions.	85
	26	Mode spectrum including temperature anisotropy effects.	86
Chapter IV	1	Spectrum comparing numerical approach with standard analytic theory.	104
	2	Growth rate spectra for flattened, rounded and peaked μ profiles.	106
	3	Resistive dependence of growth rate.	107
	4	Growth rate versus resistivity for different k numbers.	108
	5	Growth rate spectra for different m numbers.	109
	6	Growth rate versus resistivity for various m numbers.	109
	7	Eigenfunctions with the flattened profile for different resistivities.	111
	8	Flattened profile eigenfunctions for different k numbers.	113

	Figure.		Page.
Chapter IV	9	Growth rate spectrum with profiled temperature.	114
	10	FLR dependence of growth rate and frequency.	115
	11	Resistive dependence of growth rate and frequency including FLR.	117
	12	FLR dependence of growth rate at smaller resistivity than figure IV 10.	118
	13	Eigenfunctions when FLR terms are included.	119
	14	Eigenfunctions when computations fail.	120
	15	Effect of FLR on the growth rate spectrum.	120
	16	The production of an extra mode by increased FLR.	121
	17	Eigenfunctions of the 'additional' mode as FLR varies.	122
	18	Eigenfunctions of the 'additional' mode as k varies.	123
	19	Growth rate versus resistivity with two resonant surfaces present.	124
	20	Eigenfunctions from figure IV 19.	125
	21	Growth rate spectrum with two resonant surfaces.	126

	Figure.		Page.
Chapter V	1	Asymptotic behavior of the series expansion for Δ.	160
	2	Comparison with Coppi's results at $\beta = 0$.	162
	3	Illustrating the regime wherein FLR is effective.	164
	4	The dependence of Δ on growth rate, g, in the FLR dominant regime.	165
	5	The dependence of the cut-off Δ upon beta.	167
	6	Δ (g) with larger B_θ than figure V4.	168
	7	Nyquist plot at g=0 relating to figure V4.	170
	8	Nyquist plots with increased growth rate, demonstrating further instabilities.	172
	9	Δ (g) for the new instabilities.	173
	10	The instabilities of figure V9 at different temperatures.	174
	11	Instabilities with small FLR and outward pressure gradient.	175
	12	Instabilities with small FLR and inward pressure gradient.	177
	13	Instabilities with FLR just less than the transition value.	178
	14	A case showing four types of instabilities.	180

	Figure.		Page.
Chapter V.	15	Sketch showing the transition to large q_F behavior as q_F increases.	179
	16	A collection of 'type 4' instabilities.	182
	17	The dependence of the growth rate of 'type 4' modes on B_θ with inward pressure gradient.	183
	18	Sketch of the interaction of a 'type 3' mode with the main tearing mode.	184, 185
	19	Sketch of the low q_F limit of 'type 1' modes when $\nabla p > 0$.	186
	20	'Additional', FLR driven, instabilities with outward pressure gradient.	187
	21	The dependence of the growth rate of 'type 4' modes on B_θ with outward pressure gradient.	188
	22	The result of altering the effect of resistivity on a 'type 4' mode.	189
	23	The result of reducing the effect of FLR on a 'type 4' mode.	191
	24	The result of reducing the effect of beta on a 'type 4' mode.	192

List of Tables.

	Table.		Page.
Chapter III.	1	Comparison of the cut-offs of figure III4 with the theory of chapter II.	64
	2	The comparison in a less favourable regime.	65
	3	The comparison for the cut-offs of figure III1.	65
Chapter V.	1	Parameters relating to figure V4.	165
	2	Parameters relating to figure V6.	168
	3	The dimensions of $\Delta(g)$ curves for 'type 4' modes as the effect of resistivity varies.	190

Chapter I.

Background and Introduction.

1) The System Studied.

Attempts at confining high temperature plasmas in the hunt for methods of achieving controlled thermonuclear fusion have been consistently frustrated by the multitude of instabilities inherent in hot inhomogeneous discharges. The joint effects of reduced collision frequency and increased ion Larmor radius, as ion temperature rises with improved technology, make the finite Larmor radius (FLR) corrections to the magnetohydrodynamic (MHD) fluid equations of increasing significance.

Whilst the majority of existing and proposed containment devices are toroidal in form, the effects of the complex physics associated with FLR may be adequately assessed using a cylindrical model, thus avoiding the geometrical complications of the torus. The system studied is thus an infinite, cylindrical, Z=1 plasma column bounded by a rigid conducting wall. Conventional cylindrical coordinates (r,θ,z) may thus be employed relating to the radial, azimuthal and axial directions respectively. Linear stability of the plasma column is studied on the assumption that initial equilibrium states exist depending only on the radial coordinate. Permeating the plasma, the equilibrium magnetic field has both axial and azimuthal components ($\underline{B}=(0,B_\theta(r),B_z(r))$) so that effects of magnetic curvature, shear and torsion are included in the model.

As the equilibria considered are independent of θ and z, the perturbations are Fourier analysed in these coordinates so that separate modes vary as $\exp(i(m\theta+kz))$. The initial

effect of toroidicity is to produce periodicity in z, thus quantising k. Growth rate spectra, $\gamma(k)$, plotted in subsequent chapters must therefore be viewed with the knowledge that, in a practical system, such a plot is restricted to a series of discrete points, whose separation in k varies inversely with the periodic 'length' of the apparatus.

In the absence of FLR effects, the stability of models of the type considered has been extensively investigated in the literature. Two distinct types of macroscopic (fluid-like) instabilities have been found. Using collisionless models with the plasma surrounded by a vacuum region, kink modes arise (1) when a resonant surface $(k+\frac{mB_\theta}{rB_z}=0=(\underline{k}.\underline{B}))$ occurs in the vacuum. These involve delocalised perturbation of the plasma column. A resistive plasma model allows such modes to occur with a resonant surface within the plasma (6),(7) as experimentally observed. Typically, such resistive resonant surface effects may be expected to arise in the cooler, outer regions of the plasma column. Further discussion of these appears in chapters IV and V.

Localised interchange modes may occur (1) at resonant surfaces lying within the plasma. Such modes are known (8) to be subject to stabilisation by FLR effects and are considered in depth in this context in chapters II and III. Their MHD stability has been carefully analysed in the literature. Using the energy principle of Bernstein et al.(5), Suydam (2) heuristically produced a necessary stability criterion for these modes defining the magnitude of adverse (inward) pressure gradient that can be stabilised against interchange phenomena by a given magnetic shear $\left(\frac{d}{dr}\left(\frac{B_\theta}{rB_z}\right)\right)$.

The basis of this criterion has been made more rigorous by Newcomb (9) in a careful, detailed analysis of the problem that also yields necessary and sufficient stability conditions.

The importance of resonant surface effects in the stability analysis is plainly evident from the above work. Indeed, the incorporation of such phenomena gives rise to the differences between the work described in chapter III and that of Bowers (10) who considered straight field equilibria ($\underline{B}= (0,0,B_z)$). As may be seen from calculations below, the relevance of such regions arises since the perturbation causes no local distortion of the magnetic field in the collisionless limit. Shear stabilisation is thus effective by reducing the width of the layer for which the field perturbation is small. Resistivity allows $(\underline{E}.\underline{B})' \neq 0$ in such a region so that magnetic field perturbation need not imply large plasma perturbation; the perturbed plasma diffuses across the lines of force. In the resistive limit, therefore, shear stabilisation is ineffective and indeed has an adverse effect(7).

Shafranov(1) discussed the reliability of the cylindrical model in its application to the macroscopic (fluid-like) instabilities of confined plasmas. He concludes that , whereas toroidal curvature has a small effect on delocalised kink-modes, the effect is larger on the more localised interchange modes, and produces increased stability as the aspect ratio, of the torus concerned, rises. This effect has been analysed in detail by Mercier (3,4), in the collisionless limit from the energy principle; stabilisation arises from the favourable influence of the toroidal magnetic field being curved towards the plasma on the inside of the torus. Thus, larger pressure gradient (averaged around the

poloidal plane) may be stabilised by a given magnetic shear (in the collisionless limit). The stability criteria presented in chapter II may, therefore, be relaxed slightly if applied to toroidal systems.

2) Finite Ion Larmor Radius Effects.

In order to grasp the importance of these phenomena in containment experiments, compare the thermal Larmor radius ,a^i, and the ion-ion collisional mean free path, λ^i, to typical apparatus dimensions, $L_\perp$, of the order of 1 metre. For a plasma with kilovolt ions in a 1T magnetic field with number density $10^{19} m^{-3}$ we find:

$$a^i : L_\perp : \lambda^i = 5\times10^{-3} : 1 : 1500.$$

Thus, in directions normal to the magnetic field, particle localisation arises as a result of the gyro orbits rather than from any collisional process. Such localisation is relevant since it occurs on a scale small, but not insignificant , compared to the apparatus dimensions.

The first indication that FLR effects might have a stabilising influence on confined plasma was given by Rosenbluth, Krall and Rostoker (13) in an investigation of their influence on the electrostatic flute instability in weakly unstable plasmas. They employed a technique of direct solution of the Vlasov equation by integration along particle orbits and found that the MHD dispersion relation, of the form: $\omega^2 = -c^2$ was replaced by $\omega(\omega - k v_d) = -c^2$ where v_d is the ion drift velocity. Such a replacement is common in all subsequent work and is responsible for the stabilising effects associated with the ion diamagnetic drift. As shown by Schmidt (15) , the effect is the result of inhomogeneities in the fields present. These cause the influences of the field

quantities averaged around the gyro orbits to differ significantly from those evaluated at the guiding centres. Since this effect is neglegible on the minute electron gyrations , it causes the electron and ion motions to be relatively phase shifted. As shown by Hoh(16) and Bowers (10), the phase shift results in currents and charge distributions that partially cancel those driving any instability present.

A procedure for obtaining fluid equations capable of representing these effects was discussed by Chew, Goldberger and Low(11) and developed by subsequent authors. Roberts and Taylor (14) first showed that the results of (13) could be obtained from fluid equations using the stress tensor given by Thompson (12) derived from expansion of the Vlasov equation. Further use of such a stress tensor was made by Kulsrud (23) in a discussion of FLR stabilisation of the interchange instability in the Stellerator; his mathematical technique was applied by Stringer (24) to a similar situation with an analysis based on the FLR modified guiding centre approach discussed in Schmidt (15). Kulsrud's technique yields an FLR modified Suydam criterion and is again used in chapter II in a more general situation.

A consistent ordering scheme for the development of FLR fluid equations was outlined by Rosenbluth and Simon (17) in a discussion of the flute instability in the presence of an equilibrium inhomogeneous radial electric field. This implies, in general, an initial rotating plasma subject to perturbation. These authors found, for their straight magnetic field, zero beta, situation an optimumum plasma rotation for stability with the centre of mass rotation equal to half the ion diamagnetic rotation. Pearlstein and Krall (18) developed

this method including finite-beta effects and Kennel and Greene (19) performed a general expansion using localised rather than global coordinates.

The stress tensors derived by the above techniques have been shown by Ware (20) to contain contributions from the heat flux of perpendicular (gyration) energy. He showed that the stress tensor could be obtained from the collisional expansion of Herdan and Liley (21) if terms in the collision frequency were neglected and heat flux terms were retained in the derivation. As terms in $1/\nu$ are present in (21), the neglect of these, as $\nu \to 0$, appeared to be a dubious step at the time, but has since been justified by Hosking(25) on consideration of further work by Liley(22). The latter derives the stress tensor by expansion of moment equations rather than of the Boltzmann equation itself. A collisionless derivation of this sort has been carried out by Macmahon(26).

Bowers (10,27,28) developed the approach of reference(17) and produced equations including finite-beta and axial wavelength terms. The latter removes the purely electrostatic nature of the perturbations, so that distortion of the magnetic field lines results. In reference (28), a detailed account of instabilities in a rotating theta pinch is presented. This work is extended to systems containing equilibrium B_θ in chapter III and hence considers the complications of superimposed resonant surface effects. Using a coordinate system defined by the equilibrium magnetic field (rather than by the total field), Bowers (29) developed a stability analysis including the effects of magnetic field curvature and torsion.

3) <u>FLR Ordering.</u>

As this thesis makes considerable use of the collisionless

FLR stress tensor in the cylindrical coordinate system, it is pertinent to outline the ordering restrictions inherent in its derivation from the Vlasov equation. These are discussed in detail by Bowers (10) and by Kennel and Greene(19).

Define an FLR ordering parameter, ε:

$$\varepsilon = \frac{v_t^i}{\Omega^i L_\perp} = \frac{\alpha^i}{L_\perp} = \frac{\text{Ion Larmor radius}}{\text{Plasma Scale Length normal to } \underline{B}.}$$

where v_t^i is the ion thermal velocity and Ω^i is the ion gyro frequency.

Bowers (10) used:

$$\frac{u_\perp}{\varepsilon v_t^i} \sim \frac{E_\perp}{\beta \varepsilon v_t^i} \sim \frac{\omega}{\varepsilon^2 \Omega^i} \sim 1 \qquad \text{I1}$$

where $u_\perp$ is the hydromagnetic velocity normal to $\underline{B}$, $\perp$ and $/\!/$ suffices refer to vector components relating to directions perpendicular and parallel to $\underline{B}$ and ω is the frequency of the instabilities.

The ordering of ω is such that currents produced by finite gyro radius phenomena are of sufficient magnitude to influence the perturbation of the lowest order hydromagnetic velocities. $E_\perp$ is ordered so that it produces variations on time scales no shorter than $1/\omega$.

There remains the ordering of $E_{/\!/}$, β and B_θ/B_z. Recall from Bowers (28) that the motion of particles and perturbations along $\underline{B}$ is described by a time-scale:

$$\frac{1}{T} \sim \frac{C_A}{L_{/\!/}}$$

where C_A is the Alfven speed and $C_A \sim v_t^i/\sqrt{\beta}$. Thus:

$$\varepsilon^2 \Omega^i \sim \frac{C_A}{L_{/\!/}} \sim \frac{v_t^i}{L_{/\!/}\sqrt{\beta}}$$

hence: $\frac{1}{L_{/\!/}} \sim \frac{\varepsilon\sqrt{\beta}}{L_\perp}$ using the definition of ε. I2

Therefore, in the cylindrical system considered in this work:

$$\frac{1}{L_{/\!/}} \sim \frac{k+mB_\theta}{rB_z} \sim \frac{\varepsilon\sqrt{\beta}}{L_\perp}$$

Since $m \geq 1$, $\frac{1}{L_\perp \text{perturbations}} \left(\sim \frac{m}{r}\right) \geq \frac{1}{L_\perp \text{equilibrium}} \left(\sim \frac{1}{r}\right)$

hence, we choose:

$$k \sim \varepsilon \sqrt{\beta}\, \frac{1}{L_\perp} \; ; \quad L_\perp \text{perturbation} \sim L_\perp \text{equilibrium} \qquad I3$$

and:

$$B_\theta \sim \varepsilon \sqrt{\beta}\, B_z \qquad I4$$

This ordering of B_θ ensures that, in the $\beta \sim 1$ limit, the timescale associated with the $\nabla |B|$ and curvature drifts of particles does not dominate that of the FLR effects that are the subject of interest. In chapters II,III and V a $\beta \sim \varepsilon^0$ ordering is employed in order to include the maximum number of physical quantities; chapter IV uses $\beta \sim \varepsilon^2$, following Coppi (31), in order to simplify the resistive equations studied. $\beta \sim 1$ implies $j_z B_\theta \sim \varepsilon^2 j_\theta B_z$ so that, in lowest order, the divergence of the magnetic stress tensor reduces to the gradient of a scalar magnetic pressure:

$$\text{e.g.:} \quad j_\theta B_z = \frac{d}{dr}\left(\frac{B_z^2}{2\mu_0}\right)$$

The allowable magnitude of $E_{//}$ may be determined from the induction equation. Magnetic field perturbations produced by variations in $E_{//}$ must be at most of comparable magnitude to those arising from $E_\perp$. Hence:

$$\frac{E_{//}}{L_\perp} \sim \frac{E_\perp}{L_{//}}$$

so that:

$$\frac{E_{//}}{B} \sim \varepsilon \sqrt{\beta}\, \frac{E_\perp}{B} \qquad I5$$

Expansion of the Vlasov equation using this ordering of quantities produces a fluid-like description of the effects of FLR. The study of modes with scale lengths comparable to the Larmor radius (32,33) is not susceptible to a fluid-like analysis and requires complex kinetic calculations.

4) The Dispersion Equation of the System in the Collisionless Limit.

Pott(30) expanded the Vlasov equation in the manner of Bowers (10,27) and considered perturbations of the drift kinetic equation produced, Fourier analysed in θ,z and time. Retaining equilibrium B_θ, Pott(30) found that, in the limit of the ordering used, two types of solution were possible. The first describes localised microinstabilities of the type considered by Bowers (10,28) and the second, fluid-like macroinstabilities. These are characterised by purely convective perturbations of density, pressure ($p_\perp$ & $p_{//}$), axial velocity, axial heat flux and the fourth moment of the distribution function. Thus they are incompressible and adiabatic.

$$\text{i.e.} (\nabla \cdot \underset{\sim}{u})' = 0 = (\nabla \cdot (\underset{\sim}{q}^{\perp} + \underset{\sim}{q}^{//}))' \qquad \text{I6}$$

Pott's expansion and derivation appears in appendix A in order to show how the expressions for the various perturbed quantities are related to the Lagrangian displacement ξ defined as :

$$\xi = \frac{u_r'}{\omega_1} \qquad \text{I7}$$

where ω_1 is the Doppler shifted frequency:

$$\omega_1 = \omega + \frac{m u_\theta}{r} + k u_z \qquad \text{I8}$$

and thus depends on the equilibrium velocity $\underline{u} = (0, u_\theta, u_z)$.

In the manner of Bowers (10,28), Pott(30) expanded in ε the centre of mass momentum equation:

$$\rho \frac{\partial \underline{u}}{\partial t} + \rho (\underline{u} \cdot \underline{\nabla}) \underline{u} - \underset{\sim}{j} \wedge \underline{B} + \underset{\sim}{\nabla} p + \underset{\sim}{\nabla} \cdot \underline{\underline{\tau}} = 0 \qquad \text{I9}$$

To first and second orders, pressure balance resulted:

$$\nabla \left(P_\perp + \frac{B_z^2}{2\mu_0} \right) = 0 \qquad \text{I10}$$

In third order, after linearising and perturbing, high order pressure contributions were eliminated by taking the z component of the curl of I9 expressed to this order.

Eventually, after substituting in the expressions for the perturbed quantities that appear in appendix A, he produced the differential dispersion equation for the system considered:

$$\frac{d}{dr}\left(F\frac{d\xi}{dr}\right)+G\xi=0 \qquad \text{I11}$$

where:

$$F=\rho r^3\omega_1^2+r^3\bar{k}^2\left(\sum_{\text{species}}(P_{//}-P_{\perp})-\frac{B_z^2}{\mu_0}\right)$$

$$-m\omega_1 r^2\frac{d}{dr}\left(\frac{P_{\perp}^i}{\Omega^i}\right)+\frac{mr^2\bar{k}}{\Omega^i}\left(P_{\perp}^i\frac{du_z}{dr}+\frac{d}{dr}q_z^{\perp i}\right)$$

$$+\frac{mr^2}{\Omega^i B_z}\frac{dB_z}{dr}\left(kq_z^{\perp i}+\frac{m}{2r}q_\theta^{\perp i}\right)$$

$$G=\frac{-(m^2-1)}{r^2}F+r^2\frac{d}{dr}\left[\rho\left(\omega_1-\frac{mu_\theta}{r}\right)^2\right]$$

$$+k^2r^2\frac{d}{dr}\left(\sum_{\text{species}}(P_{//}-P_{\perp})-\frac{B_z^2}{\mu_0}\right)$$

where: $$\bar{k}=k+\frac{mB_\theta}{rB_z}$$

(Note that the second term in G corrects an algebraic error in the work of Bowers (10,28)).

Equation I11 forms the basis of the study of the collisionless instability of the system considered. Its solution will be expounded in detail in chapters II and III of this work and appears in less depth in reference (30).

The inclusion of the complete FLR stress tensor in the momentum equation has thus added a variety of physical phenomena to the dispersion equation in addition to the familiar diamagnetic contribution that constitutes the third term of F. These additional effects appear in the

fourth and fifth terms.

The fourth term of F, linear in $\bar{k}$, will be subsequently shown to have a destabilising influence. In particular, the adverse effects of sheared axial velocity become more important when ion temperature rises. Melchoir and Popovich(34) found that,although FLR tended to stabilise Kelvin-Helmholtz instability in many cases, situations existed for which the plasma was unstable only when FLR terms were included; these authors employed a simple Cartesian model. The equation shows that a radial gradient of $q_z^{\perp i}$ has a similar effect.

The fifth term of F arises only in high beta situations, where $\nabla|B|$ effects are significant; it includes the influence of the collisionless heat flux, $q_\theta^{\perp i}$, another consequence of FLR.

An MHD treatment of the problem yields the first two terms of F apart from the temperature anisotropy corrections in the second that give rise to firehose instability(35).

G manifests the effects of the cylindrical geometry. The form of the first term gives rise to the well-known differences in character of the m=1 mode since studies in the MHD limit (1) have revealed that it exerts a stabilising influence when $m > 1$. The second term of G introduces rotational destabilisation since this is the only term in which the frequency, ω, is not Doppler shifted by the rotation. (Note that $\omega_1 - \frac{m u_\theta}{r} = \omega + k u_z$). The final term in G incorporates the effects of total pressure gradient ($\frac{d}{dr}(p_\perp + p_{//})$ on using equation I10) and is responsible for driving Suydam instabilities and the dangerous m=1 kink mode of the diffuse pinch (36).

The solution of equation I11 and the investigation of the

consequences of the various physical effects thereby described forms the content of chapters II and III. It is found that the less familiar effects, arising from the gyro-viscous stress tensor used, are, in some cases, at least as important in the stability considerations of a hot cylindrically confined plasma as the more widely discussed diamagnetic contributions.

An investigation of resistive effects in the FLR limit begins in chapter IV. A discussion of the literature relevant to resistive instabilities is postponed until the beginning of chapter V, however, as that chapter employs techniques more commonly used in this context.

Chapter II.

Solution of the Collisionless Eigenvalue Equation Using an Analytic Approach.

1) Introduction.

In the limit $u_\theta \to 0$, $u_z \to 0$, $q_\theta^{\ell i} \to 0$, $q_z^{\ell i} \to 0$, Pott's collisionless eigenvalue equation (eq. I11 and ref.30) consists of terms of a similar nature to those of the equation solved by Stringer (24). and Kulsrud (23). The differences that arise are due to the more rigorous inclusion of cylindrical geometry and agree with the results of other authors (17,28). As the analytic approach employed in references (24) and (23) was so successful in simpler physical situations, this chapter attempts to follow an analogous course of investigation with the more complete Pott equation.

The method requires that the instability be localised in the neighbourhood of a resonant surface defined by:

$$\bar{k}_{r=r_s} = \left. \frac{k+mB_\theta}{rB_z} \right|_{r=r_s} = 0$$

In the MHD limit, the radial thickness of a perturbation of given m about the resonant surface is determined by two competing influences. The interchange instability arises at the resonant surface where its helical pitch matches that of the magnetic field. On either side of the surface, the amount of energy required for perturbation is determined by the mismatch in the two helices. Hence, steep shear $\left[\frac{d}{dr}\left(\frac{B_\theta}{rB_z}\right)\right]$ confines the mode to a very thin layer. The magnitude of the perturbation is restricted by the kinetic energy involved in a growing mode. Thus, singularity , and hence infinitely narrow perturbation, occurs only at zero growth rate. Finite Larmor radius effects introduce oscillation

into the growing modes and thus significantly increase the kinetic energy of perturbations near the resonant surface when the growth rate is small. Thus, with these effects included, cut-off is possible with a finite eigenfunction; the theory developed below thus essentially applies close to marginal stability.

Since, close to the origin, eigenfunctions vary as r^{m-1}, mode localisation increases dramatically as m rises. This will be seen in computed eigenfunctions in chapter III (figure III6). Thus, the technique and results of this chapter are most applicable for $m \gg 1$ and totally inapplicable to m=1.

2) Method.

The method begins by Taylor expanding in the region of the resonant surface:

$$\bar{k} \simeq \alpha x \qquad \text{where} \quad \alpha = \left.\frac{d\bar{k}}{dr}\right|_{r=r_s} = m \left.\frac{d}{dr}\left(\frac{B_\theta}{rB_z}\right)\right|_{r=r_s} \qquad \text{II1}$$

$$x = r - r_s$$

All other equilibrium quantities are taken as constant in this region, it being assumed that they vary only on a length scale large compared to that of the radially localised instability.

Pott's equation now takes the form:

$$\frac{d}{dx}\left[(Ax^2+Bx+C)\frac{d\xi}{dx}\right]+\left[E(Ax^2+Bx)+D\right]\xi=0 \qquad \text{II2}$$

where A to E are constants, in this approximation, depending only on equilibrium quantities at the resonant surface. In order to remove terms linear in x, a linear transformation of independent variable from x to w is required. Since w=0 implies $x \neq 0$, the perturbation calculated is not centred about the origin of x. Unless this shift is small, the localisation approximation II1 will be invalid; this, therefore, places a further constraint upon the regime of validity of the theory.

The transformation required may be summarised as follows:

put $$\gamma_1 = r_s^3 \alpha^2 \left(\sum_{\text{species}} (p_{//} - p_\perp) - \frac{B_z^2}{\mu_0} \right) \quad \text{II3}$$

$$\gamma_2 = \frac{m \alpha r_s^2}{2\Omega} \left(p_\perp \frac{du_z}{dr} + \frac{dq_z^\perp}{dr} + \frac{q_z^\perp}{B_z} \frac{dB_z}{dr} \right) \quad \text{II4}$$

$$\gamma_3 = \rho r_s^3 \omega_1^2 - m\omega_1 r_s^2 \frac{d}{dr}\left(\frac{p_\perp}{\Omega}\right) + \frac{m^2 r}{\Omega^2 B_z} \frac{dB_z}{dr}\left(\frac{1}{2}\frac{dR}{dr} - \frac{p_\perp}{\rho}\frac{dp_\perp}{dr}\right) \quad \text{II5}$$

The $q_\theta^\perp$ terms in Pott's equation have been substituted using:

$$q_\theta^\perp = \frac{1}{\Omega}\frac{dR}{dr} - \frac{2p_\perp}{\Omega\rho}\frac{dp_\perp}{dr} + \frac{2B_\theta}{B_z} q_z^\perp \quad \text{II6}$$

so that $k + \frac{m q_\theta^\perp}{2r}$ becomes: $\frac{m}{2r\Omega}\frac{dR}{dr} - \frac{m p_\perp}{\rho r \Omega}\frac{dp_\perp}{dr} + k q_z^\perp$

Here R is the fourth moment of the zero order distribution function f_0:

$$R = \frac{\pi M}{2} \int_0^\infty \int_{-\infty}^{\infty} v_\perp^5 f_0(v_\perp, v_z, r) \, dv_\perp \, dv_z \quad \text{II7}$$

Specification of f_0 or its moments ρ , $P_{\perp 0}$, $P_{//0}$, $q_{z0}^\perp$, u_{z0}, R determines the equilibrium under study.

With γ_1, γ_2 and γ_3 defined above, the required transformation is:

$$w = \frac{x\gamma_1 + \gamma_2}{(\gamma_3\gamma_1 - \gamma_2^2)^{1/2}} \quad \text{II8}$$

It is convenient to define also:

$$X = \left(\frac{m^2 - 1}{r_s^2}\right)(\gamma_3\gamma_1 - \gamma_2^2)/\gamma_1^2 \quad \text{II9}$$

$$Y = \frac{r_s^2 \frac{d}{dr}\left(\rho(\omega_1 - \frac{m}{r}u_\theta)^2\right) + k^2 r_s^2 \frac{d}{dr}\left(\sum_{\text{species}}(p_{//} - p_\perp) - \frac{B_z^2}{\mu_0}\right)}{r_s^3 \alpha^2 \left(\sum_{\text{species}}(p_{//} - p_\perp) - B_z^2/\mu_0\right)} \quad \text{II10}$$

From eq.II8 we clearly require that $\frac{\gamma_2}{\gamma_1}$ be very much less than the scale size of x (or w). Expressions II3 and II4 show that this indicates that $\frac{du_z}{dr}$, $\frac{dq_z^\perp}{dr}$ and $q_z^\perp \frac{dB_z}{dr}$ are responsible for the radial displacement of the perturbation that limits the applicability of the theory. The eigenfunction displacement will be considered more thoroughly in chapter III

by numerical means.

The quantity Y (eq.II10) contains the instability driving forces from the function G of the eigenvalue equation. Omitting the first term in the numerator and pressure anisotropy, the Suydam criterion (2) may be expressed as $Y < \frac{1}{4}$ for stability. Thus, the rotational effects of the first term are seen to decrease stability.

Using the quantities w,X and Y, Pott's equation becomes:

$$(w^2+1)\frac{d^2\xi}{dw^2} + 2w\frac{d\xi}{dw} + \left[-(w^2+1)X + Y\right]\xi = 0 \qquad \text{II11}$$

This equation appears to be precisely of the form of that solved by Stringer (24), with X and Y replacing $k_n^2\alpha$ and $\frac{1}{4}\chi^2$ of that work respectively. However, the rotational contribution to Y involves the frequency of the perturbation and is, in general, complex. Thus, in the present calculation, Y is complex whereas χ^2 in Stringer's work is real. As Stringer's final result is not an analytic function because it involves the arguments of complex numbers, generalisation of the manipulation is required.

Following Stringer (24), the technique of solution proceeds by considering only the case $|Y| \gg |X|$ for which the driving forces are sufficiently strong to induce instability. Two overlapping ranges of w are taken: (i) $w \ll \sqrt{\frac{Y}{X}}$, (ii) $w \gg 1$. Assume that walls and axis are distant from the resonant surface and take homogeneous boundary conditions at large w:

$$\xi \to 0 \quad \text{as} \quad |w| \to \infty$$

Since equation II11 is symmetric about w=0 and the boundary conditions are homogeneous, group theory indicates that ξ is either symmetric or anti-symmetric about w=0. Hence either $\xi = 0$ or $\frac{d\xi}{dw} = 0$ at w=0.

The solution in region (ii) is the same for modes of

either symmetry. In this limit equation II11 reduces to a spherical Bessel's equation of imaginary argument. The solution convergent at large w is:

$$\xi \propto K_\eta (w\sqrt{X}) / w^{1/2} \qquad \text{II12}$$

where $\eta = \frac{i}{2}(4Y-1)^{1/2}$

Note that: $$w\sqrt{X} = \frac{1}{\Gamma_5}(m^2-1)^{1/2}\left[x + \frac{\gamma_2}{\gamma_1}\right]$$

The displacement constraint on $\frac{\gamma_2}{\gamma_1}$ can now be more precisely written as: $$\frac{(m^2-1)^{1/2}}{\Gamma_5}\frac{\gamma_2}{\gamma_1} \ll 1 \qquad \text{II13}$$

Since X vanishes for m=1, the outer decaying solution cannot be found for this case and the method of solution is clearly invalid. (The solution in region (i) decays only as $w^{-\frac{1}{2}}$, insufficiently rapidly for localised theory to apply).

In region (i), II11 reduces to Legendre's equation so that the general solution is:

$$\xi = A\,P_{\bar\nu}(iw) + B\left[Q_{\bar\nu}(iw) \pm P_{\bar\nu}(iw)\right] \quad \text{for} \quad w \gtrless 0$$

where $\bar\nu = -\frac{1}{2} + \frac{i}{2}(4Y-1)^{1/2}$

as in Stringer.

Note that the $P_{\bar\nu}$ correction to the second solution moves the branch cut from the standard position joining $w=\pm i$ via $w=0$ to that joining these points through infinity. The coefficients A and B for the cases of a) even-symmetry and b) odd-symmetry may be found from expressions for $P_{\bar\nu}(0)$, $Q_{\bar\nu}(0)$, $P'_{\bar\nu}(0)$, $Q'_{\bar\nu}(0)$ taken from reference (37).

For even-symmetry (as given by Stringer) we find:

$$\xi \propto \frac{\pi}{2}\left(i - \cot\frac{\pi\bar\nu}{2}\right)P_{\bar\nu}(iw) + Q_{\bar\nu}(iw) \qquad \text{II14}$$
$$(0 < w < \sqrt{Y/X})$$

and for odd-symmetry:

$$\xi \propto \frac{\pi}{2}\left(i + \tan\frac{\pi\bar\nu}{2}\right)P_{\bar\nu}(iw) + Q_{\bar\nu}(iw) \qquad \text{II15}$$

Expressions II14 and II15 must match II12 in the overlapping

region of validity: $1 \ll w \ll \sqrt{Y/X}$. The condition for this matching determins the eigenfrequency ω . Below, we concentrate on the calculation for the odd-symmetry case as this was not considered at all by the previous authors (23,24). Even symmetry modes are dealt with in an entirely analogous manner.

Write $u = (4Y-1)^{1/2}$ so that $\eta = \frac{iu}{2}$, $\nu = -\frac{1}{2} + \frac{iu}{2}$

At large w, reference 37 yields the asymptotic form of II15 in terms of gamma functions. Using the properties of gamma functions (37), this solution may be expressed as:

$$\xi = \frac{2B}{u w^{1/2}} \left(\frac{\pi u/2}{\sinh(\pi u/2)} \right)^{1/2} \cos\left(\frac{u}{2} \ln(8w) + \psi \right) \qquad \text{II16}$$

where

$$\psi = -\frac{i}{2} \ln\left(\frac{\tanh(\frac{\pi u}{2})}{\pi u/2} \right) - 2i \ln\left[\Gamma\left(1 + \frac{iu}{2}\right) \right] + i \ln\left[\Gamma(1+iu) \right] + \tan^{-1}\left(e^{-\pi u/2}\right) - \frac{\pi}{4}$$

Note that, since Y is complex, u will in general be complex also so that the gamma functions in ψ cannot be further simplified.

Using reference (37), the small argument expansion of II12 yields:

$$\xi = \frac{2C}{u w^{1/2}} \sqrt{\frac{\pi u/2}{\sinh(\pi u/2)}} \sin\left[\frac{u}{2} \ln\left(\frac{w\sqrt{X}}{2} \right) - i \ln\left[\frac{\left(\frac{\pi u}{2} / \sinh\left(\frac{\pi u}{2}\right)\right)^{1/2}}{\Gamma(1 + iu/2)} \right] \right] \qquad \text{II17}$$

In the matching region, therefore, the two solutions are rapidly oscillating functions. Matching is thus achieved by equating the amplitude and phase of the spatial oscillations. The latter is arbitrary to any multiple of π ; different phase matchings produce eigenfunctions with different numbers of nodes. Phase matching gives:

$$\sqrt{X} = H_n^{\substack{odd \\ even}}(4Y) \qquad \text{II18}$$

where:

$$H_{n\ even}^{odd}(4Y) = 16\exp\left[\frac{2}{u}\left\{-3i\ln\left[\Gamma\left(1+\frac{iu}{2}\right)\left(\frac{\sinh\left(\frac{\pi u}{2}\right)}{\pi u/2}\right)^{1/2}\right]\right.\right. \qquad \text{II19}$$

$$\left.\left. + i\ln\left[\Gamma(1+iu)\left(\frac{\sinh(\pi u)}{\pi u}\right)^{1/2}\right] \pm \left[\tan^{-1} e^{-\pi u/2} - \frac{\pi}{4}\right] - u\pi\right\}\right]$$

with $u = (4Y-1)^{1/2}$

The even mode result, derived analogously, has been incorporated and differs only by the sign choice shown.

In the zero FLR limit, we require , following Kulsrud(23), that $X \to 0$ as $u \to 0$ (Suydam marginal stability). Taking this limit, II19 indicates that $\sqrt{X} \sim 16\exp\left[-\frac{2\pi n}{u}\right]$. Clearly, n must be positive for any physical solution. Thus, n may take values $1, 2, \ldots\ldots \infty$. Since larger X implies greater growth rate, the most unstable mode will be that which maximises H. Evidently, n must equal 1 when $Re(u) > 0$ to maximise growth rate. The latter assumption concerning u is based upon the theory being a perturbation of that of Stringer (24) for which u was real and positive. Similarly, since

$$\tan^{-1}\left[e^{-\pi u/2}\right] - \frac{\pi}{4} \leq 0 \quad \text{for} \quad 0 < u < \infty$$

even-symmetry modes are the most unstable (taking the - sign in II19). Henceforth, we shall be concerned purely with the most unstable Suydam mode of the system for which the dispersion relation has been shown to be:

$$\sqrt{X} = H_{1\ even}(4Y) \qquad \text{II20}$$

The primary localisation constraint on the theory, $|Y| \gg |X|$ may be re-written in terms of Y alone:

$$|Y| \gg \left| H_{1\ even}(4Y) \right|^2 \qquad \text{II21}$$

for the mode considered.

The dispersion equation II20 may be expanded in terms of convenient parameters:

$$\zeta = 1 \pm \left[1 - \left\{A4 + \frac{A3}{A2} H^2 \left(A2\left[1 + A5(\zeta - A1)^2\right]\right)\right\}\right]^{1/2} \qquad \text{II22}$$

H(z) will henceforth denote $H_{1even}(z)$. The parameters of equation II21 are defined as follows:

with $$u^i = \frac{1}{\rho}\frac{d}{dr}\left(\frac{p_\perp^i}{\mathcal{R}^i}\right) \quad ; \quad \mu = \frac{B_\theta}{r_s B_z}$$

$$\zeta = \frac{\omega_1 r_s}{\frac{1}{2} m u^i} \quad ; \quad \left(\omega_1 = \omega + \frac{m u_\theta}{r} + k u_z\right) \qquad \text{II23}$$

$$A1 = \frac{u_\theta}{\frac{1}{2}u^i}\left[1 + \frac{\rho r_s \mu}{u_\theta}\frac{du_z}{dr}\Big/\frac{d\rho}{dr}\right] \qquad \text{II24}$$

$$A2 = \frac{-\frac{4}{r_s}\left(\frac{\mu}{d\mu/dr}\right)^2\left[\frac{d}{dr}\left(\sum_{species}(p_{//}-p_\perp) - \frac{B_z^2}{\mu_0}\right) - \frac{(\rho du_z/dr)^2}{d\rho/dr}\right]}{\frac{B_z^2}{\mu_0} - \sum_{species}(p_{//}-p_\perp)} \qquad \text{II25}$$

$$A3 = \frac{-16 r_s^3 \mu^2\left[\frac{d}{dr}\left(\sum_{species}(p_{//}-p_\perp) - \frac{B_z^2}{\mu_0}\right) - \frac{(\rho du_z/dr)^2}{d\rho/dr}\right]}{(m^2-1)\rho u^{i2}} \qquad \text{II26}$$

$$A4 = \frac{1}{\rho \mathcal{R}^{i2} u^{i2}}\left[\frac{4}{B_z}\frac{dB_z}{dr}\left(\frac{1}{2}\frac{dR^i}{dr} - \frac{p_\perp^i}{\rho}\frac{d\rho}{dr}\right) + \left\{\frac{\left(\frac{d}{dr}q_z^{\perp i} + p_\perp^i\frac{du_z}{dr} + \frac{q_z^{\perp i}}{B_z}\frac{dB_z}{dr}\right)^2}{\frac{B_z^2}{\mu_0} - \sum_{species}(p_{//}-p_\perp)}\right\}\right] \qquad \text{II27}$$

$$A5 = \frac{(u^i)^2 d\rho/dr}{4 r_s^2 \mu^2\left[\frac{d}{dr}\left(\sum_{species}(p_{//}-p_\perp) - \frac{B_z^2}{\mu_0}\right) - \frac{(\rho du_z/dr)^2}{d\rho/dr}\right]} \qquad \text{II28}$$

As H(z) is real when z is real (see Stringer (24)), the Schwartz reflection principle (38) requires that $H(z^*)=(H(z))^*$; hence, the sign choice in II22 merely produces either real modes or complex conjugate values of ζ. This is in accord with the properties of the original differential equation. When evaluating ζ , therefore, it is sufficient to consider only one of the two possible solutions to the dispersion equation, II22 in order to extract the growth rate of any instability.

The quantity U^i describes the degree of FLR introduced into the problem. For clarity, it is best to consider equilibria not involving significant axial velocity, u_z. A1 then describes the net plasma rotation velocity at the singular surface,

$$u_\theta = \frac{1}{\Omega' \rho}\frac{dp_\perp^i}{dr} - \frac{E_r}{B_z}\left\{1 + \frac{B_\theta u_z}{B_z}\right\} \qquad \text{II29}$$

normalised to the FLR effect, U^i.

A2 is a 'Suydam parameter', as the condition $A2<1$ is merely a reiteration of the Suydam stability criterion, modified for the effect of pressure anisotropy. (See ref.(30)) Thus (A2-1) is a measure of the degree by which the equilibrium is MHD unstable due to the effects of adverse pressure gradients.

In order to ascribe a physical context to the quantity R^i in A4, estimate the zero order distribution function, f_0, as a two temperature Maxwellian distribution. This yields $R^i=2P_\perp^2/\rho$, which gives:

$$\frac{1}{2}\frac{dR^i}{dr} - \frac{P_\perp^i}{\rho}\frac{d\rho_\perp^i}{dr} = P_\perp^i \frac{d}{dr}\left(\frac{P_\perp^i}{\rho}\right) = \frac{P_\perp^i}{M^i} K \frac{dT_\perp^i}{dr} \qquad \text{II30}$$

Thus, the first term of A4 describes the collisionless $\underline{B}\times\underline{\nabla}T_\perp^i$ (Righi-Leduc) heat flux. This term is likely to be negative (taking $dT_\perp^i/dr<0$). In the absence of strong fire-hose

destabilisation, the second term of A^4 is positive; this term arises, however, from the quantity γ_2 .(eq.II4). The constraint II13, that arose from the invalidating influence of these terms of moving the perturbation from the resonant surface, limits the magnitude of this positive contribution to A^4 that can be considered within this localised calculation.

A5, the final parameter, incorporates the influence of density gradient. The inclusion of this term introduces the rotational destabilisation caused by the cylindrical geometry that is a feature of this work.

3) Results I - Deductions from the Dispersion Equation.

Two results are immediately apparent upon inspection of the dispersion relation, equation II22.

i) Since the argument of the square root contains $-A^4$, we expect $A^4 > 0$ (due to the dominance of its second term) to destabilise and $A^4 < 0$ (due to a Righi-Leduc contribution) to have a stabilising influence.

ii) The case A5=0 yields marginal stability with $\zeta = 1$ as found by Stringer (24).(Note that, in the present case, ζ is Doppler shifted by the rotation present). For $A5 \neq 0$, this situation is repeated when A1=1 as the rotational contribution to the argument of H at marginal stability vanishes in this case as well. In the absence of u_z, A1=1 implies:

$$u_\theta = \tfrac{1}{2} U^i$$

or, using II29

$$\frac{E_r}{B_z} = \frac{1}{2}\left(\frac{1}{\rho \Omega^i} \frac{dP_1^i}{dr} + \frac{P_1^i}{2\rho\Omega^i B_z^2} \frac{d(B_z^2)}{dr} \right) \qquad \text{II31}$$

At low beta, the special case of rotation described by Rosenbluth and Simon (17) is immediately evident. The case A1=1 is clearly a finite-beta generalisation of this special case.

We now investigate the dispersion relation II22 in the neighbourhood of marginal stability. Consider first a set of parameters (A1to A5) giving real ζ (stable case) and investigate ζ as a function of (say) A2. Since, by hypothesis, ζ is real, the square root of II22 is real and hence all derivatives of ζ with respect to A2 are real. Thus, Taylor expansion is possible to calculate a real value of ζ at A2+δ(A2). This expansion will only fail when $|\partial\zeta/\partial(A2)| \to \infty$. Hence, at marginal stability, the derivative of ζ with respect to any of the 5 parameters diverges. In the case of Stringer (A5=0) this divergence occurred when the argument of the square root vanished; this pertains for the case A5≠0,A1=1 discussed above. Otherwise, differentiation of II22 with respect to A2 yields at marginal stability:

$$1-\zeta = 2(\zeta-A1)A3A5H(\Delta)H'(\Delta) \qquad \text{II32}$$

where $\Delta = A2(1+A5(\zeta-A1)^2)$

and the prime denotes differentiation with respect to Δ.

The marginal stability value of, for example, A2, the Suydam parameter, can, in principle, be obtained by simultaneous solution of II22 and II32 for ζ and $A2_{crit.}$. Although this, by definition, provides a necessary and sufficient criterion for stability against the interchange modes considered, the solution of these equations is neither obvious nor trivial. A useful sufficient condition can be obtained by calculating the value of the required parameter for a given real value of ζ. Since, in the cases A5=0 and A1=1, ζ =1 at marginal stability, this is a suitable selection at which to evaluate the sufficient stability condition. The only requirement of

the calculation is the iteration of the parameter under study to reduce the argument of the square root in II22 to zero when $\zeta = 1$ has been substituted. This may be carried out readily without the aid of a computer and requires merely a graph of H(z) along the real z axis of the type given in Stringer (24) and Kulsrud(23). The sufficient criterion for A2 is thus:

$$H^2(A2\delta) = \nu A2 \qquad \text{II33}$$

where $\delta = 1 + A5(1-A1)^2$; $\nu = (1-A4)/A3$

The additional four parameters A1, A3, A4, A5 have thus been reduced to two by the consideration of the sufficient stability criterion rather than of the more precise marginal stability conditions.

Figure II1 plots this sufficient criterion on A2, the modified Suydam parameter, against the two parameters δ and ν. The criterion thus states that points lying below the curves correspond to stable plasma equilibria. As δ increases, the destabilising effects of the centrifugal forces are clearly apparent as the curves become compressed to smaller values of $A2_{\zeta=1}$. The effect of varying A4 may also be seen on this diagram as it is a linear function of ν. It appears that the effect of A4 will be greatest at small δ values when rotational driving forces are least. Note that, according to this sufficient criterion, $\delta = 1$, which corresponds to the A1=1 case discussed above, is the most stable case of rotation. Recall that, in this case, marginal stability corresponds to the sufficient criterion. At other values of δ, the degree by which the sufficient condition is too severe may be seen by comparing figures II1 and II10 and will be discussed later.

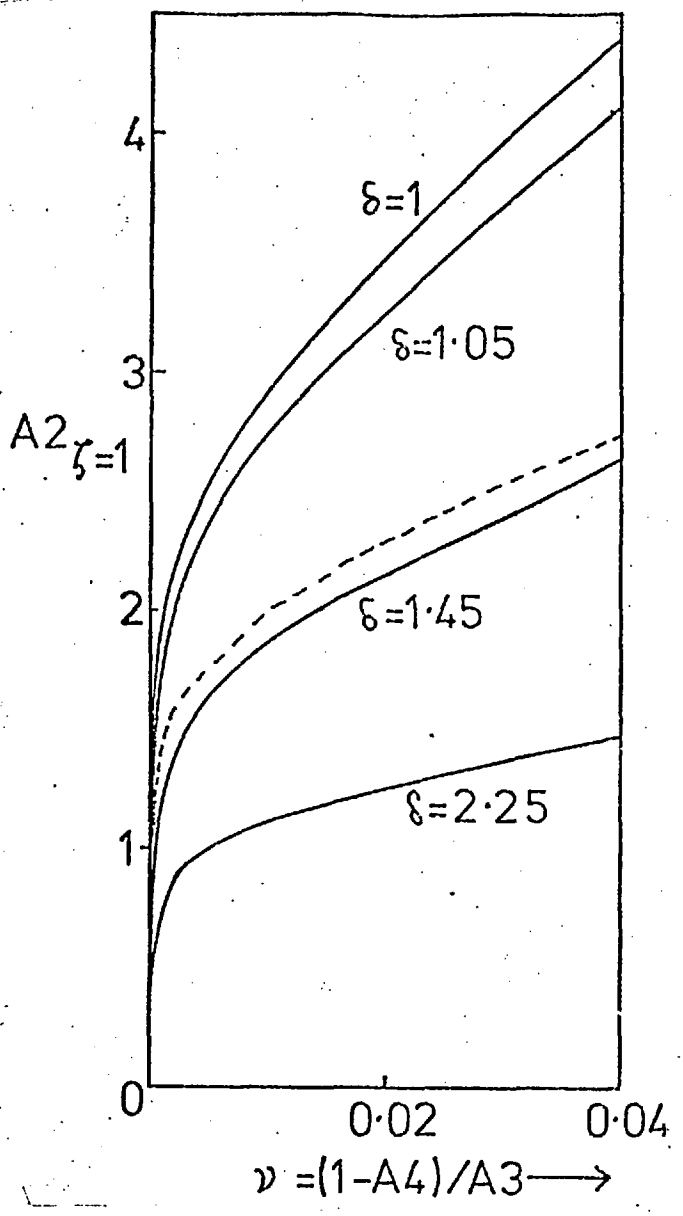

Figure II1 - The sufficient stability criterion $A2 < A2_{\zeta=1}$ for various $\delta = 1+A5(1-A1)^2$. The dashed line indicates marginal stability for A1=-2, A4=0 A5=0.005 from figure II10.

4) Results II - Computations.

In order to study the behavior of ζ as a function of the parameters of the problem, numerical solution of the dispersion relation, equation II22, was required. As this is an analytic differentiable function, Newton-Raphson iteration was employed. Routines to evaluate complex gamma and digamma functions $\left(\frac{1}{\Gamma}\frac{d\Gamma}{dz}\right)$ were obtained from the Cern library, available on the computer used. In order to initiate the iteration procedure, the

explicit case A5=0 was used as a first approximation. Subsequently, ζ was followed as the parameter of interest was varied throughout the desired range of values. As marginal stability conditions were approached, the violent behavior of ζ in the region of the cut-off inevitably caused the method to fail. Since a) the derivatives of ζ are known to tend to infinity at marginal stability and b) curves of both $Re(\zeta)$ and $Im(\zeta)$ were available above cut-off, the critical region was completed by simultaneous extrapolation of the two curves towards a common parameter value. Whilst the extrapolation cannot describe ζ accurately owing to its sensitive parameter dependence in this region, the cut-off value of the parameter against which ζ was plotted (usually A2) could be determined with reasonable precision.

The sequence of diagrams II2 to II5 illustrates the dependence of ζ on the Suydam parameter, A2, for different degrees of plasma rotation, measured by A1. Variation of A3 is implicit in the variation of m; A3 was taken to be $1600/(m^2-1)$ upon consideration of Stringer's (24) data for $H_\beta TX$. The figures take A4=0, A5=0.05.

The effect of rotation upon the frequency of oscillation of unstable modes is the most immediately striking feature of figures II2 to II5. Only when A1=1, does $Re(\zeta)$ take a constant value when $Im(\zeta)\neq 0$. In this case the square root in equation II22 has its argument real and negative when ζ is complex. The combination A1=1, $Re(\zeta)=1$, on consideration of the definitions II23, II24 (with $u_z=0$), implies $Re(\omega)=0$. Thus, in this case, the instability is absolute, with the equilibrium plasma rotating through the growing stationary

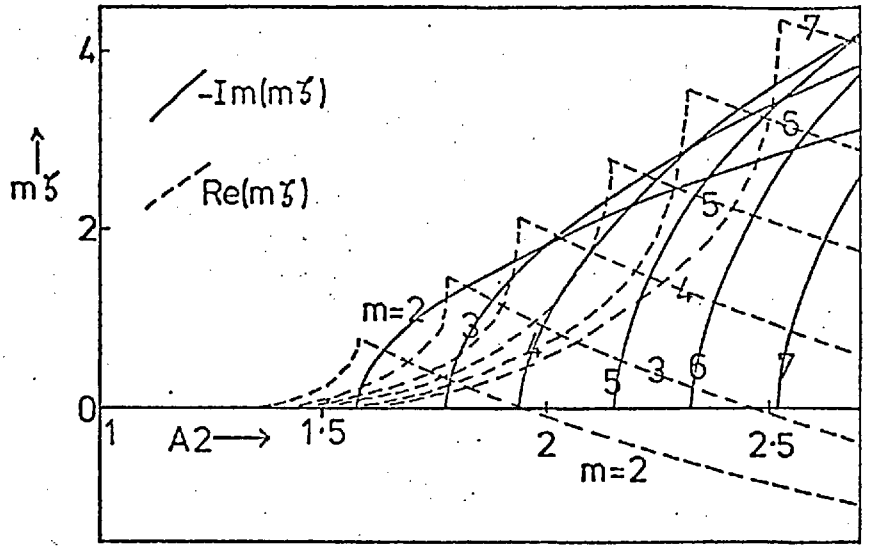

Figure II2 - Real and imaginary parts of the normalised complex frequency $m\zeta$ plotted against the Suydam parameter, A2, for A5=0.05, A1=-2, A4=0, A3=1600/(m^2-1). Note that the second stable solution has been omitted below marginal stability.

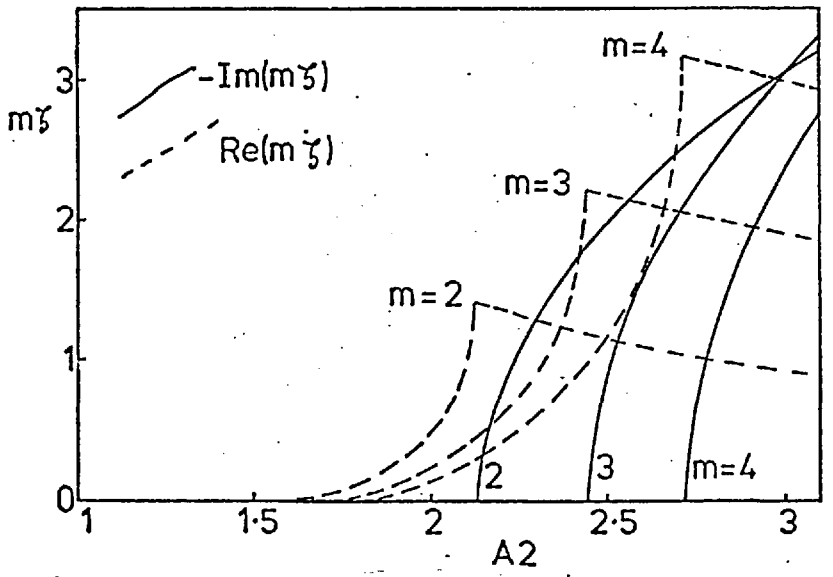

Figure II3 - $m\zeta$ versus A2 with A1=0 and other parameters as in figure II2.

perturbations. For other rotations, including the case of stationary equilibrium, Re(ω) is non-zero. However, as increasingly more unstable plasmas are considered, so Re(ζ) approaches A1 more closely and hence |Re(ω)| becomes smaller.

Three features are apparent in the growth rates in figures II2 to II5 : i) For a given m number, cut-off occurs at smaller

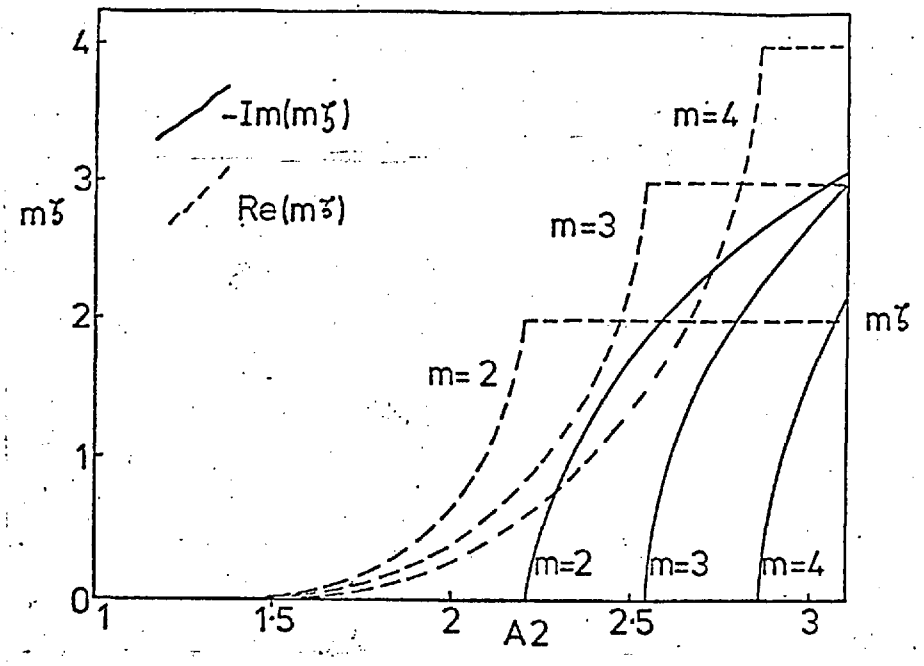

Figure II4 - mζ versus A2 with A1=1 and other parameters as in figure II2.

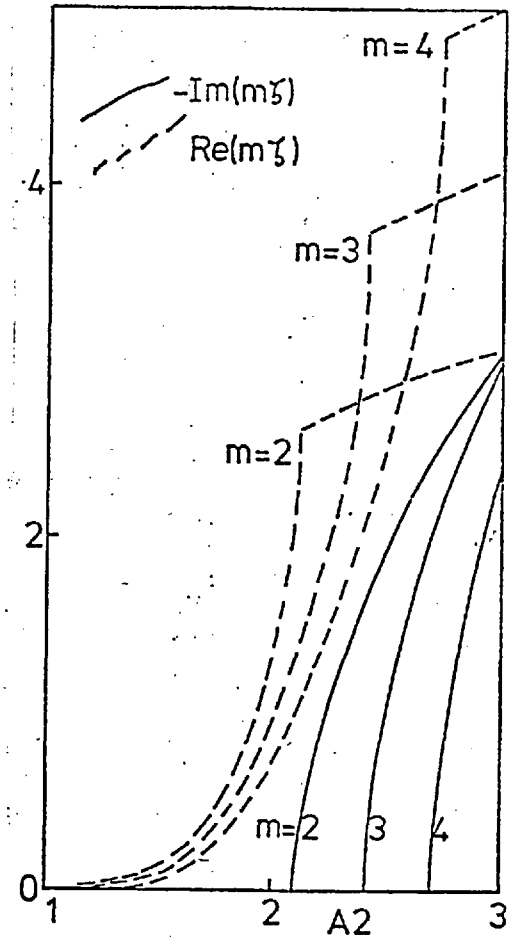

Figure II5 - mζ versus A2 with A1=2 and other parameters as in figure II2.

values of A2 as |A1-1| increases. This is the destabilising rotational effect discussed above. ii) Modes become unstable

in order of increasing m as A2 rises. This occurs since the effect of FLR depends upon the azimuthal spatial derivative of the perturbation and hence increases with m. iii) As A2 rises beyond the critical value, so modes with greater m become the most unstable. The dominant instability thus increases in m as plasmas with more adverse pressure gradient are considered.

Comparison of figure II6 with II2 reveals the effects of including a negative contribution to A^4 from Righi-Leduc heat flux. The effect on the oscillation frequency is most marked below marginal stability. As is evident from the dispersion equation, for the stable branch indicated, $Re(\omega)$ is reduced so that the relative rotation of plasma and perturbation is increased. Elsewhere, a lesser reduction in $Re(\omega)$ is apparent. The stabilising effect of negative A^4 on the growth rate operates both by delaying cut-off until larger A2 (pressure gradient) is present and by reducing the

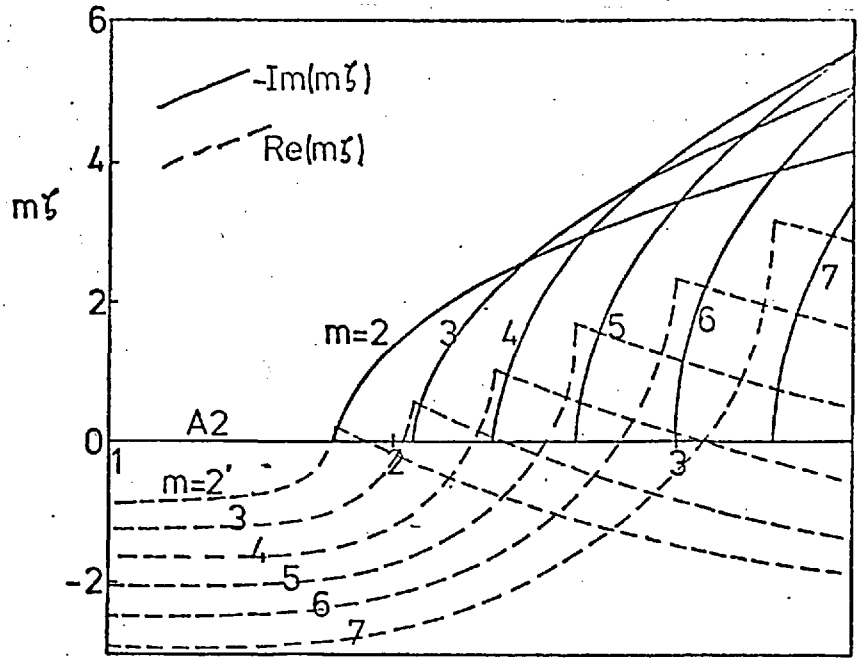

Figure II6 - mζ versus A2 with A1=-2, A^4=-1, A5=0.05, A3=1600/(m^2-1).

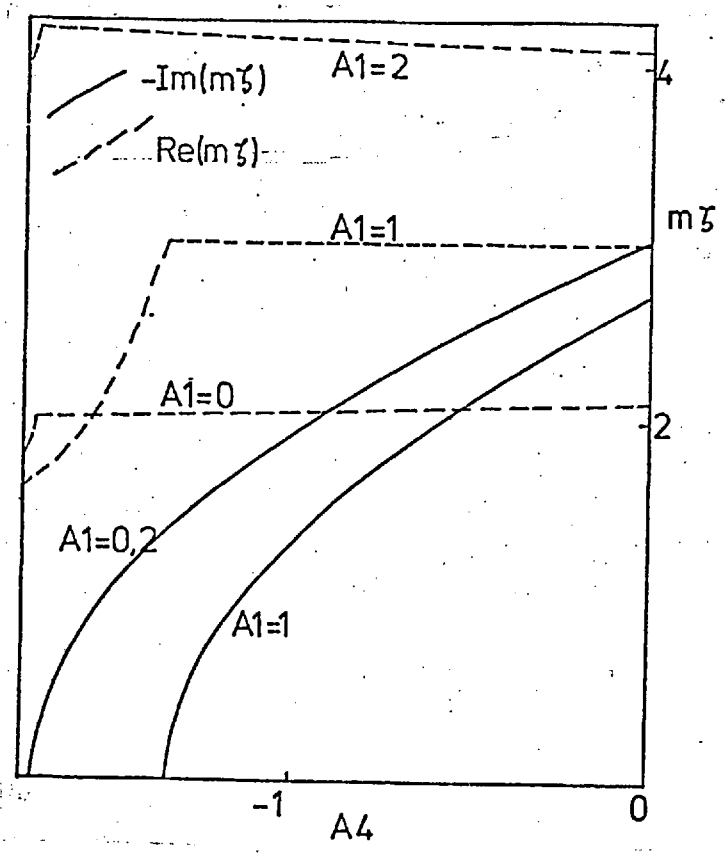

Figure II7 - mζ versus A4 with A1=0,1 and 2, A2=3, A3=1600/(m^2-1),m=3, A5=0.05.

growth rate of unstable modes. As the magnitude of these influences rises with increasing m number, the dominant m for a given unstable A2 tends to be reduced.

The effect of increased -A4 for various rotations appears in figure II7. Observe that the growth rate reduction is greatest for the weakest rotation (smallest |A1-1|) and that, for A1≠1, the effect on the oscillation frequency is to marginally reduce Re(ω) and hence the rotation of the perturbation. (Recall Re(ζ)=A1 implies Re(ω)=0)

The potential of Righi-Leduc heat flow as a stabilising agency must, however, be viewed with caution. The leading term of A4, in expression II27, may be written:

$$\frac{4\,\frac{d}{dr}(\ln T_i')\,\frac{d}{dr}(\ln B_z)}{\left(\frac{d}{dr}(\ln p_i')\right)^2} \sim -2\beta$$

As, in practice, beta is limited to values considerably less than one, large negative values of A^4 are never likely to occur. Destabilisation by positive A^4 due to the second term of II27 has not been considered here due to the limitations in the theory discussed above.

A systematic examination of the effects of varying rotation (A1) appears in figures II8 and II9. In figure II8, rotational destabilisation is apparent; the effects of adverse pressure gradient dominate in figure II9 so that flatter growth rate plots occur. The violent dependence of ζ on A1 close to marginal stability is clearly apparent in figure II8. Again, the effects of rotational destabilisation increase as m rises so that, as found by Bowers (10) for simpler configurations, although modes become unstable in the

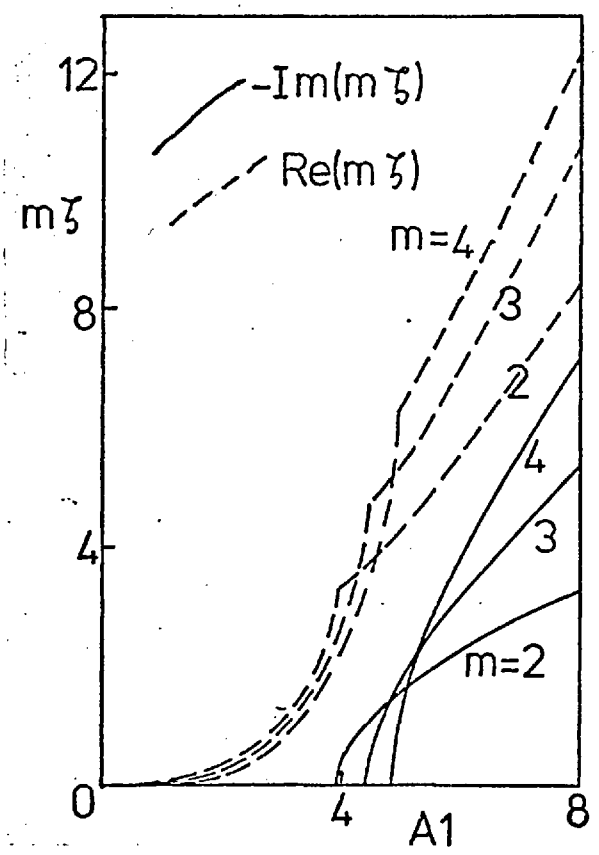

Figure II8 - $m\zeta$ versus A1 (rotation). A2=1.6, $A3=1600/(m^2-1)$, A5=0.05, $A^4=0$.

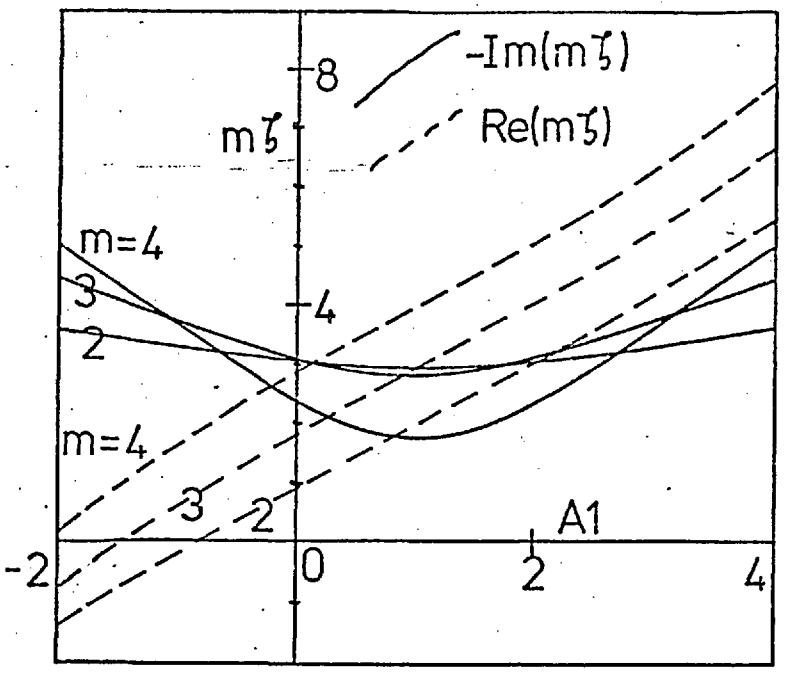

Figure II9 - mζ versus A1 (rotation), A2=3, A3=1600/(m^2-1), A5=0.05, A4=0.

order of their m numbers, higher m numbers become dominant as rotation increases. Figure II9 clearly demonstrates A1=1 (rather than A1=0) to be the most stable rotation possible. The region $0<A1<1$ demonstrates stabilisation as rotation increases. These curves clearly reflect the $(\zeta-A1)^2$ term in the dispersion law by their quasi-symmetry about A1=1. Similarly, the pseudo-anti-symmetry of the corresponding oscillation frequencies about A1=1 (at which $Re(\omega)=0$) is evident.

Figure II10 summarises the marginal stability conditions on A2 for various rotations. To the accuracy of the computations, the A1=2 and A1=0 curves are coincident. The utility of the sufficient stability criterion discussed earlier may be seen by comparing the A1=-2 curve of figure II10 with the δ =1.45 curve of figure II1. They, of course, agree as $1/A3\to 0$ ($\nu\to 0$) and the former exceeds the latter by only 5% at 1/A3=0.03.

Comparison of figures II11 and II10 shows the increased

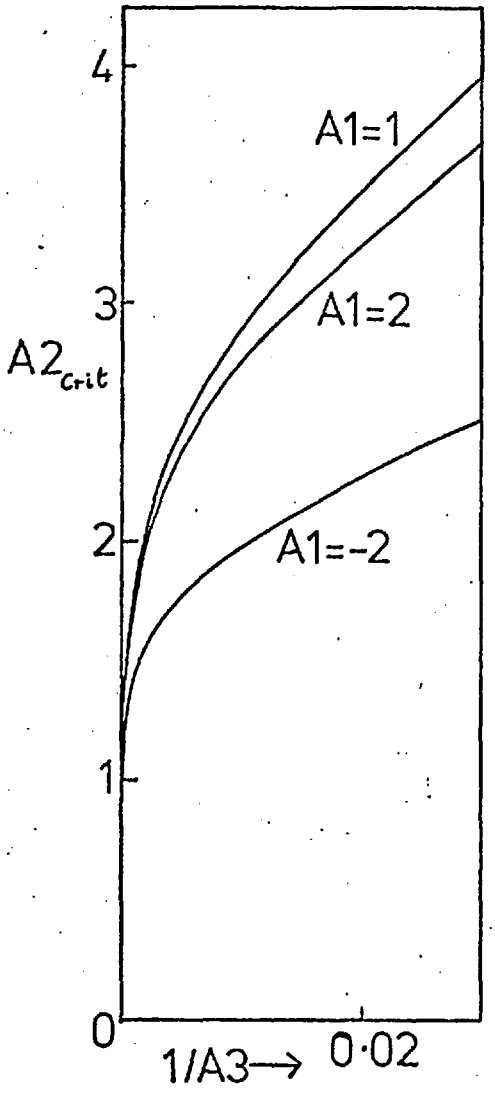

Figure II10 - Values of the Suydam parameter, A2, at marginal stability ($A2_{crit}$) versus the principle FLR effect, 1/A3, for different values of A1 (rotation). A4=0, A5=0.05.

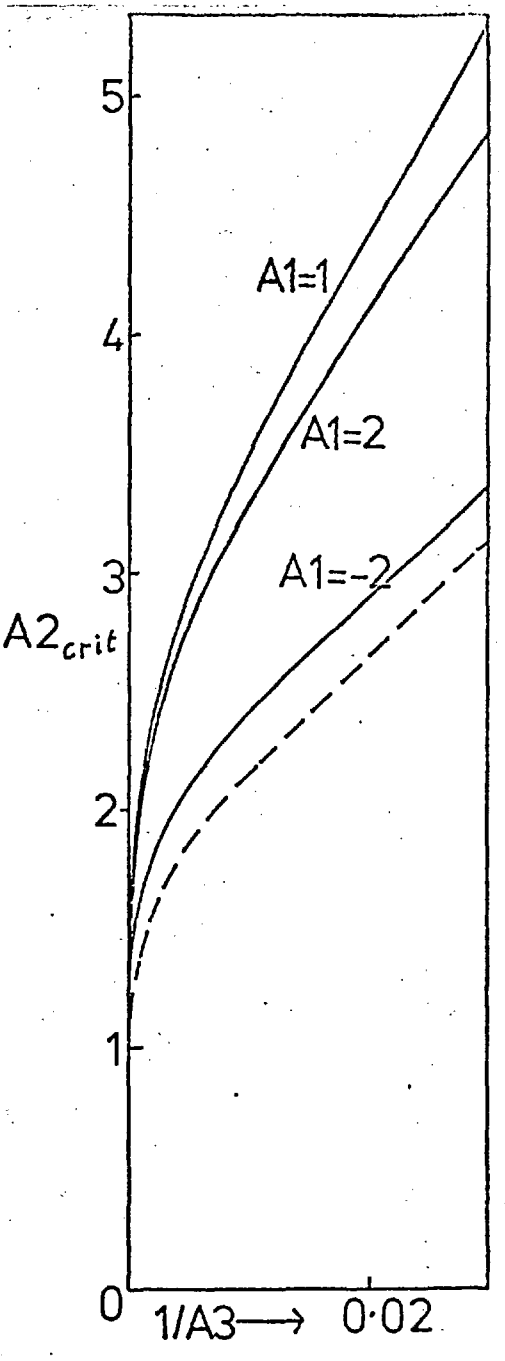

Figure II11 - Values of $A2_{crit}$ versus 1/A3 with A5=0.05 and A4=-1 (Righi-Leduc). The broken line displays the sufficient condition of figure II1 for A1=-2, A4=-1, A5=0.05.

stabilisation (larger $A2_{crit}$) due to the inclusion of a strong Righi-Leduc contribution to A4. Note that this increase is still less than one half of the stabilisation by 1/A3, the dominant FLR term. Closer examination of figure II11 reveals that, even with the large -A4 included, the

sufficient criterion of fugure II1 is only 7% too severe on $A2_{crit.}$ with A1=-2 and 1/A3=0.03.

5) Conclusion.

The method of Kulsrud (23) and Stringer (24) can be applied to the equation derived by Pott (30) in order to investigate the effect of further physical phenomena upon plasma stability to interchange modes. Rotation is the principle effect included and is found to interact with FLR phenomena in a manner such that the plasma is most stable when it possesses finite rotation given by equation II31.

Although an explicit marginal stability criterion could not be derived, analogous to that of Suydam (2), a sufficient criterion was produced that can be made to yield useful results without the need to program an electronic computer. An accurate plot of the function $H_{1even}(z)$ (eq. II19) along the appropriate part of the real z axis is all that is required. The results of this sufficient criterion are only 5 to 10% stricter on the pressure gradient than precise marginal stability requirements in the regime studied wherein rotational destabilisation competes with rather than totally dominates the pressure gradient.

Righi-Leduc terms, a secondary effect of FLR are shown to have a stabilising effect, small compared to the more familiar terms, unless the collisionless heat flux is given an artificially large value.

Chapter III.

Numerical Solution of the Collisionless Eigenvalue Equation.

1) Introduction.

Whilst the semi-analytic solution of Pott's (30) eigenvalue equation in the previous chapter provided a general understanding of the effects of the many terms present, the constraints of the approach do not allow thorough investigation of the complete range of equilibria encompassed by the model. In particular, three situations require further study. 1) As will be seen in section 3, modes with small m numbers are poorly described by the analytic approach and, especially when close to marginal stability, give rise to the fastest growing instabilities present. 2) When rotational effects dominate the pressure gradient driving forces, the radial localisation approximations of chapter II tend to break down. In this limit, the effects of the inclusion of equilibrium B_θ, and hence, magnetic field curvature may be investigated by comparing the results with those of Bowers (10) who considered the straight field limit. 3) It was noted in chapter II that the phenomena comprising the second term in the parameter A^4 (equation II27) tended to displace the dominant part of the perturbation away from the resonant surface (defined by: $\bar{k}_{r=r_s}=k+mB_\theta/r_sB_z \quad r=r_s=0$). Large displacements of this type violate the most basic assumptions of the analysis of chapter II and must therefore be investigated by alternative means.

2) Numerical Method.

The eigenvalue equation (eq. I11 & ref. 30) takes the same form as that solved by Bowers (10) :

$$\frac{d}{dr}\left(F\frac{d\xi}{dr}\right)+G\xi = 0 \qquad \text{III1}$$

However, in the present case, the main perturbations of interest are associated with F becoming small at some radius within the plasma. No resonant surface phenomena were possible in the straight magnetic field case of Bowers(10). The mode localisation effects that were so essential to the development of the analytic theory of chapter II are the main source of difficulty in a numerical solution; any discrete mesh must have sufficient resolution to describe the eigenfunction in the vacinity of a resonant surface. Thus, although the underlying ideas in the numerical method are the same as those employed by Mc Namara (43) in the program used by Bowers (10), considerable effort in developing a new, reasonably reliable code was required in order that meaningful results could be produced.

The functions F and G (eq. I11) contain the multitude of physical quantities defining the equilibrium of the plasma. In order that these might be compared and assigned numerical values for the purposes of computation, a series of scale frequencies was defined, each member characterising a particular physical effect:

Alfvén frequency: $$W_A = \frac{B_{z0}}{r_x \sqrt{\rho_0 \mu_0}} \qquad \text{III2}$$

Electric rotation frequency: $$W_E = \frac{E r_x}{r_x B_{z0}} \qquad \text{III3}$$

Ion drift frequency: $$W_F = \frac{K T_{\perp 0}^i}{e r_x^2 B_{z0}} \qquad \text{III4}$$

Axial velocity frequency: $$W_Z = \frac{u_{z0}}{r_x} \qquad \text{III5}$$

Axial heat flux frequency: $$W_{QZ} = \left(\frac{q_{z0}^{\perp i}}{\Omega_0' r_x^3 \rho_0} \right)^{1/2} \qquad \text{III6}$$

Temperature anisotropy frequency:

$$W_M = \left(\frac{K \Sigma (T_{//} - T_\perp)_o}{M^i r_x^2} \right)^{1/2} \quad \text{III7}$$

Here, subscript $_o$ refers to a value on axis and subscript $_x$ refers to a value at the wall. In addition, the following were also required to define the problem:

Azimuthal mode number: m

Pitch of mode: kr_x/m

Normalised plasma pressure:

$$\beta = \frac{n_o K \Sigma (T_\perp)_o}{B_{zo}^2 / 2\mu_o}$$

Normalised radial coordinate:

$$a = \frac{r}{r_x}$$

Equilibrium profiles of the following quantities were also required:

n (number density), $\frac{E_r B_{zo}}{a B_z E_{r_x}}$, $T_\perp^i$, $\Sigma_{\text{species}} T_\perp$, $\Sigma_{\text{species}} (T_{//} - T_\perp)$,

$\mu = \frac{B_\theta}{a B_z}$, $q_z^{\mu i}$, u_z.

With the exception of μ, these were all normalised to unity on axis. For convenience and for clarity of the magnitude of destabilising effects, most profiles were taken to be constant. The exceptions were number density, which was usually Gaussian, μ which was usually Lorentzian to approximate the pitch from a central current channel and ion temperature which was usually constant, but given a steep profile in the investigation of the Righi-Leduc effect. As in chapter II, $q_\theta^{\ i}$ was evaluated by estimating the fourth moment, R , using a double-Maxwellian velocity distribution in lowest order. The radial dependence of B_z was derived from the equilibrium

pressure balance requirements (eq. I10):

$$p_\perp + \frac{B_z^2}{2\mu_0} = \text{constant}$$

so that: $$B_z = B_{z0}\left(1 + \beta\left(1 - \bar{n}\sum_{\text{species}}\overline{T_\perp}\right)\right)^{1/2} \qquad \text{III8}$$

where $\bar{n}$ and $\sum_{\text{species}}\overline{T_\perp}$ define the respective normalised profiles.

The boundary condition appropriate to the problem is that ξ vanish at the rigid, conducting wall where a=1. At the axis, a=0, symmetry requirements demand that:

$$\xi = 0 \qquad \text{for } m \neq 1 \text{ or}$$

$$\frac{d\xi}{da} = 0 \qquad \text{for } m = 1$$

Numerical solution of equation III1 subject to these boundary conditions must seek an estimate of the most unstable value of ω(i.e. that with the largest negative imaginary part) by approximating the eigenfunction at a set of discrete points. To this end, the plasma radius, $0 \leq a \leq 1$ was divided into a number, N, of equal steps. Empirically, it was found that as few as fifteen could be employed to obtain a rough estimate of the frequency required when localisation was poor, but, typically N=20 was used for a first approximation. Thus, differencing III1 yields:

$$\xi_{n+1}\left(\frac{F_n}{\delta^2} + \frac{F_n'}{2\delta}\right) + \xi_n\left(G_n - \frac{2F_n}{\delta^2}\right) + \xi_{n-1}\left(\frac{F_n}{\delta^2} - \frac{F_n'}{2\delta}\right) = 0 \qquad \text{III9}$$

where the vector components ξ_n, F_n, F_n', G_n denote the respective functions evaluated at a =n/N and the mesh step, δ, equals 1/N. Since both F and its first derivative F' are separately required in III9, equilibrium quantities were, in fact, evaluated $\delta/100$ on either side of each mesh point so that, for example:

$$F_n = \frac{1}{2}\left[F\left(\frac{n+.01}{N}\right) + F\left(\frac{n-.01}{N}\right)\right]; \quad F_n' = 50N\left[F\left(\frac{n+.01}{N}\right) - F\left(\frac{n-.01}{N}\right)\right]$$

In this way, both F_n and F'_n were obtained with only two evaluations of F(a), thus minimising the computational effort involved. This technique also ensured that high order derivatives of the equilibrium profiles were not explicitly required by the calculation. As these could have been reasonably supplied only by coding them explicitly as separate subprograms, this feature added to the ease with which different profiles could be inserted into the computations.

The implementation of the axial boundary condition on the m=1 mode remains the only problem. For this mode, both F and G have an a^3 dependence near the axis. Thus, differentiating equation III1 three times at a=0 yields:

$$4 F''' \frac{d^2\xi}{dq^2} + G''' \xi = 0$$

Symmetry demands that $\xi_{-1} = \xi_1$, so that differencing at a=0 gives: $\frac{8 F_0'''}{\delta^2}(\xi_1 - \xi_0) + G_0''' \xi_0 \approx 0$

Since $F_0''' \approx \frac{1}{\delta}\left(F''\left(\frac{\delta}{2}\right) - F''\left(-\frac{\delta}{2}\right)\right) = 2\frac{F''\left(\frac{\delta}{2}\right)}{\delta} \approx 2\frac{F'(\delta)}{\delta^2}$

and similarly $G_0''' \approx \frac{2G'(\delta)}{\delta^2}$

the boundary condition may be written:

$$\xi_0\left(\frac{2G_1'}{\delta^2} - \frac{16F_1'}{\delta^4}\right) + \frac{16}{\delta^4} F_1' \xi_1 = 0 \qquad \text{III10}$$

for m=1.

Thus, since the derivatives of the equilibrium functions F and G were readily obtainable from the coding required for the difference equation III9, the boundary condition III10 is in a form readily suited to the numerical scheme.

The difference equations III9, together with the boundary conditions thus define a homogeneous matrix equation for ξ_n:

$$A_{ij}\,\xi_j = 0, \quad j = 0, N \qquad \text{III11}$$

The matrix $\underline{\underline{A}}$ is evidently tri-diagonal. For a solution to III11 to exist, the determinant of $\underline{\underline{A}}$ must vanish. Thus, the frequency of the perturbations was estimated by iterating, in the manner discussed below, until $\det(\underline{\underline{A}})$ was reduced to zero. Since many such iterations were often required, it was essential to compute $\det(\underline{\underline{A}}(\omega))$ as fast as possible.

The elements of $\underline{\underline{A}}$ depend linearly on F and G which are each quadratic in the frequency ω. Thus, before iteration began, the three quadratic coefficients of each element of $\underline{\underline{A}}$ were calculated from the equilibrium data specified and stored. The computation involved in the evaluation of the determinant was thus reduced to the evaluation of a quadratic for each element of $\underline{\underline{A}}$, followed by the determinant calculation from the recursion formula: (see Fox & Mayer (39))

$$D_{n+1} = A_{2,n+1}D_n - A_{1,n+1}A_{3,n}D_{n-1}$$

Here $A_{1,n}$, $A_{2,n}$, $A_{3,n}$, denote the three elements of the nth row of $\underline{\underline{A}}$ and the D_n denote the intermediate determinants in the sequence. Thus:

$$D_0 = A_{1,0}\ ,\ D_{-1} = 1\ ,\ \det(\underline{\underline{A}}) = D_N\ .$$

In order to determine the roots of the determinant, an iteration algorithm was required. Muller's method of quadratic interpolation (40) was found to be adequate. This method approximates the function concerned by a quadratic in the region of three guesses at a root; an improved approximation is then obtained by taking the root of the quadratic closest to the supplied guesses. The procedure was initiated by selecting three points randomly around a single initial guess. In order to produce an algorithm capable of finding roots whose moduli might vary by several orders of magnitude, the modulus of the difference of each

point from the initial guess was scaled by a small fraction of the modulus of the supplied estimate of the root. Of the four points selected in this way (one supplied and three generated) , the one that produced the determinant of largest magnitude was discarded in the manner of Martin (41). Once the procedure had been initiated in this way, the three guesses were in turn sequentially replaced by the results of the application of the iteration algorithm.

In order to gain an estimate of the eigenfrequency of the most unstable mode of a given parameter set, all the roots of the determinant associated with a mesh of as few points as possible were obtained. This was achieved by iterating, starting from a random point in the complex plane. As each root, ω^i , was determined to the accuracy required (three significant figures in each of its real and imaginary parts with 'zero' defined as being less than 10^{-4}) it was stored and deflated from every subsequent determinant evaluation by explicitly dividing by $\prod_i(\omega-\omega^i)$. Since all of the coefficients of ω and ω^2 in F and G of the eigenvalue equation are real, the roots determined are either real or in complex conjugate pairs. Thus, whenever a complex root was determined, its complex conjugate was also added to the list of known values to be deflated from subsequent calculations.

Having selected the most unstable eigenfrequency from the large number computed using the small mesh, its accuracy was improved by attempting to follow its behavior as the number of mesh points was gradually increased. For weakly unstable cases, where localisation was greatest, fifty or even one hundred mesh steps were required before acceptable convergence of this procedure was obtained.

Since a large number of the modes found in the initial small mesh computations consist of unphysical numerical oscillations, the technique employed does not, in itself, guarantee that the most unstable mode of the initial numerical problem corresponds to that of the continuous differential problem; there remains the possibility that the actual fastest growing mode consists of short wavelength oscillations not resolvable on a coarse mesh. The main defence against this possibility lies within the results of analytic theory. In the pure MHD limit it is known that the growth rate of the instabilities decreases monotonically as the number of nodes in the eigenfunction increases. (see Goedbloed et al. (42)). Thus, we expect the most unstable mode to have a relatively smooth eigenfunction and hence be resolvable on a relatively coarse mesh of the type used in the initial procedure. The analytic results of Kulsrud (23), that were further developed in chapter II, indicate that this property is maintained when the ion-drift FLR terms are included. Applying the numerical technique to equilibria incorporating the theoretically less common effects in the eigenvalue equation investigated is thus seen to involve the intuitively justifiable assumption that the instability studied is, in fact, the most unstable. Further justification of this assumption appears in chapter IV (figure IV17) when the method, on application to a more complicated system of resistive equations, detected a mode with an oscillatory eigenfuntion as the most unstable.

Two checks were employed to reveal any numerically inaccurate, deceptive results. Firstly, the ability of a coarse mesh calculation to iterate complex roots in conjugate

pairs was ascertained, before this result was employed to shorten the calculation. This verified that the numbers printed out were, in fact, roots of the determinant investigated. Secondly, the eigenfunctions themselves were regularly plotted to ensure that they satisfied the boundary conditions imposed. Whilst accurate modes could often be plotted only with an eigenfrequency iterated to seven significant figures or more, owing to the numerically unstable procedure of inverting the difference equations , III9, it was found that additional iterations of the root-solving algorithm required for this did not alter the frequency to its initial three figure accuracy.

One final technique deserves mention. Computing a large number of zeros of a determinant is obviously a very uneconomical way of obtaining a starting value from which to seek an accurate result. The growth rate of an instability is clearly a continuous function of the parameters defining the equilibrium. Thus, perturbation methods were sometimes employed to determine the dependence of the complex frequency of a particular mode on a parameter of the system. This suffers the disadvantage that it will not reveal ranges of the parameter in question for which a different mode is dominant. As the functions employed had large numbers of roots, small parameter perturbations had to be used in order to ensure that the correct mode was found at each step. For this, collisionless, problem the effort in covering a range of parameter space by perturbation methods was comparable to that of distinct calculation at a pre-determined set of points; the advantages of each method could be exploited where required. In chapter IV, economic computing will be seen to be feasible

only by the adoption of perturbation methods.

3) Suydam Modes.

The primary reason for the introduction of magnetic field shear into a confined plasma is to restrict the growth of the electrostatic flute modes that appear in the straight field limit. (See Rosenbluth and Simon (17)). When equilibrium B_θ is introduced into the theta-pinch, the flute modes become electromagnetic interchange instabilities that tend to be localised in the region of the resonant surface ($\mu + kr_x/m = 0$) as discussed in chapter II. As will be seen in figure III6 the localisation of the modes tends to be poorest at low m numbers so that the previous analytic theory cannot be expected to apply. In this limit, the numerical treatment of these modes, presented below, is required to complement and compare with the results of chapter II; the m=1 mode can be studied only by numerical means.

Firstly, in order to provide a basis for comparison, consider the behavior of the interchange modes in the absence

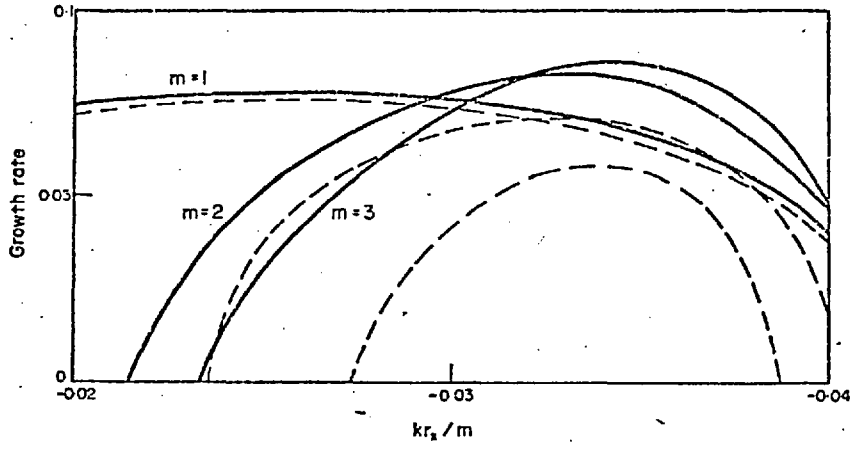

Figure III1 - The variation of the growth rate of Suydam modes with normalised axial wavenumber for different azimuthal wavenumbers with $\beta = 0.5$, $W_A = 10$, $n = \exp(-0.5(a/0.3)^2)$, $\mu = 0.01/(0.25+a^2)$. $W_F = 0$ on solid lines, $W_F = 0.0035$ on broken lines.

of finite Larmor radius effects. (W_F=0). Figure III1 (solid lines) demonstrates the dependence of the growth rate of Suydam modes upon axial wave-number in this limit. Since, as marginal stability is approached in this MHD limit, the kinetic energy of the perturbation tends to zero, the modes become too localised to be resolved on a discrete mesh; the curves are therefore extrapolated below $\gamma \approx 0.02$. (Note that, throughout this chapter, all frequencies are expressed in arbitrary units defined by W_A=10). As the Suydam criterion (2) (A2<1 in the notation of chapter II) is violated, for the profiles used, when $kr_x/m=-0.02$, figure III1 indicates that the cut-offs of the m=2 and m=3 modes shown are in reasonable agreement with this result. At large k, these modes cut-off just beyond $kr_x/m = -0.04$ at which value the resonant surface collapses into the origin.

The m=1 mode is clearly an exception. Physically, the m=1 mode differs in that it is the only type of instability for which symmetry constraints allow the centre of mass of the cross-section of the plasma to move. Thus, the low $|k|$ cut-off occurs only when the resonant surface approaches the rigid containing wall.

This sharp cut-off of the m=1 instability is clearly illustrated in figure III2. When cut-off occurs, the steep gradient in the kink-like m=1 perturbation arises close to the wall. Since the plasma pressure is minute in this region, the interaction is electromagnetic. Ampère's law indicates that the surface currents induced in the perfectly conducting walls are:

$$I_\theta' \propto B_{z\,wall}' \propto \xi_{wall} = 0$$
$$I_z' = \frac{1}{\mu_0} B_{\theta\,wall}' = \frac{k B_z}{\mu_0} \left.\frac{d\xi}{dr}\right|_{wall} \qquad \text{III12}$$

Before the resonant surface reaches the wall, $\left.\frac{d\xi}{dr}\right|_{wall}$ is

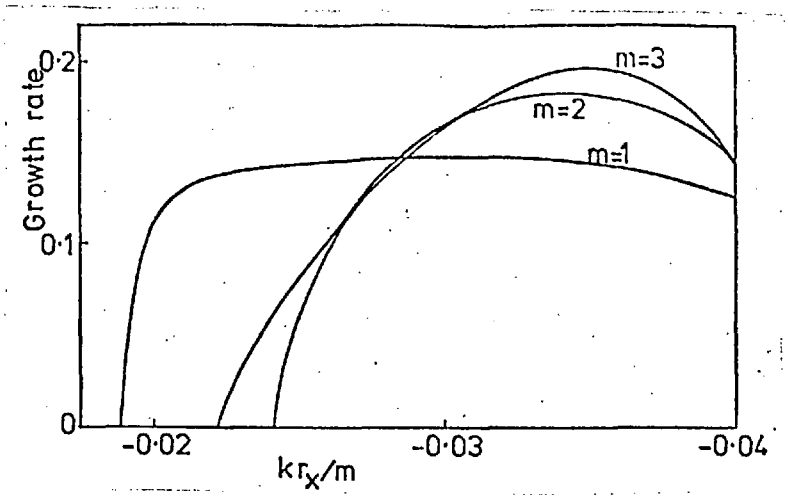

Figure III2 - The variation of the growth rate of Suydam modes with normalised axial wavenumber for different m numbers with $\beta = 0.5$, $W_A = 10$, $n = \exp(-0.5(a/0.3)^2)$, $W_F = 0$, $\mu = 0.04/(1+a^2)$.

small so that interaction is minimised. $I_z' = 0$ when the resonant surface occurs at the wall since, by definition, $\bar{k}_{wall} = 0$ in that case. When the surface has passed through the wall, however, $\bar{k}_{wall}$ is finite and $\frac{d\xi}{dr}\Big|_{wall}$ is very large so that I_z' becomes significant and generates the mode cut-off. The manner of this interaction explains the abrupt nature of the m=1 cut-off illustrated in figure III2. A further example appears in figure III8.

The centre of the kr_x/m spectrum shown in figure III1 is dominated by the higher m modes; observe, however, that, as the resonant surface moves into regions of more adverse pressure gradient, the modes become unstable in order of their m numbers. Largest growth rates are seen to occur when the resonant surface lies in the region of greatest pressure gradient.

The effect of magnetic field shear on the instabilities may be seen by comparing figures III2 and III1 (solid lines). In the former case a considerably less steep profile of magnetic

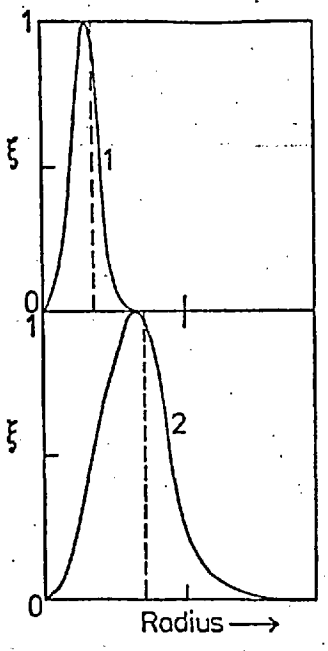

Figure III3 - Eigenfunctions in the absence of FLR: $W_F=0$, $W_A=10$, $\beta=0.5$, $n=\exp(-.5(a/0.3)^2)$, $kr_x/m=-0.035$, $m=3$
1) $\mu=0.01/(0.25+a^2)$;
2) $\mu=0.04/(1+a^2)$.
The broken lines indicate the resonant surfaces.

pitch was employed. Note that, although the two sets of curves have the same general shape, growth rates are much greater in figure III2. Comparison of the eigenfunctions of the two examples for m=3 at $kr_x/m=-0.035$ in figure III3 indicates that weaker shear produces considerably broader eigenfunctions. This is intuitively expected since the region on either side of the resonant surface, for which the mismatch between perturbation and magnetic field helices is sufficiently small for interchange effects to be energetically favoured is considerably broader in the weak shear case.

The result of increasing the effect of FLR (W_F) for a fixed axial wavenumber is portrayed in figure III4. Note that, in this case, the electric field (W_E) was zero so that the plasma had a net equilibrium rotation given by the ion drift arising from the Hall terms of Ohm's law (eq. A7). The m=1 mode in this diagram is seen to be affected only weakly by FLR in comparison with the higher m instabilities; W_F increases in effectiveness as m rises, however. This may be understood as the effect arises in the stress tensor, $\underline{\underline{\tau}}$.

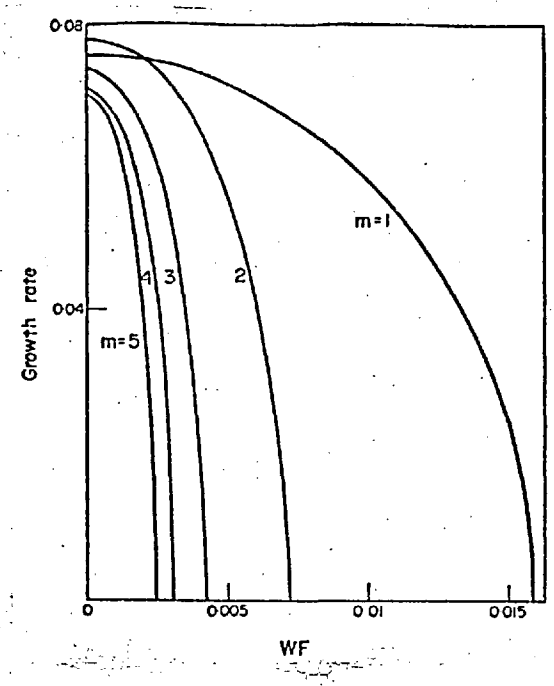

Figure III4 - The stabilisation of Suydam modes by FLR effects, with $W_A=10$, $\beta=0.5$, $kr_x/m \stackrel{A}{=} -0.03$, $n=\exp(-0.5(a/0.3)^2)$, $\mu=0.01/(0.25+a^2)$.

Larger m implies larger $\frac{1}{r}\frac{\partial}{\partial\theta}$ and hence that $\underset{\sim}{\nabla}\cdot\underset{\equiv}{\tau}$ will exert a greater influence upon the perturbations. The phase-shifted ion currents that cause FLR stabilisation thus increase in magnitude as m rises.

Figure III5 indicates that, as W_F rises, the frequency of oscillation of the perturbations ($Re(\omega)$) rises in proportion to mW_F. Since $Re(\omega)$ is positive for the examples shown in this figure, this agrees with the result of chapter II that, when $A1>1$, then $Re(\zeta)>1$ at marginal stability. ($A1=1.77$ at the resonant surface for the curves of figure III5).

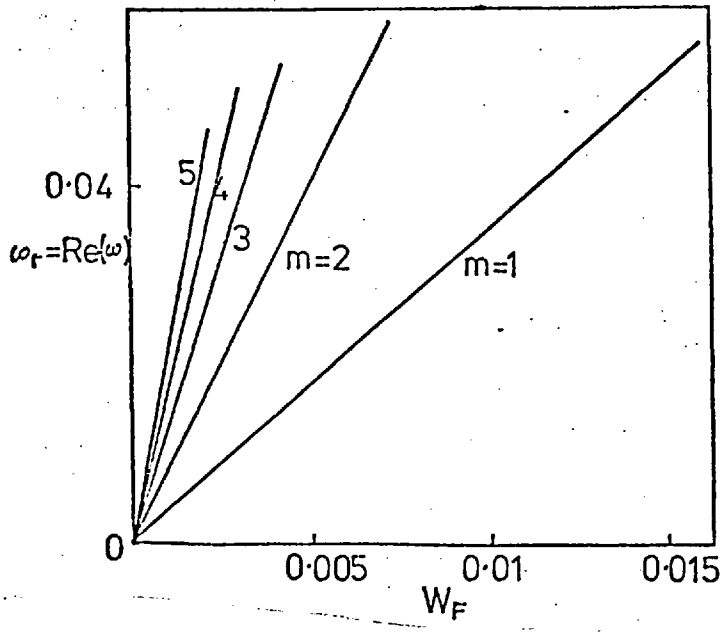

Figure III5 - Frequency of oscillation of the instabilities of figure III4.

At this point, some idea of the temperatures involved in these stabilisation effects is pertinent. Using the expressions III2 and III4 , we deduce that, with B_z=1T, n= $10^{19}m^{-3}$, r_x=0.3 m, T^i =500 eV and W_A=10, then W_F=0.003. Thus, in figure III4, the m=2 mode cuts off at an ion temperature of about 1 keV for the parameters quoted.

The effect of FLR on the axial wavenumber (k) spectrum is indicated by the broken lines of figure III1. Note that the region of sharply varying modes, close to the MHD cut-off, that could not be previously resolved is completely stabilised. As the stabilising efficiency of FLR increases with m, the peaks of the separate spectra now occur in reverse order of m number.

Increased ion temperature causes the eigenfunction to become complex, a small imaginary part being generated as W_F rises. This signifies the superposition of a small amplitude radial travelling wave upon the main, growing, standing wave component. Figure III6 illustrates this effect at a given value of W_F for various m numbers. Note the expanded scale on the imaginary parts in this diagram. Imposed normalisation ensures that ξ is real on the first mesh point near the axis at which it is non-zero. As m increases at constant W_F, so the corresponding growth rate falls until, when γ =0, Im(ξ) vanishes. (All coefficients in the eigenvalue equation are then pure real). Since, in the special Rosenbluth and Simon (17) case of rotation (A1=1 in chapter II) the eigenvalue equation may be transformed to be purely dependent upon ω^2 which is then real in all cases, the eigenfunction, ξ , is then also real. Thus, the phase-shifted component of the perturbation is a result of the

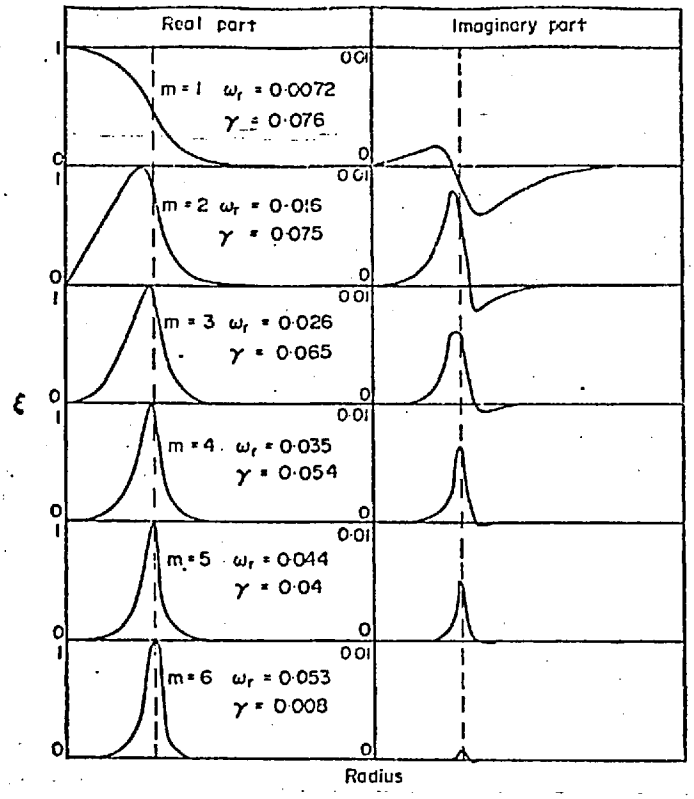

Figure III6 - Radial dependence of the complex eigenfunctions of figure III4 with $W_F = 0.002$.

destabilising influence of non-optimal ($A1 \neq 1$) rotation in the equilibrium.

Figure III6 also indicates the increased degree of mode localisation at larger m numbers. At $m \gtrsim 5$ they appear symmetric about the resonant surface and show little of the distortion associated with proximity to the axis. As FLR rises from zero, in the manner of figure III4, the mode structure varies little apart from the introduction of the imaginary, phase-shifted, part at small W_F and the subsequent contraction of the latter as cut-off is approached. In particular, finite gyro-radius phenomena make no significant alterations to the scale length of the perturbation as W_F increases from zero to the magnitude required to quench the instability. Recall, however, that very narrow MHD modes are stabilised by very little FLR. This can largely be explained by observing from figures III4 and III5 that the reduction in

$|\omega|$ is a small fraction of the growth rate in the MHD limit. Thus, the kinetic energy associated with the perturbation and hence the width of the resonant region, varies little (fractional change in kinetic energy $\propto \frac{\delta|\omega|^2}{|\omega|^2}$) as ion temperature is raised. FLR thus converts the kinetic energy of the MHD absolute instabilities into that of rapid, but stable, oscillations at large W_F.

Before proceeding with further results, a more quantitative comparison of the numerical output of this chapter with the theory of the last is in order. Precise agreement cannot be expected owing to the contrasting approximations, and hence regimes of validity, associated with the two calculations; localisation effects require that chapter II be valid for large m and this chapter for small m . Table III1 compares the value of the Suydam parameter, A2 (eq. II25) calculated for figure III4 with values estimated from figure II10 using the cut-off W_F's from figure III4 to evaluate A1, A3 and A5 (eqs. II24, II26, II28) at the resonant surface.

Table III1

No. of mesh points N	m W_F cut-off	A1	A2	$\frac{1}{A3}$	A4	A5	$A2_{crit.}$ from fig.II10
100	2 0.0072	1.77	3.92	0.031	0	0.038	3.8 ± 0.1
100	3 0.004	1.77	3.92	0.026	0	0.012	3.7 ± 0.05
100	4 0.003	1.77	3.92	0.027	0	0.007	3.75 ± 0.05
100	5 0.0025	1.77	3.92	0.03	0	0.005	3.9 ± 0.05

In this case the modes have large growth rates in the MHD spectrum of figure III1 and correspondingly broad, well resolved eigenfunctions. The correspondence of the actual

Suydam parameter with the cut-off value predicted from figure II10 is seen to be remarkably good. The predicted value is, in all cases, slightly too small and thus too pessimistic of the requirements for stability.

When the growth rate is smaller in the MHD limit so that the eigenfunction is correspondingly thinner and less well resolved, less precise agreement between the two results is found as shown in table III2 with $kr_x/m=-0.025$ using the parameters of figure III1.

Table III2.

N	m	$W_{F\,cut\text{-}off}$	A1	A2	$\frac{1}{A3}$	A4	A5	$A2_{crit.\ from\ fig.II10}$
50	2	0.0051	1.84	2.01	0.011	0	0.024	2.9 ± 0.05
100	3	0.0021	1.84	2.01	0.005	0	0.004	2.5 ± 0.03

Table III3 displays the comparison for the cut-offs of figure III1 (broken lines).

Table III3.

N	m	kr_x/m at cut-off	A1	A2	$\frac{1}{A3}$	A4	A5	$A2_{crit.\ from\ fig.II10}$
30	2	-0.0245	1.85	1.88	0.005	0	0.011	2.45
100	3	-0.028	1.8	2.99	0.016	0	0.01	3.2

Agreement appears better for the larger m number in both tables III2 and III3 as the differing numbers of mesh points cannot account for the discrepancies involved. Thus, in these cases, the increasing mode localisation that arises as m becomes larger appears to reduce the disagreement between the numerical and theoretical results. Note that, in the last two tables presented, the theory of chapter II over

estimated the size of A2 that could be stabilised by the FLR effects present so that the effects of delocalisation at low m appear unfavourable to stability.

In order to investigate the effects of the Righi-Leduc terms that appeared in the first term of A^4 in chapter II, an ion temperature profile with a steep gradient in the neighbourhood of the resonant surface was employed. As this had the dual effect of altering $T_\perp^i$, and hence the effect of the familiar diamagnetic terms, as well as introducing a $q_\theta^{\perp i}$ contribution, computations were performed both with and without the heat flux terms included. The results are shown in figure III7. Clearly, in spite of the very steep temperature profile employed, the Righi-Leduc terms have only a minor stabilising influence on the instabilities. This can be understood in the context of the theory of chapter II since, for the parameters and profiles employed in figure III7, the value of the quantity A^4 (equation II27) is found to be only -0.13. Thus, whilst larger values of this quantity can be expected to produce a greater stabilising

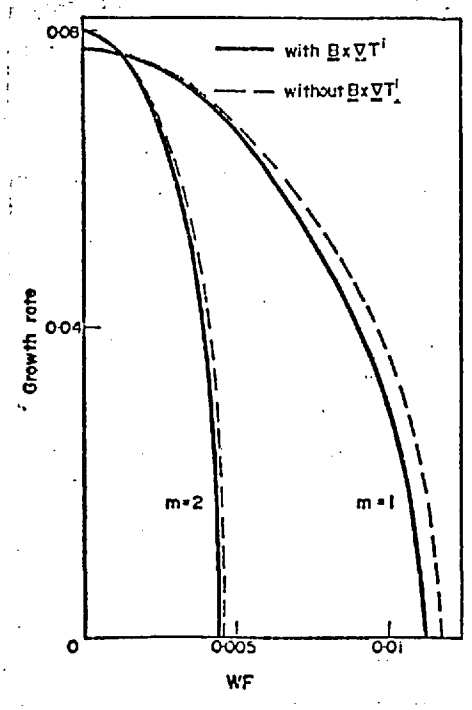

Figure III7 - FLR stabilisation of Suydam modes illustrating the effect of the Righi-Leduc heat flow.
$W_A=10$, $\beta=0.5$, $kr_x/m=-0.03$,
$\mu=0.01/(0.25+a^2)$,
$n=\exp(-0.5(a/0.3)^2)$,
$T_\perp^i \propto \exp(-50a^4)$.

influence, they can only arise in exceedingly unlikely physical situations. q_θ^{i} entered the problem as a physically conceptually difficult cross-effect in the stress tensor whereby the distortion of the distribution function constituting heat flow contributed to the equation of motion of the plasma. Its effect in realisable configurations may thus intuitively be expected to be of smaller magnitude than formally considered in the expansion of the Vlasov equation that lead to the eigenvalue equation considered.

So far, the calculations have been confined to phenomena associated with a single resonant surface within the plasma. Current distributions confined to surface layers tend to arise in pinch-like devices and give rise to profiles of μ that are peaked off axis. Modes posessing two resonant surfaces, one on each side of the peak of μ, are then possible. Such a situation is modelled in figure III8. Clearly, no resonant surfaces exist when $-kr_x/m$ exceeds the peak value of μ, but as the former is reduced below the peak, two surfaces appear in the plasma. Further reduction of the mode pitch causes the innermost surface to contract into the axis so that when $-kr_x/m < \mu_{axis}$ only the outermost resonant surface remains. At very small mode pitch this expands through the bounding wall.

The MHD (solid) curves of figure III8 are readily explained in terms of the behavior of the resonant surfaces. Maximum growth rates occur where the two resonant surfaces coalesce, $d\mu/da = 0$ and A2 diverges. In this region, growth rates exceed those of the single resonant surface case (figure III1) by almost a factor of two, indicating the destabilising influence of the extra surface. Increase of

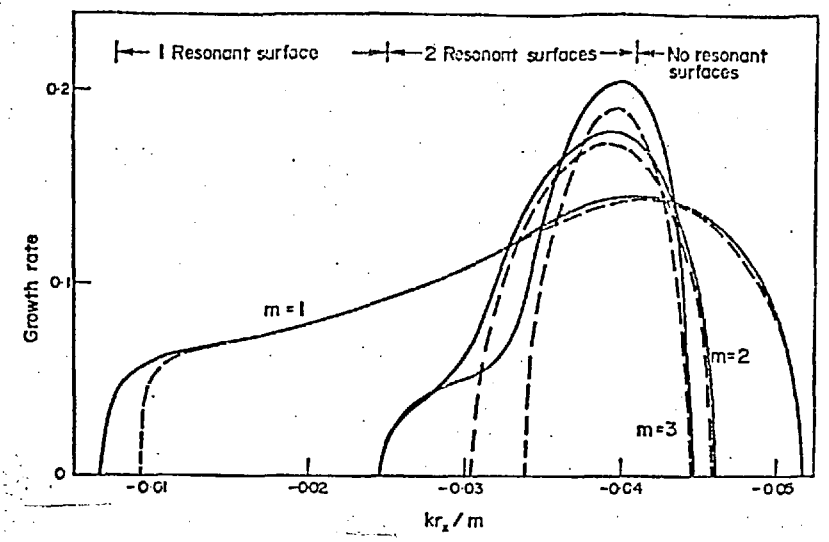

Figure III8 - The variation of the growth rate of Suydam modes with normalised axial wavenumber with:
$\beta = 0.5$, $W_A = 10$, $n = \exp(-0.5(a/0.3)^2)$,
$\mu = 0.003(1/(0.08+(a-0.4)^2) + 1/(0.08+(a+0.4)^2))$
$W_F = 0$ on solid lines, $W_F = 0.005$ on broken lines.

$-kr_x/m$ beyond this value removes the resonant surfaces from the plasma so that, for $m > 1$ at least, sharp cut-offs occur. The low $|k|$ cut-off of the $m > 1$ modes occurs as the inner resonant surface contracts into the axis. Although the outer surface remains, it is stable to Suydam instability ($A2 = 0.15 \ll 1$) since the plasma density, and hence pressure, is small at the radius concerned. The m=1 mode is plainly insensitive to the Suydam criterion. At large $|k|$ a gentle cut-off is present after the resonant surfaces vanish, but at small $|k|$

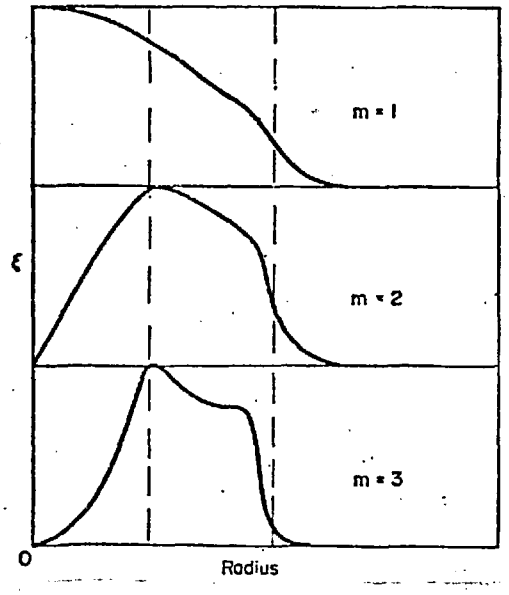

Figure III9 - Radial dependence of the complex eigenfunctions of figure III8 with $W_F = 0$, $kr_x/m = -0.035$.

the truncation of the curve indicated arises as the outer resonant surface passes through the wall.

The eigenfunctions associated with two resonant surface phenomena are of inherent interest. Figure III9 displays these for the case $kr_x/m = -0.035$ for which figure III8 shows that both resonant surfaces play an important role. All three modes in figure III9 display prominent features associated with each resonant surface. $d\xi/dr$ is greatest, in all cases, at the outermost surface where the plasma density and hence inertia is less. The m=3 mode, in particular, appears to indicate that the relative ease of perturbation at the two resonant surfaces allows large displacement of the volume of plasma in the intervening region. Figure III10 portrays the m=1 mode as the axial wavenumber is varied through the spectrum of figure III8. Note that a prominent feature exists at the outer resonant surface throughout. As this passes through the wall, the large perturbation gradient involved generates the perturbed wall currents causing cut-off as described

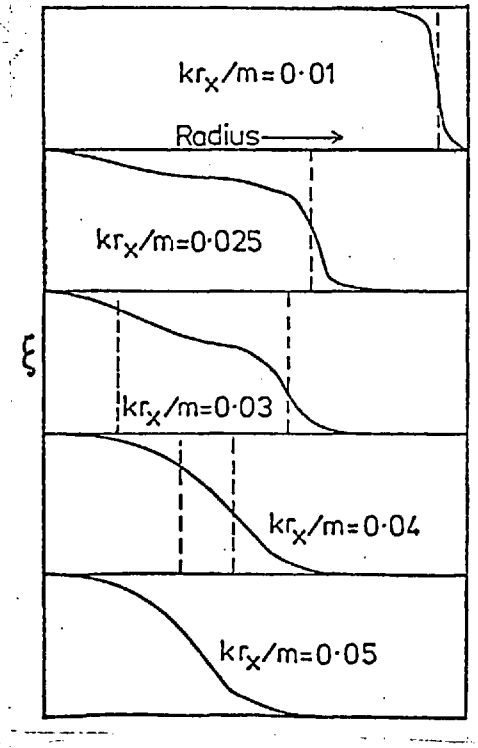

Figure III10 - Eigenfunctions of the m=1 mode of figure III8.

previously. At larger $|k|$, the mode concentrates around the radius at which μ is maximum. Close to their low $|k|$ cut-off, explained above, m>1 modes were found to show only a very small feature at the outer resonant surface compared to a large, highly localised perturbation near the axis.

The broken curves of figure III8 indicate the effect of FLR on the perturbations. Note that, as the ion temperature profile is constant and the density profile Gaussian, the FLR terms of the eigenvalue equation vary only slightly, due to finite β effects, between wall and axis. Thus, increased W_F succeeds in stabilising the low $|k|$ end of the m=1 mode where $d\xi/dr$ is largest. In a physical situation, reduced ion temperature near the wall would reduce this effect. The higher m modes are influenced more strongly by FLR. As in the single surface case, the greatest influence arises near the low $|k|$ cut-off where the most localised perturbations occur that are the most difficult to resolve on the discrete mesh of the numerical scheme.

4) Rotational Effects.

Instabilities associated with a rotating cylindrical plasma were studied extensively by Bowers (10,27,28) in the absence of B_θ in the stationary state. The work of this section pursues these effects into situations with B_θ present.

Just as the pressure gradient term in G of the eigenvalue equation (I11) drove the Suydam modes, so the term containing $\frac{d}{dr}\left[\rho\left(\omega_1 - \frac{m u_\theta}{r}\right)^2\right]$ produces rotational effects. Since ω_1 contains the Doppler shift, mu_θ/r, this term is independent of u_θ; it does, however, comprise the only term in ω in the equation not involving the combination

$\omega+mu_\theta/r$ and, as shown in chapter II thus gives rotation its destabilising influence.

When the pressure gradient effects responsible for the Suydam modes are small compared to the rotational term and axial velocities negligible, the axial wavenumber, k, and the azimuthal magnetic field B_θ are only important in the combination $k+mB_\theta/(rB_z)$. This is the component of the wavenumber in the direction of the magnetic field, $(\underline{k}.\underline{B})/B$. Thus, phenomena pertaining to k=0 in Bowers (10,28) work occur at $(\underline{k}.\underline{B})=0$ in the present case. An example of this may be seen in figure III11 for which $B_\theta/(rB_z)$ was taken to be 0.05, independent of radius. The slight deviations from symmetry of the diagram about $kr_x/m = -0.05$ arise from the residual influence of the pressure gradient as a large axial beta was employed. Whilst figure III11 differs little from the results of Bowers apart from the shift in wavenumber, the m=1 mode deserves further comment. The diagram plots the behavior of the most unstable mode for each m. The discontinuities that appear in the frequency ($Re(\omega)$) of the m=1 mode clearly indicate that different modes dominate in different parts of the spectrum. It was found that the dominant mode in the centre of the spectrum, characterised by the largest frequency of oscillation, possessed a radial node whereas the outer wings of the diagram are produced by the more familiar 'kink'-type seen previously in the $W_E=0$ limit (e.g. figure III6). The former type of m=1 mode will henceforth be described as the 'wobbling' mode.

The dominance of the wobbling mode at k=0, $B_\theta=0$ was ascribed by reference (28) to result from the requirement that the centre of mass of the plasma should not move so

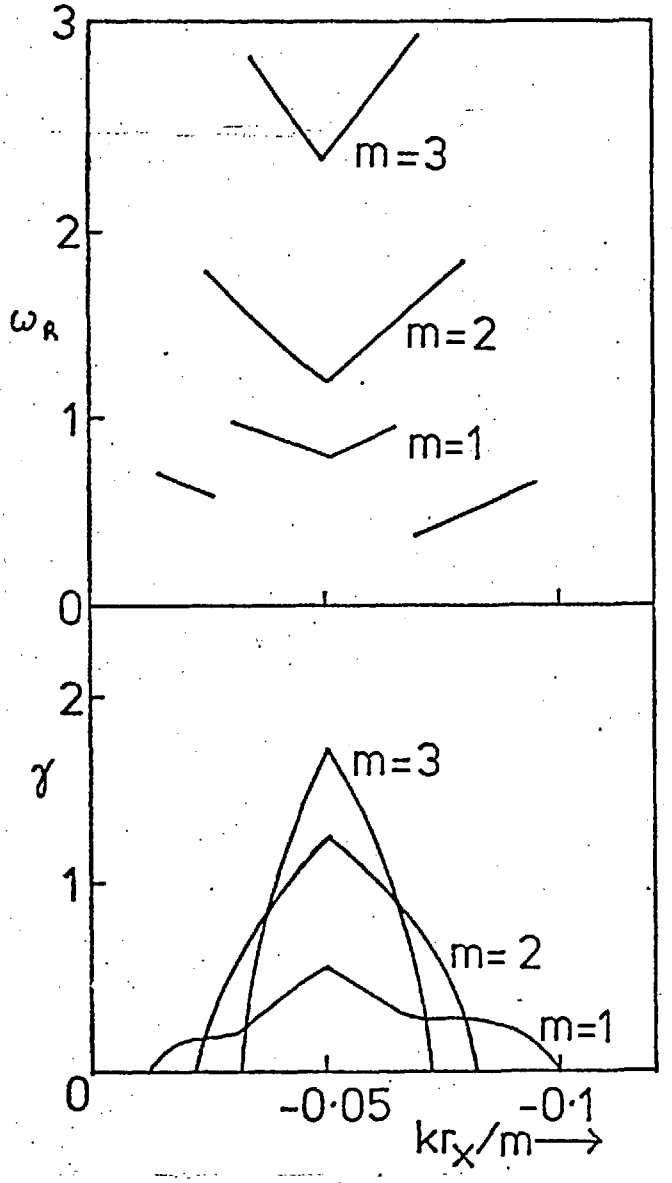

Figure III11 - Growth rate, (γ) and frequency (ω_R) versus normalised axial wavenumber for W_A=10, μ=0.05, n=exp(-0.5(a/0.3)^2), β=0.5, W_E=1, W_F=0.01.

that the kink mode could not arise. This requirement may be violated for k=0 when either $B_\theta \neq 0$ or the plasma extends to the wall. In the former case, equation III12 indicates that an electromagnetic wall reaction can occur and in the latter, finite plasma pressure at the rigid wall causes a net force on the plasma column. The effect of increasing the latter may be seen in figure III12 where the width of the density distribution is varied. At sufficiently large wall pressure, the growth rate of the kink mode can be made to exceed that of the wobbling mode. The form of the eigenvalue equation

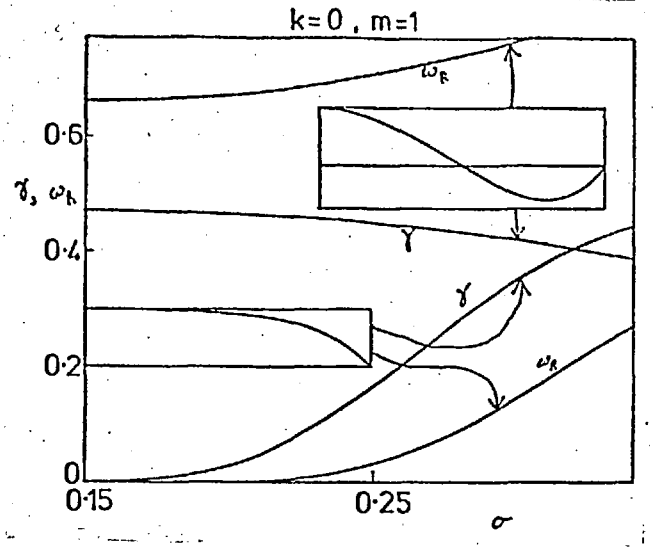

Figure III12 - The dependence of the growth rate (γ) and frequency (ω_R) of the two m=1 modes at k=0 upon the width of the density profile, σ. $\mu_\cdot$=0, W_A=10, W_F=0, W_E=1, n=exp(-0.5(a/σ)^2).

solved indicates that, at low beta, properties associated with k=0 when B_θ=0 are associated with $\bar{k}$=k+mB_θ/(rB_z)=0 in the case of figure III11. In this case, however, since k≠0 when $\bar{k}$=0 there is no implicit constraint on motion of the centre of mass of the plasma cross section. The reason for the weakness of the m=1 kink mode when $\bar{k}$=0 everywhere and the plasma is cold and tenuous near the wall lies in the characteristic of the perturbation in this limit of leaving the direction of the magnetic field unaltered. This feature causes neighbouring plasma cross sections not to interact with one another so that, again, the centre of mass of each must remain fixed and the kink mode is subdued.

Resonant surface effects must again be considered when μ ($\propto B_\theta/(rB_z)$) is a function of radius. A range of values of k now exists for which $\bar{k}$=0 at some radius within the plasma. As the rotational effects considered are, however, considerably stronger than the effects of pressure gradient, localisation is poor so that the constraints of chapter II are readily violated.

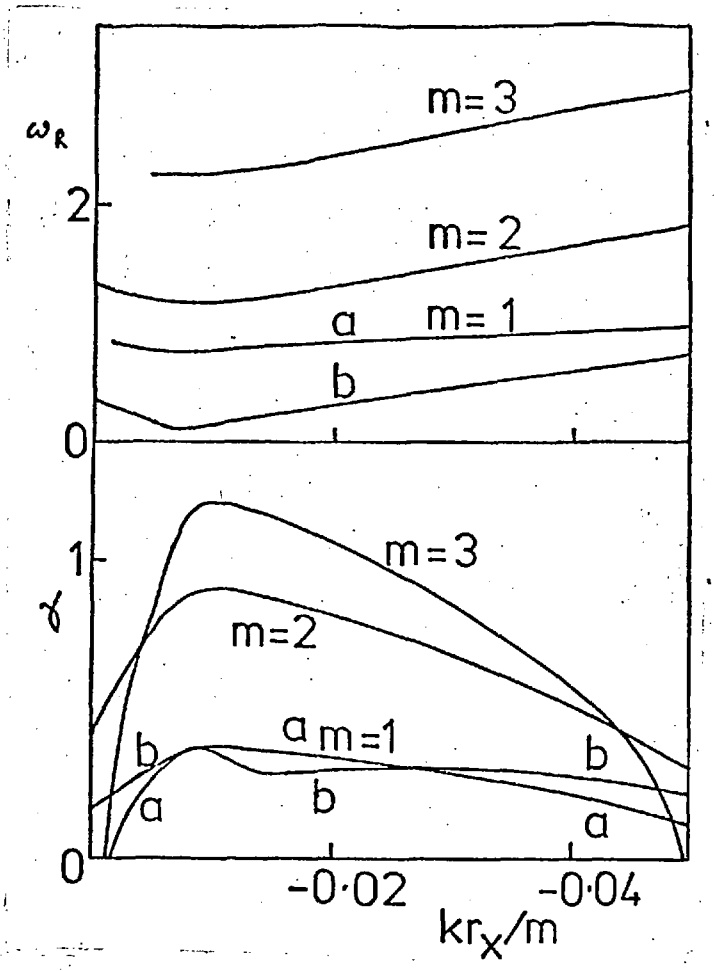

Figure III13 - The variation of growth rate (γ) and frequency (ω_R) of rotationally dominated modes with normalised axial wavenumber with: β =0.5
W_E=1, W_F=0, μ =0.01/(0.25+a^2),
n=exp(-0.5(a/0.3)^2).
a) The m=1 'wobbling' mode.
b) The m=1 'kink' mode.

Figure III13 employs the Lorentzian profile of μ used in section 3 for the study of Suydam modes. ($0.008<\mu<0.04$). Clearly, whilst the unstable range of kr_x/m is determined largely by the existence of a resonant surface, this range extends beyond that of μ in both limits for all the m numbers shown. Clearly, these excursions from resonant k values are less than those of figure III11 displaying the stabilising influence of magnetic shear in demanding energy to bend the field lines.

The most unstable mode pitch (kr_x/m) occurs with a resonant surface much closer to the wall than in figure III1.

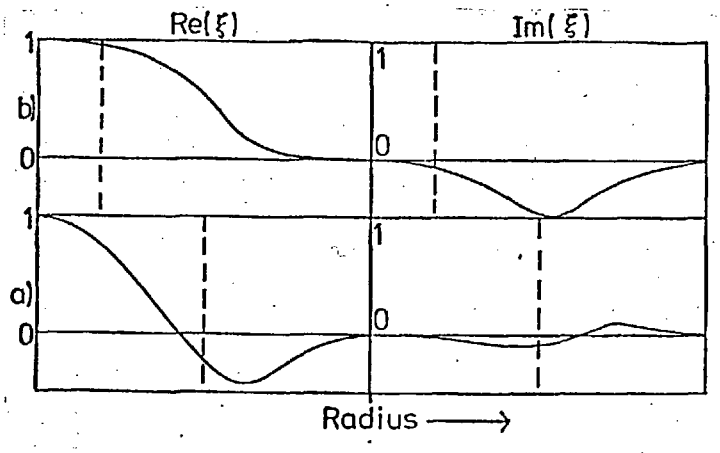

Figure III14 - Eigenfunctions for the m=1 modes of figure III13.
a) 'Wobbling' mode with $kr_x/m=-0.02$.
b) 'Kink' mode with $kr_x/m=-0.035$.
Broken lines denote the resonant surfaces.

As the centrifugal force at a particular radius depends on ρr for a given rotation frequency, u_θ/r, this tendency for the most unstable pitch to decrease is qualitatively explained. Thus, as rotation succeeds pressure gradient as the dominant driving force for instabilities, so the most unstable resonant surface occurs at larger radius.

The m=1 mode merits further discussion. Figure III13 shows that, whilst the wobbling mode dominates the kink mode near the most unstable k number, the difference in growth rate is slight. The two types of eigenfunction concerned are portrayed in figure III14 and clearly display none of the localisation to the resonant surface seen in figure III6. At k=0, the kink-type mode dominates, indicating the influence of plasma-wall interaction. Equation III12 shows that, in this limit, the wall current is proportional to B_θ. The manner in which the growth rate increases as the magnitude of μ is reduced is displayed in figure III15. From this, we conclude that, for this example, the wall interaction allowing the kink-type mode derives principly from the broad equilibrium plasma density distribution employed.(see fig.III12)

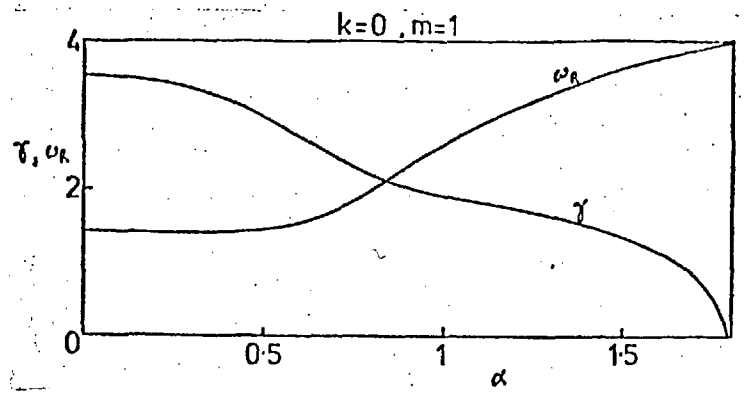

Figure III15 - The dependence of growth rate, γ, and frequency, ω_R, on the magnitude of B_θ for the k=0, m=1, kink-type mode.
$W_F=0$, $W_E=1$, $W_A=10$, $\beta=0$, $n=\exp(-0.5(a/0.3)^2)$, $\mu=\alpha(0.01/(0.25+a^2))$.

Figure III16 employs narrower density and pitch profiles. Although μ_{wall} is less than that for figure III13, the greater centralisation of the plasma mass has produced the most unstable resonant surface much closer to the axis. In addition, the m=1, k=0 instability has a considerably reduced growth rate due to the smaller plasma-wall interaction.

Comparison of figures III16 and III17 reveals the distinctly curious effect of including FLR (W_F). Whereas, near the large $|k|$ cut-offs of the $m>1$ spectra, gyro-viscous stabilisation is plainly evident, in the vicinity of the spectral peak of m=2, larger growth rate has arisen. This phenomenon will be discussed later. The contribution of beta may be seen by comparing figures III17 and III18. Larger B_z and hence increased gyro-frequency caused by finite beta reduces the destabilising influence that the FLR appears to have generated in figure III18.

The two m=1 modes behave differently under the influences of β and W_F so that the window of dominance of the wobbling mode varies considerably as a result. Finite beta is seen to encourage the kink-type mode whereas the wobbling mode, that possesses the more complicated eigenfunction containing

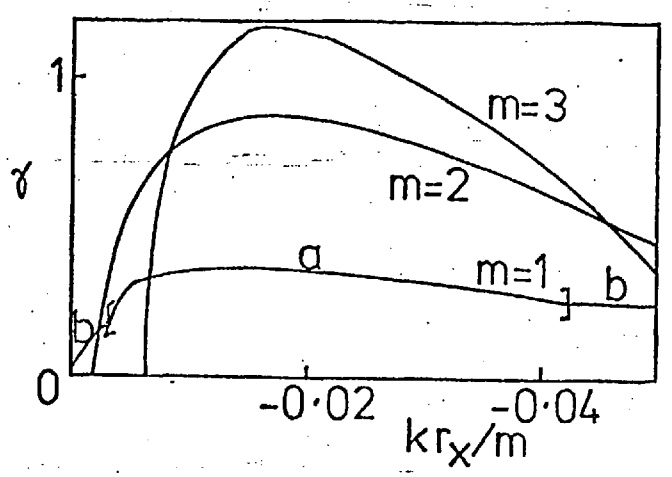

Figure III16 - Axial wavenumber dependence of the growth rate of rotational modes. $W_E=1$, $W_A=10$, $\beta=0.5$, $n=\exp(-0.5(a/0.14)^2)$, $\mu=0.004/(0.1+a^2)$. a and b denote dominance of wobbling and kink-type m=1 modes respectively in the regions indicated.

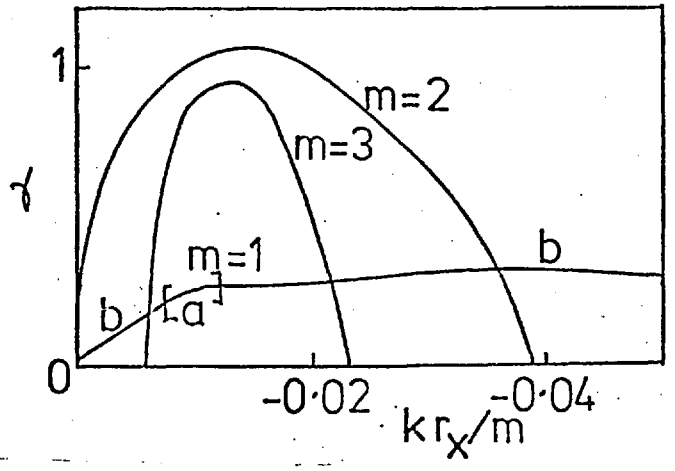

Figure III17 - Growth rate spectrum with FLR included ($W_F=0.04$) and other parameters as in fig. III16. The window of dominance of the m=1 wobbling mode is indicated.

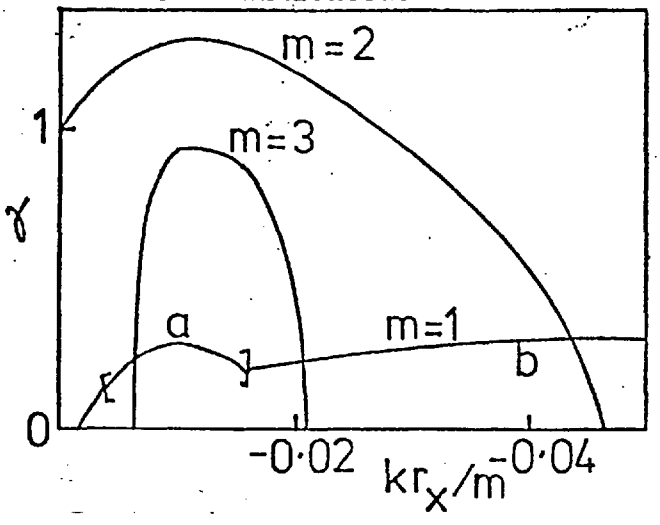

Figure III18 - Growth rate spectrum with $\beta=0$ and other parameters as in figure III17. The window of dominance of the m=1 wobbling mode is indicated.

the larger derivatives, is readily stabilised by increased W_F. Temperature increases thus cause the wobbling mode to be less important than the kink. Additional computations have revealed that reduction im electric rotation (W_E) leads to kink mode dominance so that, as W_E falls to zero, the spectrum of figure III1 finally results.

An explanation for the peculiar effect of FLR on the rotational modes may be gained from figure III19. As W_F rises, the Hall term in equation II29 gives an increasing contribution to the net plasma rotation. When $W_E > 0$, this contribution augments the ExB rotation and vice-versa. Thus, with W_E=0.5, the increased rotation due to the initial rise in W_F causes destabilisation. Further increase causes gyro-viscous stabilisation to dominate so that cut-off results. Rapid stabilisation when W_E=-0.5 is explicable since rotation decreases and gyro-viscosity increases as W_F rises. The m=1 mode in the diagram is of the kink type. As the effect of

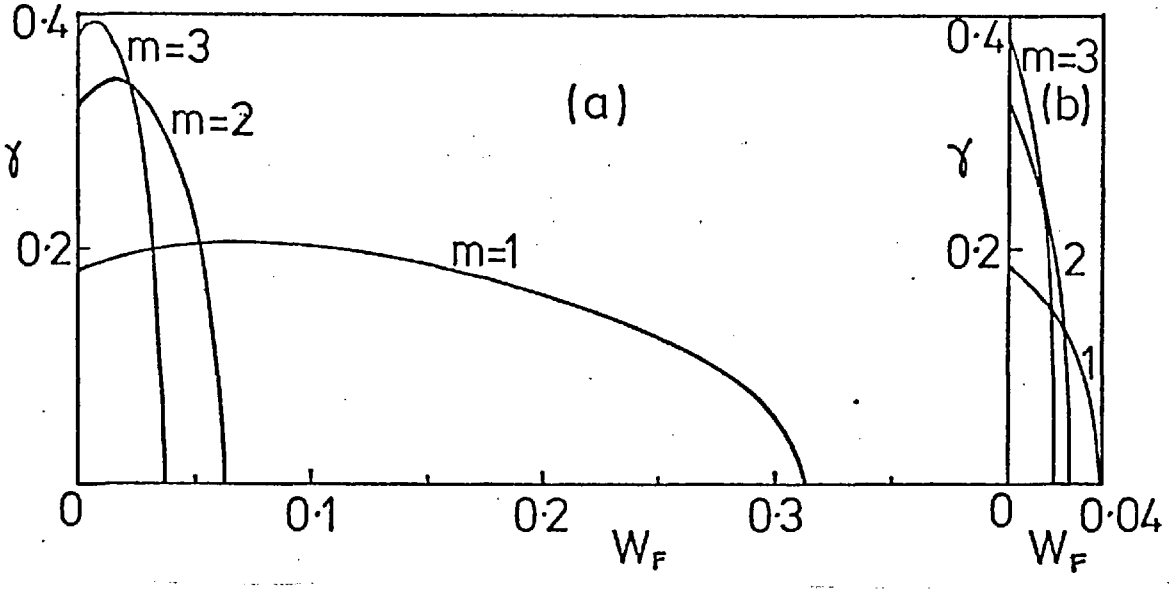

Figure III19 - FLR stabilisation of rotational instability, β=0.5, W_A=10, kr_x/m=-0.028, μ=0.01/(0.25+a^2), n=exp(-0.5(a/0.3)^2). a) W_E=0.5, b) W_E=-0.5.

gyro-viscosity is greater in the eigenvalue equation, I11 for larger $d\xi/dr$, the peak growth rate for the wobbling mode occurs at smaller W_F than for the much smoother kink mode. Nearer marginal stability, the destabilising effect of any rotation present is, by definition, small so that the peak growth rate occurs at a smaller W_F as, for example, the large $|k|$ cut-off of figure III16 is approached. Thus, the effect of FLR in figure III17 of stabilising at large $|k|$, but increasing growth rate at smaller $|k|$ is readily explained.

The very mild influence of FLR on the m=1 kink mode, discussed above, is emphasised by figure III19. Figure III20 employs a profile of ion temperature with a steep gradient in the region of the resonant surface. Whilst this has only minor significance for the $m > 1$ instabilities, the dependence of the m=1 mode growth rate on W_F is considerably altered. Even for the very large ion temperatures (W_F) considered, no cut-off is apparent. Observe that no peaking phenomenon occurs at small W_F. This suggests that the roles of rotation

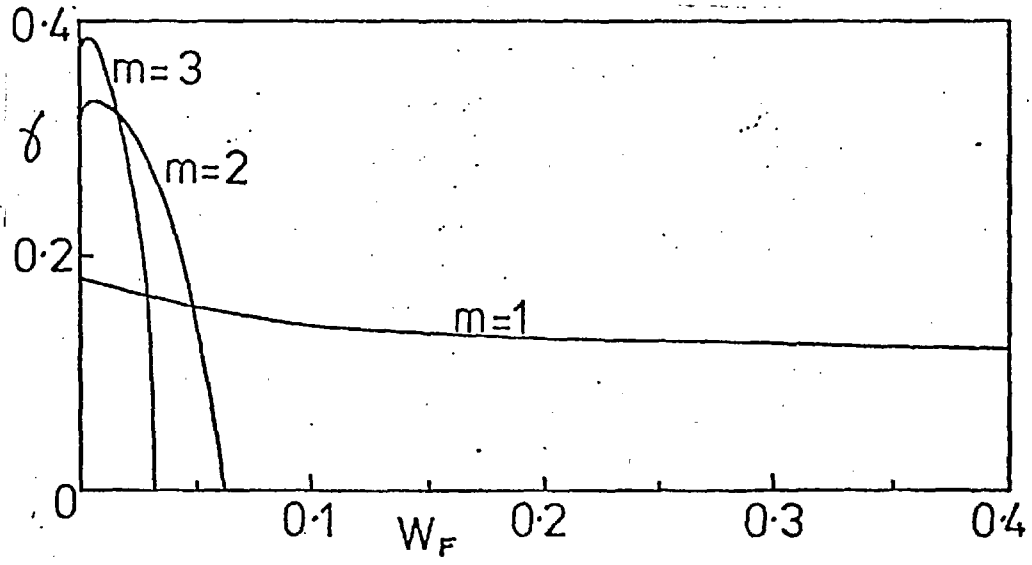

Figure III20 - The effect of an ion temperature profile on figure III19.
$T_i^i \propto \exp(-50a^4)$, $W_E=0.5$.

and gyro-viscosity have been reversed at small W_F and that the two effects tend to cancel at high ion temperatures. Such an extreme sensitivity to profile indicates the caution required when attempting to apply numerical results of this type in a qualitative way to any real plasma.

As the rotation included is such a strong destabilising influence, the temperatures concerned are very large. In order to gain some estimate, consider $B_z = 1T$, $n = 10^{19} m^{-3}$, $r_x = 0.3m$ as for figure III4. This indicates that the m=2 mode is stabilised at $T_I^i \sim 10keV$. As modern devices operate at considerably lower temperatures, the influence of a large ExB rotation of positive sign might easily become more dangerous as the ion temperature is raised.

Finally, in this section, we consider the effect of varying the electric rotation, W_E. $W_E=0$ corresponds to the Suydam limit discussed extensively in section 3. As mentioned above, reduction in W_E causes the kink-type m=1 mode to dominate the wobbling mode. Figure III21 portrays the dependence of growth rate on W_E when FLR is included.

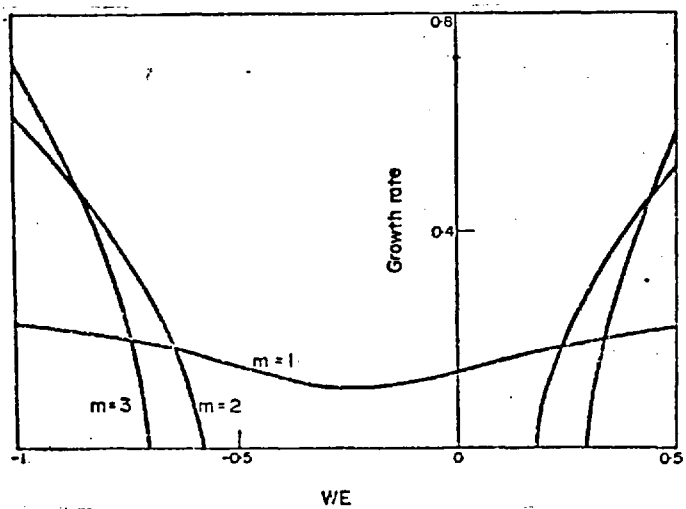

Figure III21 - The dependence of growth rate upon ExB rotation when FLR is included. $W_A=10$, $\beta = 0.5$, $W_F=0.01$, $kr_x/m=-0.03$, $n=\exp(-0.5(a/0.14)^2)$, $\mu = 0.01/(0.25+a^2)$.

In its absence, of course, such a diagram would be symmetric about $W_E=0$. Inclusion of FLR makes the plot appear symmetric about $W_E=-0.2$. At this point, equation II24 yields A1=1.04 which agrees with the A1=1 prediction of chapter II within the limits of the numerical error of the computation. The diagram emphasises the relative insensitivity of the m=1 mode to rotational destabilisation compared with $m>1$ modes.

5) Heat Flux Modes.

As heat fluxes entered the problem via peculiar cross-effects in the stress tensor rather than via an energy equation, their influence cannot be readily understood. Previously, in section 3, the effects of the Righi-Leduc flux were considered; here we consider the role of axial heat flow, $q_z^{\perp i}$. Recall that this involves only the flux of gyration (perpendicular) energy.

The study of the effects of $q_z^{\perp i}$ allows investigation of the second term of A4 in equation II27. This could not be adequately described by the localised theory of chapter II as its magnitude was severely limited by the constraints of that theory. The main features of the results discussed below also apply to the effects of $dq_z^{\perp i}/dr$ and to a large extent to those of du_z/dr as well; these are the other contributions to the relevant term of A4.

Figure III22 displays the effect of the parameter W_{QZ} on the growth rate for both directions of axial heat flow. At large W_{QZ}, the main effect of this parameter is to allow the function F of the eigenvalue equation (I11) to vanish within the plasma even when the growth rate is non zero. Thus, including the terms of immediate interest, F=0 implies:

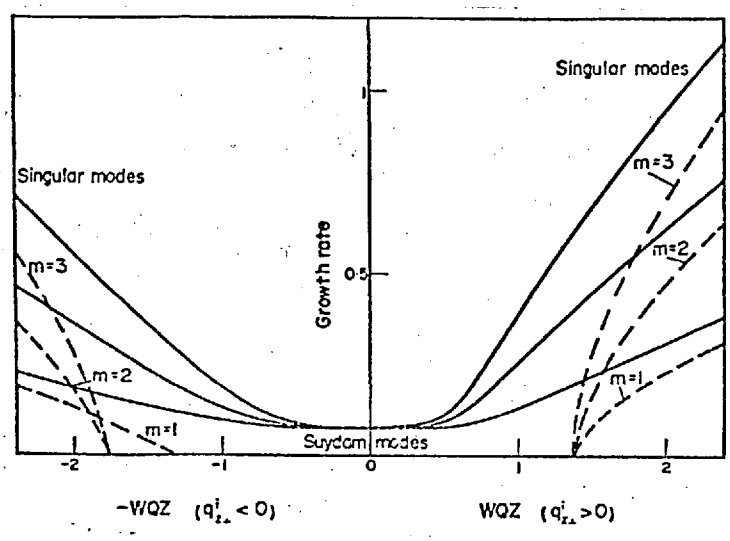

Figure III22 - The dependence of growth rate upon the axial flux of the ion energy associated with thermal velocity perpendicular to the magnetic field. The right hand half concerns $q_z^{\perp i}$ in the positive z direction and the left hand half, $q_z^{\perp i}$ oppositely directed. Solid lines relate to $W_F=0$ (no FLR), broken lines have $W_F=0.03$. $\beta^F=0.5$, $W_A=10$, $kr_x/m=-0.03$, $n=\exp(-0.5(a/0.3)^2)$, $\mu=0.01/(0.25+a^2)$.

$$\rho\omega_1\left(\omega_1 - m\frac{d}{dr}\left(\frac{p_\perp^i}{\Omega^i}\right)\right) = \frac{B_z^2}{\mu_0}\left(k+\frac{mB_\theta}{rB_z}\right)^2 - \left(k+\frac{mB_\theta}{rB_z}\right)\frac{m\,q_z^{\perp i}}{\Omega^i r B_z}\frac{dB_z}{dr} \qquad \text{III13}$$

where $q_\theta^{\perp i}$ has been substituted from equation II6 and the Righi-Leduc contribution omitted. Since the appropriate choice of k will make the right hand side of equation III13 negative for any non-zero $q_z^{\perp i}$, this implies that unstable heat flux modes of this type always exist if all k values are allowed. Since equation III13 applies at every point within the plasma, it describes a continuum of instabilities, the most unstable mode of which is plotted in the large $q_z^{\perp i}$ parts of figure III22. Caution must be exercised at this point, however, since the vanishing of F within the plasma causes a singularity in the eigenfunction at that point. Since the ordering approximations on the scale length of the perturbation break down in such a situation, the physical reality of the singular modes at

large $q_z^{\perp i}$ is questionable.

The importance of investigating the form taken by the eigenfunctions is emphasised by a situation of this sort wherein the growth rates are independent of changes in mesh size, but the modes appear unphysical. Such modes will be further discussed in section 7.

The effects of finite W_F, as indicated by the broken lines of figure III22, are largely accounted for by the presence of the diamagnetic term in equation III13. The apparent peculiarity of the m=1 mode in this case arises from a change in dominant mode with $W_{QZ} \simeq -2.5$; this was indicated by a frequency change in the results calculated.

At smaller W_{QZ} the growth rate curves displayed merge into those of the Suydam modes discussed in section 3 . Recall from chapter II that the heat flux contribution to A^4 was shown to move the mode localisation away from the

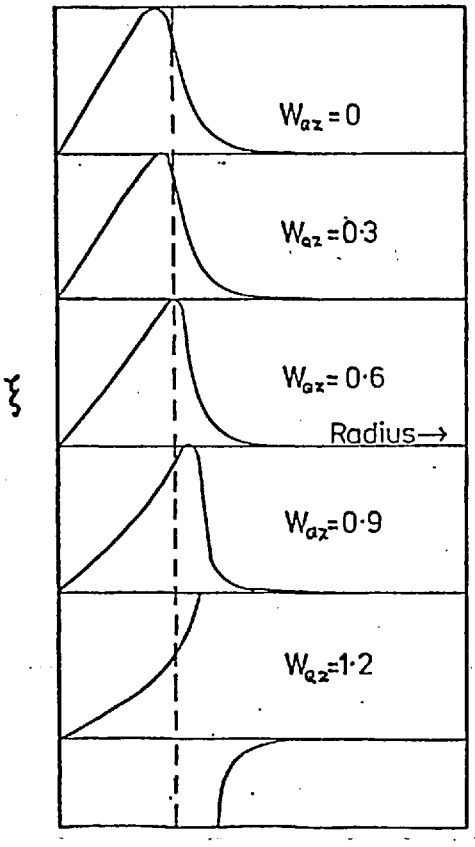

Figure III23 - Eigenfunctions for the m=2 mode of figure III22 with $q_z^{\perp i} < 0$, $W_F = 0$.

resonant surface. This effect may be observed in the computed eigenfunctions when the Suydam modes are perturbed by small amounts of axial heat flux. Figure III23 demonstrates this for the m=2 mode of figure III22 with $q_z^{\perp i} < 0$. As the mode is displaced by the increased heat flux, so the sharp gradient present becomes steeper until a singularity develops. The position of the singularity is given by that of the minimum of the (negative) right hand side of equation III13. This clearly indicates that, at this stage, the stress tensor contribution of $q_z^{\perp i}$ completely dominates the more familiar interchange driving force.

It must be stressed that $q_z^{\perp i}$ was included in the description of the equilibrium without reference to any possible mechanism by which it might be produced. Whilst this is formally consistent with the derivation of the eigenvalue equation, it probably implies a velocity distribution function of a type unlikely to occur in practice. Thus, the extreme conditions that produce the singular instabilities probably correspond to unphysical situations and the useful results of this section are largely the demonstration of the manner in which Suydam modes are perturbed by small amounts of $q_z^{\perp i}$.

6) Pressure Anisotropy.

Two effects occur as the temperature anisotropy parameter, W_M, is increased from zero. At small values, the main effect is to increase the magnitude of the interchange mode driving force which is proportional to $\frac{d}{dr}\left(\sum_{\text{species}}(P_\perp + P_{//})\right)$. The effect upon the growth rate is thus, at small W_M, a general magnification by $\frac{1}{2}\left(1 + \frac{\sum(dP_{//}/dr)}{\sum(dP_\perp/dr)}\right)$ evaluated at the resonant surface as seen in figure III24.

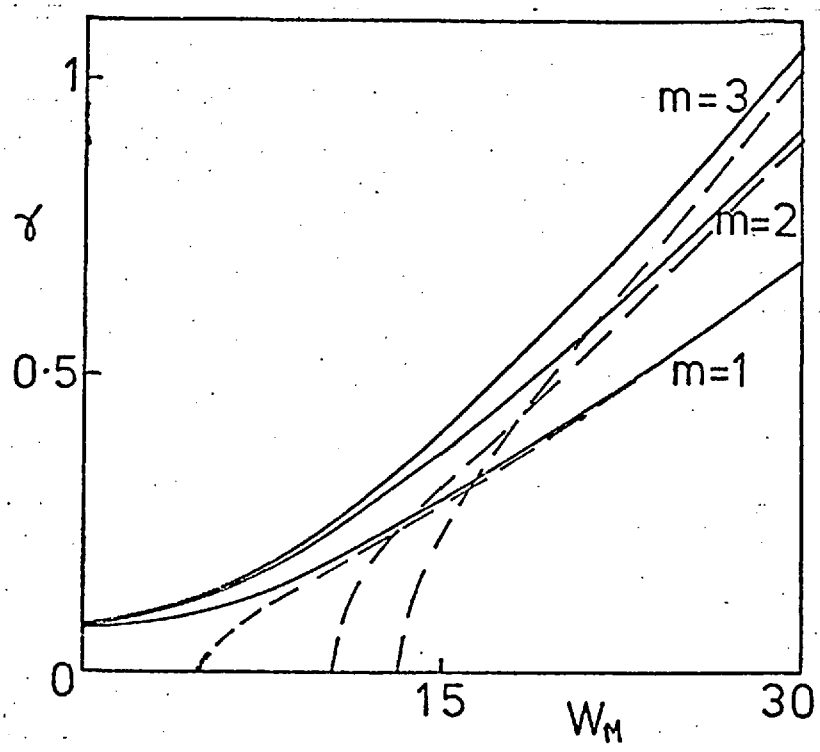

Figure III24 - Dependence of growth rate, γ, upon temperature anisotropy, W_M. W_A=10, kr_x/m=-0.03, β=0.5, n=exp(-0.5(a/0.3)^2), μ=0.01/(0.25+a^2). W_F=0 on solid lines, W_F=0.02 on broken lines.

As the growth rate rises, with increasing W_M, so the width of the perturbation about the resonant surface rises due to the increased kinetic energy involved. This is displayed in figure III25. Clearly, the destabilisation mechanism displayed in figure III24 is the addition of extra parallel energy to the plasma that may be released into the magnetic field distortion when the interchange mechanism operates.

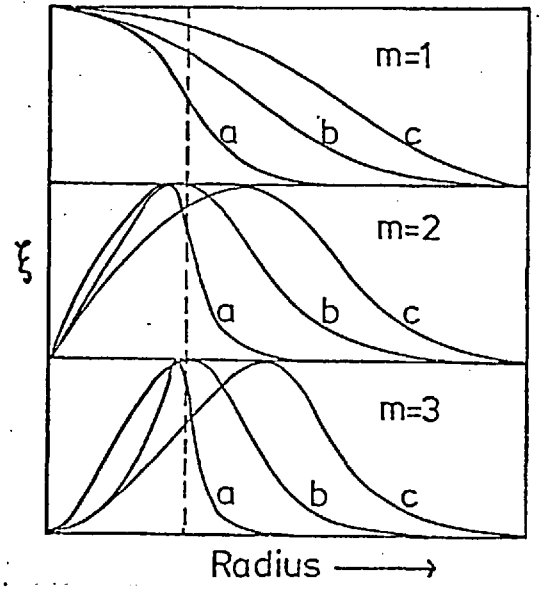

Figure III25 - Eigenfunctions for the W_F=0 curves of figure III24; a) W_M=0, b) W_M=15, c) W_M=30.

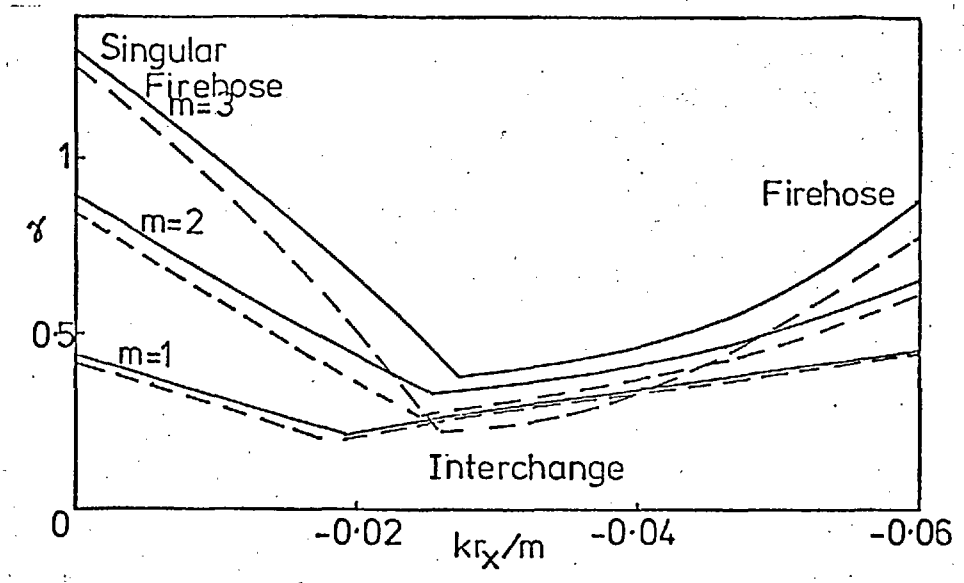

Figure III26 - Growth rate, γ, of the dominant mode versus normalised axial wavenumber: $W_A=10$, $W_M=15$, $\beta=0.5$, $W_E=0$, $n=\exp(-0.5(a/0.3)^2)$, $\mu=0.01/(0.25+a^2)$. $W_F=0$ on solid lines, $W_F=0.02$ on broken lines.

At larger values of W_M, the effective Alfven speed, $C_{eff.}$, given by: $C_{eff}^2 = \frac{1}{\rho}\left(\frac{B_z^2}{\mu_0} - \sum_{species}(P_{//}-P_{\perp})\right)$ becomes imaginary so that the growth rates increase due to this additional effect. This is the fire-hose instability (35) driving mechanism. Note, from the function F of equation I11 that the terms responsible vary as $\left(k+\frac{mB_\theta}{rB_z}\right)^2 C_{eff}^2$. Thus, the axial wavenumber spectrum of figure III26 displays, at the extremes of k where $(k+mB_\theta/(rB_z))$ is large within the plasma, a significant contribution from the fire-hose instability. Observe that, because of the presence of this mode, associated with large $(\underline{k}.\underline{B})$ rather than with the presence of a resonant surface, no cut-off wavenumber is present for the set of parameters used.

At the low $|k|$ end of the spectrum of figure III26, the fire-hose instabilities present result as $(k+mB_\theta/(rB_z))^2$ becomes large due to the non-cancellation of the B_θ contribution. As the Suydam term in G of the eigenvalue equation I11 is proportional to k^2, it makes only a small contribution in this

limit. Thus, as in the case of heat flux modes, the growth rate is given by an F=0 dispersion law:

$$\omega_1\left(\omega_1 - \frac{m}{\rho r}\frac{d}{dr}\left(\frac{p_\perp'}{\mathcal{R}i}\right)\right) = \left(k + \frac{mB_\theta}{rB_z}\right)^2 C_{eff}^2$$

and is accompanied by singular instabilities of non-physical appearance, localised near the origin where the maximum growth rate is produced. Clearly, such eigenfunctions indicate failure of the analysis in this limit. The firehose instability that dominates the spectrum when $\left(k + \frac{mB_\theta}{rB_z}\right)^2$ becomes large at large $(-kr_x/m)$ (to the right of figure III26) differs in this respect. In this case, the Suydam term in G makes a significant contribution and the resulting instabilities are spread out over the entire plasma radius.

The inclusion of FLR is indicated by the broken curves of figure III26. Clearly it has little effect on strongly unstable firehose modes, but produces considerable growth rate reduction of the $m > 1$ modes in the interchange-like part of the spectrum. The m=1 (kink-type) mode again shows very slight succeptibility to FLR effects.
(Note that figure III26 differs from figure 17 of reference (30). This arises from a program error in the temperature anisotropy term of F discovered subsequent to publication).

7) Some Comments on Singular, F=0, Instabilities.

In sections 5) and 6) of this chapter, large axial heat flow and large temperature anisotropy respectively were shown to produce continua of singular modes characterised by F of the eigenvalue equation, I11, vanishing within the plasma. The instabilities calculated in these cases corresponded to the most unstable part of the continua and hence related to F vanishing as the one particular point within the plasma that produced the largest growth rate. Normal mode analysis

provides a poor description of the perturbations in situations of this sort; in reality, the displacement has a growth rate varying with radius. Thus, as the instability develops, the mode becomes increasingly more localised about the most unstable region. As the growth rate is a smooth function of radius, the perturbations cannot be expected to reach the singular stage, indicated by the normal mode analysis, before non-linear limitations become significant. Thus, the unphysical nature of the normal modes does not necessarily constitute grounds for dismissing the possibility of such instabilities.

8) Conclusion.

This chapter has attempted to indicate the effect of the plethora of physical parameters, associated with the collisionless eigenvalue equation, I11, upon the growth rate of instability. The manner in which Suydam modes, highly localised near the resonant surface, blend into the delocalised instabilities associated with other physical influences has been discussed in all cases. In particular, the effect of axial heat flux in moving the dominant region of the modes, eventually producing unphysically singular perturbations has been illustrated. This demonstrates the effects of the second term of A4 (equation II27) of chapter II that violated the approximations of that theory.

Of primary significance is the manner in which rotational influences interact with interchange modes. The m=1 mode is shown to be dominated by its interchange-like (wobbling) second harmonic in certain situations, but its more familiar, kink-type first harmonic tends to be the most important when rotational destabilisation is small. Minimum growth rate is found to result for the Rosenbluth and Simon(17) special case

of rotation, generalised for finite beta effects, for which the centre of mass rotation equals half the diamagnetic rotation.

When strong destabilising forces are present, large amounts of FLR and hence unreasonably high ion temperatures are required to produce significant stabilisation. Thus, we conclude that, in general, the finite ion Larmor radius effect is only of importance in those equilibria which are very close to marginal stability.

Chapter IV.

A Numerical Approach to Resistive Instabilities.

1) Introduction.

The computational investigation of the solution of Pott's collisionless equation, I11, employed a technique in which the eigenfunction was calculated over the whole width of the plasma. Once a numerically defined function has been determined whose roots can be iterated, the investigation of the dependence of the growth rate of an instability upon the parameters of the system may be relatively easily performed.

The most flexible numerical technique employed in linear instability theory is clearly that of linearising the equations, applying fourier analysis upon the ignorable spatial coordinates (θ and z in cylindrical, radially dependent equilibria) and investigating the long-time evolution of a random perturbation. This has been successfully employed by many authors to very detailed models. (Sykes and Wesson (44), Killeen (43), Furzer et al.(46)). The disadvantage of such a method is that lengthy computations must be performed for each of a series of parameter values, whereas, in the root-solving scheme, parameter perturbation methods may be used, once the growth rate has been found for one case. By this means, when the method succeeds, the growth rate curve may be plotted at small parameter intervals with minimal computational effort.

The collisionless Pott (30) equation is, however, only second order and is therefore, numerically a comparatively simple case to consider. Increasing the order of the system of perturbation equations, or the number of dimensions upon

which the equilibrium depends, rapidly increases the size of the determinants to be numerically iterated and hence reduces the feasibility of obtaining roots with reasonable computational economy. For these reasons, the direct numerical approach was only applied to low beta plasma when finite resistivity was included. As will be seen below, this produces a fourth order set of eigenvalue equations; the sixth order set produced when finite beta effects are included is investigated in chapter V using deeper analytical investigation.

Solving the eigenvalue equations across the full width of the plasma allows an investigation into the limits of validity of previous analytic theory (discussed at the beginning of chapter V) and indeed, complements these results in many ways. Computations of this sort have been performed by Wesson (60) for resistive instabilities using a sheet pinch model. Wesson's results tend to those of (7) in the low resistivity limit where the latter work is most accurate. Whilst Wesson's (60) tearing mode eigenfunctions have similar characteristics to those displayed in this chapter, the present work includes the complications of cylindrical geometry which will be seen to be of importance in considering the region of breakdown of the analytic (7) results. In addition, FLR effects will, of course, be considered.

The work of Furth et al. (47) was not applicable to the resistive m=1 mode due to the separate solution of the region around the resonant surface ('inner' region near $\underline{k}.\underline{B}=0$) and the remainder of the plasma. As inertial terms are present everywhere, in the present work, such solutions are possible.

The general problem of resistive instabilities has been considered by many authors. These, e.g.(47), solve separately for the resistive boundary layer about the resonant surface (inner region) and the surrounding hydromagnetic region. Matching is achieved by requiring the identity of $\Delta = \frac{r_s}{B_r'} \frac{dB_r'}{dr}\Big|_{r_s-\delta}^{r_s+\delta}$ (calculated from the outer region) with $\Delta \cdot \frac{L_R}{B_r'} \frac{dB_r'}{dx}\Big|_{\frac{x}{L_R}\to -\infty}^{\frac{x}{L_R}\to \infty}$ (from the 'inner' region) where $x = r - r_s$ and L_R is the resistive scale width of the layer. The computations of Furth et al.(47) concentrate upon calculating Δ from the 'outer' hydromagnetic region, whereas much of the work of other authors evolves around the evaluation of Δ in the 'inner' region. (Coppi, Greene & Johnson (6)). A detailed consideration of this work is deferred until the beginning of chapter V which contains further calculation upon these lines.

2) The System of Equations.

As discussed above, the system was reduced to a simultaneous pair of second order differential equations by restricting consideration to low beta plasma so that the effects of compressibility could be neglected. (This will be checked below).

Thus, we use:

Ohm's Law:

$$\underset{\sim}{E} + \underset{\sim}{u} \wedge \underset{\sim}{B} = \underline{\eta} \cdot \underset{\sim}{j} + \frac{1}{ne}\left(\underset{\sim}{j} \wedge \underset{\sim}{B} - \underset{\sim}{\nabla} p_e \right) \quad \text{IV1}$$

Incompressibility:

$$\nabla \cdot \underset{\sim}{u} = 0 \quad \text{IV2}$$

Conservation of Mass.

$$\frac{D\rho}{Dt} = 0 \quad \text{where} \quad \frac{D}{Dt} = \frac{\partial}{\partial t} + \underset{\sim}{u} \cdot \underset{\sim}{\nabla} \quad \text{IV3}$$

Pressure Equation.

$$\frac{Dp}{Dt} = 0 \quad \text{where heat fluxes have been neglected.} \quad \text{IV4}$$

Momentum Equation.

$$\rho \frac{D\underset{\sim}{u}}{Dt} + \underset{\sim}{\nabla} p + \underset{\sim}{\nabla} \cdot \underset{\equiv}{\tau} - \underset{\sim}{j} \wedge \underset{\sim}{B} = 0 \qquad \text{IV5}$$

where $\underset{\equiv}{\tau}$ is the gyro-viscous stress tensor.

Resistivity Variation.

$$\frac{D\eta}{Dt} = 0 \qquad \text{IV6}$$

Maxwell's Equations.

$$\underset{\sim}{\nabla} \cdot \underset{\sim}{B} = 0 \qquad \text{IV7}$$

$$\mu_0 \underset{\sim}{j} = \nabla \wedge \underset{\sim}{B} \qquad \text{IV8}$$

$$\nabla \wedge E = -\frac{\partial B}{\partial t} \qquad \text{IV9}$$

In addition, we employ $p_e = p_i = p/2$.

We again consider the equilibrium to be that of a cylindrical plasma bounded by rigid, conducting walls. Steady state plasma diffusion arising from the inclusion of resistive effects is neglected. This omission is justified since the instabilities expected have growth rates dependent upon fractional powers of resistivity whereas the diffusion velocity of the 'steady state' varies in proportion to η. This point is discussed more fully in chapter V and is confirmed by the growth rates computed.

Using the finite Larmor radius parameter, ε, we define an ordering scheme identical to that used by Coppi (31) and consistent with that outlined in chapter I, section 3.

$$\beta \sim \varepsilon^2$$

$$\frac{B_\theta}{B_z} \sim \varepsilon^2 , \quad \frac{E_\theta}{B_z} \sim \frac{E_r}{B_z} \sim \varepsilon v_r^i , \quad \frac{1}{L_{//}} \sim \frac{\varepsilon^2}{L_\perp} , E_z \sim \varepsilon^2 E_\theta$$

$$u_\perp \sim \varepsilon v_r^i , \quad u_z \sim \varepsilon v_r^i$$

$$\frac{\partial}{\partial t} \sim \varepsilon^2 \Omega^i \sim \frac{\eta}{\mu_0 L_\perp^2}$$

The last ordering appears to contradict the preceeding paragraph. However, the effect of the resistivity depends

on the scale length of the perturbation which is, in practice, shorter than that of the equilibrium. Thus, this last ordering arises as a consequence of taking:

$$L_{\perp\,\text{perturbation}} \sim L_{\perp\,\text{equilibrium}}$$

for convenience purposes. So long as the Larmor radius remains much smaller than the perturbation scale length, the theory is still valid. For the tearing mode, Coppi (6) has shown that this applies for large FLR effects, the latter causing an increase in the width of the perturbation about the resonant surface. This point is, again, of deeper significance in chapter V where it is fully discussed.

The validity of the incompressible approximation, IV2, may now be investigated.

The axial component of IV5 yields to lowest order:

$$u_z \sim \frac{1}{\omega L_{//}} \frac{p}{\rho} \sim \frac{\varepsilon^2 / L_\perp}{\varepsilon^2 \Omega^i} v_t^2$$

$$\therefore \quad u_z \sim \varepsilon v_t$$

IV1 yields to lowest order the purely collisionless result:

$$u_r = \frac{E_\theta}{B_z} - \frac{1}{\rho \Omega^i r} \frac{\partial p^i}{\partial \theta} \qquad \text{IV10}$$

$$u_\theta = -\frac{E_r}{B_z} + \frac{1}{\rho \Omega^i} \frac{\partial p^i}{\partial r} \qquad \text{IV11}$$

therefore:

$$\underset{\sim}{\nabla}\cdot\underset{\sim}{u} = \frac{1}{r B_z}\left(\frac{\partial}{\partial r}(r E_\theta) - \frac{\partial E_r}{\partial \theta}\right) - \frac{1}{e B_z r}\left(\frac{\partial p^i}{\partial \theta}\frac{\partial}{\partial r}\left(\frac{1}{n}\right) - \frac{\partial p^i}{\partial r}\frac{\partial}{\partial \theta}\left(\frac{1}{n}\right)\right)$$

so that:

$$\underset{\sim}{\nabla}\cdot\underset{\sim}{u} = -\frac{1}{r B_z}\frac{\partial B_z}{\partial t} - \frac{1}{e r B_z}\left(\frac{\partial}{\partial r}\left(\frac{1}{n}\right)\frac{\partial p^i}{\partial \theta} - \frac{\partial p^i}{\partial r}\frac{\partial}{\partial \theta}\left(\frac{1}{n}\right)\right)$$

Since, from IV5, $\left(p + \frac{B_z^2}{2\mu_0}\right)$ is constant, both in equilibrium and perturbation, to lowest order, $\frac{B_z'}{B_z} \sim \beta \frac{p'}{p}$ so that $\frac{\partial B_z}{\partial t} = 0$ to lowest order. Hence, on consideration of IV3 and IV4, $\underset{\sim}{\nabla}\cdot\underset{\sim}{u}$ vanishes to lowest order in ε, consistent with equation IV2.

The stress tensor $\underline{\underline{\tau}}$ is taken to consist of

merely the gyro-viscous terms. Although the parallel viscous terms are of a lower order in collision frequency than the FLR terms, the former make contributions $\sim\left(\frac{B_\theta}{B_z}\right)^2$ to the equations (due to transforming the tensor from magnetic field to cylindrical coordinates) and are hence neglected in this work. Further discussion of this appears in chapter V.

In order to manipulate the equations into a suitable form, define $\xi = \frac{u_r'}{\omega_1}$ and seek perturbations of the form $\exp(i(\omega t+m\theta+kz))$. ω_1 is defined as $\omega_1 = \omega + \frac{m u_\theta}{r}$

IV9 and the θ component of IV1 yield respectively:

$$E_z' = \frac{k_r}{m} B_\theta' - \frac{\omega_r}{m} B_r' \quad ; \quad \frac{E_\theta'}{B_z} = \omega_1 \xi + \frac{im p'}{2\Omega' \rho r} \qquad \text{IV12}$$

Convective perturbations for density, pressure and resistivity are found from IV3, IV4 and IV6 respectively, using which, the z-component of IV1 yields:

$$\frac{\omega_1 r}{m}\left(B_r' - \bar{k}\xi B_z\right) + \frac{1}{\Omega' \rho}\frac{dp}{dr}\left(\bar{k}\xi B_z - B_r'\right) + \eta_{//} j_z' + i\xi j_z \frac{d\eta_{//}}{dr} = 0$$

Using IV8 and IV7, we substitute for j_z' to obtain:

$$\frac{d}{dr}\left(r^3 \frac{dB_r'}{dr}\right) - (m^2-1) r B_r' = -m r \xi \left(\frac{1}{\eta_{//}}\frac{d\eta_{//}}{dr}\right)\frac{d}{dr}(rB_\theta) \qquad \text{IV13}$$

$$+ \frac{i\mu_0 r^3}{\eta_{//}}\left(B_r' - \bar{k}\xi B_z\right)\left(\omega_1 - \frac{m}{\rho r \Omega'}\frac{dp}{dr}\right)$$

where $\bar{k} = k + \frac{mB_\theta}{rB_z}$

The momentum equation, IV5 is developed in a manner entirely analogous to the collisionless problem, but is here not complicated by heat fluxes, finite beta effects et cetera, in the stress tensor. We take the z-component of the curl of IV5. Only B_r' cannot be eliminated in terms of ξ. The ensuing algebra finally yields:

$$\frac{d}{dr}\left[\left(\rho r^3 \omega_1^2 - \frac{m\omega_1 r^2}{\Omega'}\frac{dp_i}{dr}\right)\frac{d\xi}{dr}\right] + \xi\left[-\frac{(m^2-1)}{r^2}\left(\rho r^3 \omega_1^2 - \frac{m\omega_1 r^2}{\Omega'}\frac{dp_i}{dr}\right) + r^2\omega^2 \frac{d\rho}{dr}\right] \qquad \text{IV14}$$

$$= \frac{1}{\mu_0}\left(\bar{k} B_z \left(\frac{d}{dr}\left(r^3 \frac{dB_r'}{dr}\right) - (m^2-1) r B_r'\right) - m B_z B_r' \frac{d}{dr}\left(r^3 \frac{d\bar{k}}{dr}\right)\right)$$

Substitution from IV13 yields:

$$\frac{d}{da}\left(F_1 \frac{d\zeta}{da}\right) + G_1 \zeta - \alpha\psi = 0 \qquad \text{IV15}$$

where $\zeta = \frac{\xi}{r_x}$, $\psi = \frac{B_r}{B_z}$, $a = \frac{r}{r_x}$, r_x = wall radius.

$$F_1 = \left(\bar{n}\, a^3 \omega_1^2 - m W_F a^2 \omega_1 \frac{d}{da}(\bar{n}\bar{T})\right) W_R \qquad \text{IV16}$$

$$G_1 = i\left(\frac{kr_x}{m} + \frac{B_\theta}{aB_z}\right)^2 \frac{a^3}{\bar{\eta}}\left(\omega_1 - \frac{2mW_F}{\bar{n}a}\frac{d}{da}(\bar{n}\bar{T})\right) m^2 W_A^2 \qquad \text{IV17}$$

$$-\frac{(m^2-1)}{a^2}F_1 + \left[a^2\omega^2 \frac{d\bar{n}}{da} + \left(\frac{kr_x}{m} + \frac{B_\theta}{aB_z}\right) m^2 W_A^2 a \left(\frac{1}{\bar{\eta}}\frac{d\bar{\eta}}{da}\right)\frac{d}{da}\left(\frac{a^2 B_\theta}{aB_z}\right)\right] W_R$$

$$\alpha = \frac{mia^3}{\bar{\eta}}\left(\frac{kr_x}{m} + \frac{B_\theta}{aB_z}\right)\left(\omega_1 - \frac{2mW_F}{\bar{n}a}\frac{d}{da}(\bar{n}\bar{T})\right) W_A^2 \qquad \text{IV18}$$

$$- m W_A^2 \frac{d}{da}\left(a^3 \frac{d}{da}\left(\frac{B_\theta}{aB_z}\right)\right) W_R$$

where $\bar{n}, \bar{\eta}, \bar{T}$ are profiles of number density, resistivity and temperature normalised to unity at a=0 so that $\rho = \bar{n}\rho_0$, $\eta = \bar{\eta}\eta_0$ and $T = \bar{T}T_0$.

$$W_A = B_z/(\mu_0 \rho_0 r_x^2)^{1/2} \quad \text{Alfvén frequency.}$$

$$W_F = kT_0/(2eB_z r_x^2) \quad \text{Ion drift frequency.} \qquad \text{IV19}$$

$$W_R = \eta_{\parallel 0}/(\mu_0 r_x^2) \quad \text{Equilibrium resistive diffusion frequency.}$$

Equation IV13 may be cast into similar form:

$$\frac{d}{da}\left(F_2 \frac{d\psi}{da}\right) + G_2 \psi - v\zeta = 0 \qquad \text{IV20}$$

with

$$F_2 = a^3 W_R \qquad \text{IV21}$$

$$G_2 = -\frac{(m^2-1)}{a^2}F_2 - \frac{ia^3}{\bar{\eta}}\left(\omega_1 - \frac{2mW_F}{\bar{n}a}\frac{d}{da}(\bar{n}\bar{T})\right) \qquad \text{IV22}$$

$$v = -ma\left(\frac{1}{\bar{\eta}}\frac{d\bar{\eta}}{da}\right) W_R \frac{d}{da}\left(a^2 \frac{B_\theta}{aB_z}\right) \qquad \text{IV23}$$

$$- \frac{mia^3}{\bar{\eta}}\left(\frac{kr_x}{m} + \frac{B_\theta}{aB_z}\right)\left(\omega_1 - \frac{2mW_F}{\bar{n}a}\frac{d}{da}(\bar{n}\bar{T})\right)$$

Equation IV11 gives:

$$u_\theta = -\frac{E_r}{B_z} + \frac{W_F}{\bar{n}a}\frac{d}{da}(\bar{n}\bar{T})$$

Equations IV15 and IV20 form the basis of the computational

study of this chapter.

An important property of these equations is now apparent. Consider the set of parameters (W_A, W_F, W_R, kr_x/m, $B_\theta/(aB_z)$) which produces the results (ζ, ψ, ω). On multiplying equations IV15 and IV20 throughout by an arbitrary factor f^3 we see that the parameters (W_A, fW_F, fW_R, fkr_x/m, $fB_\theta/(aB_z)$) produce the results (ζ, $f\psi$, $f\omega$). As the low resistivity limit (low W_R) is of interest in comparison with analytic theories, this property is of great utility in ensuring that the resulting difference equations (see below) are well-conditioned for numerical solution.

As no artificial gravity to drive an interchange mode has been included in the derivation of IV15 and IV20, the only instabilities possible are the rippling mode arising from convection of resistivity and the tearing mode resulting in topology change of the magnetic field. The former will be eliminated in the bulk of the investigation by choosing constant profiles of $\bar{T}$ and $\bar{\eta}$; the latter mode will be the prime subject of investigation.

3) Numerical Procedure.

The numerical problem consists of differencing equations IV 15 and IV20 on a discrete mesh and constructing a determinant from the resulting algebraic equations the zeros of which approximate the complex eigenfrequencies, ω. This is entirely analogous to the investigation of the collisionless equation, but is complicated by the fact that the perturbation equations constitute a fourth order differential set as opposed to the second order one previously considered.

At the rigid conducting wall (a=1) $\zeta = \psi = 0$. Thus, on dividing the interval $0 < a < 1$ into N discrete segments and

defining the vectors $\zeta_n = \zeta(\frac{n}{N})$ and $\psi_n = \psi(\frac{n}{N})$ we can set $\zeta_N = \psi_N = 0$. As in the collisionless case, symmetry considerations determine the boundary conditions at the origin:

$$0 = \left.\frac{d\zeta}{da}\right|_{a=0} = \left.\frac{d\psi}{da}\right|_{a=0} \quad \text{for } m = 1$$

$$0 = \zeta_0 = \psi_0 \quad \text{for } m \neq 1$$

The space step may be defined as $\delta = 1/N$ so that differencing IV15 yields:

$$\frac{F_{1n}}{\delta^2}(\zeta_{n+1} + \zeta_{n-1} - 2\zeta_n) + \frac{F'_{1n}}{2\delta}(\zeta_{n+1} - \zeta_{n-1}) + G_{1n}\zeta_n - \alpha_n\psi_n = 0 \quad \text{IV24}$$

and IV20 gives:

$$\frac{F_{2n}}{\delta^2}(\psi_{n+1} + \psi_{n-1} - 2\psi_n) + \frac{F'_{2n}}{2\delta}(\psi_{n+1} - \psi_{n-1}) + G_{2n}\psi_n - \nu_n\psi_n = 0 \quad \text{IV25}$$

where the vectors F_{1n}, G_{1n}, F_{2n}, G_{2n}, α_n, ν_n denote the continuous functions evaluated at the nth. mesh point. In fact, in order to minimise computation, these functions were evaluated 0.01δ on either side of each mesh point, as in the collisionless case, so that, for example:

$$F_{1n} = \frac{1}{2}\left(F_1\left(\frac{n+0.01}{N}\right) + F_1\left(\frac{n-0.01}{N}\right)\right)$$

and

$$F'_{1n} = 50N\left(F_1\left(\frac{n+0.01}{N}\right) - F_1\left(\frac{n-0.01}{N}\right)\right)$$

analogous with the procedure adopted in chapter III.

The boundary condition of m=1 at a=0 remains the only problem. For this case, differentiate IV15 and IV20 three times at a=0 to obtain (analogous to the collisionless case):

$$\left.\begin{aligned} 4F_1''' \frac{d^2\zeta}{da^2} + G_1'''\zeta - \alpha'''\psi = 0 \quad \text{IV26} \\ 4F_2''' \frac{d^2\psi}{da^2} + G_2'''\psi - \nu'''\zeta = 0 \quad \text{IV27} \end{aligned}\right\} \text{ at } a=0$$

Here we have used the symmetry requirements that each of G, F, α and ν together with their first and second derivatives vanish at a=0 when m=1.

The symmetry of the mode requires that $\zeta_{-1} = \zeta_1$, $\psi_{-1} = \psi_1$ so that differencing at n=0 yields:

$$8F_{10}'''(\zeta_1-\zeta_0)/\delta^2 + G_{10}'''\zeta_0 - \alpha_0'''\psi_0 = 0 \qquad \text{IV28}$$

$$8F_{20}'''(\psi_1-\psi_0)/\delta^2 + G_{20}'''\psi_0 - \nu_0'''\zeta_0 = 0 \qquad \text{IV29}$$

Now $F_1'''(0) \simeq \frac{1}{\delta}\left(F_1''\left(\frac{\delta}{2}\right) - F_1''\left(-\frac{\delta}{2}\right)\right) = 2\frac{F''\left(\frac{\delta}{2}\right)}{\delta} \approx 2\frac{F'(\delta)}{\delta^2}$

and similarly for the other functions, so that IV28 and IV29 become:

$$\frac{16F_{11}'}{\delta^4}(\zeta_1-\zeta_0) + \frac{2G_{11}'}{\delta^2}\zeta_0 - \frac{2\alpha_1'}{\delta^2}\psi_0 = 0 \qquad \text{IV30}$$

$$\frac{16F_{21}'}{\delta^4}(\psi_1-\psi_0) + \frac{2G_{21}'}{\delta^2}\psi_0 - \frac{2\nu_1'}{\delta^2}\zeta_0 = 0 \qquad \text{IV31}$$

Equations IV30 and IV31 contain only functions that are readily available from the coding required for all points of the mesh.

In order to describe the solution of the difference equations define the vector W_n:

$$W_{2n} = \psi_n \quad ; \quad W_{2n-1} = \zeta_n$$

so that equations IV24 and IV25 may be written:

$$R_{2n-1}^1 W_{2n-3} + R_{2n-1}^3 W_{2n-1} + R_{2n-1}^4 W_{2n} + R_{2n-1}^5 W_{2n+1} \qquad \text{IV32}$$

$$R_{2n}^1 W_{2n-2} + R_{2n}^2 W_{2n-1} + R_{2n}^3 W_{2n} + R_{2n}^5 W_{2n+2} \qquad \text{IV33}$$

where

$$R_{2n-1}^1 = \frac{F_{1n}}{\delta^2} - \frac{F_{1n}'}{2\delta} \; ; \; R_{2n-1}^3 = G_{1n} - \frac{2F_{1n}}{\delta^2}$$

$$R_{2n-1}^4 = -\alpha_n \; ; \; R_{2n-1}^5 = \frac{F_{1n}}{\delta^2} + \frac{F_{1n}'}{2\delta}$$

$$R_{2n}^1 = \frac{F_{2n}}{\delta^2} - \frac{F_{2n}'}{\delta} \; ; \; R_{2n}^2 = -\nu_n$$

$$R_{2n}^3 = G_{2n} - \frac{2F_{2n}}{\delta^2} \; ; \; R_{2n}^5 = \frac{F_{2n}}{\delta^2} + \frac{F_{2n}'}{2\delta}$$

The coefficients R_j^i are, in general, quadratic in the unknown frequency, ω, and complex. For speed of iteration it is convenient to calculate and store the three quadratic coefficients for each R_j^i. This is the largest storage

requirement of the problem, needing 60N words of core.

The difference equations IV32 and IV33, repeated for all n, clearly constitute a quin-diagonal homogeneous matrix equation. Hence, the calculation of the eigenfrequencies, ω, requires the evaluation of the quin-diagonal determinant so that its zeros may be found by iteration. The Muller's algorithm, coded for the collisionless equation, was used for this latter purpose; the evaluation of the determinant requires further comment.

A method of evaluating a quin-diagonal determinant for root-solving purposes must be as rapid as possible, since many iterations may be required, use as little working storage as possible, since large numbers of mesh points are desirable, and yet remain free from gross numerical errors. In order to maintain speed, the quin-diagonal structure of the determinant must be employed to greatest effect. Consider the determinant:

$$
\begin{vmatrix}
a_1^3 & a_1^4 & a_1^5 & & & & & & \\
a_2^2 & a_2^3 & a_2^4 & a_2^5 & & & & & \\
a_3^1 & a_3^2 & a_3^3 & a_3^4 & a_3^5 & & & & \\
 & a_4^1 & a_4^2 & a_4^3 & a_4^4 & a_4^5 & & & \\
 & & & & & & & & \\
 & & & & & & & & \\
 & & & & & & & & \\
 & & & & & & a_{N-5}^1 & a_{N-5}^2 & a_{N-5}^3 & a_{N-5}^4 & a_{N-5}^5 \\
 & & & & & & & a_{N-4}^1 & a_{N-4}^2 & a_{N-4}^3 & a_{N-4}^4 & a_{N-4}^5 \\
 & & & & & & & & a_{N-3}^1 & a_{N-3}^2 & a_{N-3}^3 & a_{N-3}^4 \\
 & & & & & & & & & a_{N-2}^1 & a_{N-2}^2 & a_{N-2}^3
\end{vmatrix}
$$

Three methods of evaluation are apparent (39, 48, 49):

a) Diagonals 1 and 2 may be eliminated from row n by subtracting multiples of preceeding rows. Thus, row 1 may

be used to eliminate a_2^2 and a_3^1, row 2 to remove a_3^2 and a_4^1 etc. This leaves an upper triangular matrix whose determinant is the product of the diagonal elements.

b) The matrix may be reduced to (upper) Hessenberg form by eliminating diagonal 1. Then we may set W_{N-2} =1 and calculate W_{N-3} to W_1 in turn by scanning up the rows of the matrix. The determinant is then given by $a_1^3W_1+a_1^4W_2+a_1^5W_3$. (see reference 39 page 105).

c) The elimination of diagonals 1 and 5 reduces the matrix to tri-diagonal form. This is the form that resulted in the collisionless case and the determinant may be evaluated using the same recursion formula (see reference 7).

Since the determinant calculated must approach zero as the iteration scheme for ω converges, one of the diagonal elements of the final matrix produced by method a) must tend to zero. This clearly means that, close to convergence, the quin-diagonal matrix is ill-conditioned for the eliminations required in method a). Whilst this could be overcome by pivoting (swapping rows) to ensure that the final diagonal element tended to zero after elimination, this incurs time-consuming complexity.

Method c) is by far the simplest to program and hence the most attractive to use. However, if, for some set of parameters, the matrix were ill-conditioned to the eliminations required, pivoting to correct for this would not be possible as it would destroy the final tri-diagonal form.

The second method (b), although more complicated than (c) and hence marginally slower, has two advantages. Firstly, pivoting may be incorporated if found necessary to improve the conditioning towards elimination and secondly, the final

recursion involved yields the eigenvector without further computation.

In practice, method c) was used for the bulk of the computations as this was found sufficiently accurate when scaling (see section 2) of the parameters of the problem was employed to produce numerical stability in the determinant evaluation. When eigenfunctions were required, method b) was employed. The agreement of values of ω iterated by these two methods separately provided a good defence against spurious results generated by numerical instability.

For a given set of parameters, using a mesh of N steps, all of the roots of the quin-diagonal matrix were calculated by repeated iteration, dividing out known roots from the calculated determinant at each evaluation. Since equation IV15 is quadratic in ω and equation IV20 linear, $3(N-1)$ such roots were found for $m\neq1$ and $3N$ for $m=1$.(allowing for boundary conditions).

Two possible sources of numerical error exist: 1) Errors in the evaluation of the roots of the discrete (differenced) problem. 2) Deviation of these roots from those of the continuous (differential) problem. The first was checked in two ways. Demanding that the iteration scheme calculate more roots than were analytically known to exist for the discrete problem and observing that the scheme always diverged after calculating the correct number, asserted that all roots had been effectively divided out. In the limit $W_F=0$ with resistivity profiled so that $\underline{\nabla}_\perp(\eta\underline{\nabla}_\perp\underline{B})=0$ in the steady state, Furth et al.(7) showed that $\mathrm{Re}(i\omega)$ is only positive when $\mathrm{Im}(i\omega)=0$. Otherwise, complex values of $i\omega$ occur in complex conjugate pairs. Three types of roots were found to the

discrete problem when $W_F=0=d\bar{\eta}/da$. These corresponded to the two mentioned above plus a selection that were zero to the accuracy of the calculations; these became finite when either of W_F or $d\bar{\eta}/da$ was made non-zero.

As there always exist eigenfunctions describing the oscillation of the discretised mesh, there are always roots of the determinant that bear no relation to those of the differential problem. Eigenfunctions with few nodes, a property that characterises the most unstable, may be represented, if only approximately, with a mesh of only 20 points. It was found that the most unstable eigenfunction, that of primary interest, was usually of this type and the corresponding root for ω could be improved by using the value calculated from a 20 point mesh as an initial guess for a search on one of finer spacing. Typically, meshes of 50 or 100 points were finally employed, the roots being sought by gradual increases in the number of mesh points. The magnitude of the final discrepancy could be estimated only by varying mesh size. A variation of $\lesssim$ 10% when the mesh size was doubled was considered to constitute a reasonable approximation.

The technique of selecting the one required root from the selection of 54 calculated is clearly extremely uneconomical with computer time. However, once found, the dependence of a root upon the various parameters of the problem could be investigated by parameter perturbation methods as discussed in section 1. This only broke down when the parameter change required to avoid skipping to an incorrect root became unreasonably small; such behavior was characterised by the mesh becoming too coarse to resolve the eigenfunction as the

parameter concerned was varied.

4) Comparison of Results with Previous Theory.

As the numerical approach adopted calculates the eigenfunction across the whole plasma, a comparison of the results obtained with those of conventional theory in the absence of FLR is required in order to distinguish the influence of the latter from effects merely due to the breakdown of the approximations of the analytic theory. Explicit growth rates could be extracted from published theory by substituting values of the logarithmic derivative discontinuity of B_r' (Δ) taken from reference (47) into the expression for the growth rate in terms of this quantity found in reference (7). The former reference calculates Δ for three separate profiles (peaked, rounded and flattened) as a function of the position

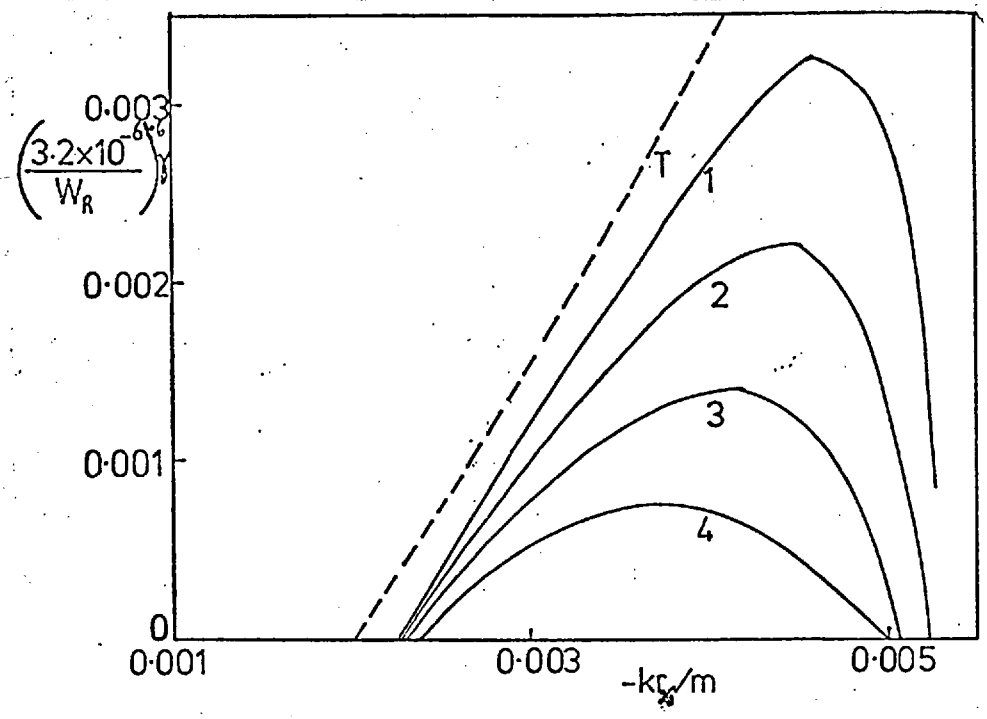

Figure IV1 - Growth rate scaled by $(W_R)^{3/5}$ versus axial wavenumber for W_R = 1) 3.2×10^{-6}, 2) 10^{-5}, 3) 3.1×10^{-5}, 4) 10^{-4}. T was calculated from the results of Furth et al. (4). m=2, W_A=100, $\bar{n}=\exp(-0.5(a/0.3)^2$, $B_\theta/(aB_z)=5.45\times10^{-3}/(1+4a^2)$ (peaked profile)

of the resonant surface.

Figure IV1 illustrates the resistive dependence of the growth rate for the peaked profile of Furth et al.(47). (Note that, in this chapter, the frequency scale is defined by W_A=100 units.) The 'theoretical' curve, T, was calculated from the expression derived in reference (7):

$$\gamma = 0.5\, m^{2/5}\left[\frac{d}{da}\left(\frac{B\theta}{aB_z}\right)\right]^{2/5}\left(\frac{r_x}{r_p}\right)^{4/5} W_R^{3/5}\, W_A^{2/5}\, \Delta^{4/5}$$

where r_p is defined as $r_x\left[\frac{B\theta}{qB_z}\Big/\frac{d}{da}\left(\frac{B\theta}{aB_z}\right)\right]$, the scale length of the magnetic pitch profile. W_R was taken as appropriate to curve 1. The computed curves on this diagram are scaled by $(W_R)^{3/5}$ as appropriate to tearing instabilities. Hence, according to the analysis, they should all correspond to the single 'theoretical' curve. Evidently, as the resistivity increases, so the errors in the analysis become more severe. Varying kr_x/m moves the position of the resonant surface in the plasma. As the magnitude of this parameter increases, so the resonant surface moves in towards the origin. In this region, the analyses break down for two reasons. Firstly because they neglect curvature in comparison with the thickness of the resistive region and secondly since the pitch profile peaks at a=0, due to symmetry considerations, causing the resistive scale length to diverge. The computations indicate that the radius to which these discrepancies are important decreases as resistivity falls.

In figure IV2 we see the behavior of the growth rate of the more unstable rounded and flattened profiles of reference (47). With the resonant surface distant from the axis (low $\left|\frac{kr_x}{m}\right|$) the computations for the rounded and flattened profiles approach more closely the results of analysis. In particular, the computations agree well with the cut-off

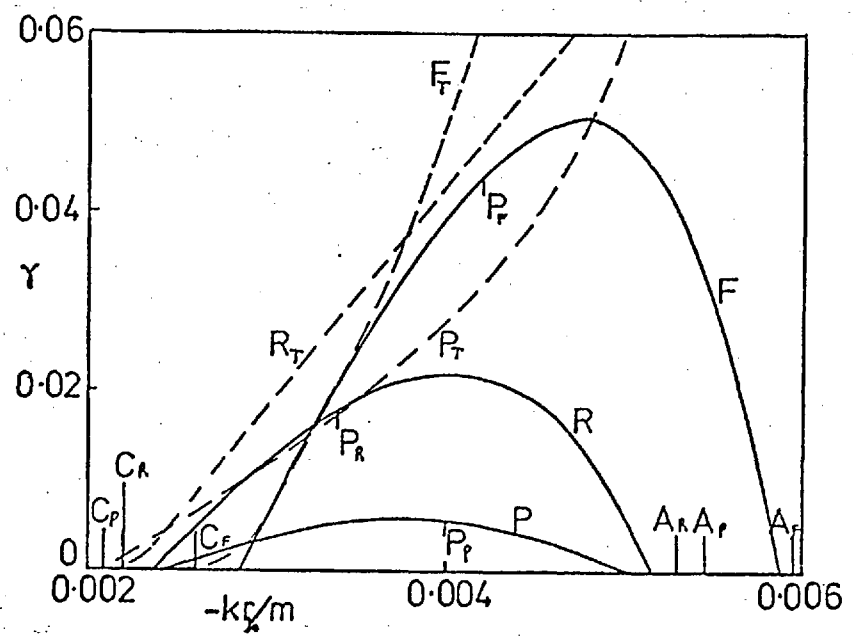

Figure IV2 - Growth rate versus axial wavenumber.
F: flattened profile, $B_\theta/(aB_z) = 0.005945/(1+(2a)^8)^{\frac{1}{4}}$
R: rounded profile, $B_\theta/(aB_z) = 0.0053/(1+(2a)^4)^{\frac{1}{2}}$
P: peaked profile, $B_\theta/(aB_z) = 0.00545/(1+4a^2)$
m=2, $W_R = 10^{-4}$, $W_A = 100$, F_T, R_T and P_T are the corresponding curves calculated from Furth et al.(4) $\left|\frac{kr}{m}x\right|$ taken from reference (47). (C_P, C_R, C_F for the peaked, rounded and flattened profiles respectively). From figure IV1, we observe that this cut-off does not depend strongly on the resistivity. Close to the axis (large $\left|\frac{kr}{m}x\right|$), the modes are cut off as the resonant surface approaches a=0. The appropriate values of $-\frac{kr}{m}x$ are indicated by A_P, A_R, A_F respectively. The peakes of the curves in figure IV2 occur with resonant surfaces near the regions of maximum pitch gradient $\left(\frac{d}{da}\left(\frac{B\theta}{aB_z}\right)\right)$ (indicated by P_P, P_R, P_F) indicating the importance of the current profile in driving tearing modes.

Figure IV3 shows the resistive dependence of the instabilities discussed above. The $-\frac{kr}{m}x$ values employed are close to those giving the maximum growth rates in figure IV2. Two features are apparent. 1) At small resistivity the curves approach the $W_R^{3/5}$ law indicated by the broken lines, but deviate at larger resistivity; the growth rates pass through

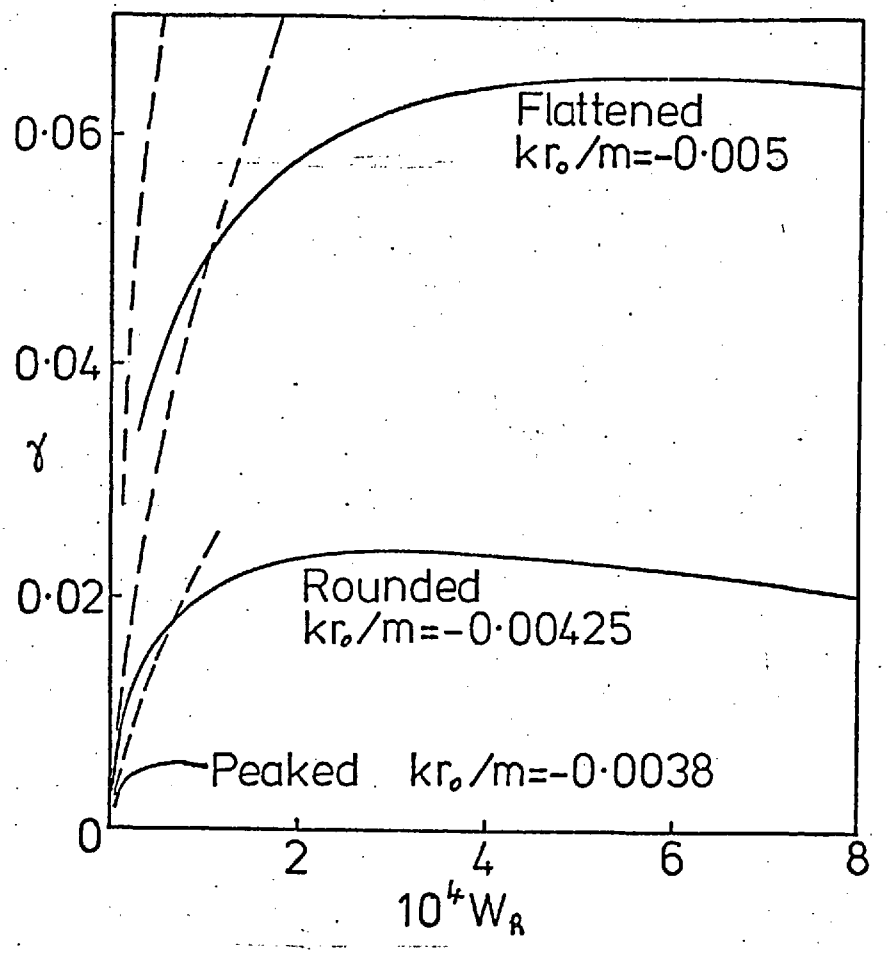

Figure IV3 - Growth rate versus resistivity for the three profiles compared to prediction from Furth et al.(4). kr_x/m values are chosen to approximate those at the peaks of the curves in figure IV2. $m=2$, $W_A=100$, $\bar{n}=\exp(-0.5(a/0.3)^2)$.

maxima and fall as W_R rises further. The analytical formulae clearly over-estimate the growth rate except at very small resistivity. The line $\gamma = 100 W_R$ passes close to the peaks; recall that the growth rate, γ, must greatly exceed the resistive diffusion of the steady state for the theory to be valid. To the right of the peaks, therefore, the basis of the initial assumptions begins to become suspect.

2) At $W_R = 10^{-4}$, the value used on figure IV2, the growth rate of the peaked profile mode is close to the maximum of its plot, whereas those of the other two profiles lie to the left of the peaks. This explains the poorer agreement with the theoretical curves found in figure IV2 for the peaked

profile.

On passing from flattened to rounded to peaked profile, the radial displacement (ξ) became increasingly localised in the region of the resonant surface and hence more difficult to compute. This localisation might be explained by the decreasing scale length of the profiles at small radius having a greater restriction on the magnitude of the perturbation in this region so that the resistively generated displacement becomes isolated about the resonant surface.

The behavior of the growth rate peak at various positions of the resonant surface is illustrated for the peaked profile in figure IV4. Curve 1 has the resonant surface furthest from the axis and hence the peak in $\gamma(W_R)$ occurs at the

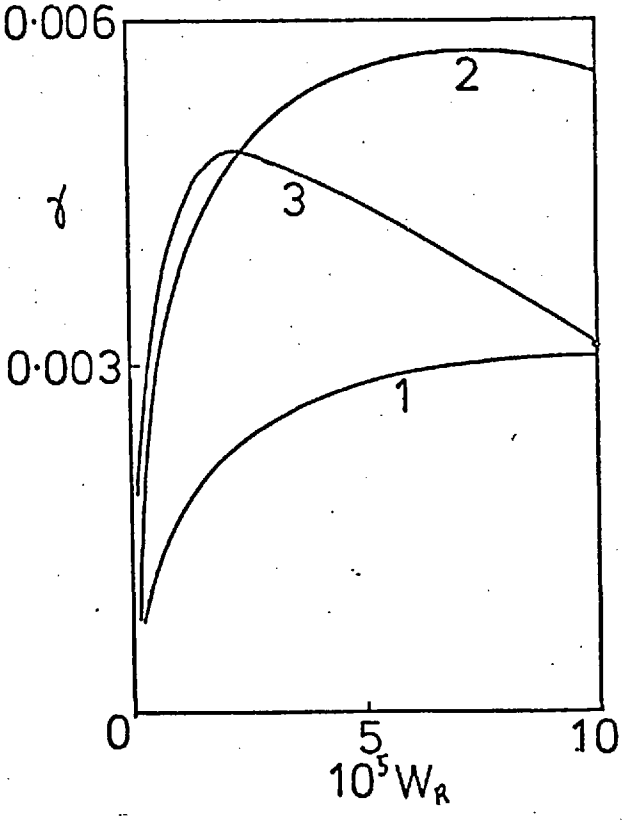

Figure IV4 - Growth rate versus resistivity for the peaked profile: 1) $kr_x/m = -0.00289$, 2) $kr_x/m = -0.0038$ 3) $kr_x/m = -0.0045$. $m=2$, $W_A=100$, $\bar{n}=\exp(-0.5(a/0.3)^2)$

largest W_R. As the surface approaches r=0, so the peak occurs at smaller resistivity confirming that deviation from the analytic behavior is connected with the singularities associated with the axis.

Figures IV5 and IV6 demonstrate the dependence of the instabilities upon azimuthal mode number for the flattened

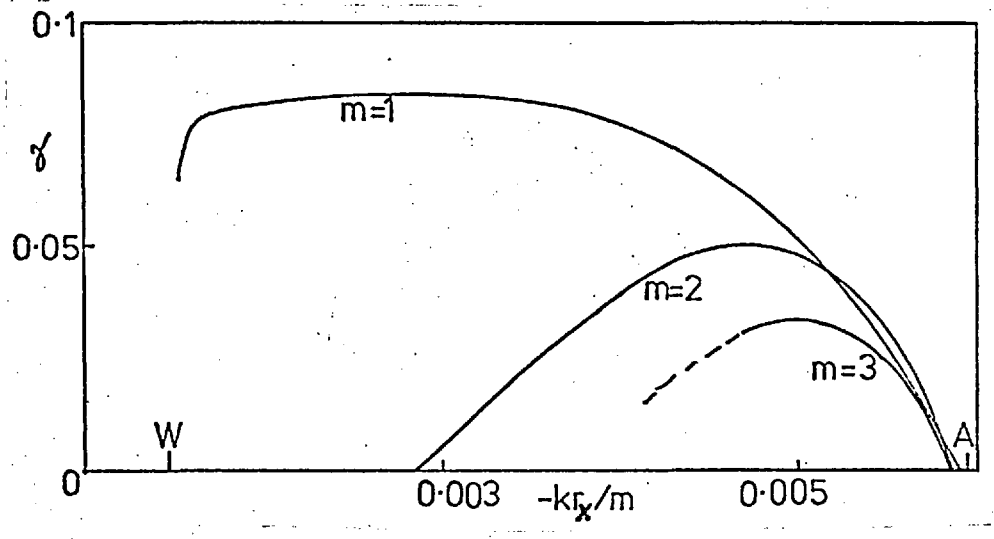

Figure IV5 - Growth rate versus axial wave number with various m numbers for the flattened profile.
W denotes $(B_\theta/(aB_z))_{wall}$,
A denotes $(B_\theta/(aB_z))_{axis}$,
$W_R=10^{-4}$, $W_A=100$, $\bar{n}=\exp(-0.5(a/0.3)^2)$.

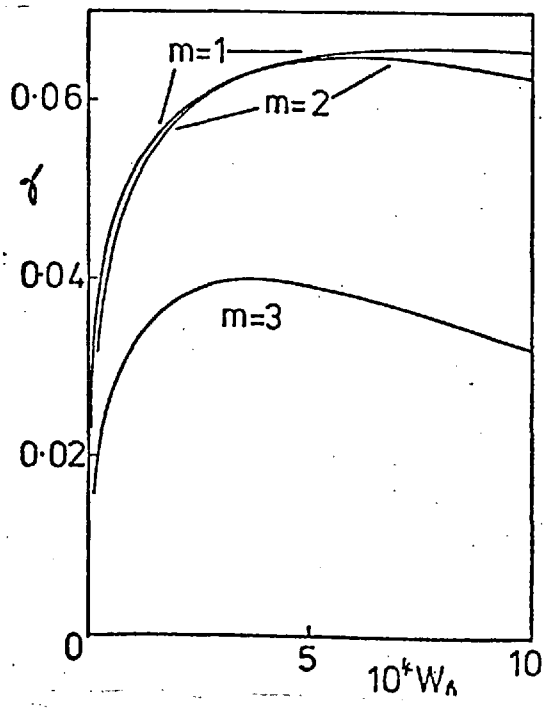

Figure IV6 - Growth rate versus resistivity with various m numbers for the flattened profile. $kr_x/m=-0.005$, $W_A=100$, $\bar{n}=\exp(-0.5(a/0.3)^2)$.

profile. The m=1 mode is particularly noteworthy as the theory of Furth et al. (47) is inapplicable to this case. The resistive dependence of this mode confirms that the instability found does not exist in the collisionless limit. From the dependence of its growth rate upon $\frac{kr}{m}x$, we see that this mode does not cut off like the higher m number instabilities until the resonant surface comes within the influence of the conducting wall. (at $kr_x/m = -0.0015$). This behavior was characteristic of the m=1 mode in the collisionless limit. Since, in the manner of collisionless modes, the instabilities become more localised about the resonant surface as the m number increases, the m=3 instability became too fine to resolve on a 100 point mesh when the resonant surface became detached from the effects of the axis. Nevertheless, a decrease in growth rate with increasing mode number is clearly displayed.

The eigenfunctions themselves indicate the reason for the ultimate failure of the analytic theory. These are portrayed in fugures IV7 a,b and c for m=1, 2 and 3 modes respectively. On the m=2 and 3 diagrams, the region within which large deviation occurs from the collisionless relationship $B_r' = \bar{k}\xi B_z$ is indicated. As resistivity is reduced, the region is seen to become narrower. Inspection shows that, for all resistivity, the scale length of the displacement, ξ, is very much less than that of the magnetic field perturbation near the resonant surface; this is the basis of the 'constant ψ' approximation used in the relevant analytic theories (see reference (7)). However, at resistivities comparable to that causing the maximum growth rate, this 'inner' region around the resonant surface occupies a

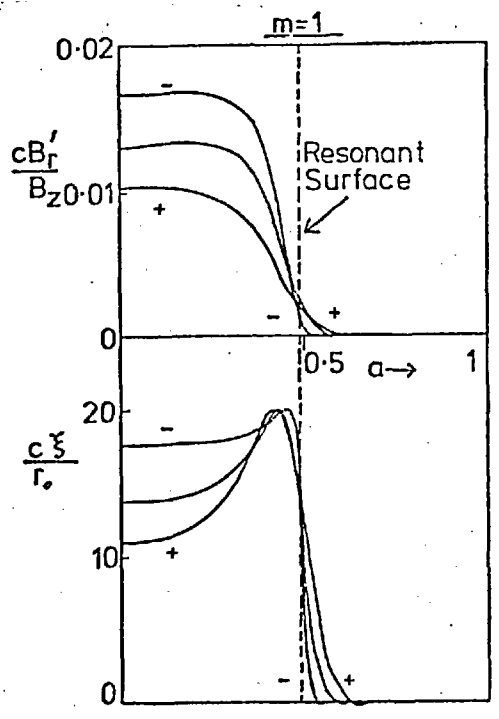

a) $W_R = 6\times10^{-4}$; 2×10^{-4} & 1.5×10^{-5}.

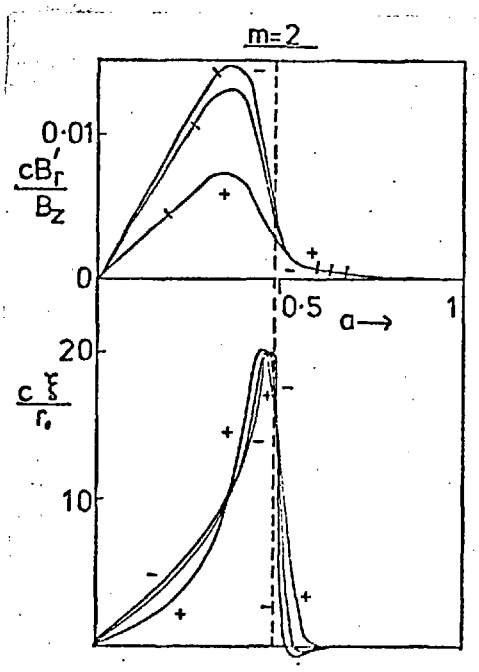

b) $W_R = 10^{-3}$, 1.5×10^{-4} & 4.5×10^{-5}.

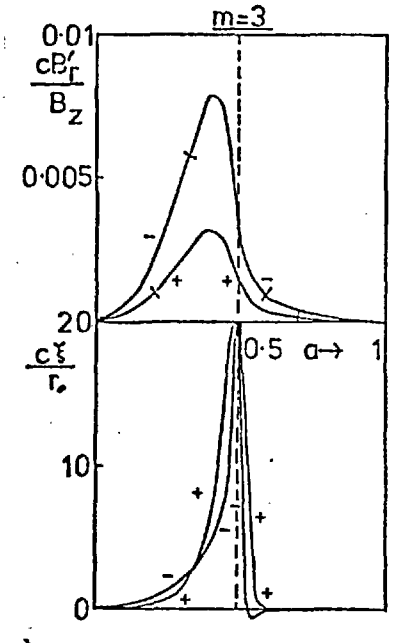

c) $W_R = 8.2\times10^{-4}$ & 4.5×10^{-5}.

Figure IV7 - Eigenfunctions with the flattened profile, $kr_x/m = -0.005$, $W_A = 100$, $\bar{n} = \exp(-0.5(a/0.3)^2)$.
+ denotes largest resistivity,
- denotes smallest resistivity.

significant fraction of the total plasma radius so that neither the 'constant ψ' nor the localisation assumptions of the analytic theory may be considered valid. Breakdown of the analytic results thus arises from the violation of the 'constant ψ' and localisation approximations. This leads to the incorporation within the resistive layer of regions of significantly lower magnetic shear $\left(\frac{d}{da}\left(\frac{B_\theta}{aB_z}\right)\right)$ than present precisely at the resonant surface so that, on average, a smaller driving force is exerted.

Since reduction of resistivity in the regime far to the left of the peak of the $\gamma(W_R)$ diagram, results in gradients of ξ on an incredibly fine scale as shown in figure IV7, the computational method failed as attempts at further resistivity reduction were made. Nevertheless, computation using a 100 point mesh managed to reach 1/200 of the peak resistivity in one particular case attempted, for which a growth rate dependence of $(W_R)^{0.52}$ was attained before computations ceased. Thus, computation and analysis cannot readily be made to describe the same situation, but are complementary in their applicability.

Figure IV8 shows the behavior of m=2 eigenfunctions as the resonant surface moves through the plasma. The negative dip in ξ beyond the resonant surface clearly increases in size as the surface approaches the wall. Increased localisation of the displacement arises due to detachment from the effects of the axis and the reduction in inertial effects in the plasma of lower density nearer the wall. The magnetic field perturbation clearly attains its maximum value when the resonant surface is near the position that gives the maximum growth rate.

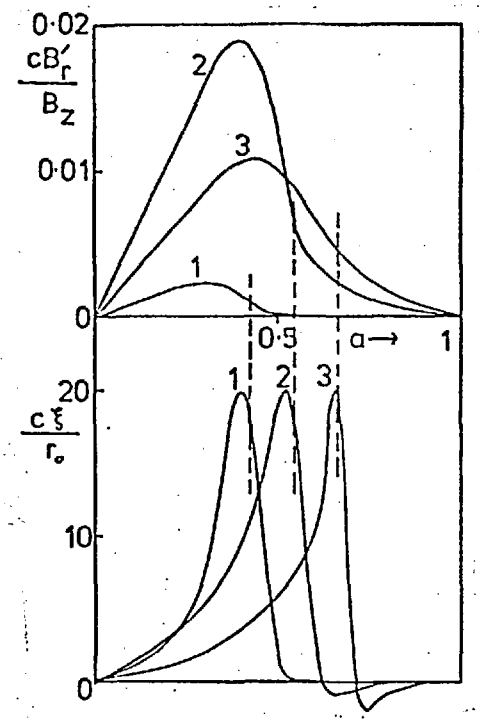

Figure IV8 - Eigenfunctions with the flattened profile. m=2, $W_R=6\times10^{-4}$, $W_A=100$, $\bar{n} = \exp(-0.5(a/0.3)^2)$.
1) $kr_x/m = -0.005$
2) $kr_x/m = -0.00425$
3) $kr_x/m = -0.00311$

Introducing a temperature profile, with resistivity varying as $T^{-3/2}$ has two main effects. Firstly, the resistivity at the resonant surface depends upon its position within the plasma and secondly, rippling modes driven by resistivity convection at the resonant surface appear. The former phenomenon is manifest by an enhancement of the growth rate at lower $\left|\frac{kr}{m}x\right|$ where the resonant surface occurs in the cooler outer regions of the plasma. Rippling modes appear when the full set of roots for a small mesh is computed in the first stages of the calculations. The cluster of roots around the origin, found previously, is replaced by a collection of further modes; those having $Re(\omega)\neq0$ occur in pairs with complex conjugate values of $i\omega$ as required by the form of the equations.

An interesting example of a case with a flat temperature profile cutting off steeply at a certain radius is shown in figure IV9. The rapid rise in resistivity at this particular radius is intended to model the interface between a confined hot plasma column, perhaps defined by limiters, and surrounding

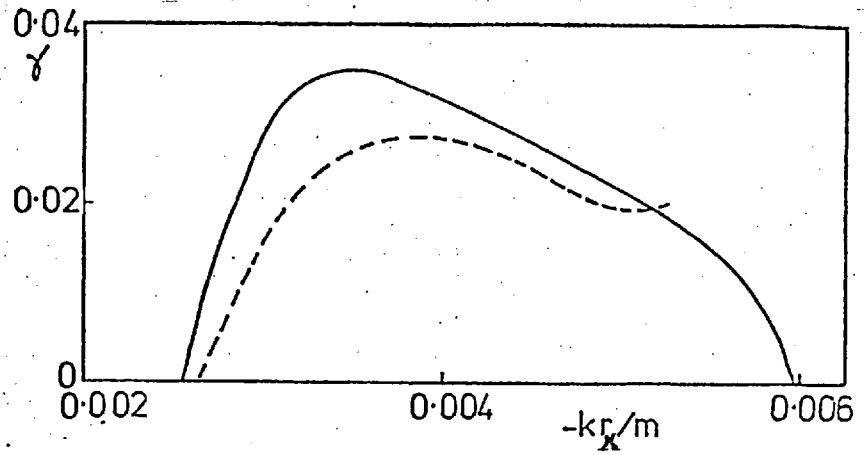

Figure IV9 - Growth rate versus axial wave-number for the flattened profile. m=2, W_A=100, $W_R=2\times10^{-6}$, $\bar{n}=\exp(-0.5(a/0.3)^2)$, $\bar{T}=0.01+0.495(\tanh(10(a+0.5))-\tanh(10(a-0.5)))$, $\bar{\eta}=(\bar{T})^{-3/2}$. The broken line arises from the tearing mode formula of Furth et al.(7), not including $d\bar{\eta}/dr$ effects.

cooler regions of low density. The rippling driving force enhances the growth rate above that predicted by the pure tearing mode formula when, at low $\left|\frac{kr}{m}x\right|$, the resonant surface lies in the highly resistive region of the plasma. This is perhaps a better model of a confined plasma than the flat resistivity profiles considered before since less emphasis is placed on the regions around r=0 where the analysis is inapplicable and the resistivity of an experimental plasma is too small for resistive modes to exist. Consideration of this last example therefore indicates a less pessimistic view of the merits of the analytical approach.

5) The Effect of FLR Terms.

As discussed in the collisionless limit, care must be taken, when considering FLR phenomena, to define the steady state rotation. In what follows, the steady state electric field (E_r) is taken as zero, so that the rotation is given by the ion pressure gradient (see equation IV11). Coppi(31) showed that, in cartesian geometry, steady state velocity merely caused a Doppler shift of the perturbations. In the

present, cylindrical, case this is not precisely true due to centrifugal effects present in the $d\bar{n}/da$ term of G_1 (eq. IV17) which depends on ω^2 rather than ω_1^2. As this does not depend on any derivative of ξ, which becomes large close to the resonant surface, the destabilising effects of rotation are of minor importance.

The first effects of including terms in W_F are the changes induced into the frequency spectrum of the roots of the coarse mesh determinant. Complex conjugate pairs of $i\omega$ no longer appear and the cluster of modes located around the origin take finite frequencies. As will be seen later, additional unstable modes arise. Although the removal of the

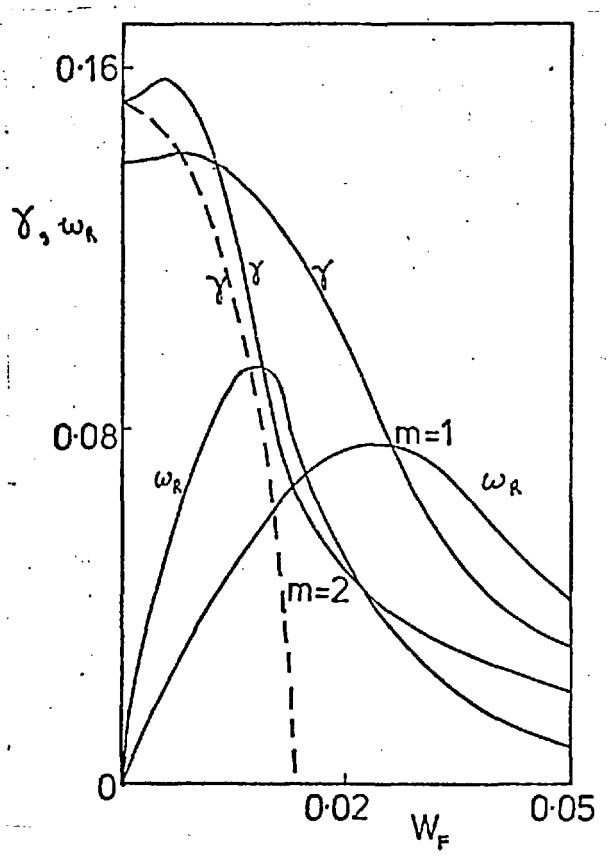

Figure IV10 - Growth rate γ and frequency ω_R versus FLR effect.
$W_R=2.5\times10^{-3}$, $W_A=100$, $kr_x/m=-0.002$,
$\bar{n}=\exp(-0.5(a/0.3)^2)$,
$B_\theta/(aB_z)=0.002(\tanh(10(a+0.5))-\tanh(10(a-0.5)))$
('tanh' profile of $B_\theta/(aB_z)$.
The broken curve shows γ for m=2 when an electron pressure term is omitted.

origin cluster speeds the computationally lengthy iteration for all the roots of the coarse mesh, the proliferation that clutters the complex plane complicates the study of the parametric dependence of any mode of interest.

Figure IV10 shows the effect of increasing the FLR factor, W_F. As will be seen below, the initial rise in growth rate is only present when W_R exceeds the value giving maximum growth rate. At large W_F, no cut-off is produced as for collisionless (Suydam) modes, but a continual growth rate reduction arises as FLR effects increase. Such behavior was described by Coppi (31). The frequency of oscillation contrasts the results of Coppi(31) in this larger resistivity regime. Although it peaks after its initial rise and gets smaller at larger W_F, Coppi's results indicate that it should be negative, tending to the diamagnetic rotation frequency as W_F becomes large. From the diagram, FLR stabilisation, as might be expected, is more effective on m=2 than on m=1 modes.

The broken curve of figure IV10 displays the results that arise if the electron pressure contribution to the Hall terms of equation IV13 is omitted. This omission reproduces the FLR induced cut-off effect that is familiar from collisionless results.

The resistive dependence of the growth rate for various values of W_F appears in figure IV11a. Figure IV11b shows the corresponding frequencies of oscillation. Note that computations ceased as the latter approached or passed through zero; this will be discussed below.

As FLR increases, figure IV11a indicates a less violent dependence of growth rate upon resistivity and a tendency for the peak growth rate to occur at larger W_R. The former behavior

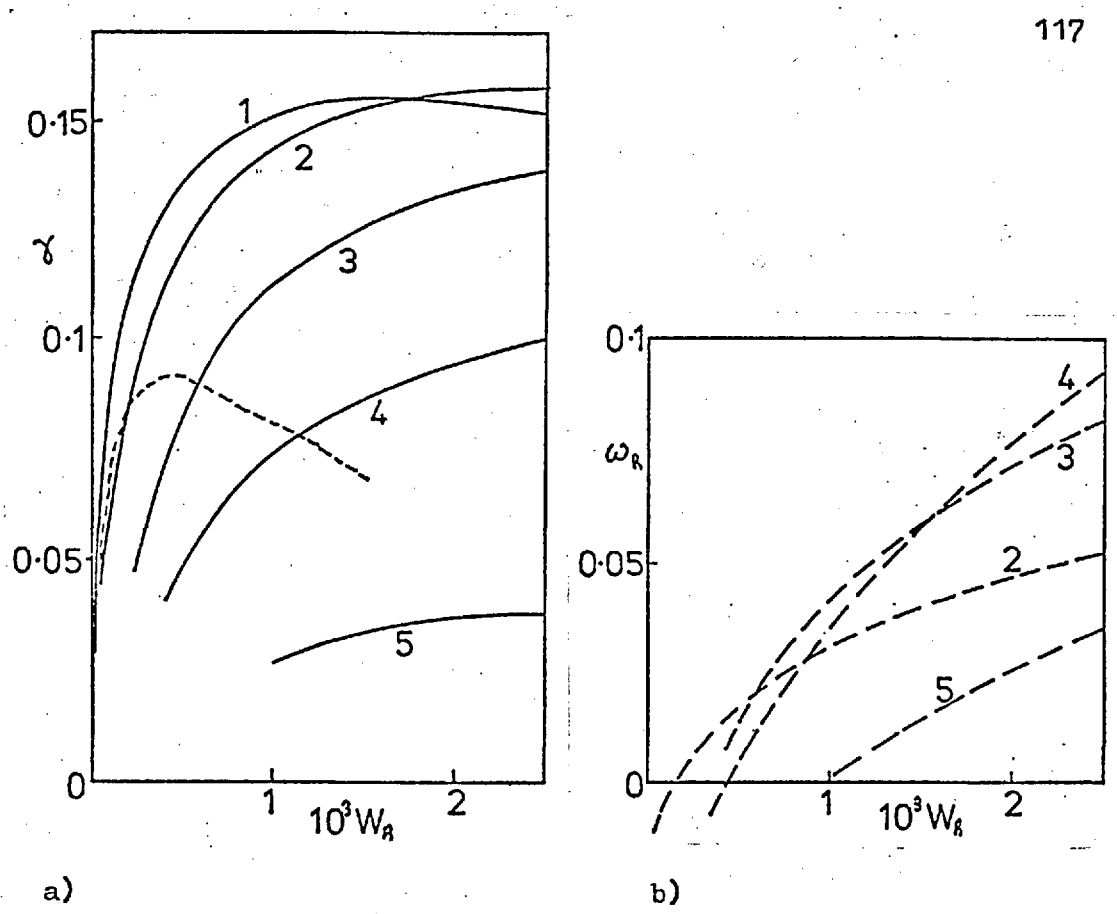

Figure IV11 - The resistive dependence of a) growth rate and b) frequency of oscillation using: 'tanh' profile of $B_\theta/(aB_z)$, m=2, $kr_x/m=-0.002$, $W_A=100$, $\bar{n}=\exp(-0.5(a/0.3)^2)$.
1) $W_F=0$, 2) $W_F=5.01\times10^{-3}$, 3) $W_F=10^{-2}$, 4) $W_F=1.5\times10^{-2}$, 5) $W_F=3\times10^{-2}$. The dashed curve of a) shows the growth rate of an additional mode with $W_F= 1.5\times10^{-2}$.

is in qualitative accord with Coppi (31) who showed that, in the limit of large W_F, growth rate varied linearly with resistivity. Owing to the behavior of steady state resistive diffusion and the very small growth rate when FLR effects are large, the validity of the perturbation theory in this limit is suspect; neglect of steady state diffusion was based upon assuming a growth rate with a fractional power law dependence upon resistivity.

When W_R is less than the value producing maximum growth rate at $W_F=0$, figure IV11a indicates that the peaking observed on figure IV10 might not appear. This is confirmed by

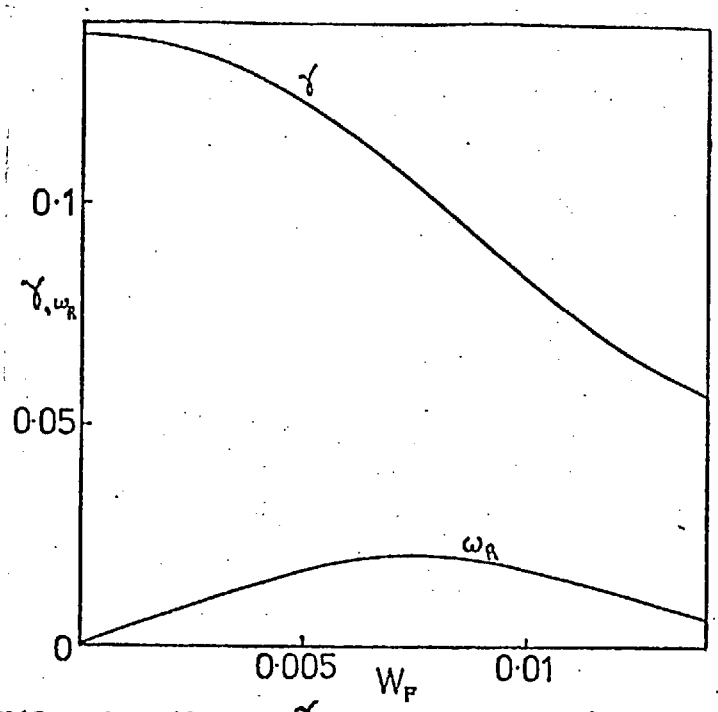

Figure IV12 - Growth rate, γ, and frequency, ω_R, versus the FLR effect. $W_A = 100$, $kr_x/m = -0.002$, $m = 2$ $\bar{n}=\exp(-0.5(a/0.3)^2)$, 'tanh' profile of $B_\theta/(aB_z)$.

figure IV12. Note that, in this case, the oscillatory frequency peaks at a considerably smaller value than in the previous, higher resistivity, case indicating that the behavior of the low resistivity limit investigated by Coppi(31) is being approached.

In order to investigate the reason for the failure of the computations at resistivities greater than in the $W_F=0$ situation consider the behavior of the eigenfunctions given in figure IV13 relevant to the computations of figure IV12. Whilst the effect on B_r' is slight, minor phase-shifted perturbations appearing in the region of the resonant surface, ξ has developed considerable modifications. Wave like features have appeared in both its real and imaginary parts on either side of the resonant surface indicating the formation of waves travelling away from the strongly perturbed resonant region. Since the amplitude of these waves increases as the ion diamagnetic drift frequency, W_F, rises we may infer

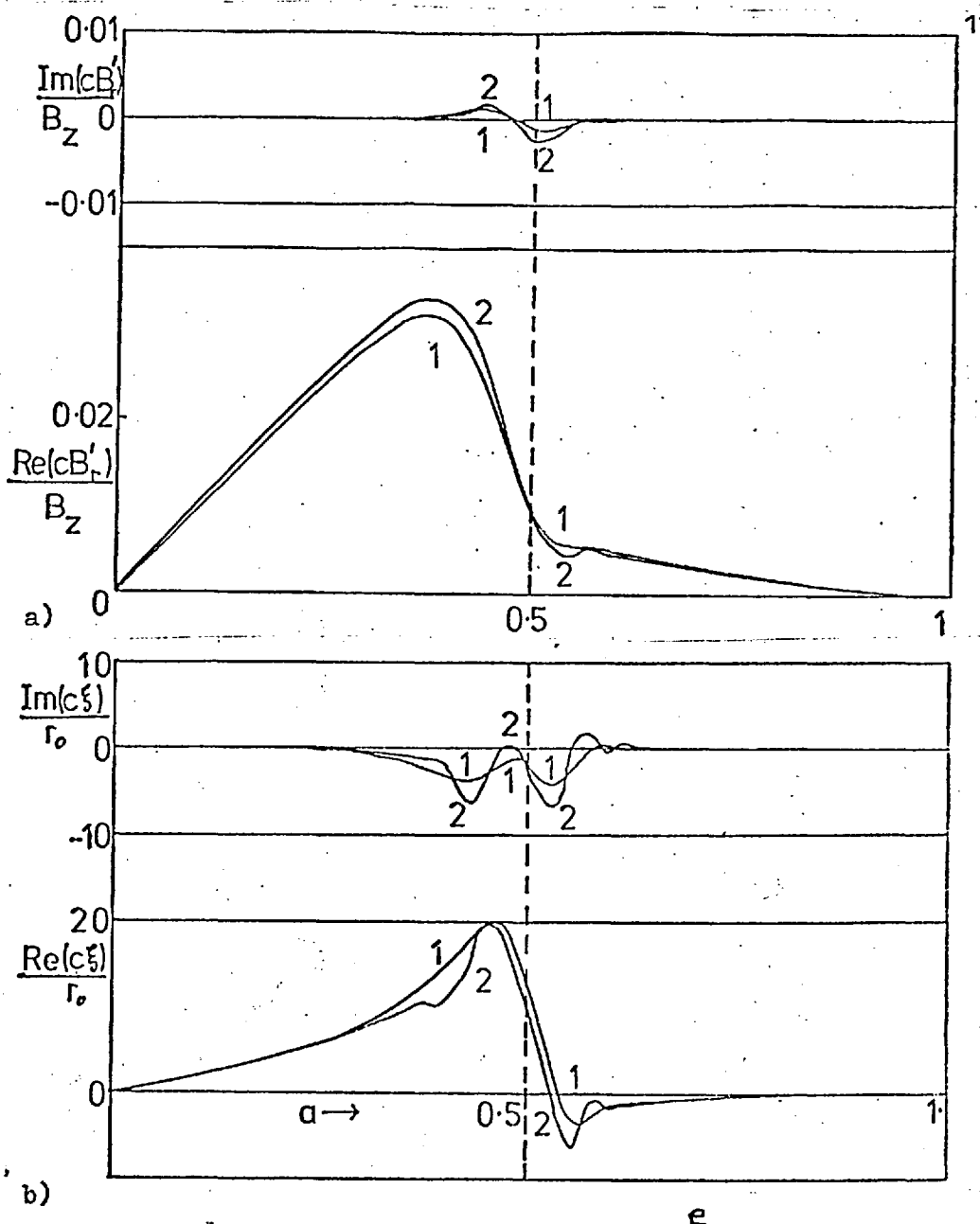

Figure IV13 - Perturbations a) B_r' and b) ξ as a function of normalised radius. 1) W_F =0.005, 2) W_F =0.012. Parameters and profiles of figure IV12.

that they arise from the ions being phase-delayed by finite Larmor radius phenomena with respect to electromagnetic effects portrayed by B_r'. An extreme example of this, even if in a less valid regime of the theory, is shown in figure IV14; this is the form of ξ at the termination of computation of curve 5 of figure IV11a.

The dependence of FLR stabilisation upon the position of the resonant surface is shown in figure IV15 which employs the flattened profile of Furth et al. (47) discussed in the

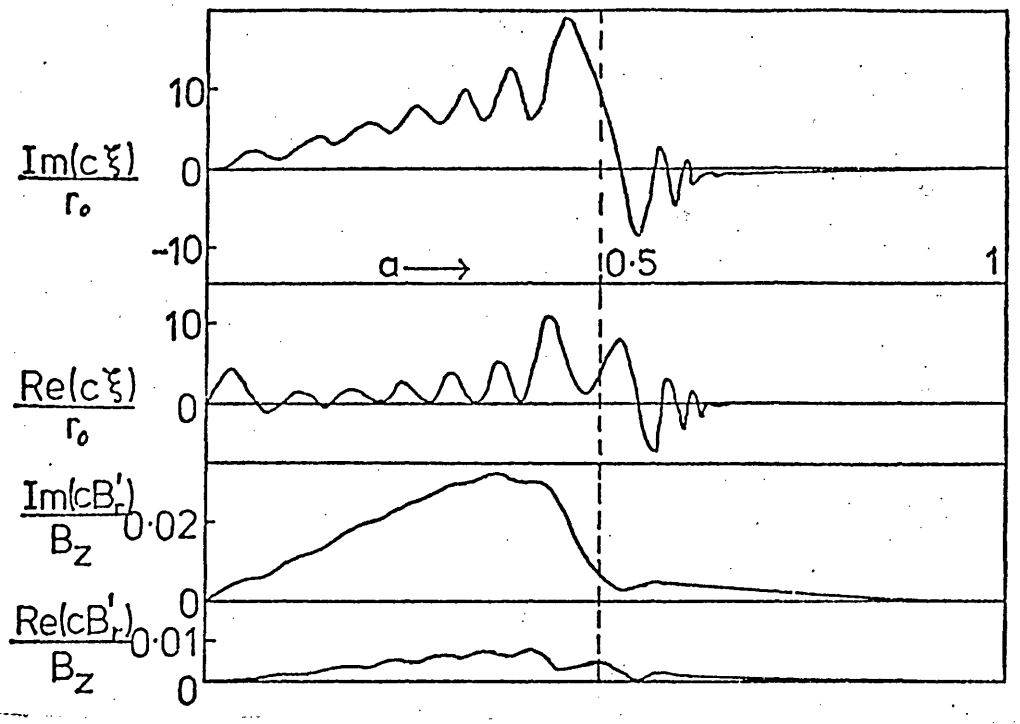

Figure IV14 - Eigenfunctions for the case: 'tanh' profile of $B_\theta/(aB_z)$, $\bar{n}=\exp(-0.5(a/0.3)^2)$, $kr_x/m = -0.002$, $m=2$, $W_F = 3\times10^{-2}$, $W_R = 9.4\times10^{-4}$.

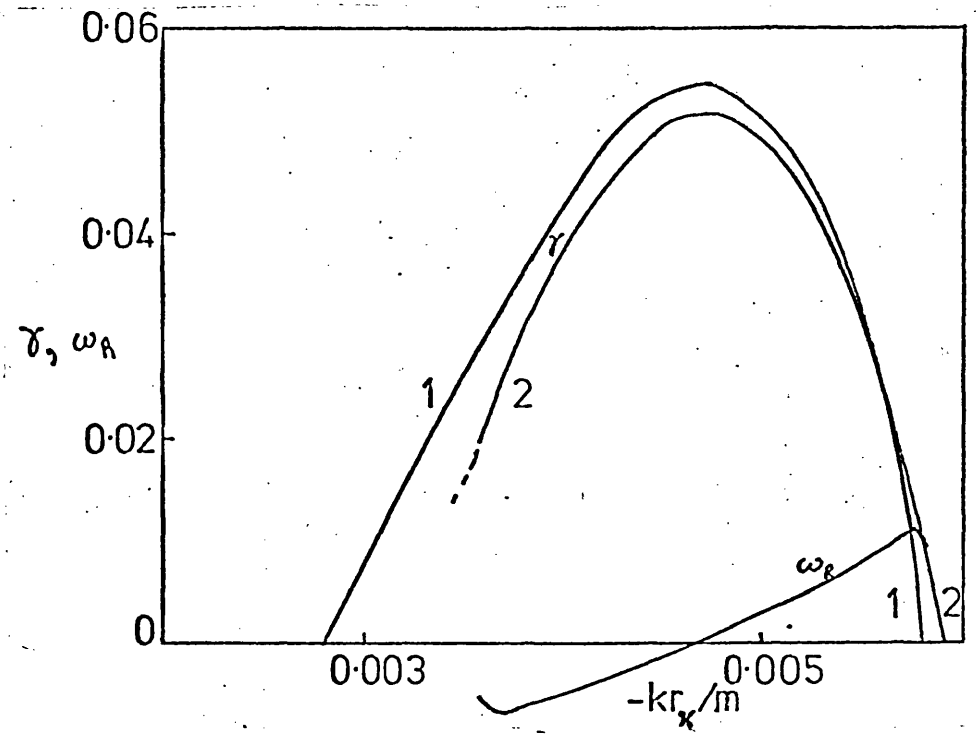

Figure IV15 - Growth rate, γ, and oscillation frequency, ω_R, versus axial wavenumber. $m=2$, $\bar{n}=\exp(-0.5(a/0.3)^2)$, $W_R=1.2\times10^{-4}$, flattened profile of $B_\theta/(aB_z)$.
1) $W_F = 0$, 2) $W_F = 1.2\times10^{-3}$.

previous section. Evidently, the stabilisation is greater with the resonant surface farther from the axis (small $\left|\frac{kr}{m}x\right|$) where the conventional driving force for the instability is weakest. Note that, in this region, where the analytical limit is most closely approached, the oscillation frequency is negative as predicted by Coppi(31).

A feature of FLR mentioned above and indicated by the broken line on figure IV11a is additional modes introduced. The curve on figure IV11a indicates that, under certain conditions of W_R, the extra mode indicated is more unstable than the more conventional tearing instability and has a growth rate strongly dependent upon resistivity. Numerical investigation has revealed that this mode depends for its existance on the electron pressure contribution to the radial induction equation (substituted from Ohm's law) IV13. Figure IV16 shows the FLR dependence of the growth rate of this mode. The initial rise might be explained by the effects

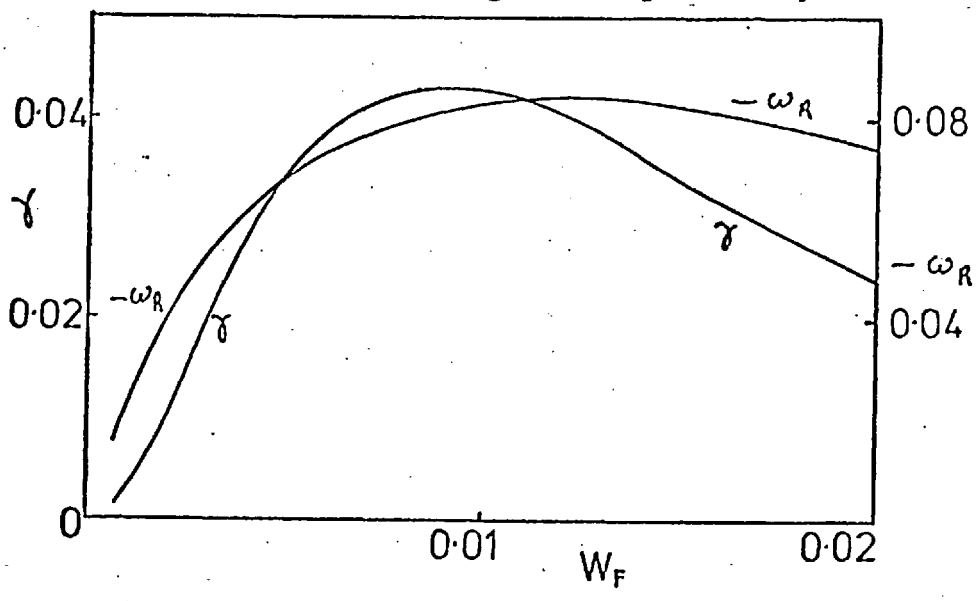

Figure IV16 - Growth rate and oscillation frequency of 'additional' modes found. 'Flattened' profile of $B_\theta/(aB_z)$, m=2, W_A=100, W_R=1.2x10^{-4}, kr_x/m=-0.005, $\bar{n}$=exp(-0.5(a/0.3)^2).

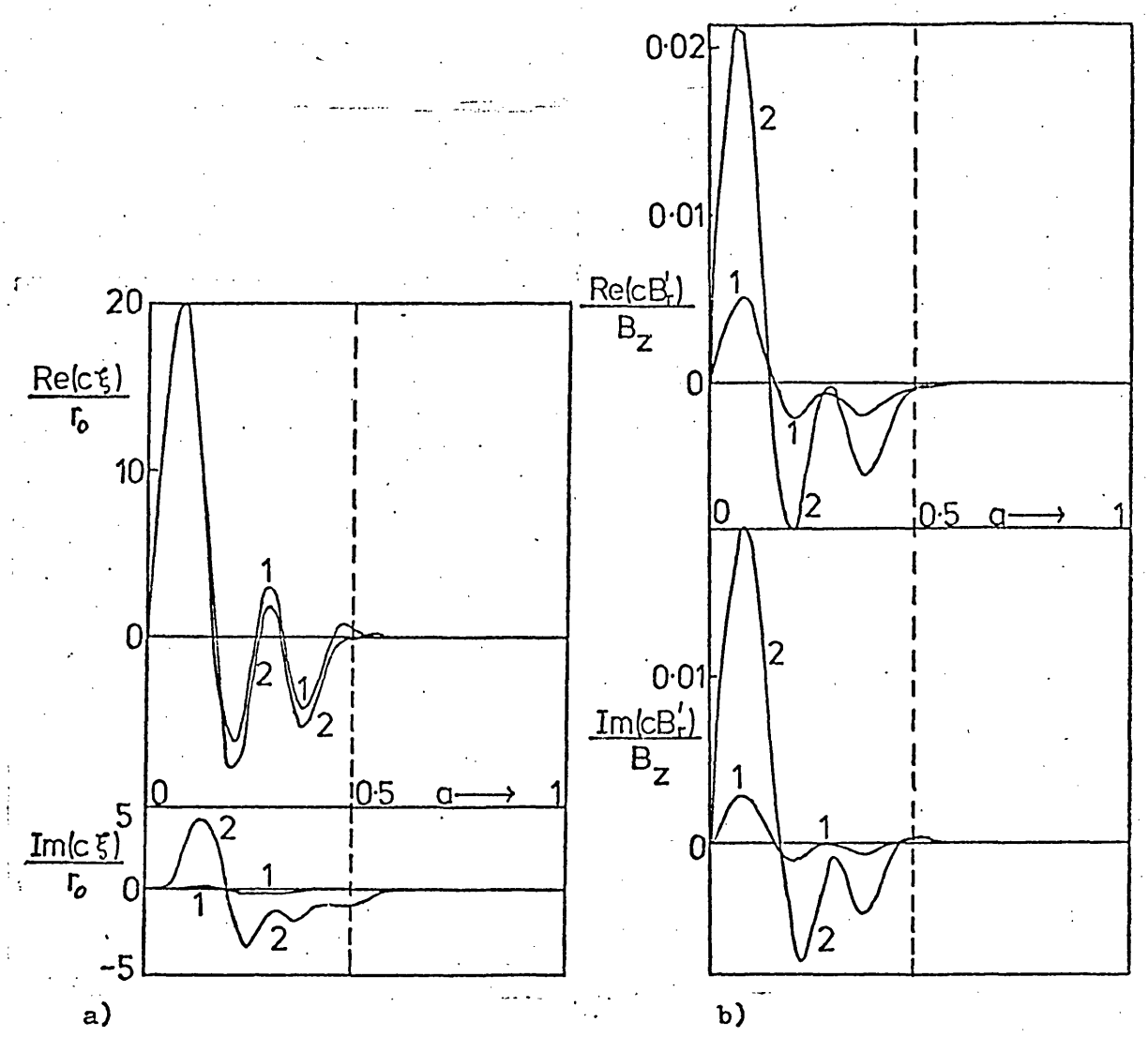

Figure IV17 - Eigenfunctions of the 'additional' mode from figure IV16. 1) $W_F = 2.8 \times 10^{-3}$, 2) $W_F = 10^{-2}$.

of the induction equation terms mentioned above, whilst the large W_F decay no doubt arises from the stabilising influence of the ion gyro-viscous stress tensor. The oscillation frequency takes the sign of the ion diamagnetic rotation but is several times larger in magnitude, being of the order of the growth rate; the mode is strongly overstable.

The eigenfunctions of these instabilities are characterised by short wavelength oscillations; these are, of course, many times longer than the mesh size and independent of doubling the number of mesh points used in the numerical scheme. Their dependence on FLR is shown in figure IV17. Note the

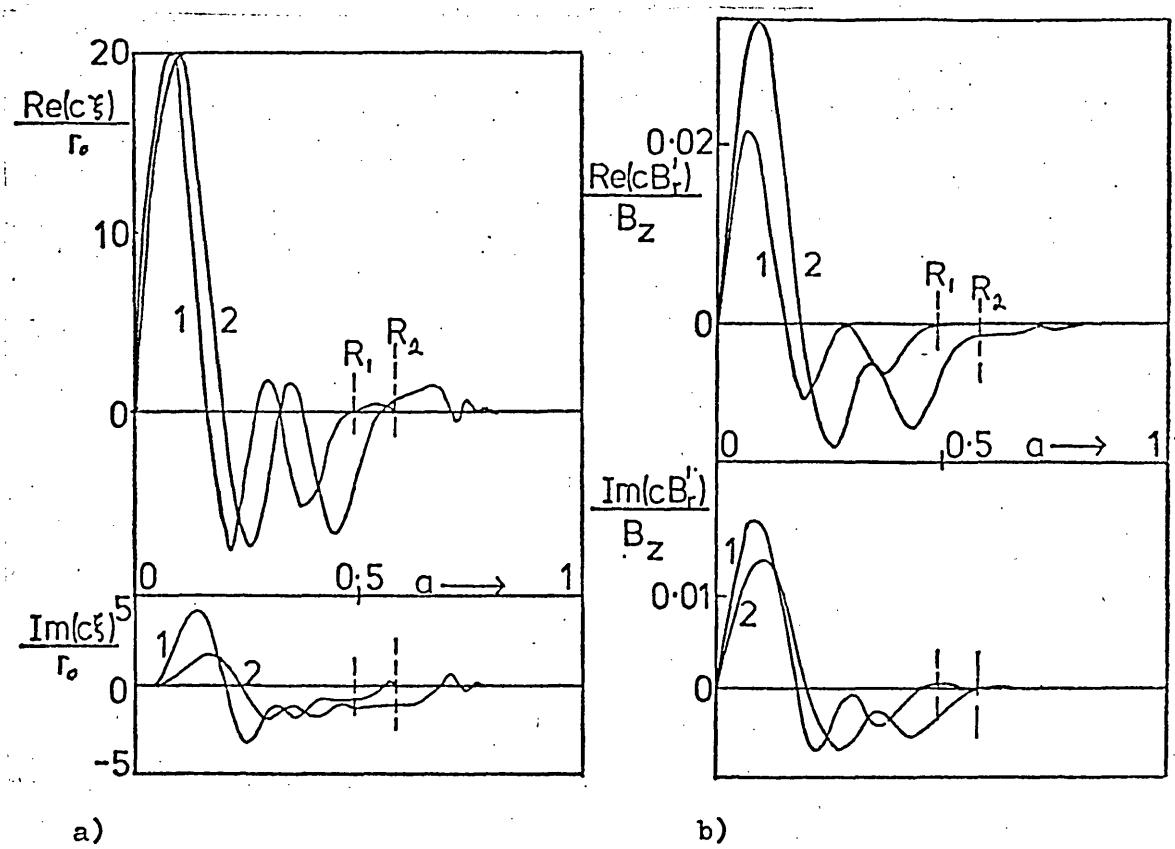

Figure IV18 - Eigenfunctions of the 'additional' mode using the flattened profile, m=2, W_{A_2}=100, $W_F=10^{-2}$, $W_R=1.2\times10^{-4}$, $\bar{n}=\exp(-0.5(a/0.3)^2)$.
1) $kr_x/m = -0.005$,
2) $kr_x/m = --0.0039$.

increase in B_r' as W_F rises and the phase difference between B_r' and ξ. The connection of the modes with the resonant surface is apparent in figure IV18 which shows their behavior as the axial wavenumber is varied. Closer investigation of the eigenfunctions reveals that, near the wall, the collisionless relationship, $B_r' = \bar{k}\xi B_z$, is satisfied. Within the radius of the resonant surface, however, B_r' and ξ are mutually phase shifted indicating that resistivity is active in this region. The effect of the small resistivity present is enhanced by the scale lengths of the perturbation being so short compared to those of equilibrium quantities.

Modes of this sort display the need for computations of

the type performed seeking solutions for the eigenfunctions across the entire plasma without confining the effects of resistivity and FLR to the narrow resonant region.

6) The Effect of Two Resonant Surfaces.

Two resonant surfaces may be present within a confined plasma when skin-current phenomena occur. This effect was modelled by selecting a Gaussian profile of $B_\theta/(aB_z)$, peaked off axis. At $W_F=0$ the instabilities encountered were, as expected, far more unstable than in any of the single surface calculations previously performed. Figure IV19 illustrates the resistivity dependence of the growth rates for different m numbers. Observe that, for this more unstable profile, the curves peak at considerably larger resistivity than

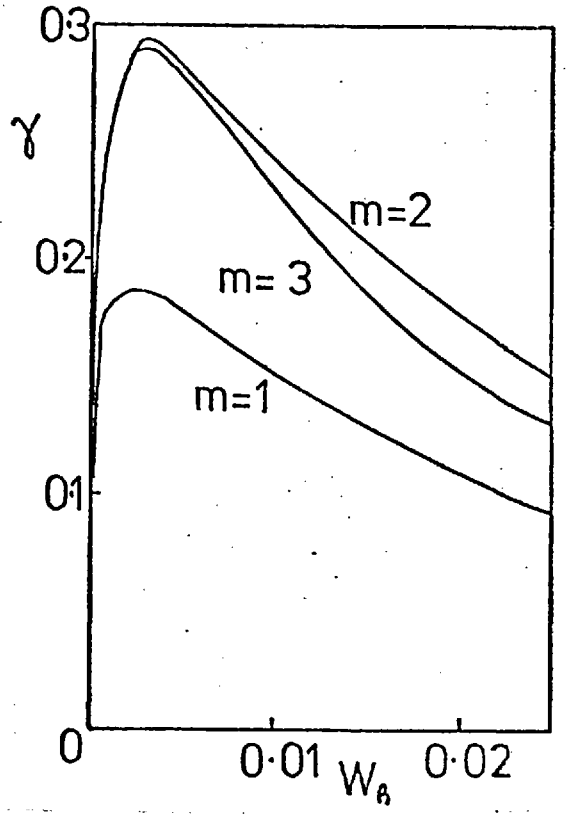

Figure IV19 - Growth rate versus resistivity with two resonant surfaces present.
$kr_x/m = -0.0025$, $W_A=100$, $\bar{n}=\exp(-0.5(a/0.3)^2)$,
$B_\theta/(aB_z)=0.004(\exp(-25(a+0.5)^2)+\exp(-25(a-0.5)^2))$.

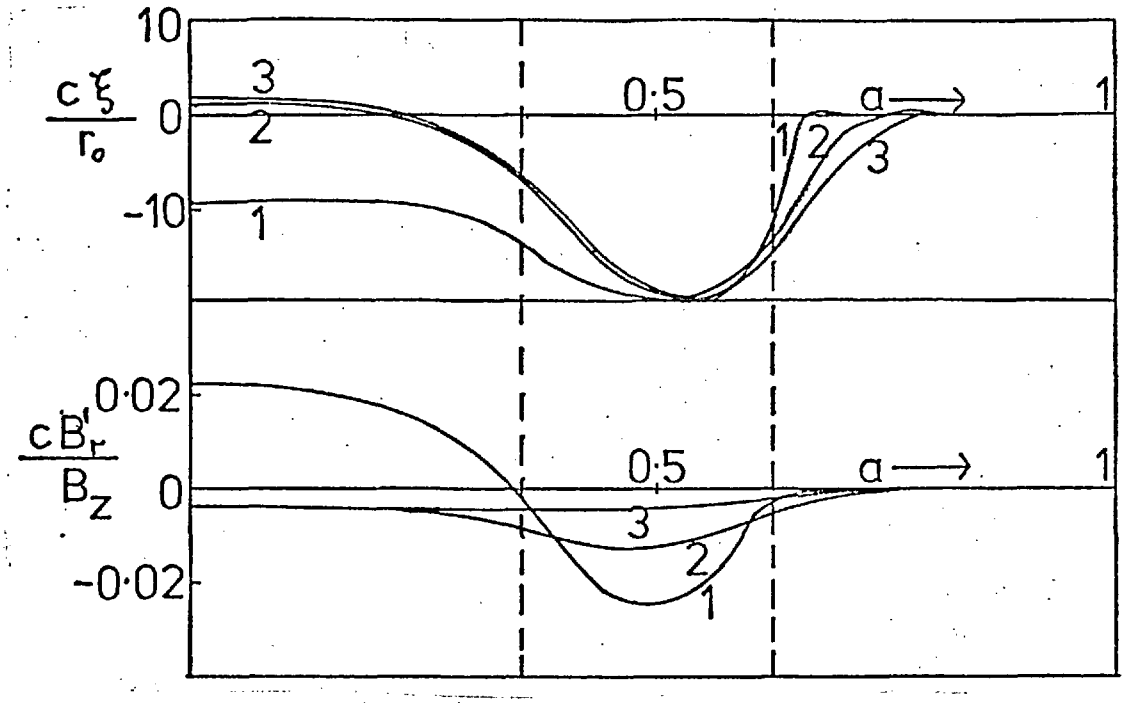

Figure IV20 - Eigenfunctions of the m=1 mode from figure IV19 1) $W_R = 7\times10^{-5}$, 2) $W_R = 2.5\times10^{-3}$, 3) $W_R = 1.25\times10^{-2}$.

previously found. The ratio of peak growth rate to W_R at the maximum remains approximately constant, however, taking a value of the order of 0.01 for all of the cases studied so far.

Figure IV20 shows the behavior of the m=1 eigenfunctions as resistivity is varied. Note the manner in which large perturbations arise between the two resonant surfaces and the way in which these penetrate into the outer regions as resistivity rises. In particular, observe that the instability loses a node as W_R passes through its most unstable value. Such behavior merely further illustrates the increasing inaccuracy of any localisation assumption as resistivity rises.

The axial wavelength dependence of the m=2 instabilities, shown in figure IV21 is explicable in terms of the pitch profile used. This has a maximum of 0.004 so that the curve of figure IV21 cuts off before this value. The peak of the diagram occurs with the resonant surfaces close to the radii

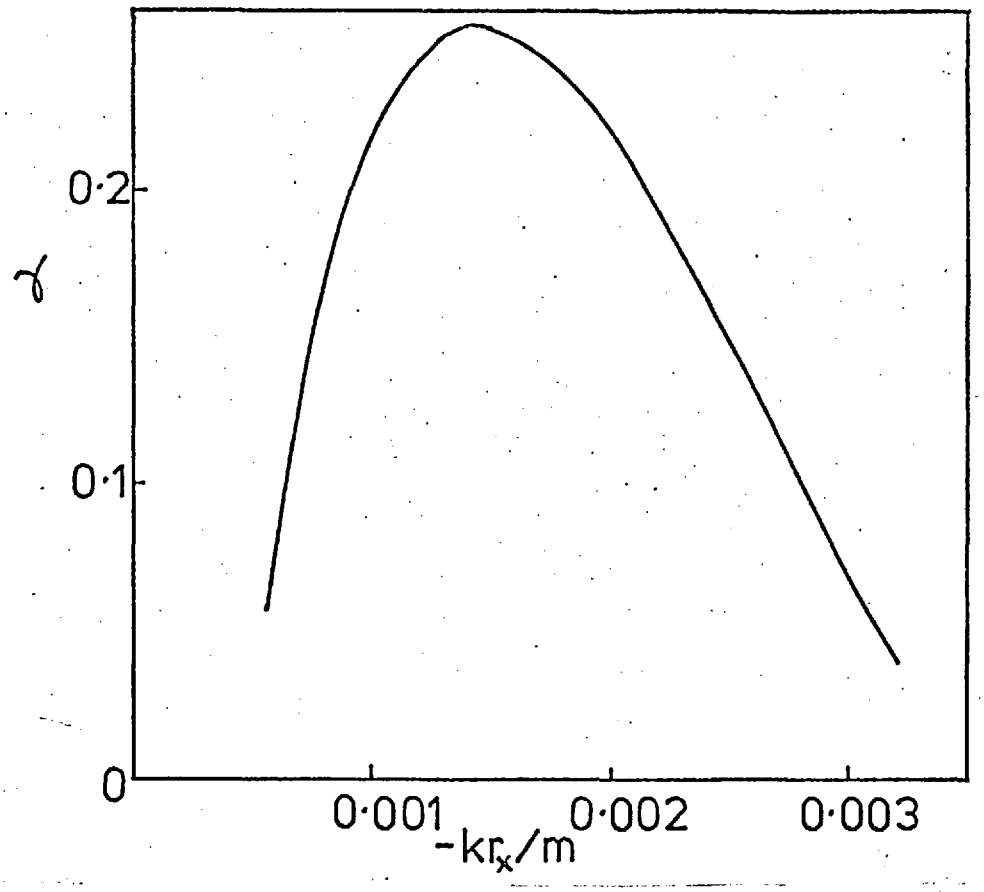

Figure IV21 - The dependence of growth rate upon axial wavenumber when two resonant surfaces are present. $m=2$, $W_A=100$, $W_R=0.025$, $\bar{n}=\exp(-0.5(a/0.3)^2)$, $B_\theta/(aB_z) = 0.004(\exp(-25(a+0.5)^2)+\exp(-25(a-0.5)^2))$. of maximum shear $\left(\frac{d}{da}\left(\frac{B_\theta}{aB_z}\right)\right)$.

FLR stabilisation of the two resonant surface case occurs in a manner exactly analogous to that discussed for the single surface situation.

7) Conclusion.

The numerical approach to the study of resistive instabilities in a low beta cylindrical plasma has revealed important results complementing and extending the published analytical approach. The effect of the breakdown of the localisation and 'constant ψ' approximations have been illustrated and additional instabilities, generated by FLR effects and not detectable by a localised approach have been discovered. In the low resistivity limit of this work, the localised analytic approach appears accurate to the degree

required of such a theory.

As a numerical technique, the iteration of the quin-diagonal determinant required an order of magnitude more computer time than the tri-diagonal one required for the computationally simpler collisionless case. This vast increase in effort may be ascribed to: 1) the excess diagonals in the determinant that required time-consuming elimination, 2) the larger dimensions of the determinant arising from the need to solve two equations simultaneously, 3) the larger number of roots present for a mesh of a given number of points. The last point has a two-fold effect. Firstly, more time is required as more roots must be found in the initial procedure and secondly, the function solved (effectively but not explicitly a polynomial) has a complexity in proportion to the number of its zeros; each root therefore requires more iterations in order for it to be determined to a given accuracy. In conclusion, therefore, the numerical method is not suitable for extension to higher order systems of equations associated with, for example, the inclusion of finite beta effects in the calculations.

Chapter V.

Finite Larmor Radius Effects and the Resistive Tearing Mode at Non-Zero Beta.

1) Resistivity and Plasma Instability.

For many years the model of a confined plasma as a column of infinitely conducting fluid surrounded by a (perfectly insulating) vacuum region has been known to provide inadequate stability criteria. The region between the hot plasma core and the cooler outer environment is better modelled using a profile of resistivity. Kink-like, non-localised, modes are then possible when the resonant surface lies within the plasma; the perturbation remains finite at the resonant surface owing to the enhanced perturbed resistive diffusion in this neighbourhood de-coupling plasma and magnetic field. Such instabilities have been called 'tearing modes' by Furth, Killeen and Rosenbluth (7).

Within the region of denser plasma, Furth et al. (7) showed that Suydam modes driven by adverse magnetic field curvature and localised about the resonant surface extended beyond MHD stability limits when finite resistivity effects were included. This is because enhanced field diffusion near the resonant surface reduces the stabilising influence of the magnetic shear. They modelled these instabilities at zero beta in rectangular geometry with incompressible plasma using a fictitious gravity to represent the destabilising influences of field curvature. This procedure has been shown to be valid only when the field curvature, and hence the driving force for instability, is extremely weak. (Hosking and Marinoff (55)). Both interchange and rippling modes, caused by convective resistivity perturbation, were shown to have faster growth

rates than tearing modes in the low resistivity limit. When modelling toroidal devices, however, the favourable curvature of the toroidal field towards the inside of the torus tends to create stability towards interchange effects. Thus, in these circumstances it is more relevant to consider the non-localised resistive-kink (or tearing) instabilities which are believed to be less affected by toroidal influences (See Shafranov (1), Glasser, Greene and Johnson (50)).

When finite beta effects are included in cylindrical geometry, thus superceeding the fictitious gravity as the interchange driving force, (Coppi, Greene and Johnson (6)) the manner in which the various modes merge into one another becomes clear. As a Suydam parameter, D, is increased towards its hydromagnetic marginal stability value, the growth rate of the resistive interchange mode becomes large thus demonstrating that it is a continuation of the infinite conductivity interchange. As the tearing mode driving force, Δ , is reduced, at small D, the growth rate of the instability no longer tends to zero with Δ , but becomes asymptotic to the Δ =0 axis. The growth rate changes from the $\eta^{3/5}$ behavior, characteristic of tearing modes to the $\eta^{\frac{1}{3}}$ behavior that characterises interchange modes. In this regime, the instability growth rate becomes dependent upon compressibility; this must be included in the calculation for consistency with the finite-beta, finite-resistivity combination. When $\Delta<0$, thus providing no tearing mode driving force, this finite-beta region occurs only when the equilibrium pressure gradient is directed into the plasma cylinder. Otherwise, branch-point behavior is exhibited, two unstable modes being present above a cut-off value of Δ. Between cut-off and branch-point,

these two modes are overstable, have equal growth rate, but oscillation frequencies opposite in sign. (Glasser et al.(50)). Thus, the tearing mode merges with the resistive interchange mode when the respective driving forces of each are sufficiently small.

Coppi (31) modified the cartesian, incompressible, low-beta, low-shear model of Furth et al. (7) to include the effects of finite ion Larmor radius (FLR) phenomena using equal electron and ion temperatures. He showed that the Hall term in Ohm's law and the gyro-viscous contribution to the stress tensor are of equal importance in his model. In the absence of finite-beta destabilising effects, Coppi found that the tearing mode is present for all Δ greater than zero just as in the absence of the FLR terms. However, at $\Delta > 0$, the growth rate of the modes is reduced by the FLR terms. At large Δ, FLR becomes insignificant. The mode is overstable for all Δ, with an oscillation frequency tending to twice the ion diamagnetic drift frequency as FLR becomes large.

The validity of Coppi's calculation depends upon the ion Larmor radius being small compared to the scale length of the perturbation in the region of the resonant surface. For the tearing mode, this is a valid approximation since Coppi showed that the width of this region becomes determined by FLR as its effect increases. When considering the resistive gravitational (modelled interchange) mode, however, Frieman et al. (52) showed that, unlike the tearing mode, this develops severe spatial oscillations near to the resonant surface, as collisional viscosity is reduced, so that the latter becomes important before the resistive layer is of the order of an ion Larmor radius wide. Thus, tearing modes may be

studied freely without the complications of collisional viscosity, whereas caution must be exercised when considering gravitational or interchange phenomena.

The form of the traceless stress tensor to be used in a fluid-like analysis of collisional plasma phenomena has been widely debated. Collisionless expansions of the Vlasov equation have shown (eg. Bowers and Haines (28)) that gyro-viscous representation of finite ion Larmor radius drift phenomena is only valid when the magnetic field curvature is small. Liley(9) has shown that an expansion of moment equations in 1/(Collision time x ion gyro frequency) = $1/(\tau\Omega)$ produces parallel viscosity, proportional to τ_{ii} in lowest order, with gyro-viscosity and collisional perpendicular viscosity arising in subsequent orders. This result is, of course, only valid so long as the collisional mean free path is considerably less than the scale lengths describing the plasma equilibrium. Parallel viscous effects, however, depend upon the square of the magnetic field curvature ($(B_\theta/B_z)^2$ in cylindrical geometry) and are thus considerably reduced in importance in situations where the gyro-viscous model of FLR effects may be used. The relevance of parallel viscosity to tearing modes has been discussed by Marinoff (52).

The influence of toroidal curvature upon tearing modes has been investigated by Glasser et al. (50) working in non-orthogonal Hamada coordinates and taking appropriate averages around flux surfaces. Such a model is far too complicated to envisage the incorporation of FLR phenomena.

2) Resistive Instability at Finite Beta Including FLR.

So far, all of the analysis of resistive instabilities involving FLR has been carried out at zero beta, using the

gravitational approximation for interchange modes. (Frieman et al. (52), Coppi(31)). A treatment of the problem in the manner of Coppi et al. (6), but now including FLR phenomena follows. These effects were omitted by reference (6) for convenience.

We shall consider instability of a cylindrical plasma, initially in a cylindrically symmetric state. The model under consideration is described by the following system of equations:

Momentum Equation

$$\rho \frac{\partial \underline{u}}{\partial t} + \rho (\underline{u}\cdot\nabla)\underline{u} = \underline{j} \wedge \underline{B} - \nabla p - \underline{\nabla}\cdot \underline{\underline{\pi}} \qquad V1$$

Ohm's Law

$$\underline{E} + \underline{u} \wedge \underline{B} = \eta \underline{j} + \frac{1}{ne}(\underline{j} \wedge \underline{B} - \nabla p_e) \qquad V2$$

Energy Equation

$$p^{\gamma}\left(\frac{\partial}{\partial t} + (\underline{u}\cdot\underline{\nabla})\right)(p\rho^{-\gamma}) = (\gamma-1)\eta |\underline{j}|^2 \qquad V3$$

Conservation of Mass

$$\frac{\partial \rho}{\partial t} + \nabla\cdot(\rho \underline{u}) = 0 \qquad V4$$

Electro-magnetic Equations

$$\underline{\nabla} \wedge \underline{E} = -\frac{\partial \underline{B}}{\partial t} \qquad V5$$

$$\underline{\nabla}\cdot\underline{B} = 0 \qquad V6$$

$$\underline{\nabla} \wedge \underline{B} = \mu_0 \underline{j} \qquad V7$$

where standard notation has been used, $\underline{\underline{\pi}}$ denoting the traceless part of the stress tensor (ref.(30) and eqns. A12 to A16). For simplicity, consider isotropic resistivity and equal electron and ion temperatures so that:

$$p_e = p_i = p/2 \qquad V8$$

The Ohmic heating term has been included in V3, but plays no

role in the final calculation owing to the ordering of plasma pressure that will be made later. In order that the stress tensor in V1 may be validly taken to be the collisionless FLR viscosity (see Bowers and Haines (28)), the appropriate ordering of the equilibrium quantities in the ion Larmor radius must be observed. (28) :

Define $\varepsilon = \frac{\text{Ion Larmor radius}}{\text{Scale length normal to } \underline{B}} = \frac{v_\chi^i}{\Omega L_\perp}$

where v_χ^i is the ion thermal velocity and Ω is the ion gyro frequency.

Then we require, as described in chapter I,

$$\frac{L_\perp}{\varepsilon\sqrt{\beta}L_{//}} \sim \frac{\beta\theta}{\varepsilon\sqrt{\beta}B_z} \sim \frac{E_{//}}{\varepsilon\sqrt{\beta}E_\perp} \sim \frac{u_\perp}{\varepsilon v_t^i} \sim \frac{E_\perp}{\varepsilon B_z v_t^i} \sim \frac{\omega}{\varepsilon^2\Omega} \sim 1 \qquad \text{V9}$$

Ordering in ε, we take $\beta \sim \varepsilon^0$ so that we retain the maximum number of physical phenomena in the equations.

This ordering of equilibrium quantities is primarily to ensure that the gyro-viscous stress tensor is an adequate representation of the ion drift phenomena that are to be considered. In addition, it produces considerable simplification in the subsequent calculation.

The displacement current is omitted from equation V7 since the instabilities to be studied occur on very slow time scales. Ohm's law, equation V2, contains the Hall terms which are of the same order as gyro-viscous effects.

Terms in the heat flux, $\underline{q}$, and its divergence are omitted throughout, in both the energy equation, V3, and in the stress tensor, $\underline{\underline{\Pi}}$. Thermal conductivity will not be considered in this work. Such effects transport energy from compressed regions and might thus be modelled by reducing the effective specific heat ratio, γ.

Heat fluxes in the stress tensor are, in the collisionless

case, (see reference (30)) finite beta effects and thus will be small for tearing modes; such collisionless heat fluxes were shown to have only a very small effect on instabilities.

It will be noted that the incompressible approximation has not been made. Incompressibility is only consistent at zero beta (Coppi (31)) when resistivity is included and its inclusion is a further consequence of considering finite plasma pressure effects. Recall, however that in the collisionless case (30), perturbations were found to be incompressible at high-beta due to the rigid coupling of plasma and magnetic field.

3) The Unperturbed State.

We consider the problem of a diffuse plasma cylinder subjected to a magnetic field $(0,B_\theta,B_z)$. All quantities depend only on radius,r. In order to demonstrate the reduction to the collisionless case (30), equilibrium velocities $(0,u_\theta,u_z)$ will be included in the first part of the calculation and subsequently dropped when specialisation to the tearing mode is made.

When considering resistive instabilities, the unperturbed state is not strictly an equilibrium. This may be seen as follows:

The θ component of V2 yields: $E_\theta - u_r B_z = \eta j_\theta$ in the unperturbed state. Thus, initially, E_θ or u_r must strictly be non-zero since j_θ is finite in order to provide the pressure balance: $j_\theta B_z = dp/dr$ from equation V1. Also, V5 and V2 (omitting Hall terms) give: $\underset{\sim}{\nabla} \times (\eta \underline{j} - \underline{u} \times \underline{B}) = - \frac{\partial \underline{B}}{\partial t}$.

Hence (without equilibrium velocity) :

$$\frac{\partial \underline{B}}{\partial t} = \frac{\eta}{\mu_0} \nabla^2 \underline{B} \qquad \text{(neglecting resistivity gradients)}$$

This describes diffusion on a time scale given by $\frac{L_1^2 \mu_0}{\eta}$. For any perturbation analysis based on this initial state to be valid, therefore, much faster timescales must be involved. Since the growth rates of resistive instabilities depend upon fractional powers of η, this condition is satisfied for sufficiently small resistivity and the motion of the initial state may be safely neglected. The physical reason for this is that the scale lengths of the perturbation, short compared to those of equilibrium quantities in the region of the resonant surface, cause the perturbed diffusion driving the modes to dominate.

4) Perturbation Analysis I - FLR Expansion.

Following Coppi (31) and Frieman et al. (52), the perturbation expansion proceeds in two stages. The first, Larmor radius, expansion occurs as a consequence of the ordering necessary for the use of the gyro-viscous stress tensor (see section 2). Secondly, the resistive expansion arises when specialising to the particular instability under study. This procedure is strictly valid so long as the first expansion parameter is very much smaller than the second as has been discussed in section 1.

Since the initial state chosen depends on radius only and it changes neglegibly on the timescale of the instabilities involved, perturbations proportional to $\exp(i(\omega t+m\theta+kz))$ are sought. Perturbed quantities are denoted by primes.

The Induction Equation.

Substituting V2 into V5 and using V7 yields:

$$\frac{\partial \underline{B}}{\partial t} = \nabla \wedge \left[\underline{u} \wedge \underline{B} - \frac{\eta}{\mu_0} \nabla \wedge \underline{B} - \frac{1}{ne} \left(\frac{(\underline{B}\cdot\nabla)\underline{B}}{\mu_0} - \nabla \left(\frac{B^2}{2\mu_0} + \frac{p}{2} \right) \right) \right]$$

To second order in ε, the z component yields:

$$i\omega_1 B_z' + \omega_1 \xi \frac{dB_z}{dr} = \Big\{ i\bar{k} B_z u_z' + B_r' \frac{du_z}{dr} - B_z (\nabla\cdot u)' \Big(1 - \frac{m}{2\pi\rho r\omega_1}\frac{d\rho}{dr}\Big) + \frac{imB_z^2}{2\pi r\rho\mu_0}\Big(\frac{1}{\rho}\frac{d\rho}{dr}\Big)\Big(i\xi\frac{dB_z}{dr} - B_z'\Big) - \frac{1}{r}\frac{d}{dr}\Big[r\eta' j_\theta - \frac{r\eta}{\mu_0}\frac{dB_z'}{dr}\Big] - \frac{m^2\eta}{r^2\mu_0} B_z' \Big\} \qquad \text{V10}$$

(Ignore at present the numbers above each term).

where:

$$\omega_1 = \omega + \frac{mu_\theta}{r} + ku_z \; ; \; \bar{k} = k + \frac{mB_\theta}{rB_z} \; ; \; \xi = \frac{u_r'}{\omega_1} \qquad \text{V11}$$

To third order in ϵ, the radial component yields:

$$i\omega_1\Big(B_r' - \bar{k}\xi B_z\Big) = \Big\{ -\frac{im}{2\pi r}\frac{B_z^2}{\rho\mu_0}\Big(i\bar{k}B_z' + \frac{B_r'}{B_z}\frac{dB_z}{dr}\Big) - i\Big(\frac{mj_z}{r} - kj_\theta\Big)\eta' + 2ik\eta B_z'/(\pi\mu_0) + \frac{\eta}{\mu_0}\Big[\frac{1}{r^3}\frac{d}{dr}\Big(r^3\frac{dB_r'}{dr}\Big) - \frac{(m^2-1)}{r^2}B_r'\Big]\Big\} \qquad \text{V12}$$

The Continuity Equation.

Equation V4 yields:

$$\rho' = i\xi\frac{d\rho}{dr} + \frac{i\rho}{\omega_1}(\nabla\cdot u)' \qquad \text{V13}$$

The Energy Equation.

Using V13, equation V3 yields:

$$\gamma p(\nabla\cdot u)' = -\omega_1\Big(-\frac{iB_z}{\mu_0}B_z' + \xi\frac{dp}{dr}\Big) + (\gamma-1)\Big(\eta'|j|^2 - 2\eta j_\theta\frac{dB_z'}{dr}\Big) \qquad \text{V14}$$

Taking $\eta \propto T^{-3/2}$, we can write the resistivity perturbation:

$$\eta' = \eta\Big(\frac{3}{2}\frac{B_z B_z'}{\mu_0 p} + \frac{3}{2}\frac{i\xi}{\rho}\frac{d\rho}{dr} + \frac{i}{\omega_1}(\nabla\cdot u)'\Big) \qquad \text{V15}$$

The Momentum Equation.

i) First Order in ϵ

To this order, V1 shows that the r and θ components of the momentum equation yield:

$$\frac{\partial}{\partial r}\Big(\frac{B_z^2}{2\mu_0} + p\Big) = 0 \quad \text{and} \quad \frac{\partial}{\partial\theta}\Big(\frac{B_z^2}{\mu_0} + p\Big) = 0 \quad \text{respectively}$$

The first of these expresses the equilibrium pressure balance of the plasma. In perturbation, the maintenance of this condition eliminates the rapid magnetosonic waves from the calculation.

Thus, for the perturbation:

$$p' = -\frac{B_z}{\mu_0} B_z' \qquad \text{V16}$$

ii) Second Order in ε.

To second order, the first order condition is duplicated since FLR expansions are essentially in ε^2. However, to second order, the FLR stress tensor enters the z component of V1. This may be written:

$$\rho i\omega_1 u_z' + \rho\omega_1 \xi \frac{du_z}{dr} = j_r' B_\theta - j_\theta B_r' - ikp' - (\nabla\cdot\bar{\bar{\pi}})_z'$$

now $$(\nabla\cdot\bar{\pi})_z' = \frac{1}{r}\frac{d}{dr}(r\pi_{rz}') + \frac{im}{r}\pi_{\theta z}'$$

which, upon substituting for π_{rz}' and $\pi_{\theta z}'$ yields:

$$(\nabla\cdot\pi')_z = \frac{im}{2r}\left[-u_z'\frac{d}{dr}\left(\frac{p}{\Omega}\right) + \left(\frac{p}{\Omega}\right)'\frac{du_z}{dr}\right]$$

where $p_i = p/2$ has been used and Ω is the ion gyro frequency.

From V7 $\quad \mu_0 j_r' = im B_z'/r$

therefore: $$\rho i\omega_1 u_z' + \rho\omega_1\xi\frac{du_z}{dr} = i\bar{k}\frac{B_z}{\mu_0}B_z' + \frac{B_r'}{\mu_0}\frac{dB_z}{dr} - \frac{im}{2r}\left[-u_z'\frac{d}{dr}\left(\frac{p}{\Omega}\right) + \left(\frac{p}{\Omega}\right)'\frac{du_z}{dr}\right]$$

Hence:

$$u_z' = \frac{\left(i\rho\omega_1\xi - \frac{m}{r}\left(\frac{p}{2\Omega}\right)'\right)\frac{du_z}{dr} + \frac{1}{\mu_0}\left(\bar{k}BB_z' - iB_r'\frac{dB_z}{dr}\right)}{\rho\omega_1 - \frac{m}{r}\frac{d}{dr}\left(\frac{p}{2\Omega}\right)} \qquad \text{V17}$$

Note that in the collisionless limit (30), when the pressure perturbation is purely convective, this reduces to $u_z' = i\xi\frac{du_z}{dr}$ as required. The denominator in V17 is a marked feature of this analysis and plays an important role in many of the results obtained. Note that the last pair of terms in the numerator arise purely as a finite beta effect. Only these remain when equilibrium velocities are neglected later in the analysis.

iii) Third Order in ε.

To this order, the off-diagonal components of the stress

tensor contribute to the r and θ components of V1. The higher order scalar pressure terms in these components may be eliminated between the two equations by taking the z component of the curl of equation V1 expressed to third order in $\mathcal{E}$. This procedure is lengthy and will be carried out separately for the distinct sets of terms involved.

a) Gyro-Viscous Terms.

We need to calculate the quantity $\left[\underline{\nabla}\wedge(\underline{\nabla}\cdot\underline{\underline{\pi}})\right]_z$.

$$\left[\underline{\nabla}\wedge(\underline{\nabla}\cdot\underline{\underline{\pi}})\right]_z = \frac{1}{r}\frac{d}{dr}\left(r(\underline{\nabla}\cdot\underline{\underline{\pi}})'_\theta\right) - \frac{im}{r}(\underline{\nabla}\cdot\underline{\underline{\pi}})'_r$$

where

$$(\underline{\nabla}\cdot\underline{\underline{\pi}})'_r = \frac{1}{r^2}\frac{d}{dr}(r^2\pi'_{rr}) + \frac{im}{r}\pi'_{r\theta} + ik\pi'_{rz}$$

$$(\underline{\nabla}\cdot\underline{\underline{\pi}})'_\theta = \frac{1}{r^2}\frac{d}{dr}(r^2\pi'_{r\theta}) - \frac{im}{r}\pi'_{rr} + ik\pi'_{z\theta}$$

where the result $\pi_{rr} = -\pi_{\theta\theta}$ has been used.

Thus:

$$\left[\underline{\nabla}\wedge(\underline{\nabla}\cdot\underline{\underline{\pi}})\right]_z = \left[\frac{3}{r}\frac{d}{dr} + \frac{d^2}{dr^2} + \frac{m^2}{r^2}\right]\pi'_{r\theta} - \frac{2im}{r^2}\frac{d}{dr}(r\pi'_{rr}) + \frac{ik}{r}\frac{d}{dr}(r\pi'_{z\theta}) + \frac{km}{r}\pi'_{rz}$$

Substitution of the expressions for the components of $\underline{\underline{\pi}}$ from equations A12 to A16, eliminating u'_θ using the relation:

$$u'_\theta = \frac{i}{m}\frac{d}{dr}(ru'_r) - \frac{kr}{m}u'_z - \frac{ir}{m}(\nabla\cdot u)' \qquad \text{V18}$$

eventually yields:

$$\left[\underline{\nabla}\wedge(\underline{\nabla}\cdot\underline{\underline{\pi}})\right]_z =$$

$$\frac{1}{r^2}\frac{d}{dr}\left\{\frac{\rho r}{4\Omega}\frac{d}{dr}\left(r(\underline{\nabla}\cdot\underline{\psi})\right) - (\nabla\cdot u)'\frac{d}{dr}\left(\frac{r^2\rho}{4\Omega}\right)\right\} - \frac{(m^2-1)}{r^2}\frac{\rho}{4\Omega}(\nabla\cdot\psi)'$$

$$+\frac{1}{r^2}\frac{d}{dr}\left\{r^2\omega_1\frac{d}{dr}\left(\frac{\rho}{2\Omega}\right)\frac{d\xi}{dr}\right\} - \frac{(m^2-1)}{r^2}\omega_1\xi\frac{d}{dr}\left(\frac{\rho}{2\Omega}\right)$$

$$+\frac{1}{r^2}\frac{d}{dr}\left\{r^2\frac{d\omega_1}{dr}\left[\xi\frac{d}{dr}\left(\frac{\rho}{2\Omega}\right) + i\left(\frac{\rho}{2\Omega}\right)'\right]\right\}$$

$$+\frac{ik}{r^3}\frac{d}{dr}\left\{r^3\left[u'_z\frac{d}{dr}\left(\frac{\rho}{2\Omega}\right) - \left(\frac{\rho}{2\Omega}\right)'\frac{du_z}{dr}\right]\right\} \qquad \text{(continued)}$$

$$+\frac{1}{r^2}\frac{d}{dr}\left\{\frac{i\bar{k}rP}{4\Omega}\frac{d}{dr}(ru_z')-iu_z'\frac{d}{dr}\left(\frac{\bar{k}Pr^2}{4\Omega}\right)\right\}-\frac{(m^2-1)}{r^2}\frac{i\bar{k}u_z'P}{4\Omega}$$

$$-\frac{P}{4\Omega B_z}\frac{du_z}{dr}\left(\frac{1}{r^3}\frac{d}{dr}\left(r^3\frac{dB_r'}{dr}-\frac{(m^2-1)}{r^2}B_r'\right)\right.$$

$$+B_r'\frac{d}{dr}\left(\frac{1}{r}\frac{d}{dr}\left(r\frac{du_z}{dr}\frac{P}{4\Omega B_z}\right)\right)$$

$$+\frac{1}{r^2}\frac{d}{dr}\left\{i\bar{k}r^2\frac{du_z}{dr}\left(\left(\frac{P}{2\Omega}\right)'-\frac{B_z'}{B_z}\frac{P}{2\Omega}\right)\right\}$$

b) Magnetic Terms.

We need to evaluate $\left[\underline{\nabla}\wedge(\underline{j}\wedge\underline{B})\right]_z$

V7 gives:

$$\left[\underline{\nabla}\wedge(\underline{j}\wedge\underline{B})\right]_z=\left[-\frac{1}{\mu_0}\underline{\nabla}\wedge(\underline{B}\wedge(\underline{\nabla}\wedge\underline{B})\right]_z$$

$$=\frac{1}{\mu_0}\left[\underline{\nabla}\wedge(\underline{B}\cdot\underline{\nabla})\underline{B}\right]_z$$

$$=\frac{1}{\mu_0}\left[\frac{1}{r}\frac{d}{dr}\left\{B_r'\frac{d}{dr}(rB_\theta)+i\bar{k}rB_zB_\theta'\right\}\right.$$

$$\left.+\frac{m}{r}\left\{\bar{k}B_zB_r'+2i\frac{B_\theta}{r}B_\theta'\right\}\right]$$

V6 gives:

$$B_\theta'=\frac{i}{m}\frac{d}{dr}(rB_r')-i\frac{\bar{k}r}{m}B_z' \qquad \text{V19}$$

Hence, upon substitution and re-arrangement,

$$\left[\nabla\wedge(\underline{j}\wedge\underline{B})\right]_z=\frac{1}{\mu_0}\left[-\frac{\bar{k}rB_z}{m}\left(\frac{1}{r^3}\frac{d}{dr}\left(r^3\frac{dB_r'}{dr}\right)-\frac{(m^2-1)}{r^2}B_r'\right)\right.$$

$$+\frac{B_r'}{mr^2}\frac{d}{dr}\left(r^3\frac{d}{dr}(\bar{k}B_z)\right)$$

$$\left.-\frac{k}{m}(4+r\frac{d}{dr})\left(B_r'\frac{dB_z}{dr}+i\bar{k}B_zB_z'\right)+\frac{2ik^2}{m}B_zB_z'\right]$$

c) Inertial Terms.

The remaining terms are:

$$\left[\underline{\nabla}\wedge\left(\rho\left\{\frac{\partial}{\partial t}+\underline{u}\cdot\underline{\nabla}\right\}\underline{u}\right)'\right]_z$$

A little manupulation involving substituting for u_θ' from V18 yields:

$$\left[\nabla\wedge\left(\rho\left\{\frac{\partial}{\partial t}+\underline{u}\cdot\underline{\nabla}\right\}\underline{u}\right)\right]_z=$$

$$-\rho r\frac{\omega_1^2}{m}\frac{d^2\xi}{dr^2}+\frac{d\xi}{dr}\left\{-\frac{\omega_1}{m}\left[\frac{d}{dr}(\rho r\omega_1)+2\rho\frac{d}{dr}(r\omega_1)\right]+\rho r\omega_1\frac{d}{dr}\left(\frac{u_\theta}{r}\right)\right\}$$

(continued)

$$+\xi\left(-\frac{1}{mr}\frac{d}{dr}\left[\rho r\omega_1\frac{d}{dr}(r\omega_1)\right]-2\frac{\rho u_\theta}{r^2}\frac{d}{dr}(r\omega_1)+\frac{1}{r}\frac{d}{dr}\left[\rho\omega_1\frac{d}{dr}(ru_\theta)\right]\right.$$
$$\left.+\frac{\rho m\omega_1^2}{r}-\frac{mu_\theta^2}{r^2}\frac{d\rho}{dr}\right)$$
$$-\frac{k}{m}\left[\frac{1}{r}\frac{d}{dr}(\rho ri\omega_1)+\rho i\omega_1\frac{d}{dr}+\frac{2im\rho u_\theta}{r^2}\right](ru_z')$$
$$+\left[\frac{1}{m}\frac{d}{dr}(\rho r\omega_1)+\frac{\rho\omega_1}{m}+\frac{\rho r\omega_1}{m}\frac{d}{dr}+2\frac{\rho u_\theta}{r}-\frac{\rho m u_\theta^2}{r^2\omega_1}\right](\nabla\cdot\underline{u})'$$

Collecting terms and using V17 to substitute selectively for u_z' yields the reduced momentum equation:

$$\frac{d}{dr}\left[\left(\rho r^3\omega_1^2-mr^2\overset{②}{\omega_1}\frac{d}{dr}\left(\frac{P}{2\Omega}\right)\right)\frac{d\xi}{dr}\right]-(m^2-1)\xi\left(\overset{⑥}{\rho r\omega_1^2}-m\omega_1\frac{d}{dr}\left(\frac{P}{2\Omega}\right)\right)$$
$$-2ik\rho r^2u_z'\overset{④}{\left(\omega_1-\frac{mu_\theta}{r}\right)}+\xi r^2\frac{d\rho}{dr}\overset{⑥}{\left(\omega_1-\frac{mu_\theta}{r}\right)^2} \qquad \text{V20}$$
$$-\frac{d}{dr}\left\{\frac{mr^2P}{4\Omega}\frac{d}{dr}\overset{②}{(\nabla\cdot\underline{u})'}+(\nabla\cdot u)'\left(\rho r^3\overset{⑥}{\omega_1}-\frac{mPr}{4\Omega}-mr^2\frac{d}{dr}\left(\frac{P}{4\Omega}\right)\right)\right\}$$
$$+(m^2-1)\frac{mP}{4\Omega}\overset{⑥}{(\nabla\cdot u)'}+\frac{\rho r^2}{\omega_1}\overset{⑥}{\left(\omega_1-\frac{mu_\theta}{r}\right)^2}(\nabla\cdot u)'$$
$$-m\frac{d}{dr}\left\{r^2\frac{d\omega_1}{dr}\left[\xi\frac{d}{dr}\left(\frac{P}{2\Omega}\right)+i\left(\frac{P}{2\Omega}\right)'\right]+\frac{i\bar{k}r^2\overset{②}{P}}{4\Omega}\frac{du_z'}{dr}-\frac{i\bar{k}rPu_z'}{4\Omega}\right.$$
$$\left.-ir^2u_z'\frac{d}{dr}\left(\frac{\bar{k}P}{4\Omega}\right)+i\bar{k}r^2\frac{du_z}{dr}\left[\left(\frac{P}{2\Omega}\right)'-\frac{B_z'}{B_z}\frac{P}{2\Omega}\right]\right\}$$
$$+(m^2-1)i\bar{k}\overset{⑥}{m}u_z'\frac{P}{4\Omega}+\frac{2ik^2\overset{②}{r^2}B_zB_z'}{\mu_0}$$
$$+\left(\frac{mPr^2}{4\Omega B_z}\frac{du_z}{dr}-\frac{\bar{k}r^3B_z}{\mu_0}\right)\left(\frac{1}{r^3}\frac{d}{dr}\left(r^3\frac{dB_r'}{dr}\right)-\overset{④}{\frac{(m^2-1)}{r^2}}B_r'\right)$$
$$+B_r'\left(\frac{1}{\mu_0}\frac{d}{dr}\left(\overset{②}{r^3}\frac{d}{dr}(\bar{k}B_z)\right)-mr^2\frac{d}{dr}\left(\frac{1}{r}\frac{d}{dr}\left[r\frac{du_z}{dr}\frac{P}{4\Omega B_z}\right]\right)\right)$$

$$=0$$

In order to verify V20, we may check the collisionless limit in which perturbations are purely convective (28) and incompressible.

ie. $u_z^1 = i\xi \frac{du_z}{dr}$; $B_r^1 = \bar{k}\xi B_z$; $B_z^1 = i\xi \frac{dB_z}{dr}$, $\left(\frac{P}{\Omega}\right)^1 = i\xi \frac{d}{dr}\left(\frac{P}{\Omega}\right)$

Substitution of these into V20 followed by considerable algebraic manipulation yields the result:

$$\frac{d}{dr}\left[F \frac{d\xi}{dr}\right] + G\xi = 0 \qquad \text{V21}$$

with:

$$F = \rho r^3 \omega_1^2 - r^3 \frac{\bar{k}^2 B_z^2}{\mu_0} - m\omega_1 r^2 \frac{d}{dr}\left(\frac{P}{2\Omega}\right) + \bar{k} \frac{mr^2 P}{2\Omega} \frac{du_z}{dr}$$

$$G = -\frac{(m^2-1)F}{r^2} + r^2 \frac{d}{dr}\left[\rho(\omega_1 - \frac{mu_\theta}{r})^2\right] - k^2 r^2 \frac{d}{dr}\left(\frac{B_z^2}{\mu_0}\right)$$

which is the collisionless equation expected upon consideration of equation I11.

Equations V10, V12, V14, V15, V17 and V20 are thus a complete set of equations for the perturbed quantities u_z^1 , $(\underset{\sim}{\nabla}\cdot\underset{\sim}{u})^1$, B_r^1, η^1, B_z^1 and ξ . Since V14, V15 and V17 are explicit expressions, this is a set of three simultaneous second order differential equations in the variables B_r^1, B_z^1 and ξ . A sixth order set of equations of this sort cannot reasonably be solved numerically across the whole plasma by the technique employed on the second order collisionless equation in chapter III since the matrices produced would be at least heptadiagonal and hence determinant calculation too slow for reasonable speed of iteration. Further analysis must therefore be employed using the properties of resistive instabilities to reduce the problem to a numerically manageable form.

5) 'Outer' Region Solution.

The first simplification of the problem to be made is to consider initial states in which the plasma velocity is negligible; ie. no greater than the resistive diffusion. (see section 3). From equation V2 we observe that this implies the

existance of a radial equilibrium electric field when the Hall term is included. Once this is realised, $u_\theta = 0$ and $u_z = 0$ may be substituted into the perturbation equations.

For resistivity to produce instability in the plasma, a region of large perturbation gradient must occur within the plasma to enhance the resistive diffusion above equilibrium rates. Outside this region, perturbation gradients are too small for resistivity to contribute (see Coppi et al. (6)). From the infinite conductivity equation V21 we see that such regions occur when F becomes small. Hence we must order both frequency, ω, and the FLR term to be small compared to their values in collisionless instabilities so that $\frac{d\xi}{dr}$ is sufficiently large near the resonant surface for enhanced resistive diffusion of the perturbations to occur. The accuracy of this ordering must be estimated from the results finally obtained. If this ordering is made, then to lowest order in the resistivity we obtain at a point within the plasma away from a resonant surface:

$$\frac{d}{dr}\left(\bar{k}^2 r^3 B_z^2 \frac{d\xi}{dr}\right) + \left(-(m^2-1)\bar{k}^2 r B_z^2 - 2k^2 r \mu_0 \frac{dp}{dr}\right)\xi = 0 \qquad \text{V22}$$

When discussing the tearing mode, we observe from Coppi et al. (6) that the pressure gradient term responsible for interchange modes must also be a very small quantity. Hence, except near $\bar{k} = 0$ ($r = r_s$) the effects of resistivity and FLR are neglegible and the perturbation is described by:

$$\frac{d}{dr}\left(r^3 \bar{k}^2 B_z^2 \frac{d\xi}{dr}\right) - (m^2-1) r \bar{k}^2 B_z^2 \xi = 0 \qquad \text{V23}$$

Near $\bar{k} = 0$, the full set of perturbation equations must be solved and the solutions matched to those of V23. This is the standard procedure for all resistive instabilities.

For the purposes of the tearing mode, it is more convenient

to work in terms of B_r' than ξ in the outer region.

Transformation of V23 yields:

$$\frac{d}{dr}\left(r^3 \bar{k} B_z \frac{dB_r'}{dr} - r^3 B_r' \frac{d}{dr}(\bar{k} B_z)\right) - (m^2-1)\bar{k} r B_z B_r' = 0$$

The form of the solution to be matched near the singularity at $\bar{k} = 0$ can be found by expanding about $r = r_s$. Following Coppi et al. (6) this takes the form:

$$B_r' = \left(c_1 + c_2\left(\frac{1}{x} + \varsigma \ln|x|\right)\right)\left(x + \frac{\varsigma}{2}x^2 \ldots\ldots\right) \qquad \text{V24}$$

where $x = \frac{r-r_s}{r_s}$, $\varsigma = \frac{m\mu_0}{\kappa B_z}\frac{dj_z}{dr}\Big|_{r=r_s}$; $\kappa = \frac{d\bar{k}}{dr}\Big|_{r=r_s}$

and c_1 and c_2 are the arbitrary constants.

Thus, the solution of the eigenvalue problem is reduced to two parts. Firstly, using profiles of the plasma current and of the magnetic field, V23 must be integrated (probably numerically) to obtain the ratio c_1/c_2 on either side of $r = r_s$. Such computations have been carried out by Rutherford et al.(12). Secondly, the full set of perturbation equations must be solved to find the change in c_1/c_2 as a function of the instability growth rate. By observing that:

$$\lim_{\varepsilon\to 0}\left[\frac{c_1}{c_2}\right]_{r_s-\varepsilon}^{r_s+\varepsilon} = \lim_{\varepsilon\to 0}\left[\frac{r_s}{B_r'}\frac{dB_r'}{dr}\right]_{r_s-\varepsilon}^{r_s+\varepsilon}$$

this matching may more conveniently be expressed as a matching of Δ, where Δ is defined as:

$$\Delta = \lim_{\varepsilon\to 0}\left[\frac{r_s}{B_r'}\frac{dB_r'}{dr}\right]_{r_s-\varepsilon}^{r_s+\varepsilon}$$

the discontinuity in the logarithmic derivative of B_r' across the resistive or 'inner' region. Only this second task involves the physics associated with FLR and resistivity and will be subject of the work that follows.

6) <u>The 'Inner' Region Solution - Discussion.</u>

The 'inner' region is that region around the resonant surface for which $|\bar{k}| = |k+mB_\theta/(rB_z)| \ll |k|$. As we assume it to be a narrow region compared to equilibrium scale lengths

in the plasma, it is consistent to treat equilibrium quantities as constants throughout and expand $\bar{k} = \alpha r_s x$ where x and α are defined in section 5. Furth et al. (7) and Coppi et al.(6) identify different modes characterised by different orderings of the equilibrium parameters. This work will concentrate on the tearing ordering which permits analysis to proceed sufficiently, when FLR is included, for a tractable numerical problem to be defined. The slow interchange ordering wherein the mode is driven by pressure gradients within the resistive region will be considered briefly in appendix B, but the equations that result are less numerically tractable than those of Coppi et al. (6), without FLR corrections, for which severe numerical problems were encountered on only a simplified version. Additional complications arise due to spatial oscillation caused by the FLR terms. This effect is discussed by Frieman et al. (52) and mentioned in section 1.

7) Perturbation Analysis II - Tearing Mode Ordering and Expansion.

Coppi, Greene and Johnson (6) argue that when the growth rate of resistive instability is sufficiently small due to small resistive layer pressure gradients, the resistive thickness becomes less than the resistive skin depth for the frequencies concerned and the perturbations become driven by influences external to the resistive region. This is the 'tearing mode' limit first considered by Furth, Killeen and Rosenbluth. (7). These modes are characterised by large perturbations in the 'outer' region which undergo rapid variations in the resistive layer. Physically, this may be pictured as the pinching or filamentation of a current layer (eg. Jukes (57)) and is known to lead to 'magnetic islands' in the non-linear limit which are thought to be possibly

involved in the disruptive instability in toroidal devices. (See (59)). In order to adopt the ordering scheme given in Coppi et al. (6) describing these modes, we define the following quantities:

ω	Complex frequency of the mode.
$W_R = \frac{\eta}{\mu_0 r_s^2}$	Equilibrium resistive diffusion frequency.
$W_H = \alpha r_s \sqrt{\frac{B_z^2}{\rho \mu_0}}$	Hydromagnetic frequency
$\beta = \frac{p}{B_z^2/2\mu_0}$	Plasma beta.
$U = \frac{\frac{dp}{dr}\left(\frac{\frac{m B_\theta}{r B_z}}{\alpha}\right)^2}{r_s B_z^2/2\mu_0}$	Suydam parameter, $U < -\frac{1}{4}$ violates the Suydam criterion.

(U = - D in the notation of reference (6)).

To describe FLR, define

$$Q_F = \frac{m}{2 r_s \Omega \rho} \frac{dp}{dr}$$

For this to be significant, we clearly need $\omega \sim Q_F$.

The tearing mode ordering from reference (6) is thus:

$$\frac{W_R}{W_H} \sim \phi^5 ; \quad \frac{\omega}{W_H} \sim \phi^3 \sim \frac{Q_F}{W_H}$$

$$\frac{r - r_s}{r_s} \sim \phi^2 ; \quad \beta \sim \phi^2 ; \quad U \sim \phi^2$$

where ϕ is merely an indicator of the relative magnitudes of the various terms and might formally be defined by any of the above expressions.

Hence the combined ordering of the various quantities in ε and ϕ is

$$\beta \sim \varepsilon^0 \phi^2$$

$$B_\theta \sim \varepsilon \phi B_z$$

$$W_H \sim \varepsilon^2 \phi \Omega$$

$$\omega \sim \varepsilon^2 \phi^4 \Omega \sim Q_F$$

$$\frac{1}{r_s} \sim \frac{\varepsilon^0 \phi^2}{r - r_s} \Rightarrow r - r_s \sim \varepsilon^0 \phi^2 r_s$$

$$k \sim \frac{\varepsilon \phi^3}{r - r_s} \Rightarrow k r \sim \varepsilon \phi$$

$$W_R \sim \varepsilon^2 \phi^6 \Omega$$

Now define the scale length and frequency characteristic of tearing modes:

$$L_R = r_s \left(\frac{W_R^2}{W_H^2} \right)^{1/5} \quad ; \quad Q_R = (W_H^2 W_R^3)^{1/5}$$

and the dimensionless quantity, $l^6 = L_R / r_s$.

We shall also need:

$L_p = p/(dp/dr)$ Scale length of plasma pressure.

$L_\rho = \rho/(d\rho/dr)$ Scale length of plasma density.

$$C_L = \frac{\gamma L_p}{L_\rho} - 1$$

$$J_p = \frac{m}{\alpha} \frac{\mu_0}{B_z} \frac{d j_z}{dr} = \frac{1}{\alpha r^2 B_z} \frac{d}{dr} \left(r^3 \frac{d}{dr} (\bar{R} B_z) \right)$$

Thus, in the manner of Coppi et al. (6) we may define normalised or 'stretched' variables in the 'inner' region:

Frequencies:

$q = \omega / Q_R$ Mode.

$q_F = Q_F / Q_R$ FLR.

Length variable:

$$X = (r - r_s)/L_R = (r - r_s)/(l^6 r_s)$$

Perturbations:

$$D = \frac{\xi_0}{r_s} \; ; \; R_0 = \frac{B r_2'}{B_z \alpha r_s L_R} \; ; \; R_2 = \frac{B r_4'}{B_z \alpha L_R^2}$$

(continued)

$$z = \frac{2}{L_R r_s}\frac{B'_{z2}}{B_z}\left(\frac{m B_\theta / r B_z}{\alpha}\right)^2$$

($B'_{z0}=B'_{z1}=B'_{r0}=B'_{r1}=0$ on expansion of the perturbation equations in $\emptyset$ to lowest orders).

The lowest significant order in $\emptyset$ of the various terms in equations V10, V12 and V20 is indicated by the juxtaposed numbers. Observe that equation V15 is redundant since η' occurs in V14, V10 and V12 only to a high order. This effects the previously mentioned elimination of the Ohmic heating terms arising principly from the low ordering of beta. The relative size of the perturbed variables to lowest significant orders is thus seen to be:

$$B'_{r2} \sim \varepsilon \emptyset B'_z \quad ; \quad B'_{r4} \sim \emptyset^2 B'_{r2}$$

$$\omega\xi = u'_r \sim \frac{v_t}{\emptyset}\frac{B'_{r_2}}{B_z} \sim \varepsilon v_t \frac{B'_z}{B_z}$$

$$(\nabla . u)' \sim \frac{u'_r}{r_s} \sim \frac{\emptyset^2 u'_r}{r - r_s}$$

Selecting the lowest order term from V20 yields:

$$\frac{d^2 B'_{r_2}}{dr^2} = 0$$

This the 'constant Ψ (ie. B'_r)' approximation of Furth et al. (7) produced by the formalism of Coppi et al. (6). Henceforth, we shall take B'_{r2} to be a constant in the inner region and later show that it is entirely consistent to neglect dB'_{r2}/dr.

To next significant order, V20 yields:

$$\omega\left(\rho r^3\omega - m r^2 \frac{d}{dr}\left(\frac{P}{2\Omega}\right)\right)\frac{d^2\xi}{dr^2} - m\frac{r^2\rho}{4\Omega}\frac{d^2}{dr^2}(\nabla . u)' \qquad \text{V25}$$

$$+ \frac{i r^2 P}{4\Omega}\frac{d}{dr}\left(\bar{k}\frac{du'_z}{dr}\right) + \frac{2 i k^2 r^2 B_z B'_z}{\mu_0} - \frac{\bar{k} B_z}{\mu_0}\frac{d^2 B'_{r_4}}{dr^2}$$

$$+ \frac{B'_{r_2}}{\mu_0}\frac{d}{dr}\left(r^3\frac{d}{dr}(\bar{k} B_z)\right) = 0$$

To lowest significant order, V10 yields:

$$0 = ik B_z u_z' - B_z (\nabla\cdot u)'\left(1 - \frac{m}{2\Omega\rho r\omega}\frac{dp}{dr}\right) \qquad \text{V26}$$
$$+ \frac{imB_z^2}{2r\Omega\rho\mu_0}\left(\frac{1}{\rho}\frac{d\rho}{dr}\right)\left(i\xi\frac{dB_z}{dr} - B_z'\right) + \frac{\eta}{\mu_0}\frac{d^2B_z'}{dr^2}$$

V12 produces:

$$i\omega(B_{r_2}' - k\xi B_z) = \frac{-im}{\Omega r}\frac{B_z^2}{\rho\mu_0}\left(ikB_z' + \frac{B_{r_2}'}{B_z}\frac{dB_z}{dr}\right) \qquad \text{V27}$$
$$+ \frac{\eta}{\mu_0}\frac{d^2B_{r_4}'}{dr^2}$$

$(\nabla\cdot\underline{u})'$ and u_z' may be substituted into V25 to V27 from V14 and V17 respectively. Transformation to the stretched variables defined above then yields:

$$q(q - q_F(1-\tfrac{1}{2}\gamma))D'' - \frac{iqq_F}{2\gamma U}l^6 Z'' + iZ - XR_2'' + R_0 J_\rho \qquad \text{V28}$$
$$-\frac{\beta}{4}\frac{q_F}{(q-q_F)}\left(iX^2Z'' + \frac{3iX}{U}Z' + \frac{iZ}{U} - \frac{R_0'}{l^6}\right) = 0$$

$$iZ'' = \frac{R_0}{l^6}\left(\frac{-XU}{i(q-q_F)}\right) + D\left(\frac{-2iU}{\gamma\beta}(q + C_L q_F)\right) \qquad \text{V29}$$
$$+ iZ\left(\frac{X^2}{i(q-q_F)} + \frac{2il^6}{\gamma\beta}(q + C_L q_F)\right)$$

$$R_2'' = iR_0(q - 2q_F) - iXqD - \frac{2ZX}{U}q_F l^6 \qquad \text{V30}$$

Where superscript prime denotes differentiation with respect to X.

The quantity C_L is proportional to $d(p\rho^{-\gamma})/dr$ and must therefore vanish in a plasma produced by adiabatic compression from an initial homogeneous state; it represents the contribution of the specific entropy profile. Note that, apart from the contribution arising via u_z', C_L prefixes the FLR parameter, q_F, in V29. The factor of 2 in V30 multiplying q_F may be found to arise due to a term involving total pressure in the initial equations (rather than just ion pressure) and hence this term would be electron-dominated in situations where $T_e \gg T_i$, not considered here.

In order to consider matching conditions with the outer

region and to justify the omission of R_0', following Coppi et al. (6) we take the large X limit of the solution of V28 to V30. Equations V28 and V29 are inhomogeneous in D and Z since R_0 is independent of X. (R_2'' in V28 may be eliminated from V30). Their general solution consists of (see below) a pair of exponentially growing modes in space, a pair of decaying modes plus a particular integral. The first must be eliminated as one pair of boundary conditions, the second can play no part in the large X solution and the particular integral matches with the outer region. Thus, for matching purposes, it suffices to find the latter.

At large X, derivatives of D and Z will be small in X in the particular integral since it neither exponentially grows nor decays.

Taking terms to highest order in X, V29 gives:

$$iZ \approx \frac{R_0 U}{\iota^6 X} - \frac{2u}{\gamma\beta x^2}(q-q_F)(q+C_1 q_F)D \qquad \text{V31}$$

V28 may be written:

$$0 \approx -XR_2'' + R_0 J_p + iZ - \frac{\beta}{4}\frac{q_F}{(q-q_F)}\frac{d}{dX}\left(X\frac{d}{dX}\left[\frac{iZX}{U} - \frac{R_0}{\iota^6}\right]\right) \qquad \text{V32}$$

Substituting for R_2'' and iZ from V30 and V31 respectively yields to highest order in X:

$$0 \approx -iXqR_0 + iqX^2 D + R_0 J_p + \frac{R_0 U}{\iota^6}$$

Hence, at large X:

$$D \approx \frac{R_0}{X}\left(1 - \frac{J_p}{iqX} - \frac{U}{i\iota^6 q X^2} \cdots\right)$$

V31 gives:

$$iZ \approx R_0\left(\frac{U}{\iota^6 X} \cdots\right)$$

Thus, from V30, substituting for Z and D and integrating yields:

$$R_2 = K_1 X + C_R J_p x^2 + \left(R_0^* J_p + C_R \frac{U}{\iota^6}\right)(X\ln|x| - X) - \frac{R_0^* U}{\iota^6}\ln|x|$$

where $R_0 = R_0^* + C_R X$ has been used and K_1 is an arbitrary constant.

Using $l^6 X = x$, we find:

$$R_2 = \frac{K_1 x}{l^6} + \frac{C_R \partial_p x^2}{2 l^{12}} + \left(R_0^* \partial_p + \frac{C_R u}{l^6} \right) \left(\frac{x}{l^6} \{ \ln|x| - \ln l^6 - 1 \} \right) \ldots$$

The total R (normalised B_r') is thus:

$$R_0 + l^6 R_2 = R_0^* + \frac{C_R x}{l^6} + K_1 x + \frac{C_R \partial_p x^2}{2 l^6}$$
$$+ \left(R_0^* \partial_p + C_R u \right)(x \ln|x| - x) - R_0^* \partial_p x \ln l^6 \ldots$$

Due to the ordering of Q_F, this is the same result as found in reference (6) so that, as in that case, we choose $C_R = R_0^* J_p l^6 \ln(l^6)$ so that we find:

$$R_0 + l^6 R_2 = R_0^* + K_1 x + R_0^* J_p x \ln|x| + \ldots\ldots\ldots$$

Comparison of this with the outer region expansion V24 shows that $K_1 = R_0^* c_1/c_2$ on matching the leading terms. Since the particular integral is unique and the large X expansion is independent of direction, only the value of K_1 differs at the opposite boundary. Hence the 'inner' and 'outer' solutions match in their respective asymptotic limits if the change in K_1 across the inner region matches the change in c_1/c_2 across the singularity in the outer region solution. As previously stated, this implies that:

$$\Delta = \frac{1}{R_0} \frac{dR_2}{dx} \Big]_{x \to -\infty}^{x \to \infty} = \lim_{\varepsilon \to 0} \left[\frac{1}{B_r'} \frac{dB_r'}{dr} \right]_{r_s - \varepsilon}^{r_s + \varepsilon}$$

from 'inner' solution. — from 'outer' solution.

These results are independent of the inclusion of FLR and appear identically in reference (6).

Note that the value of R_0' that had to be chosen for the matching is of the order of $l^6 R_0^*$. Hence, from the definition of l^6 :

$$R_0' \sim \phi^2 R_0^*$$

and may thus be omitted from the equations consistently. Henceforth, therefore, the asterisk will be dropped.

Substitution of V29 and V30 into V28 yields:

$$q(q-q_F(1-\tfrac{1}{2}\gamma))D'' \qquad \text{V33}$$
$$= R_0\left[-J_p + X\left(i(q-2q_F) - \frac{qq_F}{2\gamma i(q-q_F)}\right) - \frac{\beta q_F X^3}{4i\ell^6(q-q_F)^2}\right]$$
$$+D\left[X^2\left(-iq - \frac{iq_F(q+C_Lq_F)}{2\gamma(q-q_F)}\right) - \frac{iqq_F\ell^6(q+C_Lq_F)}{\gamma^2\beta}\right]$$
$$+ iZ'\left(\frac{3\beta X}{4U}\frac{q_F}{(q-q_F)}\right)$$
$$+iZ\left[-1 + \frac{\beta q_F}{4U(q-q_F)} + X^2\left(\frac{2i\ell^6 q_F}{U}\left(1+\frac{C_Lq_F}{4\gamma(q-q_F)}\right)\right)\right.$$
$$\left. + \frac{iqq_F\ell^{12}}{\gamma^2\beta U}(q+C_Lq_F) + X^4\left(\frac{\beta q_F}{4iU(q-q_F)^2}\right)\right]$$

8) <u>The Calculation of Δ - The Mathematical Manipulation.</u>

In order to calculate Δ as a function of q, equations V29 and V33 must be solved simultaneously to determine D and Z as functions of the constant, R_0. Δ is then determined by integrating V30 as:

$$\frac{1}{R_0}\frac{dR_2}{dX}\Big]_{X\to-\infty}^{X\to\infty} = \Delta = \int_{-\infty}^{\infty}\left\{i(q-2q_F) - iqX\frac{D}{R_0} - 2\frac{zXq_F\ell^6}{UR_0}\right\}dX \qquad \text{V34}$$

As in Coppi et al. (6) observe that contributions to Δ are made only by the parts of D and Z anti-symmetric in X. Since the coefficients of D and Z in the homogeneous parts of equations V29 and V33 are all symmetric in X, the required parts of D and Z may be found by taking only the anti-symmetric inhomogeneous terms in these equations. Thus the J_p term in V33 may be omitted without effect on the value of Δ.

Equations V29 and V33 take the form:

$$T_{DD}D'' = (T^1_{DR}X + T^3_{DR}X^3)R_0 + (T^0_{DD} + T^2_{DD}X^2)D \qquad \text{V35}$$
$$+ T^1_{DDZ}XZ' + (T^0_{DZ} + X^2T^2_{DZ} + X^4T^4_{DZ})Z$$

$$Z'' = R_0 X T^1_{ZR} + D T^0_{ZD} + (T^0_{ZZ} + X^2 T^2_{ZZ}) Z \qquad \text{V36}$$

At large X, seek asymptotic forms for D and Z of the type $\exp(-pX^2/2)$ from the homogeneous parts of equations V35 and V36. Thus to highest order in X, the value of p is found from:

$$\begin{vmatrix} T^2_{DD} X^2 - p^2 T^-_{DD} X^2 & T^4_{DZ} X^4 \\ T^0_{ZD} & T^2_{ZZ} X^2 - p^2 X^2 \end{vmatrix} = 0$$

Upon substituting the appropriate values for the coefficients, a quadratic equation for p^2 results which has the following solution:

$$p^2 = \frac{1}{i(q-q_F)}\left[1 + \frac{c_L q_F^2/4\gamma}{q(q-q_F(1-1/2\gamma))} \pm \left[\frac{q_F/2\gamma}{(q-q_F(1-1/2\gamma))}\left[1+\frac{c_L q_F}{q}\left(1+\frac{c_L q_F^2/8\gamma}{q(q-q_F(1-1/2\gamma))}\right)\right]\right]^{1/2}\right] \qquad \text{V37}$$

In the special case, $C_L=0$, wherein the specific entropy is constant in space, $d(p\rho^{-\gamma})/dr = 0$, then p^2 simplifies to:

$$p^2 = \frac{1}{i(q-q_F)}\left[1 \pm \left[\frac{q_F/2\gamma}{q-q_F(1-1/2\gamma)}\right]^{1/2}\right] \qquad \text{V38}$$

The inclusion of FLR thus splits the four asymptotic forms into two distinct pairs. Both in the incompressible FLR case of Coppi(31) and the zero FLR, compressible case of Coppi, Greene and Johnson(6) only one value for p^2 was found. This property permitted both of the previous works to achieve analytic results by these methods. In the present case, expansion will be carried out numerically using either one of the two values of p^2 available.

Physically, of course, $1/\sqrt{p}$ defines a scale length of the problem. From the results of Coppi (31) we see that in the low beta limit the scale length of the tearing mode becomes large and hence the effective p becomes small. As no such behavior is exhibited by the p values calculated above, but the resulting theory is shown below to agree excellently with that of Coppi (31) in the appropriate limit, we conclude that the subsequent terms of the series approximations to the perturbations may make an exponential contribution so that $1/\sqrt{p}$ is not necessarily a good measure of the width of the 'inner' region. The thickness of this region compared to the ion Larmor radius (ie. the size of ε in the FLR expansion) is the most severe restriction of this theory.

At this point we change independent variable from X to $G = X\sqrt{p}$. Either of the two square roots may be taken in V37, but since the solution cannot increase exponentially with X, we take the square root of p^2 with positive real part. We are free to choose the square root of p having positive real part. Thus, from this point onwards, two solutions are produced from the two values of p^2. The degree of agreement between the two values of Δ calculated from these provides a good check on the accuracy of the calculation.

For convenience, define:

$$V_{00} = pq\left(q - q_F\left(1 - \tfrac{1}{2\gamma}\right)\right) \qquad \text{V39}$$

$$V'_{0R} = \left[i(q - 2q_F) + \frac{iqq_F}{2\gamma(q - q_F)} \right] \Big/ \sqrt{p} \qquad \text{V40}$$

$$V^3_{0R} = \frac{i\beta q_F}{4\ell^6 (q - q_F)^2 p^{3/2}} \qquad \text{V41}$$

$$V^0_{DD} = \frac{-iqq_F l^6 (q + c_L q_F)}{\gamma^2 \beta} \qquad V42$$

$$V^2_{DD} = \frac{1}{p}\left(-iq - \frac{iq_F (q + c_L q_F)}{2\gamma (q - q_F)}\right) \qquad V43$$

$$V'_{DDZ} = \frac{3i\beta}{4u} \frac{q_F}{(q - q_F)} \qquad V44$$

$$V^0_{DZ} = \frac{i\beta}{4u} \frac{q_F}{(q - q_F)} - i - \frac{qq_F l^{12} (q + c_L q_F)}{\gamma^2 \beta u} \qquad V45$$

$$V^2_{DZ} = \frac{-2l^6 q_F}{up}\left(1 + \frac{c_L q_F}{4\gamma (q - q_F)}\right) \qquad V46$$

$$V^4_{DZ} = \frac{\beta q_F}{4u (q - q_F)^2 p^2} \qquad V47$$

$$V'_{ZR} = \frac{u}{l^6 (q - q_F)^2 p^{3/2}} \qquad V48$$

$$V^0_{ZD} = \frac{-2u}{\gamma \beta p} (q + c_L q_F) \qquad V49$$

$$V^0_{ZZ} = \frac{2il^6}{\gamma \beta p} (q + c_L q_F) \qquad V50$$

$$V^2_{ZZ} = \frac{-i}{p^2 (q - q_F)} \qquad V51$$

Seek solutions for D and Z of the form:

$$D = K_D(G) \exp(-G^2/2)$$

$$Z = K_Z(G) \exp(-G^2/2)$$

and put $R^* = R_0 \exp(G^2/2)$

With these substitutions, V33 gives:

$$V_{DD}\left((G^2 - 1) K_D + (K''_D - 2G K'_D)\right) \qquad V52$$

$$= (V'_{DR} G + V^3_{DR} G^3) R^* + (V^0_{DD} + G^2 V^2_{DD}) K_D - V'_{DDZ} G^2 K_Z$$

$$+ G V'_{DDZ} K'_Z + (V^0_{DZ} + G^2 V^2_{DZ} + G^4 V^4_{DZ}) K_Z$$

and V29 yields:

$$(G^2-1)K_Z + (K_Z'' - 2GK_Z') = R^{\#}GV_{ZR}^1 + K_D V_{ZD}^0 + (V_{ZZ}^0 + G^2 V_{ZZ}^2)K_Z \qquad V53$$

Here, of course, the superscript primes indicate differentiation with respect to G.

From V53:

$$G^2K_Z = \frac{(R^{\#}GV_{ZR}^1 - (K_Z'' - 2GK_Z') + K_D V_{ZD}^0 + (1+V_{ZZ}^0)K_Z)}{(1-V_{ZZ}^2)} \qquad V54$$

V37 implies:

$$\frac{V_{DZ}^4}{1-V_{ZZ}^2} - \frac{(V_{DD}^{\sim} - V_{DD}^2)}{V_{ZD}^0} = 0 \qquad V55$$

Upon substituting V54 into V52, the left hand side of V55 arises by design as the coefficient of G^2K_D. Hence, this process produces the equation:

$$\begin{aligned}
0 = {} & -V_{DD}^{\sim}(K_D'' - 2GK_D') \qquad V56 \\
& + K_D\left[V_{DD}^{\sim} + V_{DD}^0 + \frac{V_{ZD}^0}{(1-V_{ZZ}^2)}\left(V_{DZ}^2 - V_{DDZ}^1 + \frac{V_{DZ}^4}{(1-V_{ZZ}^2)}(1+V_{ZZ}^0)\right)\right] \\
& + R^{\#}G^3\left[V_{DR}^3 + \frac{V_{DZ}^4 V_{ZR}^1}{(1-V_{ZZ}^2)}\right] \\
& + K_Z\left[V_{DZ}^0 + \frac{(1+V_{ZZ}^0)}{(1-V_{ZZ}^2)}\left(V_{DZ}^2 - V_{DDZ}^1 + V_{DZ}^4\frac{(1+V_{ZZ}^0)}{(1-V_{ZZ}^2)}\right)\right] \\
& - \frac{(K_Z'' - 2GK_Z')}{(1-V_{ZZ}^2)}\left[V_{DZ}^2 - V_{DDZ}^1 + V_{DZ}^4\frac{(1+V_{ZZ}^0)}{(1-V_{ZZ}^2)}\right] \\
& - \frac{G^2V_{DZ}^4}{(1-V_{ZZ}^2)}(K_Z'' - 2GK_Z') \\
& + GV_{DDZ}^1 K_Z' \\
& + R^{\#}G\left[V_{DR}^1 + \frac{V_{ZR}^1}{(1-V_{ZZ}^2)}\left(V_{DZ}^2 - V_{DDZ}^1 + \frac{V_{DZ}^4}{(1-V_{ZZ}^2)}(1+V_{ZZ}^0)\right)\right]
\end{aligned}$$

Now expand K_D and K_Z in series of Hermite polynomials.

Only odd polynomials are required since only the anti-symmetric parts of D and Z are being calculated.

ie. put $$K_D = \sum_{m=0}^{\infty} c_m H_{2m+1}(G)$$
$$K_Z = \sum_{m=0}^{\infty} d_m H_{2m+1}(G)$$

The following properties of Hermite polynomials are required (16) :

$$\int_{-\infty}^{\infty} H_m(z)\, H_n(z) e^{-z^2} dz = 2^n n!\sqrt{\pi}\,\delta_n^m$$

$$z H_n(z) = n H_{n-1}(z) + \tfrac{1}{2} H_{n+1}(z)$$

$$\frac{d}{dz}\left(e^{-z^2} H_n(z)\right) = -e^{-z^2} H_{n+1}(z)$$

$$\frac{d}{dz} H_n(z) = 2n H_{n-1}(z)$$

From these, in the manner of Johnson et al. (51) we derive:

$$1 = \sqrt{2}\, e^{-\frac{1}{2}z^2} \sum_m \left[\frac{H_{2m}(z)}{4^m \Gamma(m+1)}\right]$$

$$z = \sqrt{2}\, e^{-\frac{1}{2}z^2} \sum_m \left[\frac{H_{2m+1}(z)}{4^m \Gamma(m+1)}\right]$$

$$z^3 = \sqrt{2}\, e^{-\frac{1}{2}z^2} \sum_m \left[\frac{(4m+3) H_{2m+1}(z)}{4^m \Gamma(m+1)}\right]$$

$$z^2 H_n(z) = n(n-1) H_{n-2}(z) + (n+\tfrac{1}{2}) H_n(z) + \tfrac{1}{4} H_{n+2}(z)$$

Using these, take $\int_{-\infty}^{\infty} e^{-G^2} H_r(G)(\ldots\ldots) dG$ of equations V53 and V56 to obtain difference equations for the d_m and c_m. (ie. equate coefficients of H_m)

V53 yields:

$$c_m = 2 d_{m+1} \frac{(1 - V_{zz}^2)}{V_{z0}^o} (2m+3)(m+1) \qquad \text{V58}$$
$$- d_m \left(\frac{V_{zz}^o}{V_{z0}^o} + \frac{1}{2} \frac{(1 + V_{zz}^2)}{V_{z0}^o} (4m+3) \right)$$
$$+ d_{m-1} \frac{(1 - V_{zz}^2)}{4 V_{z0}^o} - \frac{R_o \sqrt{2}\, V_{zR}^1}{V_{z0}^o\, 4^m \Gamma(m+1)}$$

The result of this operation upon V36 is lengthy and will not be quoted. However, substitution of V58 into this followed by the change of variable:

$$D_m = \frac{-k^m}{R_o} d_m \, i \, \Gamma(m+3/2) \sqrt{2} \qquad \text{V59}$$

(which ensures that gamma functions occur only in ratios and do not lead to subsequent numerical overflow) yields, after substitution from V39 to V51, the following three term recursion formula:

$$-(m+1/2)\frac{D_{m-1}}{U}\Bigg[\left(p^2-\frac{1}{i(q-q_F)}\right)\left(\frac{iq\ell^6 i(q-q_F)}{p} + \frac{(4m+1)\gamma\beta iq_i(q-q_F(1-1/2\gamma))}{i(q+C_L q_F)}\right) \qquad \text{V60}$$

$$+iq_F\left(\frac{2\ell^6}{p}-\frac{\beta}{i(q-q_F)}\left(\frac{3}{4}+\frac{(4m-1)C_L iq_F}{4i(q+C_L q_F)}\right)\right)\Bigg]$$

$$+\frac{D_m}{U}\Bigg[U+\frac{\beta iq_F}{8i(q-q_F)}+\frac{(4m+3)^2\gamma\beta\left\{iq\,i(q-q_F(1-1/2\gamma))+\frac{C_L(iq_F)^2}{4\gamma}\right\}}{2i(q-q_F)\,i(q+C_Lq_F)}$$

$$+\frac{(4m+3)}{p}\ell^6 i(q-q_F)\left(1+\frac{iq}{2}\left(p^2-\frac{1}{i(q-q_F)}\right)\right)\Bigg]$$

$$-\frac{D_{m+1}}{U}(m+1)\Bigg[\left(p^2-\frac{1}{i(q-q_F)}\right)\left(\frac{iq\ell^6 i(q-q_F)}{p} + \frac{\gamma\beta(4m+5)iq_i(q-q_F(1-1/2\gamma))}{i(q+C_Lq_F)}\right)$$

$$+iq_F\left(\frac{2\ell^6}{p}-\frac{\beta}{i(q-q_F)}\left(\frac{(4m+7)C_L iq_F}{4i(q+C_Lq_F)}-\frac{3}{4}\right)\right)\Bigg]$$

$$+\frac{2}{p^{1/2}}\frac{\Gamma(m+3/2)}{\Gamma(m+1)}\left[i(q-2q_F)+\frac{iq\gamma\beta(4m+3)}{2p\ell^6 i(q-q_F)\,i(q+C_Lq_F)}\right]$$

$$=0$$

Using the expressions in V57 for D and Z, the integrals in V34 for Δ may be evaluated using the properties of Hermite polynomials. This yields:

$$\Delta = \sqrt{2}\sum_{m=0}^{\infty}\left[\frac{i(q-2q_F)}{\sqrt{p}}\,\frac{\Gamma(m+1/2)}{\Gamma(m+1)}\sqrt{2}\right. \qquad \text{V61}$$

$$\left.-\left(\frac{4}{\rho R_0}\,2^{2m}\Gamma(m+3/2)\right)\left(iq\,c_m+\frac{2q_F}{u}\,l^6 d_m\right)\right]$$

c_m may be eliminated from this using V58. Finally, after employing the transformation of variable V59, an expression for Δ in terms of the D_m results:

$$\Delta = \sum_{m=0}^{\infty}\left[\frac{u}{l^6}\rho^{1/2}\frac{\Gamma(m+1/2)}{\Gamma(m+1)}\left(\frac{4il^6(q-2q_F)}{\rho u}\right.\right. \qquad \text{V62}$$

$$\left.\left.+\frac{2\gamma\beta(4m+2)}{u\rho^2 i(q-q_F)}\right)+D_m\left(\frac{2\gamma\beta(4m+3)}{\rho^2 u i(q-q_F)}+\frac{4l^6 i(q-2q_F)}{\rho u}\right)\right]$$

The recursion formula V60, with the boundary conditions $D_{-1}=0$ and $D_m\to 0$ as $m\to\infty$, plus expression V62 for Δ define the numerical problem to be solved below.

From V37 we see that $\rho^2-\frac{1}{i(q-q_F)}$ vanishes as $q_F\to 0$. Thus, if we set $q_F=0$ in V60, the coefficients of D_{m+1} and D_{m-1} vanish, leaving an explicit expression for D_m. This is, as required, identical to the result obtained by Coppi, Greene and Johnson (6) (equation 150 in that work). In this limit we see that the terms of the summation are $\sim\frac{1}{m}\frac{\Gamma(m+1/2)}{\Gamma(m+1)}\sim\frac{1}{m^{3/2}}$. Hence, the partial summation up to finite m, which is all that can be computed numerically, converges as $1/m^{\frac{1}{2}}$. This property is of importance in what follows.

9) The Numerical Problem.

The numerical solution of V60 requires that the sequence, D_m be truncated at some large value of m (=M) by setting $D_{M+1}=0$; the resulting tri-diagonal matrix is then inverted. This approximates the large m boundary requirement of the convergence

of D_m; the degree of error depends on the magnitude of D_{M+1} in a hypothetical exact solution to the recursion formula. The effect of this error may be seen by considering the general solution to the problem:

$$D_m = a_1 S(m) + a_2 B(m) + P$$

where S(m) and B(m) are complementary functions and P the particular integral. Typically, one of the former (say S) will converge for large m and the other diverge. Thus, the large m boundary condition is, accurately, $a_2=0$. The effect of the truncation is thus to make a_2 small, but finite, so that the last few D_m calculated will be in serious error due to the contribution from B. The precise number of such terms is determined by the magnitude of a_2 and hence the severity of the truncation error. In evaluating Δ from V62, therefore, the series was summed until, for some $m=M^T \leq M$ the contributions began to diverge. (The equality applies for $q_F=0$).

Figure V1 shows the variation of the series for Δ for a particular set of parameters as larger numbers of terms were included. Note that even with FLR terms included, the series varies linearly with $1/m^{\frac{1}{2}}$ for sufficiently large m. A better approximation for Δ can be produced by extrapolating a graph of this sort to the $1/m^{\frac{1}{2}} \to 0$ limit. Numerically, this was effected by regressing the last ten partial sums found against $1/m^{\frac{1}{2}}$ and extrapolating this best fit to $1/m^{\frac{1}{2}}=0$. From figure V1 it may be seen that this extrapolation involves only a 3% change in the value of Δ calculated and is hence of the order of the errors involved in the computation; its importance is that it removes systematic error enabling the value of M used to be altered, whilst varying a parameter, without a discontinuity appearing in the calculated value of Δ as a

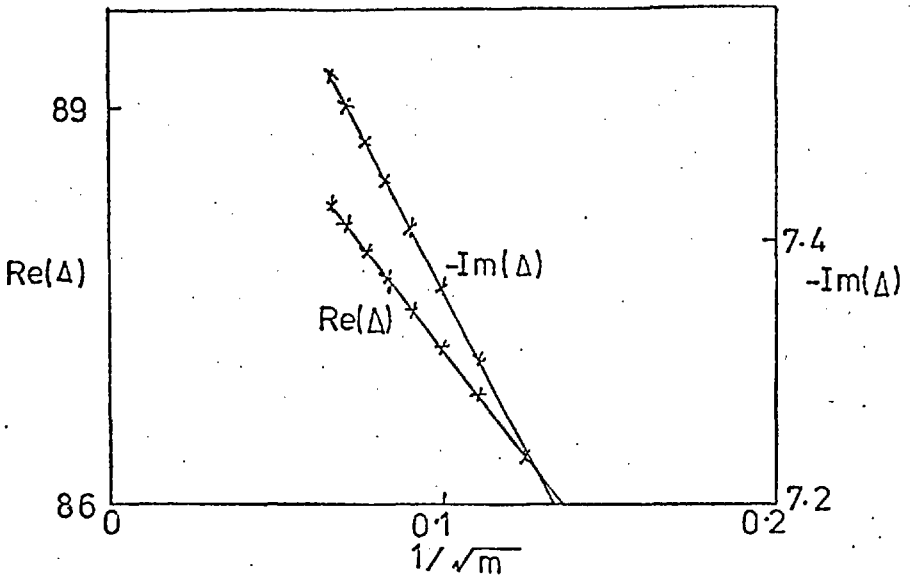

Figure V1 - Asymptotic behavior of the series expansion for Δ; m is the number of terms included in the sum.

function of the parameter changed. Further justification for this procedure was found when Δ was calculated taking the other sign in equation V37. As a function of $1/m^{\frac{1}{2}}$, the two approximations were found to converge towards one another in the $1/m^{\frac{1}{2}} \to 0$ limit as is to be expected from the nature of the analysis.

The success of the computations clearly depends upon the convergence of the series for Δ. In situations when p is very large, the scale length involved in the Hermite expansion becomes very short and hence large numbers of terms are required. From V37, we see that this is likely to occur when $q \to q_F$ or $q \to q_F(1-1/(2\ell))$. In regimes such as this, considerable computational difficulty was experienced and M as large as 1000 was frequently used. Situations more typical of the tearing mode, however, were accurately soluble using typically 250 terms; excellent agreement to less than 1% was found between computations using the two different values of p^2.

The only remaining constraint on Δ to be satisfied is that it should be real. This can be achieved via iteration by

varying the real part of the normalised frequency, q, until the imaginary part of Δ, calculated by the above procedure, is reduced to zero. Clearly, this is a problem of root-solving a real function (the imaginary part of Δ) and was carried out using a linear interpolation algorithm, a standard method for this purpuse.

The iteration above serves to compute the function $\Delta(g)$ where g is the normalised growth rate (-Im(q)). Computation of g(P) at fixed $\Delta = \Delta_0$, where P is an arbitrary parameter of the problem, involves root-solving the complex function $\Delta(q) - \Delta_0$. This involves considerably more computational effort than the calculation of $\Delta(g)$, but was attempted, when required, using the Muller's algorithm coded for the work of chapter III.

10) Checks on the Calculation.

There are two limits in which these calculations can be checked with previously published work:

a) In section 8, it was observed that setting $q_F=0$ reduced V60 to the results of Coppi et al.(6). The coding of the equations was checked by taking this limit and comparing the results with those obtained from the explicit formula for Δ given in reference (6). Excellent agreement was found, but, since this is the limit in which the two values of p^2 coincide, this cannot be used as an indication of the accuracy of the finite q_F calculations.

b) At non-zero FLR, Coppi's calculations (31) apply to the $\beta=0$ (and hence U=0) limit. Computations were performed for a suitable set of parameters taking the $\beta=0$ limit; the results of this are shown in figure V2. Note the accurate agreement between the curves constructed from the present calculation and the points derived from Coppi's work.(31).

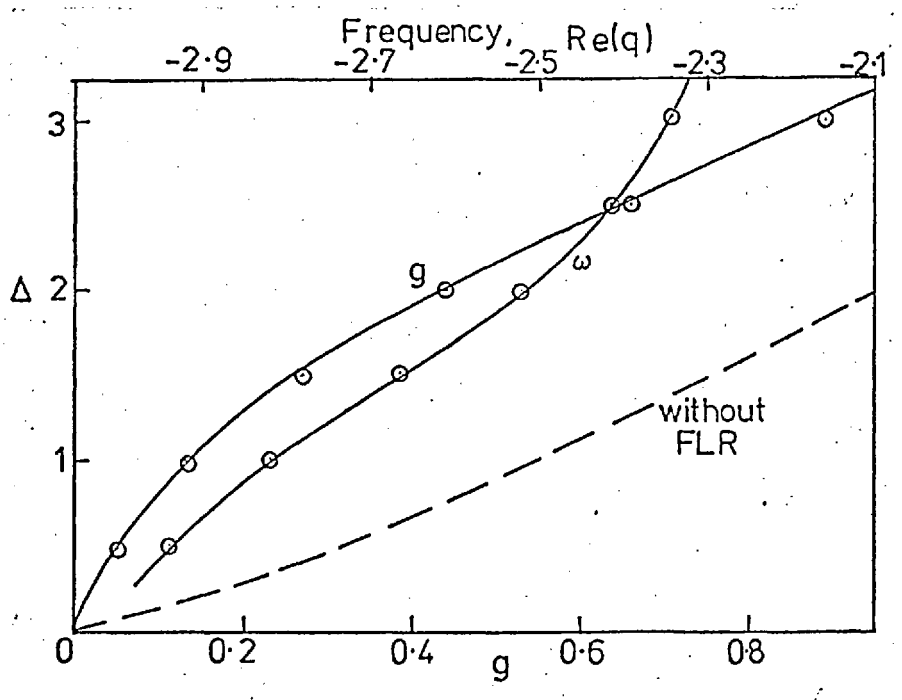

Figure V2 - Comparison of the calculation in the β=0 limit with the results of Coppi(6). The circled points were calculated from Coppi's work; the bold lines arise from the present theory.

The minute deviations that appear can largely be explained by the errors involved in extracting data from the 2in. square graph in Coppi's (31) figure 3.

11) Nyquist Techniques - General Comments.

Glasser, Greene and Johnson (50) investigated their dispersion relation, $\Delta(q)=\Delta$, using Nyquist plots. This involves searching for ranges of unstable values of Δ by mapping the lower half of the complex q plane onto the complex Δ plane. Any part of the real Δ axis enclosed within the mapped region will exhibit instability. Numerically, this may be attempted by plotting Δ on the complex plane as q is varied along that part of the real axis in which significant effects are likely to occur and outside of which simpler theory (eg. (6)) provides an adequate description. In the case of FLR phenomena, we clearly wish to investigate the regime $q \lesssim q_F$.

Owing to the existance of singularities in V37 on the

real q axis, numerical methods are incapable of producing a complete Nyquist plot of the type indicated above. A little more information can be numerically extracted from the dispersion law by considering only instabilities with a growth rate larger than a specified value. This may be accomplished by computing the contour below, rather than along, the real q axis. As will be seen later, this approach yields diagrams which contain various loops in the regime $Re(q) \sim q_F$. The diagrams are still incomplete, however. The study of the behavior of such loops is a useful key to understanding the behavior of the dispersion law. Since they expand and contract rapidly as a function of the growth rate employed in the plot, maximum and minimum growth rates of modes at particular values of Δ can be estimated from the potential ability of the loops to intersect the real Δ axis. In particular, the existance of a mode at a noighbouring parameter value is often indicated by the presence of such a loop not intersecting the real Δ axis. If such intersection occurs, either the enclosed or the excluded part of the real Δ axis may have the larger growth rate. Features of this type are no doubt due to poles in the numerically defined dispersion law.

12) Results of the Computations.

In order firstly to ensure that the results blend continuously into those of (6) in the limit $q_F \ll q$ and secondly to gain an overall view of the regime in which FLR effects are important, consider the results presented in figure V3a for a set of parameters giving $q_F=-10.1$. The curve indicating the $q_F=0$ situation was derived from equations 151 and 152 of reference (6) omitting the S parameter of that work since it does not arise in the present calculation owing

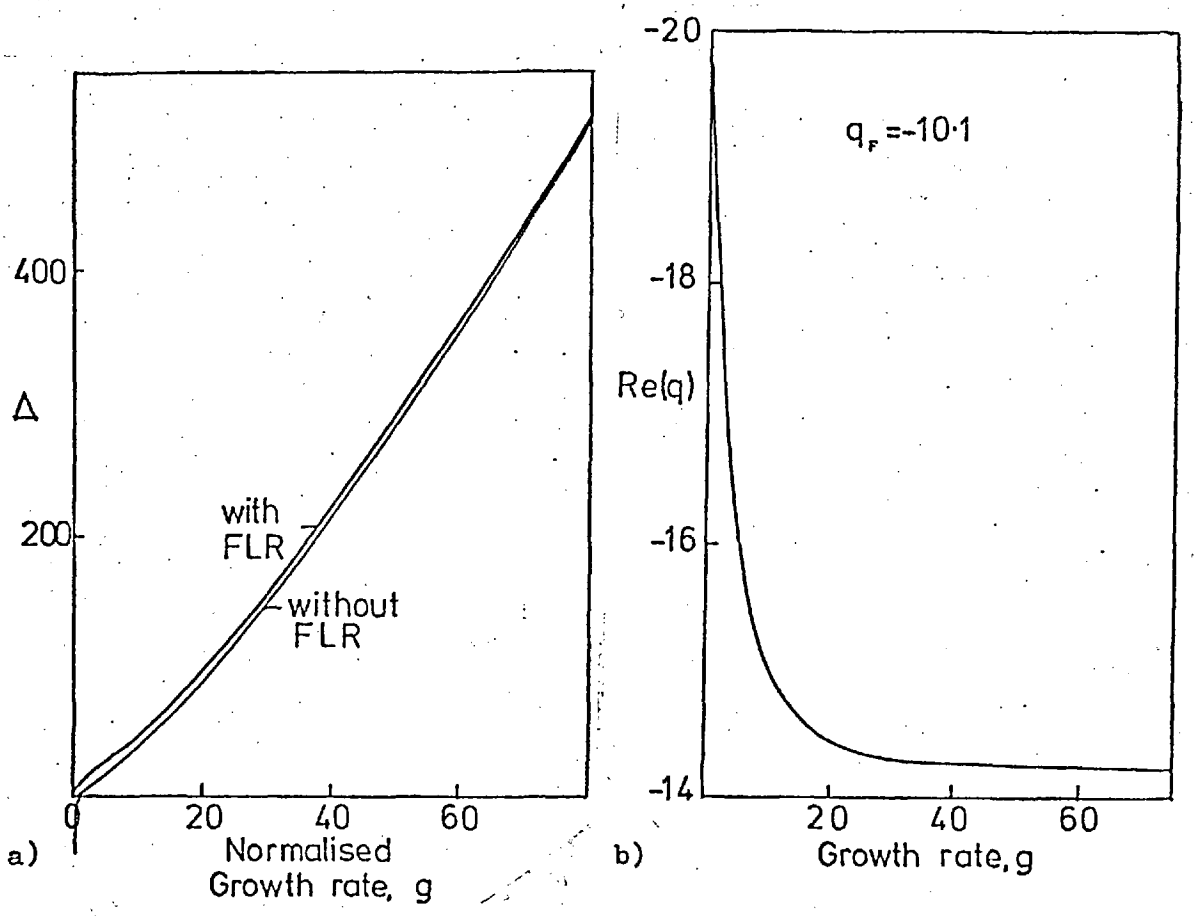

Figure V3 - B_z=2T, B_θ=0.002B_z, n = $10^{21}m^{-3}$, T = 100eV, L_B=r_s=0.1m, L_p=-0.1m, L_ρ=-0.17m (C_L=0), m=2: Q_R= $494s^{-1}$. (L_B= $(B_\theta/(rB_z))/d(B_\theta/(rB_z))/dr)$

a) The dependence of Δ on the normalised growth rate, g. FLR is most effective with $g \lesssim |q_F|$. At large g the two curves approach one another as required.

b) The frequency of oscillation corresponding to a).

to the ordering of B_θ/B_z in ε . Note that, at large q, the two curves approach one another. The major effect of the FLR terms is observed below $q \sim 2q_F$.

Figure V3b indicates the behavior of the oscillation frequency for the same set of parameters. When q_F is unimportant, at large growth rate, g, the frequency tends to a roughly constant value, small compared to the growth rate. The most marked feature is the rapid rise of the frequency towards $2q_F$ as g tends to zero. This is the value predicted by Coppi(31)

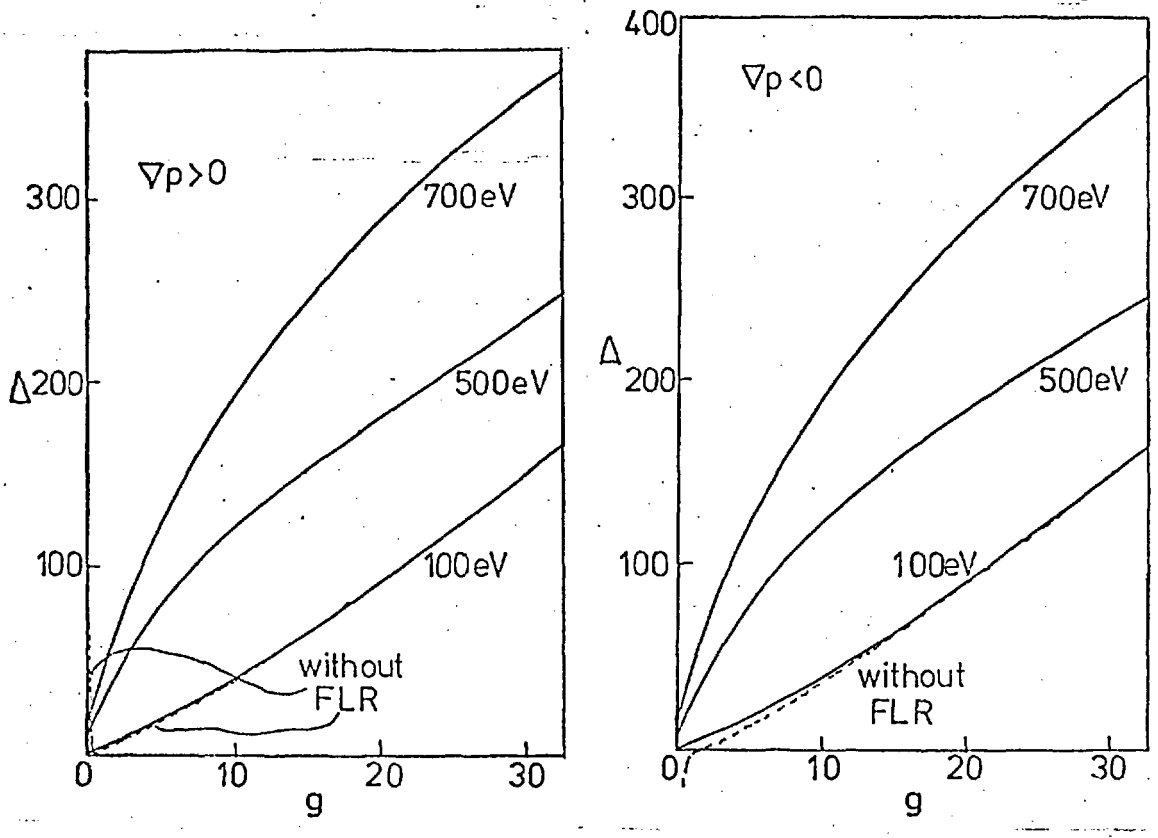

Figure V4 - (g) for B_z=6T, B_θ=0.002B_z, n=$10^{-21}m^{-3}$, r_s=0.1m.
a) L_p= 0.1m =L_B ; L_ρ=0.17m. (C_L=0)
b) L_p= -0.1m =L_B ; L_ρ=-0.17m. (C_L=0)

in the limit wherein FLR effects dominate.

In figure V4, we see the situation, B_z=6T, B_θ=0.002B_z, n= $10^{21}m^{-3}$, m=2, $|L_p|$ =0.1m = $|L_B|$, $|L_\rho|$ =0.17m where L_B is defined as:

$$1/\frac{d}{dr}\left\{\ln\left(\frac{mB_\theta}{rB_z}\right)\right\}$$ at the resonant surface.

For these conditions we find the following parameters:

Table V1.

Temperature in eV	Q_R in s^{-1}	$\|q_F\|$
100	1533	2.2
500	360	46.3
700	266	87.7

Note the large variation in the scale frequency, Q_R, due to the $T^{-3/2}$ dependence of the resistivity. The larger variation of $|q_F|$ is due to the increase in Larmor radius, as temperature rises, superimposed on the resistive decrease in the normalising

frequency, Q_R. When considering FLR effects on resistive modes, therefore, we are concerned with a strongly temperature dependent phenomenon ($q_F \propto T^{1.9}$). In the absence of FLR, q varies little with temperature and hence, for clarity, the positions of the curves have merely been indicated.

Comparison of V4a and V4b, with ∇p positive and negative respectively, reveals very close similarity in this q_F dominant regime. Both sets of curves cut off at similar sets of values of Δ instead of exhibiting any of the pressure dependent characteristics that appear in the absence of FLR. In particular, Coppi et al. (6) found that, at $q_F=0$, the $\nabla p<0$ case showed no cut-off Δ, whereas the $\nabla p>0$ case exhibited a minimum in Δ (q) below which Glasser et al.(50) later showed that an overstable branch cut off at positive Δ. In the light of collisionless theory (30), FLR induced cut off can be interpreted as stabilisation of the pressure driven interchange phenomena present when the tearing mode driving force, Δ, is small. Hence, it is analogous to the FLR stabilisation of Suydam modes.

At larger Δ we observe from figure V4 that the reduction in the normalised growth rate, g, increases for any given Δ as temperature rises. This is due to increased Q_F; resistivity variations are accounted for in the frequency normalisation. Reduction of Δ, however, reduces the degree of stabilisation.

In figure V5 the beta dependence of the cut-off Δ is exhibited. Note that this tends to zero as beta falls to zero (the limit of Coppi (31)). The cut-off of the tearing mode by FLR is thus identified as a finite beta effect not predicted by earlier theories. In toroidal devices, reference (50) indicates that, in the $q_F=0$ case, the mode must

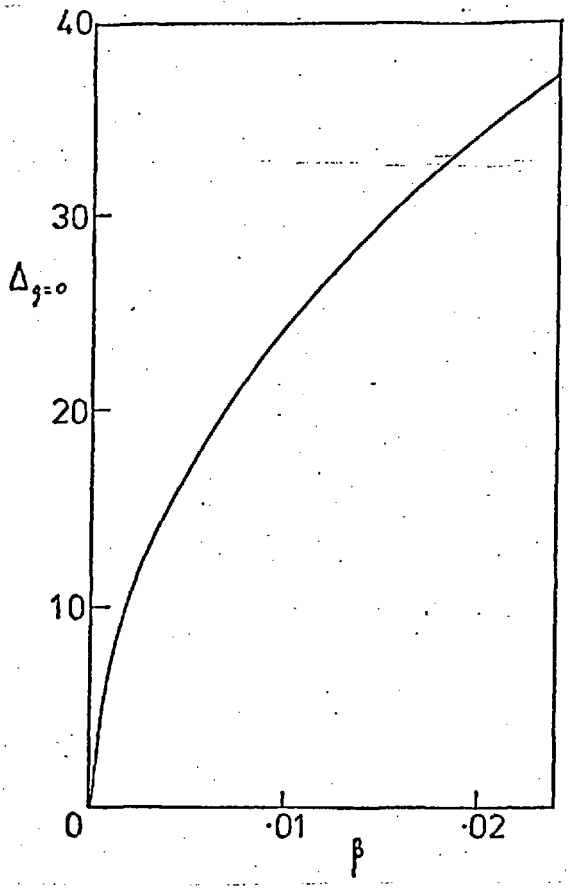

Figure V5 - Varying the magnitude of the finite beta terms included in order to study the cut-off Δ.
$B_z=6T, B_\theta=0.002B_z$,
$r_s=L_p=L_B=0.1m, L_\rho=0.17m$,
$T=1keV$.

be stabilised by creating sufficient favourable average magnetic field curvature to overcome adverse pressure gradient. Clearly such constraints may be relaxed if FLR aids the stabilisation. Devices with less favourable curvature may be considered.

Increased FLR stabilisation at higher temperatures occurs due to increased ion Larmor radius and reduced resistive scale length. Breakdown of the theory readily occurs if extremely high temperatures are considered since ε (the FLR expansion parameter) then approaches unity. The difficulties associated with identifying the scale length in this calculation were discussed in section 8. For safety, the temperature is kept sufficiently low in this work so that the ion Larmor radius is less than the scale length calculated from $1/\sqrt{p}$. If the FLR ordering fails, then the fluid model used provides an inadequate description of the situation so that

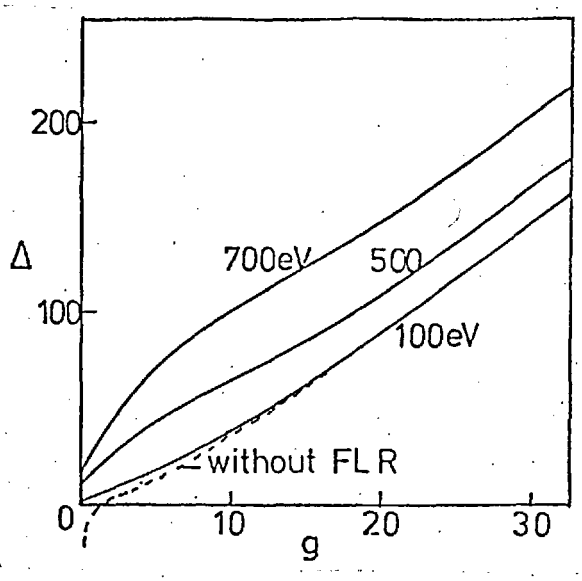

Figure V6 - $\Delta(g)$ with larger B_θ.
B_z=6T, B_θ= 0.02B_z, n= $10^{21}m^{-3}$, L_B= L_p= -0.1m, L_ρ= -0.17m, r_s= 0.1m.

particle drift and resonant effects play an important role.

Figure V6 illustrates the case: B_z= 6T, B_θ= 0.02B_z, n= $10^{21}m^{-3}$, m=2; L_p=-0.1m =L_B, L_ρ=-0.17m, r_s=0.1m. These conditions yield the parameters:

Table V2.

Temperature in eV.	Q_R in s^{-1}.	q_F.
100	3850	-0.86
500	905	-18
700	661	-35

The larger B_θ has increased the scale frequency, Q_R, of the problem and thus reduced q_F. The latter is, however, still sufficiently great to exceed the growth rate at which pressure driven effects occur in the absence of FLR. The diagram (V6) shows that, owing to reduced q_F (ie. more dominant hydromagnetic effects) the stabilisation at large Δ is considerably reduced, even when the change in scale frequencies is taken into account. However the value of the cut-off Δ has been neglegibly changed for an order of magnitude alteration in B_θ. The case of $\nabla p > 0$ is entirely analogous.

The above computations leave two basic questions

unanswered. 1) has the introduction of finite gyro radius effects at finite beta introduced any additional instabilities? 2) As systems of smaller and smaller q_F are considered, how do the instabilities found merge into those present in the $q_F=0$ limit? The latter is particularly relevant to $L_p<0$ situations wherein the inclusion of q_F has apparently created a stable range of Δ values where none was present in its absence. (see(6))

In order to study these questions, the Nyquist technique, used by Glasser et al. (50) and discussed previously, was implemented. Figure V7 shows the diagram obtained by computing Δ along the real q axis for the parameters of figure V4a (500eV). The numerical method became inaccurate, as determined by the disagreement of the Δ values determined from the different choices of p^2, between the two free ends of the curve on the diagram, although, in this region, the recursion formula was not truncated until the 1001st term. The region of breakdown began as q approached q_F, when p^2 began to diverge, and ended with $q<q_F(1-1/(2\gamma))$. The diagram for the 500eV curve of figure V4b was similar to figure V7 inverted about the real Δ axis. The work of Glasser et al.(50) indicates that A and B are joined by a loop to the right at infinity. In the absence of FLR these authors showed that the path $AD\overset{\infty}{\curvearrowright}CBA\overset{\infty}{\curvearrowright}$ was followed by curves of this sort; they pass very close to the origin on the scales of figure V7. The $L_p<0$ case took the path $AE\overset{\infty}{\curvearrowright}FBA\overset{\infty}{\curvearrowright}$.

Let us consider the behavior of $\arg(\Delta)$ in the region of the singularity at $q=q_F$. Denoting $\lambda=q-q_F$, V60 indicates that $D_m\sim\lambda^{\frac{1}{2}}$. V62 then indicates that $\Delta\propto p^{\frac{1}{2}}$, hence $\Delta\propto\lambda^{-\frac{1}{4}}$. Thus, if:

$q-q_F>0$ $\quad\arg(\Delta)=-\pi/8$

$q-q_F<0$ $\quad\arg(\Delta)=\pi/8$

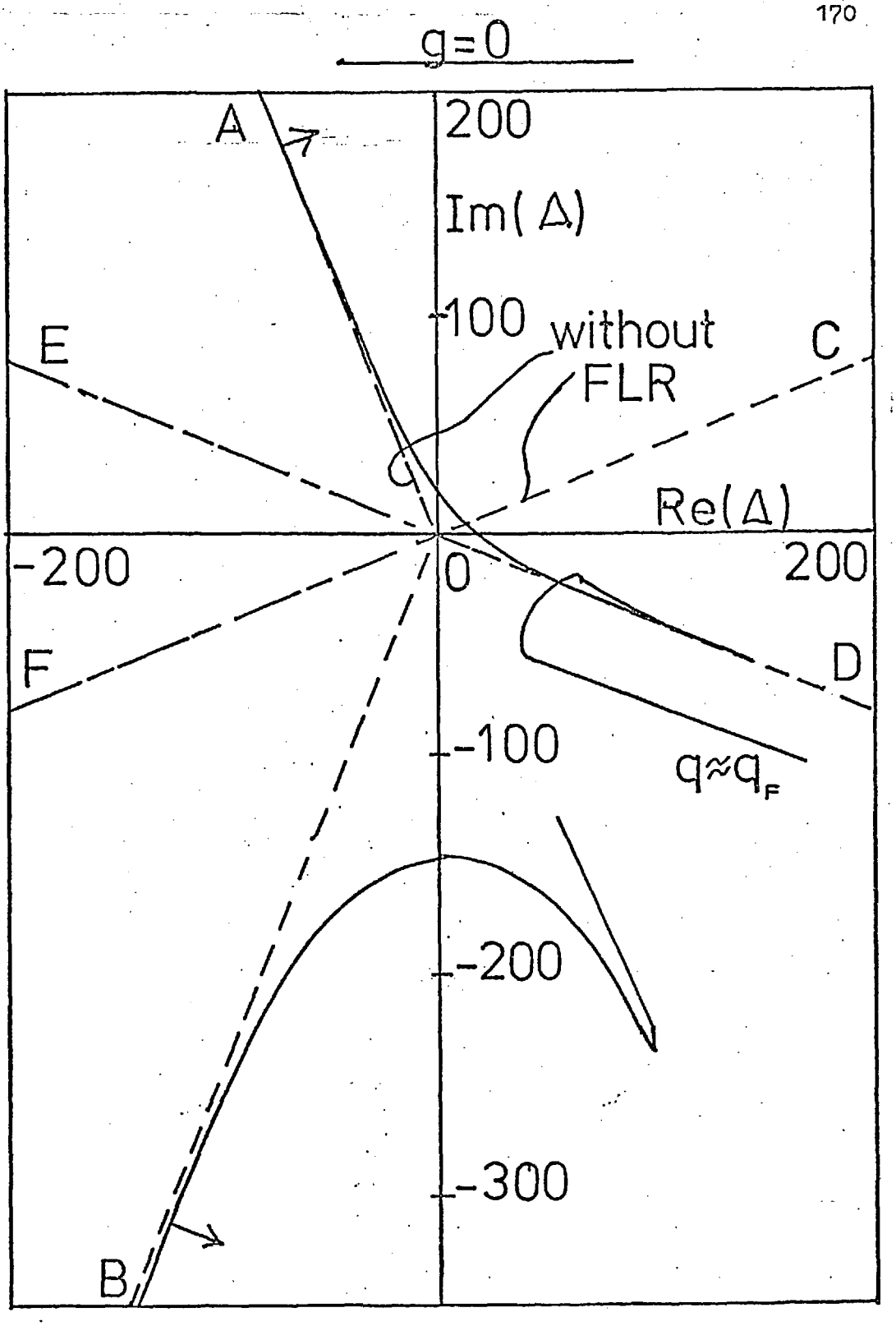

Figure V7 - Nyquist plot appropriate to : g=0, B_z=6T, B_θ=0.002B_z, n= $10^{21}m^{-3}$, T= 500eV, L_B= r_s= L_p= 0.1m, L_ρ=0.17m, (Q_R= 360.1 s^{-1})

independent of the sign of the pressure gradient. Thus, in figure V7, the curve becoming asymptotic to OD as $q \to q_F$ must return from infinity along CO. Since this must eventually join

the free end in the lower right hand quadrant, the missing segment of the curve must intersect the real axis. This indicates the existance of at least one further instability for some range of values of Δ .

In figure V8, additional modes are sought by moving the contour slightly downwards in the complex q plane thus mapping out the region in the complex Δ plane having growth rate greater than the specified value. The loops in figures V8a and V8b enclosing segments of the real Δ axis clearly indicate the presence of additional modes. Arrows on these plots indicate the direction of motion of the curves as the growth rate rises. Note that, although extra instabilities have been discovered, the numerical method was still unable to close the diagrams. This was achieved in figure V8c with a growth rate of g=10 (g=-Im(q)) indicating that, however many instabilities may exist in addition to the main tearing mode, all have a normalised growth rate less than 10 for the set of parameters used.

Figure V9 shows the dependence of Δ on the growth rate of the two modes found. It appears that both modes are present for all Δ . In both the large positive and large negative Δ limits, the growth rate of each of these new modes appears to tend asymptotically to one particular value. This behavior portrays an insensitivity of the growth rate to Δ , indicating that another driving force produces the instability. Mathematically, a pole in the function $\Delta(q)$ is indicated by each such mode. Since behavior of this sort is not indicated by the results of references (6) or (31), the possibility of these weakly growing instabilities is associated equally with finite beta and with finite ion Larmor radius

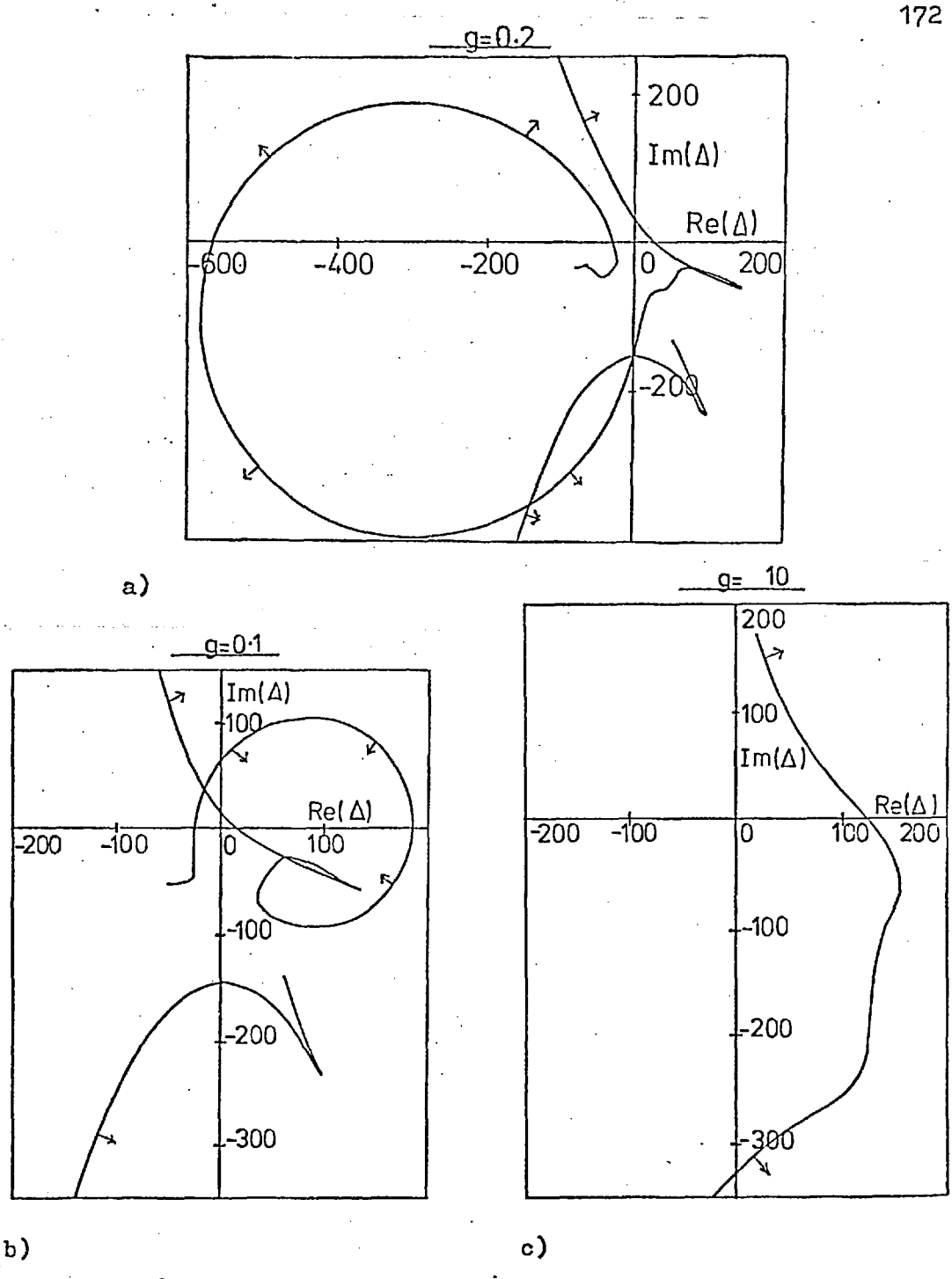

Figure V8 - Nyquist plots with increased g, demonstrating further instabilities. $B_z = 6T$, $B_\theta = 0.002B_z$, $n = 10^{21} m^{-3}$, $T = 500eV$, $L_B = r_s = L_p = 0.1m$, $L_\rho = 0.17m$, ($Q_R = 360.1\ s^{-1}$).

effects.

The relation between the new modes and figure V4a is indicated by figure V10. This diagram concerns the region close to the origin in V4a. The 500eV and 700eV tearing mode curves lie far above the top of this plot. Broken lines

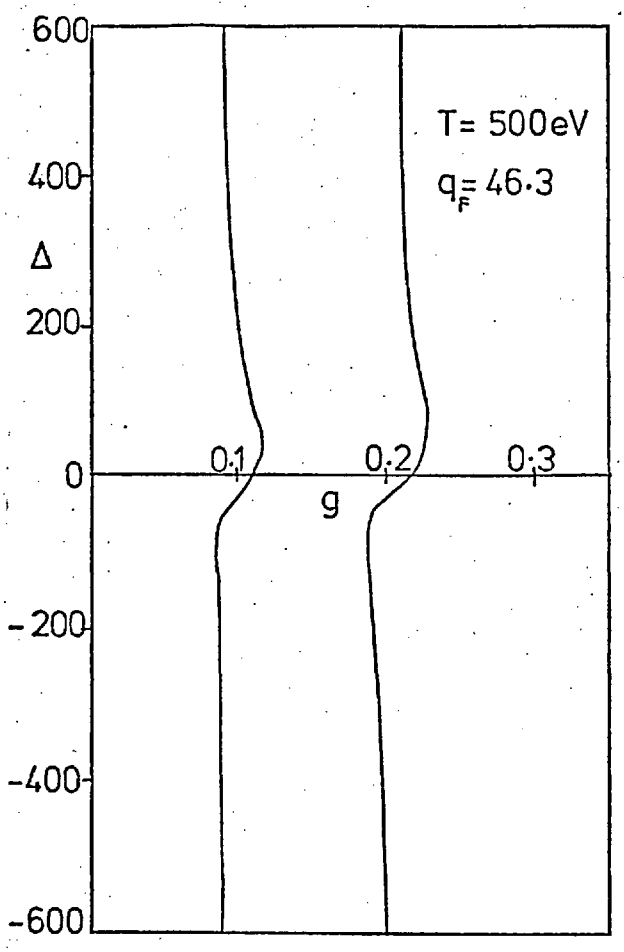

Figure V9 - Δ(g) for the instabilities found in figure V8.

indicate evaluation of the q_F=0 formula of reference (6) together with a calculation of the branch below the minimum by iteration of the same formula, thereby varying Re(q) to reduce Im(Δ) to zero. Clearly, both in position and in separation, the two modes found are associated with the minimum in the q_F=0 curves. Since this is found over such a wide temperature range, a connection with the associated physics is strongly implied. As the mimima are produced by the interchange mechanism beginning to dominate that of the tearing mode, pressure gradient effects must be important in driving the new instabilities. From Coppi et al.(6) we see that the transition region is characterised by:

$$\frac{t^{12} q^3}{\gamma^2 \beta^2} \sim \frac{2u}{\gamma \beta}$$

on comparison of the relevant terms in the series expansion for Δ in reference (6). Thus, the growth rate of this region

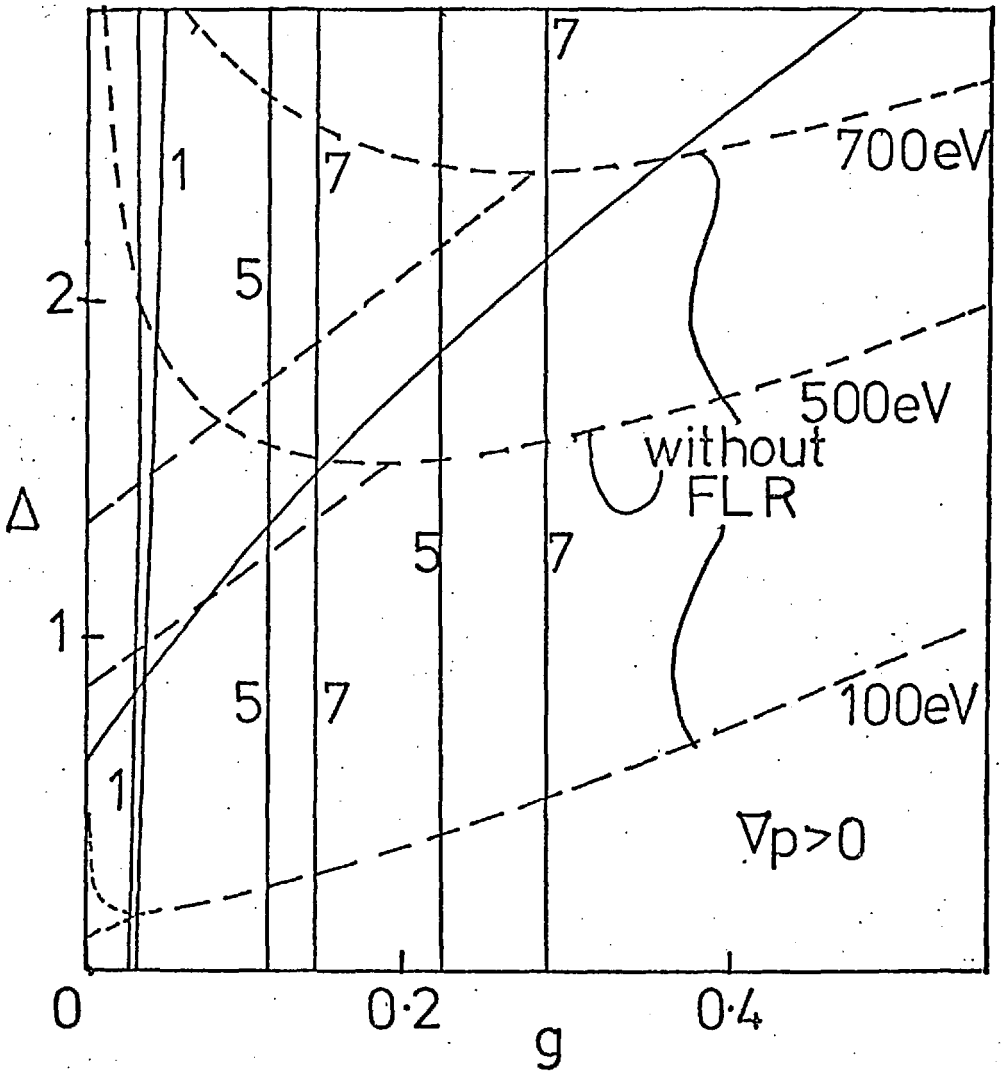

Figure V10 - The instabilities of figure V9 at different temperatures compared to the FLR-free curves for the tearing mode. Parameters as for figure V4a. Only the 100eV tearing mode curve from figure V4a lies within the diagram when FLR effects are included.

is roughly given by:

$$q_{crit.} \sim \left(\frac{2u\gamma\beta}{l^{12}} \right)^{1/3}$$

The range of q_F studied in the above examples satisfies $|q_F| \gg q_{crit.}$ so that the former completely dominates pressure-driven effects. If we define $\omega_{crit.} = Q_R q_{crit.}$ we see that $\omega_{crit.} \sim T^{-\frac{1}{2}}$ ($\omega_{crit.} \eta^{\frac{1}{3}}$) whilst $Q_F \propto T$. Hence the q_F dominant regime will always be a characteristic of higher temperatures.

In order to study the regime of lower q_F and the change-over to FLR-free characteristics, we now consider systems of

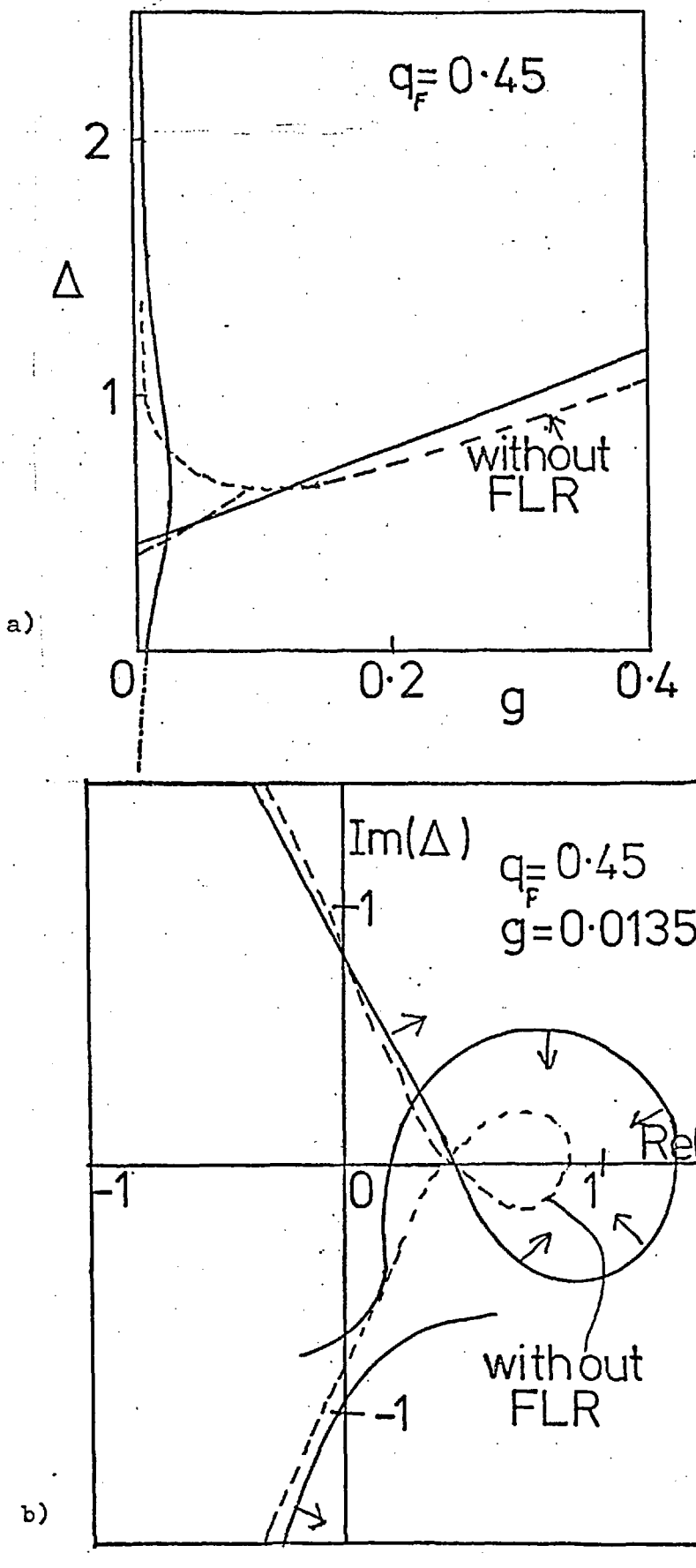

Figure V11 - Instabilities with $q_F < q_{crit.}$. $B_z = 6T$, $B_\theta = 0.1B_z$, $T = 100eV$, $m=2$, $n = 10^{21} m^{-3}$, $L_\rho = r_s = L_B = 0.1m$. ($Q_R = 7330\ s^{-1}$, $q_{crit.} = 0.5$). a) $\Delta(g)$, b) Nyquist plot.

larger B_θ. This has the effect of increasing Q_R, the scale frequency of the problem, due to a larger hydromagnetic contribution, whilst leaving beta unaltered.

Figure V11 describes the $B_\theta = 0.1B_z$ situation at 100eV with $n = 10^{21}$, $L_p = L_B = L_\rho = 0.1m$, $B_z = 6T$. For these parameters $|q_F|/q_{crit.} = 0.91$. Figure V11a shows the main tearing mode branch tending to the overstable $q_F = 0$ branch at small growth rate. The other zero Larmor radius mode to the left of the branch point has its counterpart in the instability indicated which extends beyond the range of Δ of the $q_F = 0$ result. Thus, for certain ranges of Δ, this mode is destabilised by the introduction of FLR. Consideration of figure V11b, the Nyquist plot at $g = 0.0135$, shows the latter mode as a loop expanded around the zero-FLR curve.

Figure V12a shows the more interesting case of negative pressure gradient. In the limit taken, the main mode of this diagram has the limiting characteristics of the $q_F = 0$ theory, namely that it does not cut off at any Δ. The sharp change of slope near $g = 0.9$ is of importance in interpreting the transition behavior. A Nyquist plot at $g = 0.0135$ is shown in figure V12b. The loop of the $q_F = 0$ theory has again been expanded; the main tearing mode of V12a is indicated at the intersection ,A, of the curve with the real axis. Since the smaller, complete, loop expands rapidly as g is reduced, as indicated by the g=0 curve, the behavior of the secondary mode at positive Δ is qualitatively that indicated by the chain line in figure V12a although this could not be computed exactly.

The transition from the subdominant to the dominant q_F regime may be investigated by studying the behavior of the

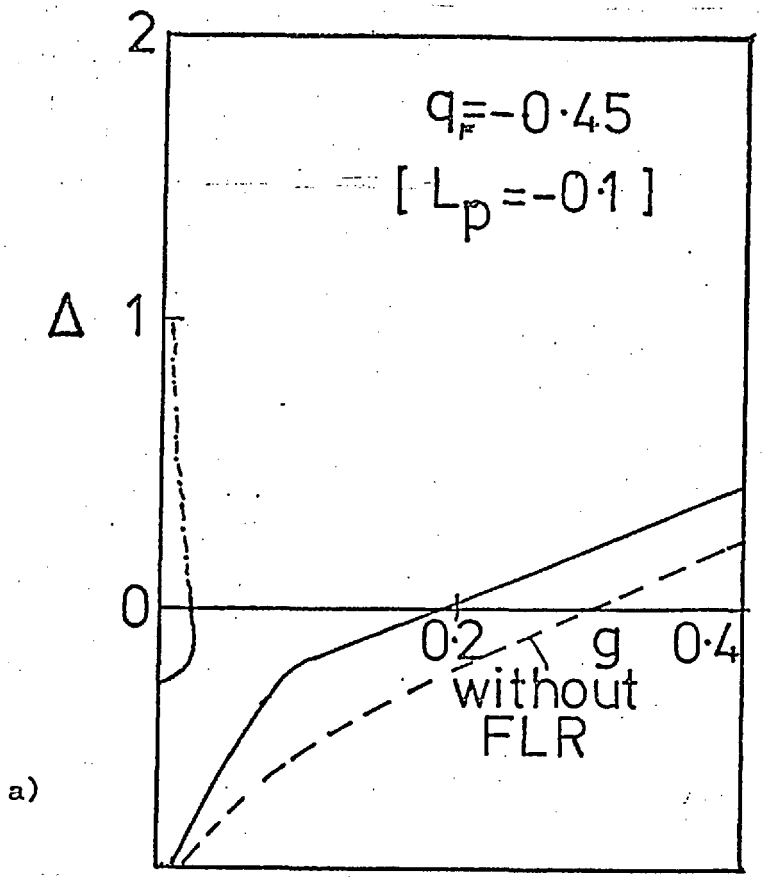

a)

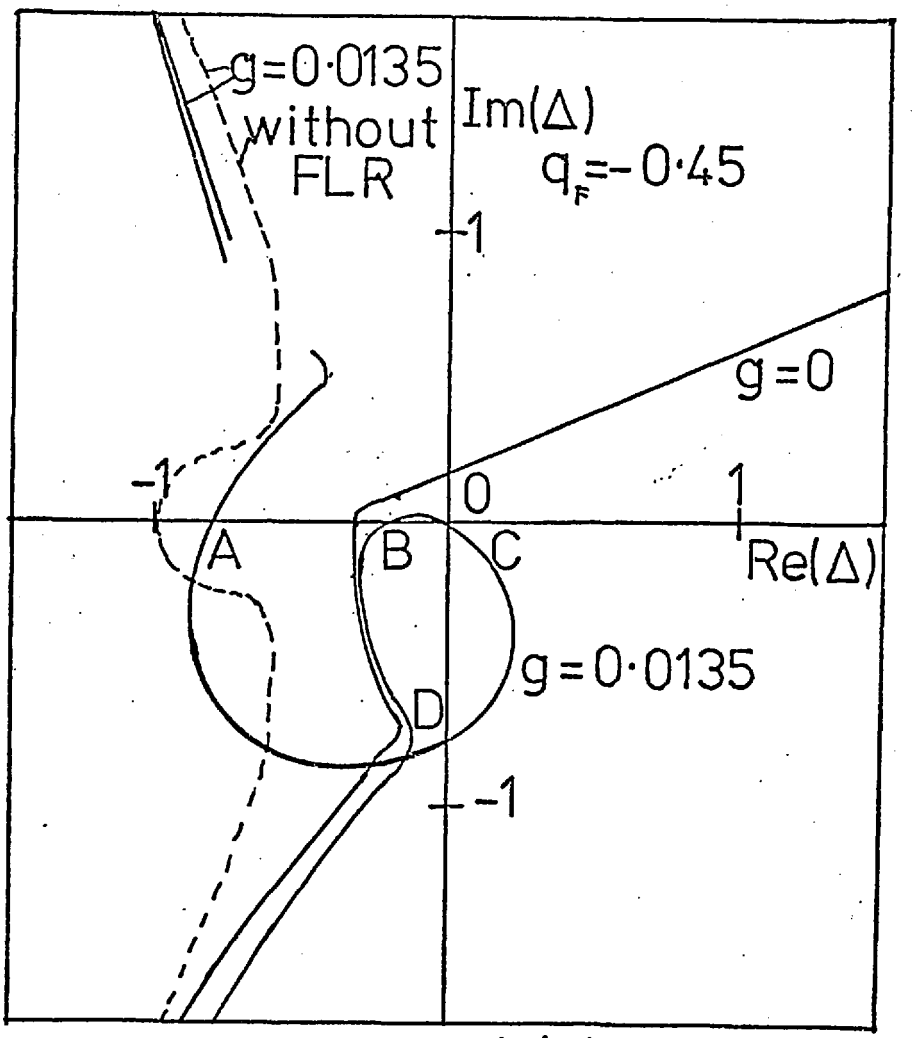

b)

Figure V12 - Instabilities with $|q_F| < q_{crit.}$. $L_p=L_p=L_B$=-0.1m. Other parameters as in figure V11.

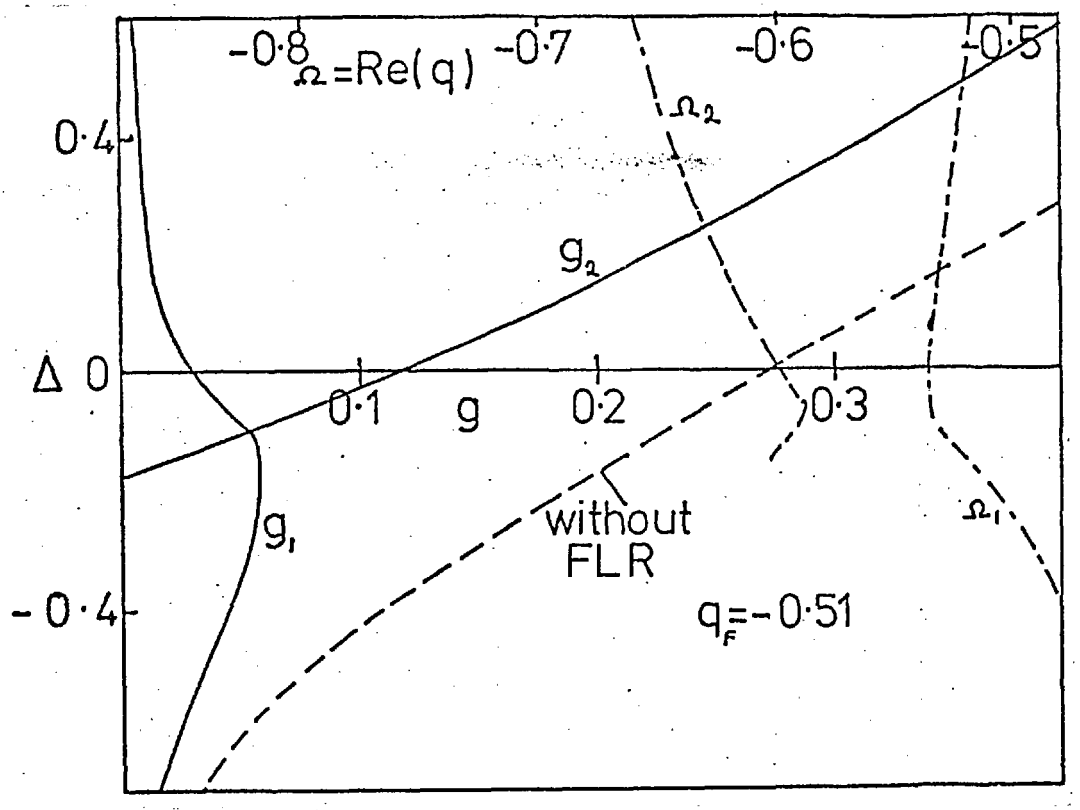

a)

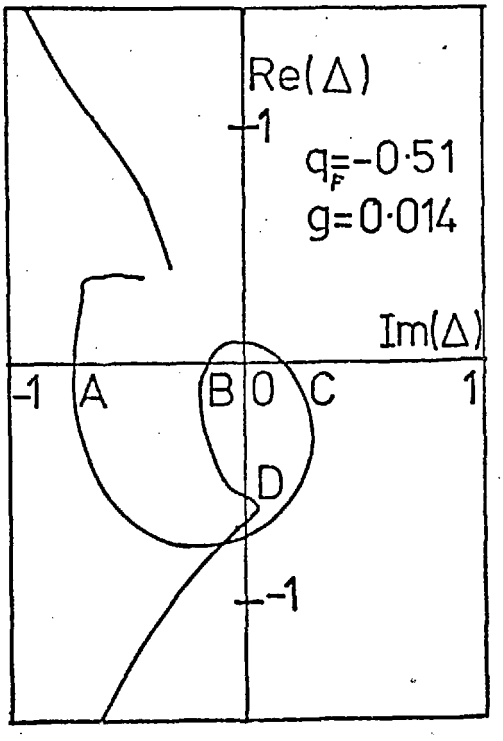

b)

Figure V13 - Instabilities with $|q_F|$ just less than q_{crit}.
B_z= 6T, B_θ= 0.075B_z, n= $10^{21}m^{-3}$, T = 100eV,
r_s= 0.1m, L_p= L_B= L_n= -0.1m.(q_{crit}= 0.46,
Q_R= 4533 s^{-1})
a) $\Delta(g)$ and $\Delta(\Omega)$ for the instabilities found.
b) Nyquist plot with g = 0.014.

crossing points, A, B and C (on figure V12b) as a function of B_θ and of growth rate, g. Clearly, in the present example, as g increases, the loop BC shrinks below the real Δ axis, thus producing the maximum in $g(\Delta)$ for the secondary mode, hence leaving A to continue as the main mode.

Figure V13a shows the case with $B_\theta = 0.075B_z$ for which $|q_F|/q_{crit.} = 1.1$. Note that this reduction in B_θ has passed through the transition region (the transition is at $B_\theta/B_z = 0.094$ and could not be accurately computed). Observe that the peak of the secondary mode occurs at a larger growth rate than in figure V12a. The corresponding Nyquist plot of figure V13b appears similar in form to figure V12b, but, considering V13a, we conclude that, as g rises, the loop AC, rather than BC, rises above the real Δ axis. Since the transition itself must be the limit of the behavior both from above and below, we deduce that this corresponds to the coincidence of A, B and C at the peak of $g(\Delta)$. From figure V14a ($B_\theta = 0.016B_z$, $|q_F| = 3.1q_{crit.}$) we observe that the peak of the secondary mode has moved to lower g and higher Δ so that we may diagrammatically envisage the transition on the $\Delta(g)$ plot as in figure V15:

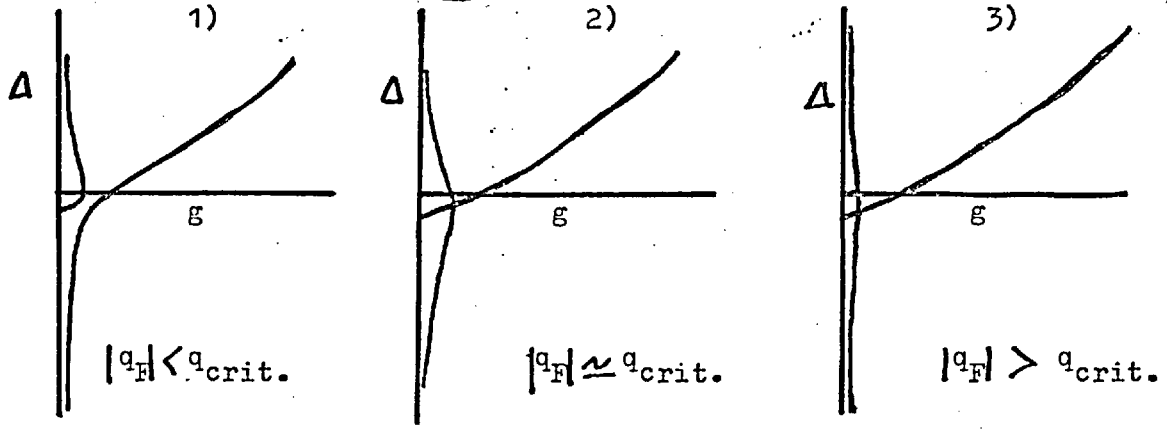

Figure V15 - Sketch showing the transition to large q_F behavior as q_F increases.

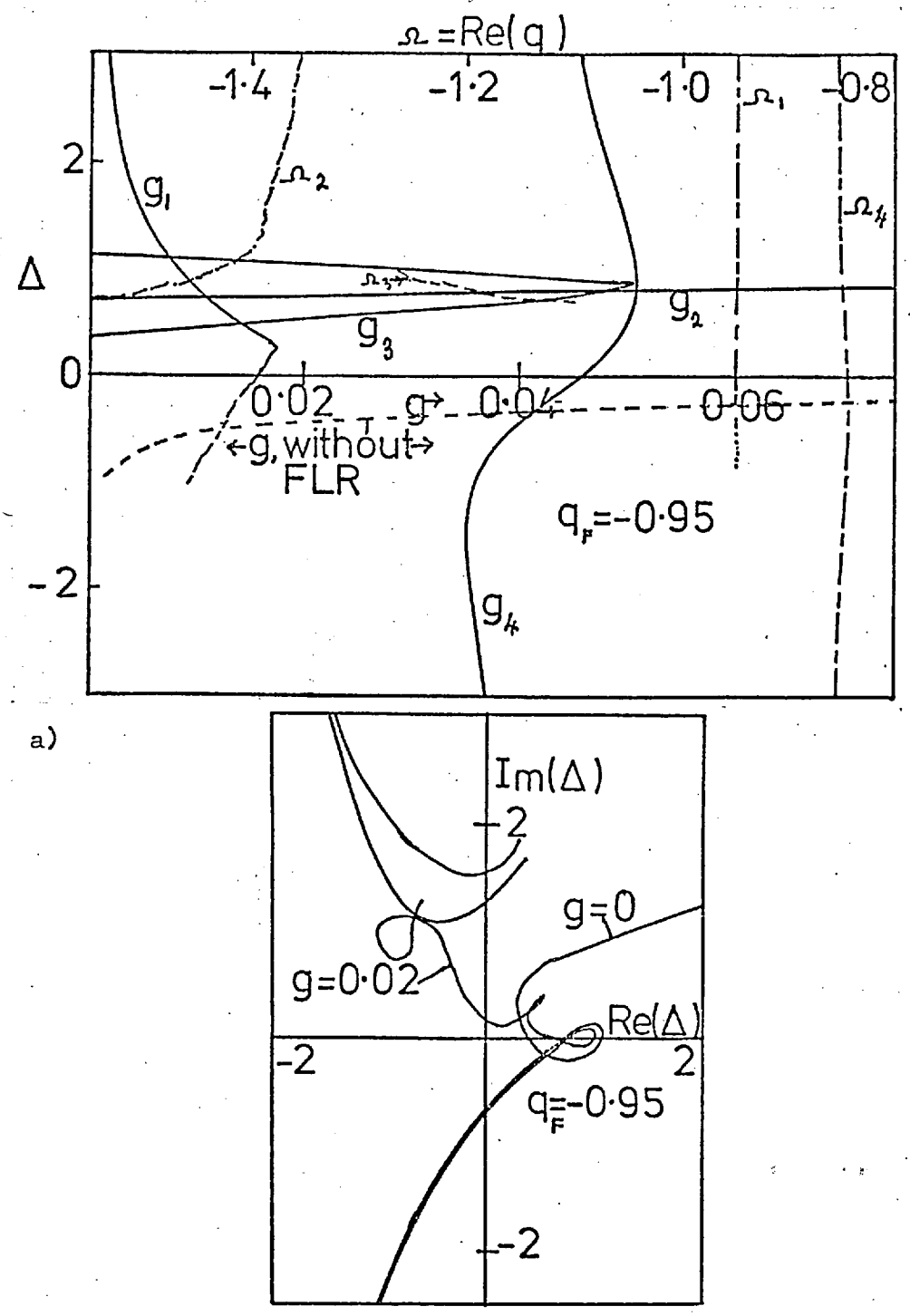

Figure V14 - A case with four types of instability present.
B_z =6T, B_θ= 0.016B_z, n =$10^{21}m^{-3}$, T = 100eV,
r_s=0.1m, L_p=L_B = L_ρ= -0.1m. (Q_R =3522 s^{-1})
a) $\Delta(g)$ and $\Delta(\Omega)$.
b) Nyquist plots.

Note that the coincidence of A, B and C implies that Re(q) for the two modes is also identical at transition. The method of calculation fails to resolve the secondary mode for

$|q_F| \gg q_{crit.}$ and hence this was not seen in figure V4b. In that regime, however, its growth rate is very small.

For $L_p > 0$, no such transition phenomenon occurs, since the tearing mode cuts off at $q_F = 0$. The secondary mode of figure V11a, however, becomes the counterpart of that discussed for $L_p < 0$ as q_F rises and, correspondingly, its maximum growth rate falls.

An interesting feature of figure V14 is the mode occurring over a small range of Δ. (approximately $0.4 < \Delta < 1.1$). On figure V14b this is seen to arise as a loop in the Nyquist plot which lies on the real Δ axis. As q_F is increased, this loop arises from the kink marked D in figure V12b; this feature deforms and passes upwards through the axis. At large q_F, this produces the closed loop corresponding to its positive L_p counterpart shown in the lower right-hand quadrant of figure V7. The manner in which a loop of the kind in figure V7 is present as the remnant of an instability occurring at a different set of parameter values is an important and useful feature in the numerical study of Nyquist plots of this kind; it is the investigation of the behavior of these as parameters were varied that led to the discovery of many of the additional FLR modes in this work. Good examples appear in the $g = 0.02$ curve of figure V14b. Tracing this curve from the lower left-hand quadrant, evidence of all the modes on figure V14a may be found although the curve crosses the real Δ axis only three times. The first crossing is the main tearing mode (2 on V14a) and the second and third correspond to the mode discussed above. (mode 3). After the cusp-like feature, the dip produces mode 1 at lower g and the subsequent loop yields mode 4.

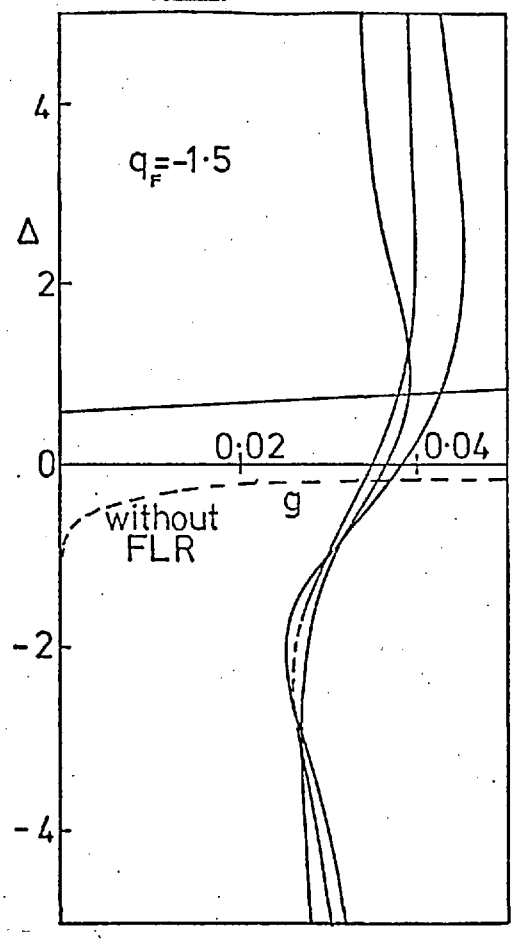

Figure V16 - A collection of 'type 4' instabilities.
B_z = 6T, B_θ= 0.005B_z, r_s= 0.1m, L_p= L_ρ= L_B= -0.1m, n = $10^{21}m^{-3}$, T = 100eV. (Q_R = 2211 s^{-1})

Mode 4 is readily identified as being of the type seen in figure V9; it occurs with $|Re(q)|$ just less than $|q_F|$ and was previously associated with a pole in $\Delta(q)$. A series of computations has revealed the behavior of this mode as a function of B_θ. At low B_θ, as exemplified by the B_θ=0.005B_z case shown in figure V16, a series of three such modes is found; the number increases as B_θ is reduced. Comparison of figure V16 with figure V9 (for whose parameters a similar diagram results for the negative L_p case) indicates that the collection of modes spreads out in g as B_θ is reduced still farther. The variation of the scale frequency with B_θ must always be considered, however. In figures V17 a and b we see the large $|\Delta|$ asymptotic g and the corresponding unnormalised growth rate (in s^{-1}) respectively as functions of B_θ. We see that, for sufficiently large B_θ, the growth rate, although rising

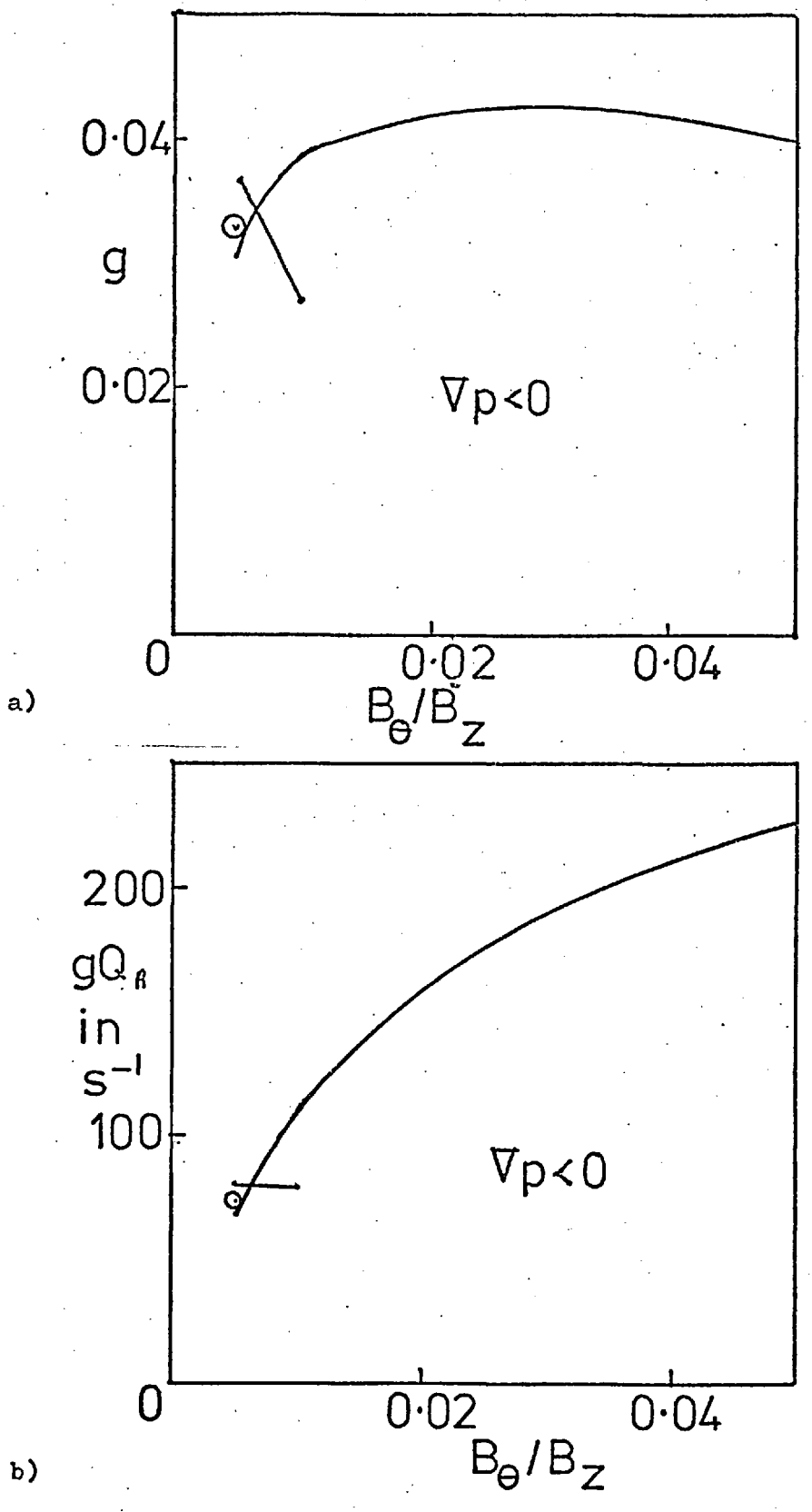

Figure V17 - The variation of a) normalised and b) unnormalised growth rate with B_θ for 'type 4' instabilities. B_z=6T, T=100eV, n= $10^{21}m^{-3}$, $L_p=L_B=L_\rho$= -0.1m, r_s= 0.1m. More than one mode is calculable at low B_θ.

rapidly, does not exceed the rise of Q_R and hence that of the main tearing mode.

Note that, at small B_θ, more than one mode is calculable. On the Nyquist diagram, this is manifested by one or more loops following that found at large B_θ before the calculation finally fails. The curves drawn indicate the behavior of the mode that persists at large B_θ. This mode was clearly identified by the position of its associated loop on the Nyquist plot.

The $B_\theta$dependence of the other modes shown in figure V14a will now be briefly considered. Mode 1 was considered in the discussion of the transition phenomenon where it was shown that g decreased as B_θ was reduced. The main tearing mode is designated mode 2. With B_θ below the transitional value, the cut-off of this mode rises to that shown in figures V7 and V16 as B_θ is reduced. Mode 3 is present as an instability for only a short range of B_θ values for which its loop on the Nyquist diagram (see figure V14b) rises through the real axis. The behavior of this loop indicates an interaction with the cut-off of the main tearing mode. This may be qualitatively understood in terms of figure V18:

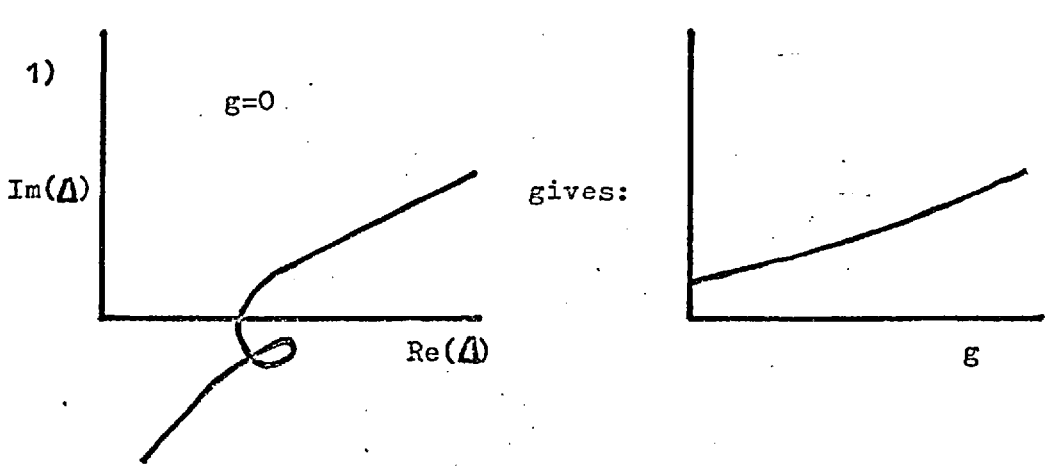

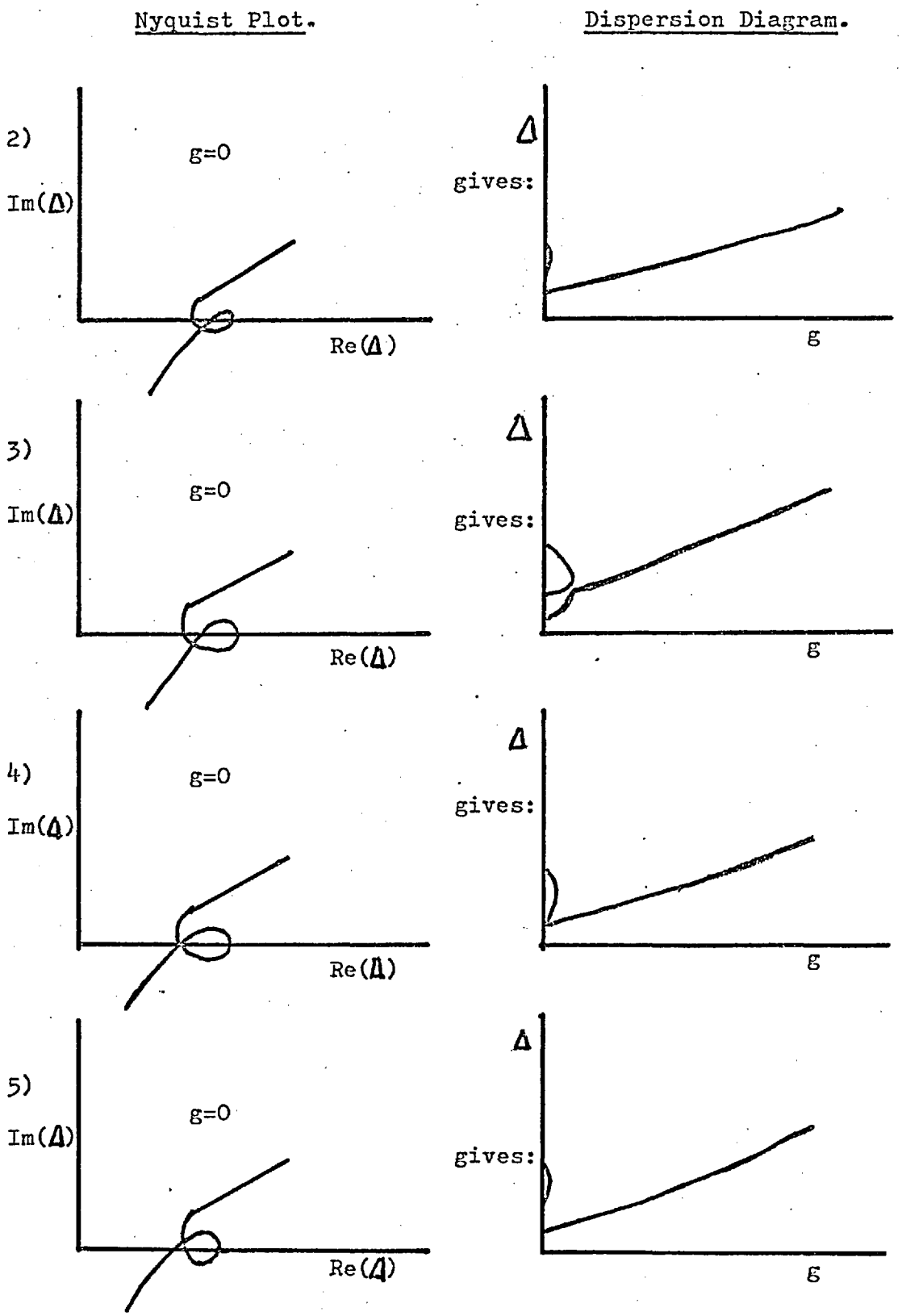

Figure VI8 - Sketch showing the interaction of a 'type 3' mode with the main tearing mode. B_θ falls progressively on passing from 1) to 5).

Stage 3) is analogous to the transition effect discussed earlier. In this case, the definition of main and additional

modes below the maximum of the former becomes indistinct.

The case of positive pressure gradient has less complications than those discussed above for $L_p < 0$; this might be expected upon inspection of figure V11a in which the approach to the $q_F=0$ limit appears self-evident. Modes analogous to types 1,2 and 4 were found upon performing systematic series of computations of the type discussed for the negative pressure gradient case.

Type 1, which was important in the transitional phenomenon, appears to tend to the pressure driven branch of the $q_F=0$ limit:

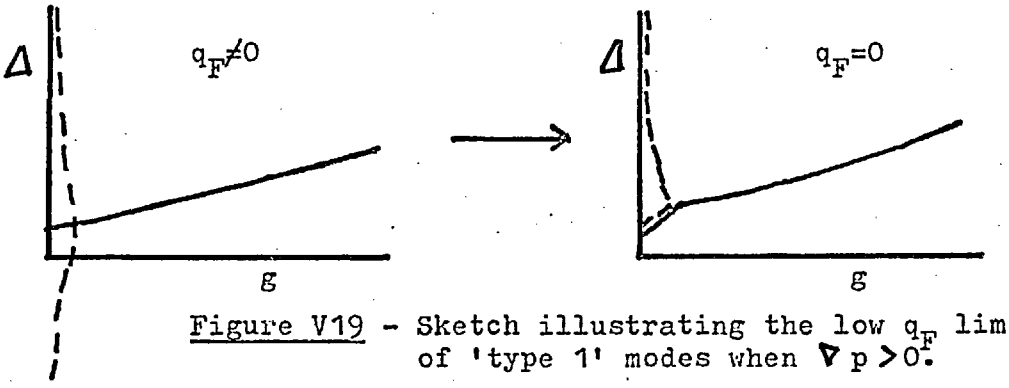

Figure V19 - Sketch illustrating the low q_F limit of 'type 1' modes when $\nabla p > 0$.

As B_θ was reduced, so that q_F rose, the peak g of this mode fell as for the $L_p < 0$ case. This may be seen in figure V20 as far as numerical accuracy allows.

The main tearing mode branch (type 2) moved its cut-off value of Δ only very slightly for a factor of ten reduction in B_θ.

Type three modes did not occur as the requisite loop in the Nyquist plot did not have to cross the real Δ axis to attain its position in figure V7.

Modes of type 4 were evident throughout the B_θ variation, but with growth rates generally less than before. The variation of the large $|\Delta|$ asymptotic growth rate of these is indicated in figure V21; figure V21b takes into account the B_θ dependence

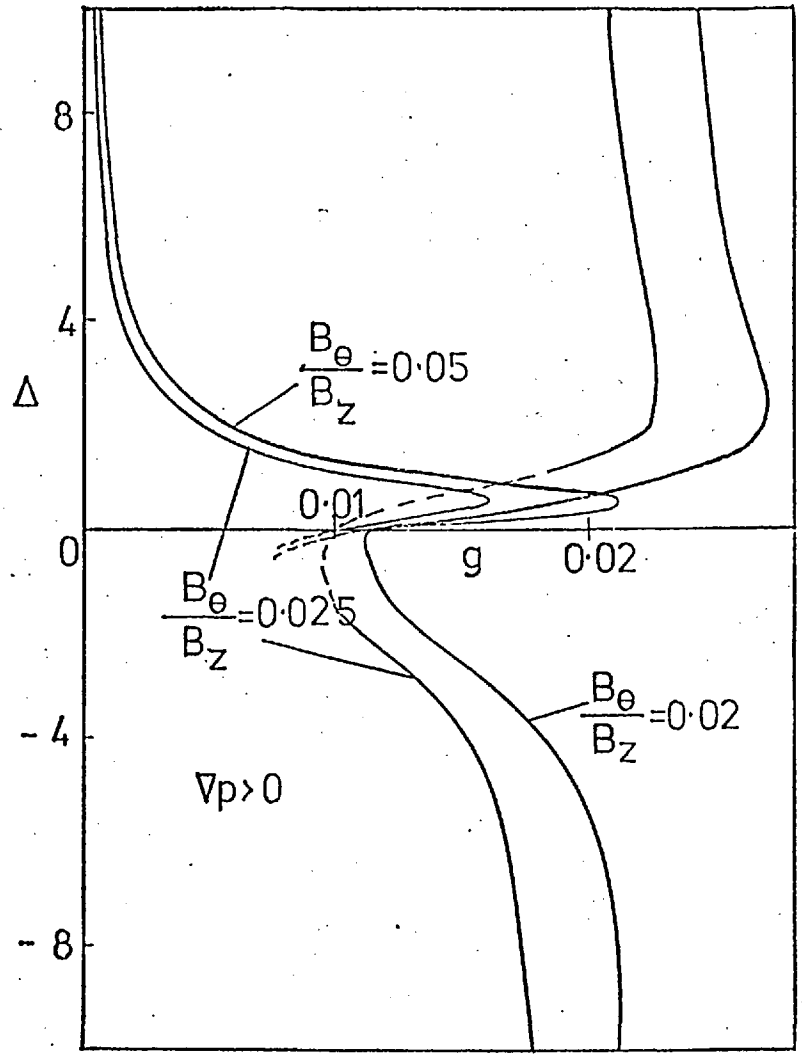

Figure V20 - Supplementary, q_F driven, instabilities with positive pressure gradient. B_z= 6T, T = 100eV, $n = 10^{21} m^{-3}$, $r_s = L_p = L_B = L_\rho$= 0.1m.

of Q_R. Since the growth rates are lower, computational difficulties are more apparent. These modes appear to approach the same low B_θ limit as those in the adverse pressure gradient case, but move to smaller growth rates at larger B_θ. As in the previous case, more than one such mode arises when B_θ is small.

The nature and physical origin of the type 4 modes appears mysterious. They are characterised by their asymptotic approach to a particular growth rate as $\Delta \to \pm\infty$. Thus, except for a region near Δ=0, their growth rate is virtually independent of Δ. These modes occur with an oscillation frequency just less in magnitude than the ion drift frequency (ie. $|\mathrm{Re}(q)| \lesssim |q_F|$).

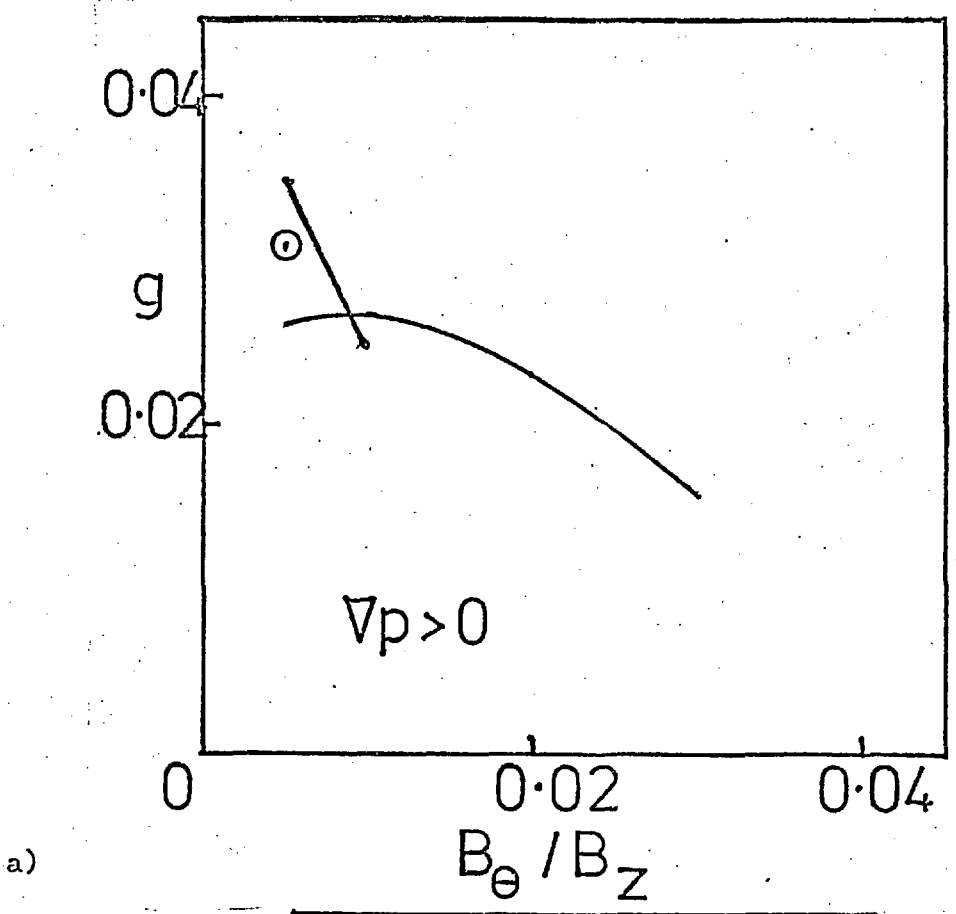

a)

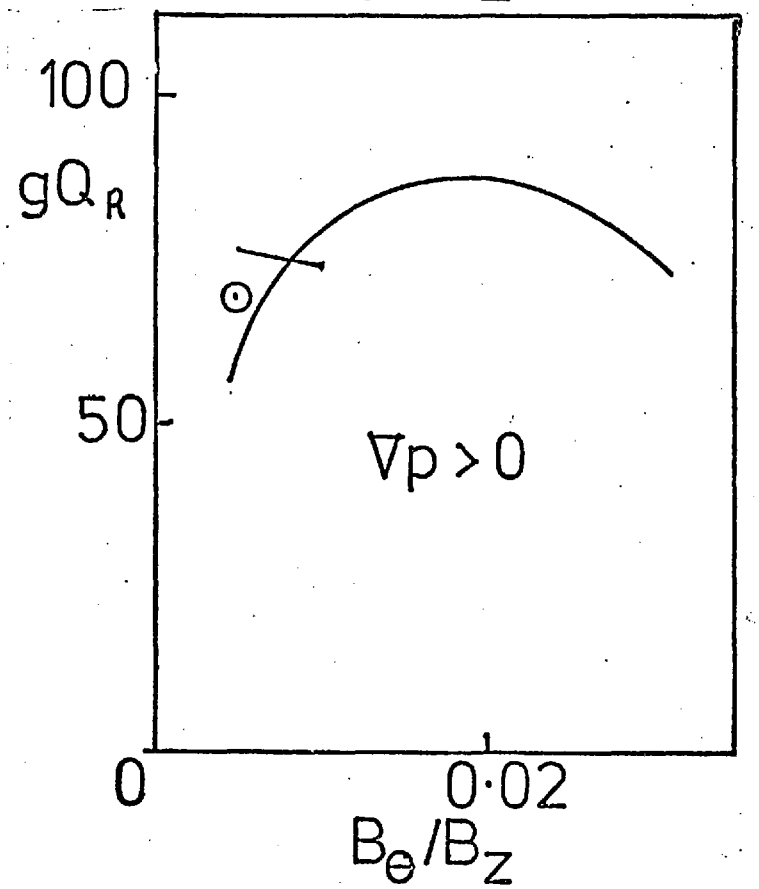

b)

Figure V21 - The variation of a) normalised and b) un-normalised growth rate with B_θ for some 'type 4' instabilities. B_z=6T, T= 100eV, $L_p=L_B=L_\rho=r_s$=0.1m, n = $10^{21}m^{-3}$. More than one mode is calculable at low B_θ.

From the results given above, they have larger growth rate with negative pressure gradient, but this is very much less than than of the main tearing mode except at small positive or at negative Δ .

In order to gain some insight into the cause of type 4 modes, the dependence of their large $|\Delta|$ asymptotic growth rate upon the three important quantities, resistivity (η), FLR (q_F) and plasma pressure (β) was investigated.

Figure V22a portrays the resistive dependence of the asymptotic growth rate with $B_\theta = 0.005 B_z$ and negative pressure gradient. At low B_θ, three modes were calculable, a fourth

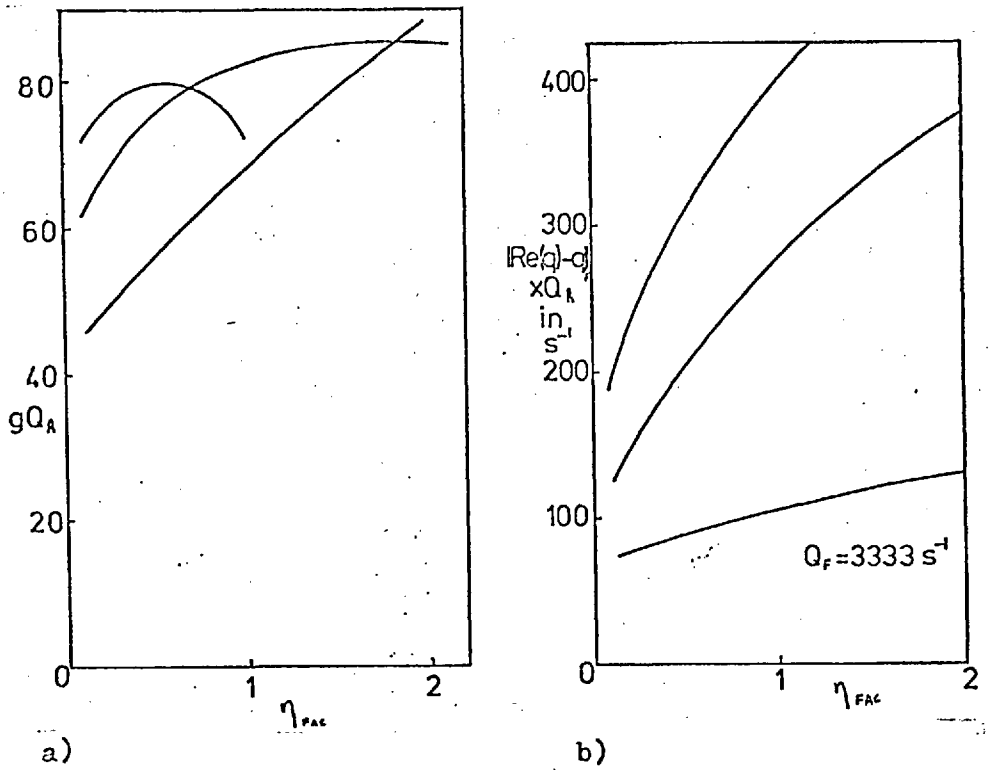

Figure V22 - The result of altering the effect of resistivity on a 'type 4' mode. $\eta = \eta_{Spitzer} \times \eta_{FAC}$. $B_z = 6T$, $B_\theta = 0.005 B_z$, $n = 10^{21} m^{-3}$, $r_s = 0.1m$, $L_p = L_B = L_\rho = -0.1m$.
a) The effect on the unnormalised growth rate.
b) The effect on the oscillation frequency.(Note that changes in frequency are a small fraction of q_F and hence subject to numerical error.)

being just detectable when the resistivity was reduced by a factor of 20. Note that, as resistivity is reduced, there is

first a peak and then a sharp drop in growth rate. The latter indicates that the mode does not exist in the collisionless limit ($\eta = 0$) and has an η^{α} $(0 < \alpha < 1)$ dependence at small resistivity. The small η ends of the curves shown have α in the range $0.05 < \alpha < 0.4$. As α varies amongst the various examples calculated, no precise value can be ascribed to the $\eta \to 0$ limit.

The shape of the $\Delta(g)$ curves also varies systematically as the resistivity is reduced. This may be seen from the following table for modes with $B_\theta = 0.005 B_z$, $n = 10^{21} m^{-3}$, $T = 100eV$, $B_z = 6T$, $L_p = L_B = L_\rho = -0.1m$, $r_s = 0.1m$, $\eta = \eta_{Spitzer} \times \eta_{FAC}$.

Table V3.

η_{FAC}		Q_R s^{-1}	$\delta(g)$	$Q_R \delta(g)$ s^{-1}	$\delta(\Delta)$
2	1	3352	0.01	33.5	2.2
	2		0.018	60.3	2.6
1	1	2211	0.013	28.7	4
	2		0.02	44.2	4.5
	3		0.015	33.1	5
0.5	1	1459	0.014	20.4	6
	2		0.024	35	6
	3		0.02	29	7
0.1	1	556	0.028	15.6	18
	2		0.028	15.6	18
	3		0.027	15.0	23
	4		0.025	13.9	22

$\delta(g)$ and $\delta(\Delta)$ refer to the separation of the two stationary points in $g(\Delta)$ that characterise type 4 modes. Thus, as

resistivity is reduced, the $\Delta(g)$ curve for each mode becomes thinner ($Q_R S(g)$ becomes smaller) in s^{-1} and taller ($\delta(\Delta)$ becomes larger). Hence, in the η =0 limit, it may reasonably be assumed that curves of Δ versus gQ_R (ie. un-normalised growth rate) vanish by collapsing into the Δ axis.

Figure V22b shows the deviation of the real part of the frequency from Q_F as a function of η_{FAC}. The sharp reduction of this quantity as $\eta \to 0$ indicates that in this limit, q approaches q_F. Thus, this implies that the type 4 modes result from a collisionless oscillation destabilised by resistivity.

In figure V23 the calculable dependence of the growth rate at Δ =1 upon FLR is shown for a particular type 4 mode. For this purpose, q_F, calculated from the parameters stated, was multiplied by an arbitrary factor $q_{F_{FAC}}$. Clearly, as $q_{F_{FAC}}$ is reduced, the growth rate of the mode becomes smaller. Reasonable extrapolation implies that the growth rate tends to zero as $q_{F_{FAC}}$ tends to zero.

The beta dependence of another such mode appears in figure V24. For this purpose, beta was reduced by the factor β_{FAC}. Evidently, the existance of type 4 instabilities depends on the inclusion of finite beta effects in the calculation.

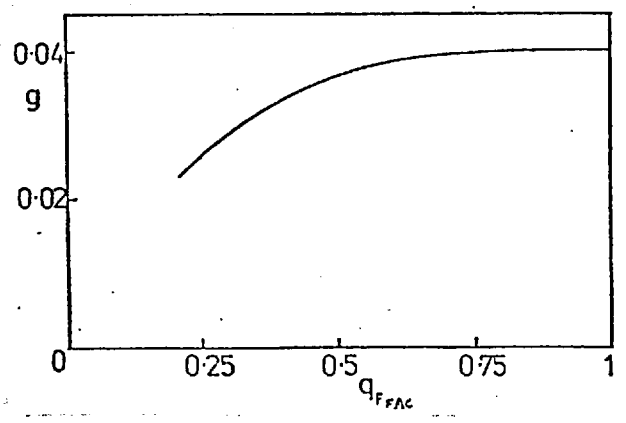

Figure V23 - The result of reducing the effect of FLR on a 'type 4' mode. q_F(used) = q_F(calculated)x$q_{F_{FAC}}$ for the parameters of figure V22.

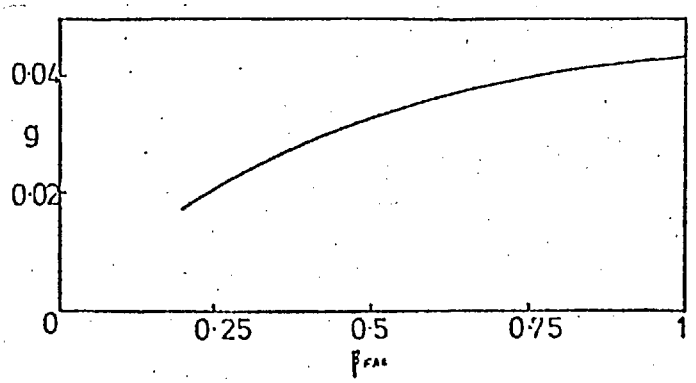

Figure V24 - The result of reducing the effect of beta on a 'type 4' mode. β (used) = β(calculated)xβ_{FAC} for the parameters of figure V22.

13) Discussion and Conclusions.

The numerical analysis has revealed two regimes of the parameter q_F: $q_F \gg q_{crit.}$ and $q_F \lesssim q_{crit.}$ where:

$$q_{crit.} = \left(\frac{2U\gamma\beta}{l^{12}}\right)^{1/3}$$

Removing normalisation, this yields corresponding conditions on Q_F with respect to $Q_{crit.}$ where:

$$Q_{crit.} = q_{crit} Q_R = (2U\gamma\beta W_R W_H^2)^{1/3}$$

Observe that $Q_{crit.}$ has the $\eta^{\frac{1}{3}}$ dependence of the resistive interchange mode. The two regimes can thus be physically identified. In the first ($Q_F \gg Q_{crit.}$), the resistive interchange contribution to the small Δ limit of the tearing mode is totally dominated by the effects of FLR, just as, in the collisionless limit, Suydam modes are stabilised by this effect. Hence, since the interchange driving force derives from adverse pressure gradient, in this limit of large Q_F, the computed results are independent of U and hence of the sign of ∇p. The second regime ($Q_F \lesssim Q_{crit.}$) is characterised by the FLR being inadequate to dominate interchange driving forces. Thus, pressure gradient effects are important and the results appear to merge with published findings (references (50) & (6)) in the q_F=0 limit. The existance of the main tearing mode cut-off associated with the first regime ($Q_F \gg Q_{crit.}$) is thus seen to be independent of beta. Since the pressure gradient effects

are unimportant, the cut-off at $\Delta = 0$ found at $\beta = 0$ by Coppi (31) merely rises to larger Δ, as seen in figure V5, as beta increases.

The study of the transition phenomenon that occurs with negative pressure gradient at small q_F revealed the existance of another mode (type 1) with growth rates that became too small to be detected as q_F became larger. This is the analogue of the resistive interchange branch, is driven principally by pressure gradient effects and was found to exist for larger ranges of Δ when FLR effects were included.

Type 4 instabilities, characterised by an asymptotic growth rate at large $|\Delta|$, were found to pervade both regimes of q_F. They were shown to depend on the simultaneous inclusion of FLR, finite beta and resistivity in the theory. As they occur with $q \simeq q_F$, they may be viewed as arising from the involvement of significant axial velocity perturbation within the theory (see equation V17) since, mathematically, they undoubtedly arise from terms in $\frac{\beta q_E}{(q-q_F)}$ arising in equations V60 and V62. From equation V37 we see that, with $q \simeq q_F$, p becomes large and hence the scale length involved in the expansion becomes small. Although a larger number of terms were required to describe these modes, compared to the main tearing modes, this indicates the existance of considerable spatial oscillation about the resonant surface. Such a behavior, analogous to that of the resistive-g mode (52)., might render important the effects of collisional viscosity due to the possibly severe perturbation derivatives involved; an investigation of this is beyond the scope of the present work as it requires a complete reformulation of the equations. The occurrence of the denominator in $q-q_F$ in equation V37 implies that the type 4 modes might possibly be described

as a form of resistive ion drift instability; the same denominator also suggests, however, that a treatment of the problem from the basis of kinetic equations might produce Landau-type damping of these modes.

The results presented, pertaining to the stabilisation of the main tearing mode, appear encouraging with respect to the relaxation of the constraints on favourable average curvature required in toroidal devices (cf. (50)) . On the comparatively long time scales required for containment, however, the additional modes found on including FLR effects could easily prove dangerous. Although these are reduced in growth rate by choosing favourable pressure gradient, the effect is not so marked as that on the main tearing mode in the absence of FLR. The type 4 modes, in particular, have greater growth rate than the normal resistive interchange branches at small positive or at negative Δ and, if they are not completely stabilised by the possible effects mentioned, could become a source of anxiety in future containment projects.

Chapter VI.

Conclusion.

The collisionless analysis in the first part of this thesis served two purposes. Firstly, the well-known stabilising nature of the diamagnetic FLR terms was illustrated and, in addition, the associated complex eigenfunctions were presented. The detailed manner in which the stabilising gyro-viscous influence interacted with destabilising Hall rotation introduced the possibility of curious effects in the stability of confined plasmas as ion temperature rises with improved technology. Secondly, the influence of the subsidiary FLR terms in the stress tensor, namely sheared axial velocity, Righi-Leduc heat flow and axial heat flux were included in the solutions of the eigenvalue equation presented. The sufficient stability criterion of figure II1 provides a concise display of the manner in which these additional features perturb the stability of localised interchange instabilities. Computational solutions in chapter III displayed the manner in which the dominance of Suydam modes is superceeded by effects due to the additional terms when these are present to sufficiently large magnitude. In particular, 'singular' modes of dubious but arguable character can be produced by large temperature anisotropy, axial heat flux (sheared or unsheared) and sheared axial velocity.

In chapter IV, the numerical study of a low beta resistive system displayed in detail the manner in which the conventional analysis of resistive instabilities breaks down when resistivity becomes too large. The linear growth rate of the tearing mode may not be as large as suspected, on the basis of published analysis, for many confinement systems. Inclusion of FLR is

seen to ripple the eigenfunctions in an alarming way, requiring care to be taken in ensuring that the analysis is consistent when these terms are considered. A peciliar new type of resistive instability, dependent upon FLR for its existance, was also found during these calculations.

The chief result of the arduous analysis of chapter V was that, when the FLR parameter exceeds a critical value, the growth rate of the main tearing mode falls to zero at a finite value of the matching parameter involved in that calculation. This cut-off is insensitive to the local magnetic field pitch $(B_\theta/(rB_z)|$ and also to the sign of the pressure gradient. Configurations, previously thought unstable to the resistive interchange, with small growth rate, may be stabilised by this effect. However, the complexity of the study of FLR phenomena in this limit was illustrated by a collection of additional modes of low growth rate but of dubious reality owing to their questionably short radial scale length.

In general, therefore, the diamagnetic FLR effects tend to have an important stabilising influence on weakly unstable configurations. Care must be taken, however, when relying upon this characteristic, in the consideration of hot plasma stability, to ensure that the less familiar, destabilising aspects of FLR phenomena are not dominant.

References.

1) V.D. Shafranov, Soviet Physics (Technical Physics) 15 175 (1970).

2) B.R. Suydam, Geneva Conference on the Peaceful Uses of Atomic Energy (1958).

3) C. Mercier, Nuclear Fusion 1 47 (1960)

4) C. Mercier, Nuclear Fusion Supplement Part 2 801 (1962).

5) I.B. Bernstein, E.A. Frieman, M.D Kruskal and R.M. Kulsrud, Proc. Roy. Soc. A244 17 (1958).

6) B. Coppi, J.M. Greene and J.L. Johnson, Nuclear Fusion 6 101 (1966).

7) H.P. Furth, J. Killeen and M.N. Rosenbluth, Phys. Fluids 6 459 (1963)

8) B. Lehnert, Plasma Physics 9 301 (1967).

9) W.A. Newcomb, Annals of Physics 10 232 (1960).

10) E.C. Bowers, Thesis, University of London (1969).

11) G.F. Chew, M.L. Goldberger and F.E. Low, Proc. Roy. Soc. A236 112 (1956).

12) W.B. Thompson, Reports on progress in Physics 24 363 (1961)

13) M.N. Rosenbluth, N.A. Krall and N. Rostoker, Nuclear Fusion Supplement Part 1 962 (1962).

14) K.V. Roberts and J.B. Taylor, Phys. Rev. Lett. 8 197 (1962)

15) G. Schmidt, 'Physics of High Temperature Plasmas' Academic Press (1966).

16) F.C. Hoh, Phys. Fluids 6 1359 (1963).

17) M.N. Rosenbluth and A. Simon, Phys. Fluids 8 1300 (1965).

18) L.D. Pearlstein and N.A. Krall, Phys. Fluids 9 2231 (1966).

19) C.F. Kennel and J.M. Greene, Annals of Physics 38 63 (1966).

20) A.A. Ware, Phys. Fluids, 9 816 (1966).

21) R. Herdan and B.S. Liley, Reviews of Modern Physics 32 731 (1960).

22) B.S. Liley, Waikato University Report.

23) R.M. Kulsrud, Phys. Fluids 6 901 (1963).

24) T.E. Stringer, Nuclear Fusion 15 125 (1975).

25) R.J. Hosking, Private Communication.

26) A. Macmahon, Phys. Fluids 8 1840 (1965).

27) E.C. Bowers and M.G. Haines, Phys. Fluids 11 2695 (1968).

28) E.C. Bowers and M.G. Haines, Phys. Fluids 14 165 (1971).

29) E.C. Bowers, Journal of Plasma Physics 6 pt.I 87 (1971).

30) R. J. Wright, D.F.R. Pott and M.G. Haines, Plasma Physics 18 1 (1976).

31) B. Coppi, Phys. Fluids 7 1501 (1964).

32) J.B. Taylor and R.J. Hastie, Plasma Physics 10 479 (1968).

33) J.W. Connor and R.J. Hastie, Plasma Physics 17 97 (1975).

34) H. Melchoir and M. Popovich, Phys. Fluids 11 458 (1968).

35) E.N. Parker, Phys. Rev. 109 1874 (1958).

36) M.N. Rosenbluth, R.Y. Dagazian and P.H. Rutherford Phys. Fluids 16 1894 (1973).

37) Bateman Manuscript Project, 'Higher Transcendental Functions' 1 McGraw Hill (1963).

38) P. Dennery and A. Krzywicki, 'Mathematics for Physicists' Harper and Row (1967).

39) L. Fox and D.M. Mayer, 'Computational Methods for Scientists and Engineers' OUP.

40) J.F. Traub, 'Iterative Methods for the Solution of Equations' Prentice Hall (1964).

41) T.J. Martin, Culham Program Documentation Note CLM-PDN3/71 (1971).

42) J.P. Goedbloed and P.H. Sakanaka, Phys. Fluids 17 908 (1974).

43) B. McNamara, Culham Report CLM-R-48 (1966).

44) A. Sykes and J.A. Wesson, Nuclear Fusion 14 645 (1974).

45) J. Killeen in 'Physics of Hot Plasmas'. ed. Rye and Taylor Oliver and Boyd (1970).

46) A.S. Furzer et al. Reports on VIIth. European Conference on Controlled Fusion and Plasma Physics, Lausanne (1975) 1 114.

47) H.P. Furth, P.H. Rutherford and H. Selberg, Phys. Fluids 16 1054 (1973).

48) J.H. Wilkinson, 'The Algebraic Eigenvalue Problem' OUP.

49) A. Ralston, 'A First Course in Numerical Analysis' McGraw Hill.

50) A.H. Glasser, J.M. Greene and J.L. Johnson, Phys. Fluids 18 875 (1975).

51) J.L. Johnson, J.M. Greene and B. Coppi, Phys Fluids 6 1169 (1963).

52) E.A. Frieman and K. Weimer, Plasma Physics and Controlled Nuclear Fusion Research IAEA, Vienna (1966) 1 595.

53) G.M. Marinoff, Journal of Plasma Physics 11 pt.II 253 (1974).

54) J.M. Greene and J.L. Johnson, Plasma Physics 10 729 (1968).

55) R.J. Hosking and G.M. Marinoff, Plasma Physics 15 327 (1973).

56) J.L. Johnson and J.M. Greene, Plasma Physics 9 611 (1967).

57) J.D. Jukes, Reports on Progress in Physics 30 333 (1967).

58) P.M. Morse and H. Feshbach;'Methods of Theoretical Physics' McGraw Hill.

59) O. Klüber, VIIth. European Conference on Controlled Fusion and Plasma Physics, Lausanne (1975) 2 50 (1976).

60) J. Wesson, Nuclear Fusion 16 130 (1966).

Appendix A.

Pott's Derivation of the Collisionless Eigenvalue Equation.

The derivation begins with the Vlasov equation for a species of particles of charge q and mass M :

$$\frac{\partial f}{\partial t} + \underset{\sim}{v}\cdot\underset{\sim}{\nabla} f + \frac{q}{M}\left(\underset{\sim}{E} + \underset{\sim}{v}\times\underset{\sim}{B}\right)\cdot\underset{\sim}{\nabla}_{v} f = 0 \qquad \text{A1}$$

This is expressed in cylindrical coordinates in both configuration and velocity space, using:

$$v_r = v_\perp \cos\alpha\,, \quad v_\theta = v_\perp \sin\alpha\,, \quad v_z = v_z$$

α is thus the gyrophase angle to the order of the calculations. (see equation I4).

The result is expanded in ε using the ordering assumptions I1 to I5 of chapter I.

To zero order:

$$\frac{\partial f_0}{\partial \alpha} = 0 \qquad \text{A2}$$

This indicates symmetry in velocity space about the magnetic field direction in lowest order.

1st order:

$$f_1 = f_{10} + 2f_{11}^R \cos\alpha - 2f_{11}^I \sin\alpha \qquad \text{A3}$$

$$2f_{11}^R = -\left[\frac{v_\perp}{\Omega r}\frac{\partial f_0}{\partial \theta} + \frac{E_{\theta 1}}{B_{z0}}\frac{\partial f_0}{\partial v_\perp} + \frac{B_{r1}}{B_{z0}}\left(v_z\frac{\partial f_0}{\partial v_\perp} - v_\perp\frac{\partial f_0}{\partial v_z}\right)\right]$$

$$2f_{11}^I = -\left[\frac{v_\perp}{\Omega}\frac{\partial f_0}{\partial r} + \frac{E_{r1}}{B_{z0}}\frac{\partial f_0}{\partial v_\perp} - \frac{B_{\theta 1}}{B_{z0}}\left(v_z\frac{\partial f_0}{\partial v_\perp} - v_\perp\frac{\partial f_0}{\partial v_z}\right)\right]$$

where Ω(the gyrofrequency)$= \frac{q B_{z0}}{M}$

2nd order:

$$f_2 = f_{20} + 2f_{21}^R\cos\alpha - 2f_{21}^I\sin\alpha + 2f_{22}^R\cos 2\alpha - 2f_{22}^I\sin 2\alpha \qquad \text{A4}$$

$$\frac{\partial f_0}{\partial t} + v_z\frac{\partial f_0}{\partial z} + \Omega\frac{E_{z2}}{B_{z0}}\frac{\partial f_0}{\partial v_z} + \qquad \text{A5}$$

$$\left[v_\perp\left(\frac{\partial}{\partial r} + \frac{1}{r}\right) + \frac{\Omega E_{r1}}{B_{z0}}\left(\frac{\partial}{\partial v_\perp} + \frac{1}{v_\perp}\right) + \frac{\Omega B_{\theta 1}}{B_{z0}}\left(v_\perp\frac{\partial}{\partial v_z} - v_z\left(\frac{\partial}{\partial v_\perp} + \frac{1}{v_\perp}\right)\right)\right] f_{11}^R$$

$$-\left[\frac{v_\perp}{r}\frac{\partial}{\partial\theta} + \frac{\Omega E_{\theta 1}}{B_{z0}}\left(\frac{\partial}{\partial v_\perp} + \frac{1}{v_\perp}\right) - \frac{\Omega B_{r1}}{B_{z0}}\left(v_\perp\frac{\partial}{\partial v_z} - v_z\left(\frac{\partial}{\partial v_\perp} + \frac{1}{v_\perp}\right)\right)\right] f_{11}^I = 0$$

$$4f_{22}^{R} = \left[\frac{v_\perp}{\Omega}\left(\frac{\partial}{\partial r} - \frac{1}{r}\right) + \frac{E_{r_1}}{B_{z0}}\left(\frac{\partial}{\partial v_\perp} - \frac{1}{v_\perp}\right) + \frac{B_{\theta_1}}{B_{z0}}\left(v_\perp \frac{\partial}{\partial v_z} - v_z\left(\frac{\partial}{\partial v_\perp} - \frac{1}{v_\perp}\right)\right)\right] f_{11}^{I}$$

$$-\left[\frac{v_\perp}{\Omega r}\frac{\partial}{\partial \theta} + \frac{E_{\theta_1}}{B_{z0}}\left(\frac{\partial}{\partial v_\perp} - \frac{1}{v_\perp}\right) - \frac{B_{r_1}}{B_{z0}}\left(v_\perp \frac{\partial}{\partial v_z} - v_z\left(\frac{\partial}{\partial v_\perp} - \frac{1}{v_\perp}\right)\right)\right] f_{11}^{R}$$

$$4f_{22}^{I} = -\left[\frac{v_\perp}{\Omega}\left(\frac{\partial}{\partial r} - \frac{1}{r}\right) + \frac{E_{r_1}}{B_{z0}}\left(\frac{\partial}{\partial v_\perp} - \frac{1}{v_\perp}\right) + \frac{B_{\theta_1}}{B_{z0}}\left(v_\perp \frac{\partial}{\partial v_z} - v_z\left(\frac{\partial}{\partial v_\perp} - \frac{1}{v_\perp}\right)\right)\right] f_{11}^{R}$$

$$-\left[\frac{v_\perp}{\Omega r}\frac{\partial}{\partial \theta} + \frac{E_{\theta_1}}{B_{z0}}\left(\frac{\partial}{\partial v_\perp} - \frac{1}{v_\perp}\right) - \frac{B_{r_1}}{B_{z0}}\left(v_\perp \frac{\partial}{\partial v_z} - v_z\left(\frac{\partial}{\partial v_\perp} - \frac{1}{v_\perp}\right)\right)\right] f_{11}^{I}$$

Taking the appropriate moments of f_{21}^{R}, f_{21}^{I}, f_{22}^{R} & f_{22}^{I} yields expressions for u_r, u_θ (ie. perpendicular components of Ohm's law), the relevant components of the stress tensor and for the flux of the energy of gyration, q_r, q_θ :

$$u_{r_1} = -\frac{1}{\rho_0 \Omega r}\frac{\partial P_{\perp 0}}{\partial \theta} + \frac{E_{\theta_1}}{B_{z0}} + \frac{B_{r_1} u_{z0}}{B_{z0}} \qquad \text{A6}$$

$$u_{\theta_1} = \frac{1}{\rho_0 \Omega}\frac{\partial P_{\perp 0}}{\partial r} - \frac{E_{r_1}}{B_{z0}} + \frac{B_{\theta_1} u_{z0}}{B_{z0}} \qquad \text{A7}$$

$$q_{\theta_1}^{\perp} = \frac{1}{\Omega}\frac{\partial R_{\perp 0}}{\partial r} - \frac{2P_{\perp 0}}{\Omega \rho_0}\frac{\partial P_{\perp 0}}{\partial r} + 2\frac{B_{\theta_1}}{B_{z0}} q_{z0}^{\perp} \qquad \text{A8}$$

$$q_{r_1}^{\perp} = -\frac{1}{\Omega r}\frac{\partial R_{\perp 0}}{\partial \theta} + \frac{2P_{\perp 0}}{\Omega \rho_0 r}\frac{\partial P_{\perp 0}}{\partial \theta} + 2\frac{B_{r_1}}{B_{z0}} q_{z0}^{\perp} \qquad \text{A9}$$

where $$R_{\perp 0} = \frac{\pi M}{2}\int_{-\infty}^{\infty}\int_{0}^{\infty} v_\perp^5 f_0 \, dv_\perp \, dv_z$$

A reasonable estimate of $R_{\perp 0}$ may be obtained (see ref.(10)) by taking f_0 to be double Maxwellian.

This gives:

$$q_{\theta_1}^{\perp} = \frac{2P_{\perp 0}}{\Omega}\frac{\partial}{\partial r}\left(\frac{P_{\perp 0}}{\rho_0}\right) + \frac{2B_{\theta_1}}{B_{z0}} q_{z0}^{\perp} \qquad \text{A10}$$

$$q_{r_1}^{\perp} = -\frac{2P_{\perp 0}}{\Omega r}\frac{\partial}{\partial \theta}\left(\frac{P_{\perp 0}}{\rho_0}\right) + \frac{2B_{r_1}}{B_{z0}} q_{z0}^{\perp} \qquad \text{A11}$$

Denoting the traceless stress tensor by $\underline{\underline{\tau}}$,

$$\tau_{rr_2} = \frac{1}{4\Omega}\left(\frac{q^1_{\theta_1}}{r} - \frac{\partial q^1_{\theta_1}}{\partial r} - \frac{1}{r}\frac{\partial q^1_{r_1}}{\partial \theta}\right) \qquad \text{A12}$$

$$+\frac{P_{\perp 0}}{2\Omega}\left(\frac{u_{\theta_1}}{r} - \frac{\partial u_{\theta_1}}{\partial r} - \frac{1}{r}\frac{\partial u_{r_1}}{\partial \theta}\right)$$

$$+\frac{B_{r_1}}{2B_{z0}}\tau_{rz_1} - \frac{B_{\theta_1}}{2B_{z0}}\tau_{\theta z_1}$$

$$\tau_{\theta\theta_2} = -\tau_{rr_2} \qquad \text{A13}$$

$$\tau_{r\theta_2} = \frac{1}{4\Omega}\left(\frac{\partial q^1_{r_1}}{\partial r} - \frac{q^1_{r_1}}{r} - \frac{1}{r}\frac{\partial q^1_{\theta_1}}{\partial \theta}\right) \qquad \text{A14}$$

$$+\frac{P_{\perp 0}}{2\Omega}\left(\frac{\partial u_{r_1}}{\partial r} - \frac{u_{r_1}}{r} - \frac{1}{r}\frac{\partial u_{\theta_1}}{\partial \theta}\right)$$

$$+\frac{B_{\theta_1}}{2B_{z0}}\tau_{rz_1} + \frac{B_{r_1}}{2B_{z0}}\tau_{\theta z_1}$$

$$\tau_{rz_1} = -\frac{1}{\Omega r}\frac{\partial}{\partial \theta} q^1_{z0} - \frac{P_{\perp 0}}{\Omega r}\frac{\partial u_{z0}}{\partial \theta} + \frac{B_{r_1}}{B_{z0}}(P_{\parallel 0} - P_{\perp 0}) \qquad \text{A15}$$

$$\tau_{\theta z_1} = \frac{1}{\Omega}\frac{\partial}{\partial r} q^1_{z0} + \frac{P_{\perp 0}}{\Omega}\frac{\partial u_{z0}}{\partial r} + \frac{B_{\theta_1}}{B_{z0}}(P_{\parallel 0} - P_{\perp 0}) \qquad \text{A16}$$

Next take perturbations of the lowest order distribution function: $f_0' = f_0'(r, v_\perp, v_z)\exp[i(\omega t + m\theta + kz)]$

Equation A5 may then be rearranged to yield:

$$f_0' = \frac{B_{z0}}{dB_{z0}/dr}\frac{\partial f_0}{\partial r} \qquad \text{A17}$$

$$-\frac{i\Omega r}{B_{z0} m}\frac{\partial f_0}{\partial v_z}\left(B_{r_1}' + \frac{i\bar{k} B_{z0} B_{z0}'}{dB_{z0}/dr}\right)$$

$$+i\left[v_z\left(B_{r_1}' + \frac{i\bar{k} B_{z0} B_{z0}'}{dB_{z0}/dr}\right) + \frac{i\bar{\omega} B_{z0} B_{z0}'}{dB_{z0}/dr} + E_{\theta_1}'\right]\cdot$$

$$\cdot\left[\frac{1}{B_{z0}}\frac{\partial f_0}{\partial r} + \frac{1}{2B_{z0}^2}\frac{dB_{z0}}{dr} v_\perp \frac{\partial f_0}{\partial v_\perp} + \frac{\bar{k} r}{m}\frac{\Omega}{B_{z0}}\frac{\partial f_0}{\partial v_z}\right]$$

$$\bar{k} v_z + \bar{\omega} + \frac{m v_\perp^2}{2\Omega r B_{z0}}\frac{dB_{z0}}{dr}$$

where: $\bar{k} = k + m\frac{B_{\theta_1}}{rB_{z0}}$; $\bar{\omega} = \omega + \frac{mE_{r_1}}{rB_{z0}}$

To lowest order in ε, $j'_{z0} = 0 = \sigma'_0$. Thus, taking the appropriate moments of A17 and summing over species yields:

$$\sigma'_0 = 0 = \left(B_{r_1}' + \frac{i\bar{k}B_{z0}B'_{z0}}{dB_{z0}/dr}\right)I_1 + \left(E'_{\theta_1} + \frac{i\bar{\omega}B_{z0}B'_{z0}}{dB_{z0}/dr}\right)I_2 \quad \text{A18}$$

$$j'_{z0} = 0 = \left(B_{r_1}' + \frac{i\bar{k}B_{z0}B'_{z0}}{dB_{z0}/dr}\right)I_3 + \left(E'_{\theta_1} + \frac{i\bar{\omega}B_{z0}B'_{z0}}{dB_{z0}/dr}\right)I_1 \quad \text{A19}$$

Here, I_1, I_2 and I_3 are integrals involving the resonant denominator present in the last part of equation A17. These correspond to those of Bowers (10,20) with $\bar{k}$ replacing k in that work.

The vanishing of the determinant of equations A18 and A19 yields the localised dispersion law for microscopic modes discussed by Bowers (10,28):

$$I_1^2 = I_2 I_3 \quad \text{A20}$$

Macroscopic modes, considered in this work, are produced by the solution:

$$B_{r_1}' + \frac{i\bar{k}B_{z0}B'_{z0}}{dB_{z0}/dr} = 0 = E'_{\theta_1} + \frac{i\bar{\omega}B_{z0}B'_{z0}}{dB_{z0}/dr} \quad \text{A21}$$

so that:

$$\bar{\omega}B_{r_1}' - \bar{k}E'_{\theta_1} = 0 \quad ; \quad B'_{z0} = \frac{iB'_{r_1}}{\bar{k}}\frac{dB_{z0}}{dr} \quad \text{A22}$$

Expanding A22 and using the induction equation,

$$-\omega B'_{r_1} = \frac{m}{r}E'_{z_2} - kE'_{\theta_1}$$

yields:

$$(\underline{E}\cdot\underline{B})' = 0 \quad \text{A23}$$

a familiar result of collisionless theory.

Substituting A21 into A17 yields:

$$f_0' = i\frac{B'_{r_1}}{\bar{k}}\frac{\partial f_0}{\partial r} \quad \text{A24}$$

Hence:

$$\rho'_0 = \frac{iB'_{r_1}}{\bar{k}}\frac{d\rho}{dr}\,; P'_{\perp 0} = \frac{iB'_{r_1}}{\bar{k}}\frac{dP_{\perp 0}}{dr}\,; q'_{z0} = \frac{iB'_{r_1}}{\bar{k}}\frac{dq_{\perp z0}}{dr} \quad \text{A25}$$

$$u'_{z0} = i\frac{B'_{r1}}{\bar{k}}\frac{du_{z0}}{dr} \quad ; \quad R'_{\perp 0} = i\frac{B'_{r1}}{\bar{k}}\frac{dR_{\perp 0}}{dr} \qquad \text{A25 (contd.)}$$

The density perturbation implies:

$$(\nabla . u') = 0 \qquad \text{A26}$$

Substitution of these perturbed quantities into A6 yields:

$$\xi = \frac{u'_{r1}}{\omega_1} = \frac{B'_{r1}}{\bar{k}} \qquad \text{A27}$$

where $\omega_1 = \omega + \frac{m u_\theta}{r} + k u_z$

A26 yields:

$$u'_{\theta 1} = \frac{i}{m}\frac{d}{dr}(r\omega_1\xi) - i\frac{kr}{m}\xi\frac{du_z}{dr} \qquad \text{A28}$$

Manipulation of equations A8 and A9 using the expression for $q^{\perp}_{z0}{}'$ yields:

$$q^{\perp\,\prime}_{r_1} = \left(\frac{m q^{\perp}_{\theta 1}}{r} + 2k q^{\perp}_{z0}\right)\xi \qquad \text{A29}$$

$$q^{\perp\,\prime}_{\theta 1} = \frac{d}{dr}\left[i\xi q^{\perp}_{\theta 1}\right] + \frac{2i}{m} q^{\perp}_{z0}\frac{d}{dr}(kr\xi) \qquad \text{A30}$$

In addition, $\nabla . B = 0$ yields:

$$B'_{\theta 1} = \frac{i}{m}\frac{d}{dr}(\bar{k} B_z r\xi) - i\frac{kr}{m}\xi\frac{dB_{z0}}{dr} \qquad \text{A31}$$

Substitution of A22 to A31 into the r and θ components of the perturbed momentum equation followed by elimination of the high order pressure terms, corresponding to equation I10, between the two resulting relationships eventually leads to the collisionless eigenvalue equation, I11, in the text of chapter I.

Appendix B.

The Resistive Interchange Ordering.

The FLR expansion produced equations V10, V12, V14, V17 and V20. Coppi, Greene and Johnson (6) outline the ordering scheme appropriate to the resistive interchange mode which, together with $\omega \sim \frac{1}{2\rho\Omega r}\frac{dp}{dr}$ may be applied to the above mentioned equations.

The ordering may be summarised as:

$$\frac{W_R}{W_H} \sim \phi^3, \quad \frac{Q_F}{W_H} \sim \frac{\omega}{W_H} \sim \phi, \quad \frac{r-r_s}{r_s} \sim \phi, \quad \beta \sim \phi^0 \qquad \text{B1}$$

with the frequencies as defined previously.

Define in addition:

$$L_R^I = r_s \left(\frac{W_R}{W_H}\right)^{1/3}$$

$$Q_R^I = (W_H^2 W_R)^{1/3}$$

Redefine:

$$q = \omega / Q_R^I$$

$$q_F = Q_F / Q_R^I$$

$$X = (r-r_s)/L_R^I$$

$$Z = \frac{2}{r_s^2}\frac{B_z'}{B_z}\left(\frac{mB_\theta/rB_z}{\alpha}\right)^2$$

$$R = \frac{B_r'}{B_z L_R^I \alpha r_s}$$

Application of the above ordering scheme (B1) to the requisite equations, followed by substitution of u_z' and $(\underline{\nabla}.\underline{u})'$ and transformation to variables D, Z, R and X yields three simultaneous linear second order differential equations for D, Z and R:

$$R'' = iR(q-2q_F) - iXqD - \frac{2zX}{u}q_F \qquad \text{B2}$$

$$iz'' = -R\left[\frac{xu}{i(q-q_F(1+\beta/2))}\right] + Du\left[-iq - \frac{2i}{\gamma\beta}(q+C_L q_F)\right] \qquad B3$$

$$+iz\left[\frac{x^2}{i(q-q_F(1+\beta/2))} + iq + \frac{2i}{\gamma\beta}(q+C_L q_F)\right]$$

$$D''_q\left(q - q_F(1+\beta/2 - \tfrac{1}{2}\gamma)\right) \qquad B4$$

$$+\frac{R}{(q-q_F(1+\beta/2))}\left[\frac{\beta}{4}x^3\frac{q_F}{i(q-q_F(1+\beta/2))}\right.$$

$$\left.+ix\left(-q_F^2\left(\frac{3\beta}{2}+2\right) - q^2 + qq_F\left(3+\frac{3\beta}{4}-\frac{1}{2\gamma}\right)\right)\right]$$

$$+D\left[\frac{ix^2}{(q-q_F(1+\beta/2))}\left(\frac{C_L q_F^2}{2\gamma} + q^2 - \frac{qq_F}{2}\left(2+\beta-\frac{1}{\gamma}\right)\right)\right.$$

$$\left.+\frac{iqq_F}{\gamma}\left(\frac{q}{2}+\frac{1}{\gamma\beta}(q+C_L q_F)\right) - \frac{i\beta q_F}{4u(q-q_F(1+\beta/2))}\right]$$

$$+iz\left[\frac{-x^4\beta q_F}{4iu(q-q_F(1+\beta/2))^2} + \frac{ix^2}{u(q-q_F(1+\beta/2))}\left(q_F^2\left(2+\frac{3\beta}{2}-\frac{C_L}{2\gamma}\right)\right.\right.$$

$$\left.\left.-qq_F\left(2+\frac{\beta}{4}\right)\right) + \frac{iqq_F}{\gamma u}\left(-\frac{q_F}{2} - \frac{1}{\gamma\beta}(q+C_L q_F)\right) + 1\right]$$

$$\frac{+\beta q_F}{4(q-q_F(1+\beta/2))}\left(R' - \frac{3ixz'}{u}\right) = 0$$

These equations thus define the 'inner' region solution. As they are a sixth order set, their asymptotic (large X) solutions are found to consist of a pair of solutions that match the 'outer' region, a pair of exponentially decaying solutions and a pair exponentially increasing. Numerical solution of B2 to B4 must, therefore, by iteration, choose initial conditions at X=0 such that the two exponentially rising solutions play no part. As matching conditions at large X are required, this is a formidable task. The paper

of Coppi et al.(6) only succeeded in computing a fourth order set of equations (with one exponentially rising solution) in the q_F=0 limit. Including FLR introduces severe spatial oscillations to the solution and hence increases computational difficulty. I do not therefore consider that the numerical determination of matching conditions from B2 to B4 is a feasible proposition.

Plasma Physics, Vol. 18, pp. 1 to 26. Pergamon Press 1976. Printed in Northern Ireland

STABILITY CONSIDERATIONS OF A HOT CYLINDRICAL PINCH

R. J. WRIGHT, D. F. R. POTT and M. G. HAINES

Physics Department, Imperial College, London SW7 2AZ, England

(*Received* 15 *April* 1975)

Abstract—An expansion of the Vlasov equation in the finite Larmor radius limit at high β leads to a differential dispersion equation which involves the less familiar physics associated with anisotropic pressure, rotation, sheared flow and heat fluxes. The stability is studied analytically and computationally; in particular the modification of Suydam modes by finite ion Larmor radius and the above effects is pursued.

1. INTRODUCTION

THE GENERAL assertion of the stabilising nature of ion gyro radius effects (FLR) upon weakly unstable fluid-like perturbations in collisionless plasmas has long been upheld (LEHNERT, 1967). Copious literature upon this subject is available (ROSENBLUTH and SIMON, 1965), (KENNEL and GREENE, 1966), (BOWERS, 1971). Detailed study of the dependence of the modes upon the many types of equilibria embraced by such theory has, however, rarely been performed. In particular there is a need to carefully distinguish the effects of FLR, diamagnetism, and rotation on stability. Considering an equilibrium with a straight magnetic field, BOWERS and HAINES (1971) developed the FLR theory of the high-beta theta-pinch and investigated computationally the effect of plasma rotation upon growth rate in a number of cases using the differential dispersion relation produced by their analysis. STRINGER (1975), using an approach based upon guiding-centre equations, investigated the effect of FLR upon interchange (Suydam) modes associated with the singularities in MHD equations at $(\mathbf{k} \cdot \mathbf{B}) = 0$ (resonant or singular surface). Such theory can be improved by beginning on the firmer basis of a strict ordering procedure applied *ab initio* to all variables so that its validity and limitations are made apparent. The purpose of this work is to develop on the lines of BOWERS and HAINES (1971), i.e. from the Vlasov equation, a differential dispersion equation based upon the cylindrical equilibrium of a system with a curved magnetic field. The differential quadratic eigenvalue problem is then solved by two separate methods to illustrate the connection with STRINGER's (1975) localized mode theory and with the computational results of Bowers. In this manner, the less familiar physics associated with temperature anisotropy, heat fluxes, sheared flow and rotation may be investigated and their influence on plasma stability in general and interchange modes in particular be illustrated.

The relevance of the ion gyroradius a^i to controlled thermonuclear fusion research is twofold. Firstly most configurations under consideration are close to the margin of stability causing a sensitivity to weak phenomena. Secondly, as one reaches fusion conditions, if the containment time τ is approximately $\sigma B^2 L_\perp{}^2 / AnK(T_e + T_i)$ with $A \geqslant 1$ then $a^{i2}/L_\perp{}^2$ is of the order of $\sigma M_i / Ae^2 n\tau$ which for D—T conditions gives $a^i/L_\perp \sim 1/\sqrt{A}$. Neoclassical thermal conduction and diffusion could make $a^i/L_\perp \sim 10^{-2}$ to 10^{-1}.

In Section 2 we discuss the details of the ordering procedure used so that those classes of equilibria included within the theory may be defined. Section 3 is concerned with the production of the differential eigenvalue equation itself using the collisionless Vlasov equation as a basis together with the assumptions of Section 2. The connection with the work of Stringer on interchange modes appears in Section 4, the influence of rotation (and to a lesser extent heat flux) upon the theory being made apparent at this stage. Results arising from the numerical solution of the equations appear in Section 5.

2. ORDERING PROCEDURE

We consider the problem of the stability of a $z = 1$ cylindrical plasma column surrounded by a perfectly conducting wall. The plasma is taken to be so hot (~KeV) that it may be considered collisionless with the ion gyroradius finite although small in comparison with the radial scale lengths of plasma quantities. All equilibrium variables depend on the radius alone.

We define $\varepsilon = v_r^i/L_\perp \Omega^i = a^i/L_\perp$ as the expansion parameter where v_r^i is the ion thermal velocity, $L_\perp$ a plasma scale length [e.g. $(1/\rho)(\mathrm{d}\rho/\mathrm{d}r)$] and Ω^i the ion gyro frequency. We consider standard FLR ordering assumptions as outlined by BOWERS (1971):

$$\frac{v_\perp}{\varepsilon v_r^i} \sim \frac{E_\parallel}{\varepsilon E_\perp} \sim \frac{E_\perp}{\varepsilon B_z v_r^i} \sim \frac{\omega}{\varepsilon^2 \Omega^i} \sim 1$$

where $v_\perp$ is the hydromagnetic velocity normal to **B**. $\perp$ and $\parallel$ suffices refer to perpendicular and parallel to **B** and ω is the frequency of the instabilities. There remains the ordering of β and of B_θ/B_z.

Recall from BOWERS (1971) that the motion of particles and perturbations along **B** is described by a time scale:

$$\frac{1}{T} \sim \frac{C_A}{L_\parallel}$$

where C_A is the Alfvén speed and $C_A \sim v_r^i/\sqrt{\beta}$. Thus

$$\varepsilon^2 \Omega^i \sim \frac{C_A}{L_\parallel} \sim \frac{v_r^i}{L_\parallel \sqrt{\beta}}$$

therefore $1/L_\parallel \sim \varepsilon \sqrt{\beta}/L_\perp$ using the definition of ε.

In cylindrical coordinates we apply symmetry considerations and Fourier analyse so that:

$$\frac{\partial}{\partial z} \to ik; \qquad \frac{1}{r}\frac{\partial}{\partial \theta} \to \frac{im}{r}$$

Thus

$$\frac{1}{L_\parallel} \sim k + \frac{mB_\theta}{rB_z} \sim \frac{\varepsilon\sqrt{\beta}}{L_\perp}$$

The cylindrical geometry determines that

$$\frac{1}{L_{\perp \text{ perturbations}}} \geqslant \frac{1}{L_{\perp \text{ equilibrium}}}$$

hence we must choose

$$k \sim \frac{\varepsilon\sqrt{\beta}}{L_\perp}; \qquad L_{\perp \text{ perturbations}} \sim L_{\perp \text{ equilibrium}}$$

$$B_\theta \ll \varepsilon\sqrt{\beta}\, B_z$$

For $\beta \sim 1$, this restriction is identical to that of BOWERS (1971) who argues that B_θ' must be of this order so that effects due to curvature drift do not dominate those due to FLR which are the subject of interest. The above ordering of B_θ illustrates the incorporations of significant FLR effects at zero beta (ROSENBLUTH and SIMON, 1965), i.e. by employing a straight magnetic field. A $\beta \sim \varepsilon^2$ ordering scheme employed by COPPI (1964) is consistent with the above arguments. In what follows we take $\beta \sim 1$ in order to include the maximum number of physical phenomena. Hence $j_z B_\theta \sim \varepsilon^2 j_\theta B_z$ pertains in this case.

The scaling of quantities in ε in this work employs a scheme wherein corresponding quantities of equilibrium and perturbation are ordered with the same power of ε. Schemes of this type, as will be seen below, produce a fluid-like description of the effects of FLR. In regions of, for example, larger B_θ, the incorporation of modes of radial scale-length much less than the plasma scale length may include the effects of finite gyration radius, but as may be seen elsewhere, such effects are not susceptible to a fluid-like analysis of the type presented below (see e.g. CONNOR and HASTIE (1975)).

3. THE DIFFERENTIAL DISPERSION EQUATION

Appendix A sketches the derivation of the FLR stress tensor by expansion of the Vlasov equation. Familiar expressions for velocities u_r and u_θ result by taking appropriate moments of the distribution function f which is not necessarily Maxwellian in lowest order. Expressions for collisionless heat fluxes result by taking different moments of the same expression for the expanded distribution function.

Appendix B indicates the calculation of the linearized perturbation of the lowest order distribution function in the form $f_0'(r) \exp[i(\omega t + m\theta + kz)]$ together with the relationships for fluid-type modes. (Primed quantities denote perturbations. Subscripts refer to ordering in ε.)

$$f_0' = \frac{iB_{r_1}'}{\bar{k}} \frac{\partial f_0}{\partial r}; \qquad B_{z0}' = \frac{iB_{r_1}'}{\bar{k}} \frac{\partial B_{z0}}{\partial r}; \qquad \bar{\omega} B_{r_1}' = \bar{k} E_{\theta_1}' \tag{1}$$

where

$$\bar{\omega} = \omega - \frac{mE_{r1}}{rB_{z0}}; \qquad \bar{k} = k + \frac{mB_{\theta 1}}{rB_{z0}} \tag{2}$$

obtained by requiring lowest order charge and axial current neutrality.

Taking the appropriate moments of f_0', we obtain expressions for u_{z0}', $p_{\perp 0}'$, $p_{\parallel 0}'$, $q_{z0}^{\perp\prime}$

$$u_{z0}' = \frac{iB_{r_1}'}{\bar{k}} \frac{\mathrm{d}u_{z0}}{\mathrm{d}r}; \qquad p_{\perp 0}' = \frac{iB_{r_1}'}{\bar{k}} \frac{\mathrm{d}p_{\perp 0}}{\mathrm{d}r}; \qquad p_{\parallel 0}' = \frac{B_{r_1}'}{\bar{k}} \frac{\mathrm{d}p_{\parallel 0}}{\mathrm{d}r}; \qquad q_{z0}^{\perp\prime} = \frac{iB_{r_1}'}{\bar{k}} \frac{\mathrm{d}q_{z0}^{\perp}}{\mathrm{d}r}$$

Substitution of these into A6 and A9 yields expressions for u_{r_1}', u_{θ_1}', $q_{\theta_1}{}^{\perp\prime}$, $q_{r_1}{}^{\perp\prime}$ which on substitution into A12 to A16 yield expressions for the components of the perturbed stress tensor in terms of B_{r_1}'.

In particular we find

$$\xi = \frac{u_{r_1}'}{\omega_1} = \frac{B_{r_1}'}{k}$$

where

$$\omega_1 = \omega + \frac{mu_{\theta_1}}{r} + ku_{z0}$$

ω_1 may be interpreted as a Doppler shifted frequency. From $i\omega_1 f_0' + u_{r_1}(\partial f_0/\partial r) = 0$ we see that f_0' satisfies $(D/Dt)(f_0 + f_0') = 0$ where D/Dt denotes the convective derivative. The perturbation ξ is thus a Lagrangian displacement of the plasma with the centre of mass velocity. The momentum equation:

$$\rho \frac{\partial \mathbf{u}}{\partial t} + \rho(\mathbf{u} \cdot \nabla)\mathbf{u} - \sigma \mathbf{E} - \mathbf{j} \wedge \mathbf{B} + \nabla p + \nabla \cdot \underset{\sim}{\tau} = 0 \tag{3}$$

is an exact moment of the Vlasov equation. To zeroth order in ε we obtain pressure balance.

$$\nabla \cdot \left(p_{\perp 0} + \frac{B_{z0}{}^2}{2\mu_0} \right) = 0$$

The first order equation is similar since the FLR expansion is essentially in ε^2.

After linearizing and perturbing the third order part of (3) we take the z component of its curl thus eliminating contributions from higher order pressure terms. The result is an equation involving perturbed quantities all of which have been calculated in terms of ξ. Following an episode of voluminous algebra during which expressions for the perturbations are substituted and the result simplified, a differential dispersion equation is produced of the form:

$$\frac{\mathrm{d}}{\mathrm{d}r}\left(F \frac{\mathrm{d}\xi}{\mathrm{d}r} \right) + G\xi = 0 \tag{4}$$

where

$$F = \rho r^3 \omega_1{}^2 + r^3 \left(k + \frac{mB_\theta}{rB_z} \right)^2 \left(\sum_{\text{species}} (p_\parallel - p_\perp) - \frac{B_z{}^2}{\mu_0} \right)$$
$$- m\omega_1 r^2 \frac{\mathrm{d}}{\mathrm{d}r}\left(\frac{p_\perp{}^i}{\Omega^i} \right) + \frac{mr^2}{\Omega^i}\left(k + \frac{mB_\theta}{rB_z} \right)\left(p_\perp{}^i \frac{\mathrm{d}u_z}{\mathrm{d}r} + \frac{\mathrm{d}}{\mathrm{d}r} q_z{}^{\perp i} \right)$$
$$+ \frac{mr^2}{\Omega^i B_z} \frac{\mathrm{d}B_z}{\mathrm{d}r}\left(k q_z{}^{\perp i} + \frac{m}{2r} q_\theta{}^{\perp i} \right)$$

$$G = -\frac{(m^2 - 1)}{r^2} F + r^2 \frac{\mathrm{d}}{\mathrm{d}r}\left[\rho \left(\omega_1 - \frac{mu_\theta}{r} \right)^2 \right] + k^2 r^2 \frac{\mathrm{d}}{\mathrm{d}r}\left(\sum_{\text{species}} (p_\parallel - p_\perp) - \frac{B_z{}^2}{\mu_0} \right)$$

Note that $q_z{}^{\perp i}$ and $q_\theta{}^{\perp i}$ are fluxes of the energy associated with the perpendicular ion thermal velocity.

The first two terms of F may be produced from M.H.D. treatment of the problem, with the addition of the effects of temperature anisotropy associated with firehose instabilities. The third term gives rise to the principal stabilizing effects of FLR and is to be found in all previous FLR analyses (e.g. BOWERS and HAINES, 1971). The following term, linear in $\mathbf{k} \cdot \mathbf{B}$, describes a secondary influence of finite gyro-radius contrasting in effect with the more familiar term. Destabilization due to shear in the axial flow appears increasingly important as ion temperature rises and BOWERS and HAINES (1971) showed that, in the case of a straight equilibrium magnetic field, this could overcome the conventional stabilizing effects of increased FLR in certain cases. We note that a radial gradient of $q_z{}^{\perp i}$ has a similar effect, and so we might regard the previous term not as a source of a Kelvin–Helmholtz instability but part of a sheared energy flux which can produce its own instability.

The final contributions to F arise purely in high-β situations, where ∇B effects are significant and include the influence of the collisionless heat flux $q_\theta{}^{\perp i}$, another consequence of FLR.

G manifests the effects of the cylindrical geometry. The form of the first term gives rise to the well-known differences in character of the $m = 1$ mode. The second term introduces rotational destabilization to the theory and replaces the fictitious gravity terms of plane geometry. Pressure gradient appears in the final term of G and is purely a finite β effect. This term is responsible for Suydam instabilities and the dangerous $m = 1$ kink mode of the diffuse pinch.

The eigenvalue equation developed thus encompasses not only the familiar simple MHD equilibria, but includes some of the more subtle effects associated with those plasmas that lie within the precisely defined limits of an FLR expansion scheme.

4. ANALYTIC APPROACH

We observe that in the limit $u_\theta \to 0$, $u_z \to 0$, $q_\theta{}^{\perp i} \to 0$ $q_z{}^{\perp i} \to 0$ the eigenvalue equation produced bears similarities to that solved by STRINGER (1975). The differences that appear are due to the more rigorous inclusion of cylindrical geometry and are in accord with results of other authors (ROSENBLUTH and SIMON, 1965), (BOWERS and HAINES, 1971). In recognition of the similarities to Stringer's equation, we apply the same technique of solution [originated by KULSRUD (1963)] in order to investigate the effects of the differences and of the additions to the physical content.

The technique involves assuming that the mode is localized in the region $\bar{k}_{r=r_s} = 0$ (the validity of this assumption may be estimated from the numerical results in Fig. 9 and is clearly not upheld for $m = 1$). $\bar{k}$ is thus approximated by:

$$\bar{k} \simeq (r - r_s) \left.\frac{\mathrm{d}\bar{k}}{\mathrm{d}r}\right|_{r=r_s}$$

and all other equilibrium quantities are approximated by their value at $r = r_s$. The inclusion in the equation of the $\mathrm{d}\rho/\mathrm{d}r$ term in G introduces the effects of rotation to the problem and requires a slight generalization of the mathematics involved. The method is developed in Appendix C.

There results the dispersion relation of the most unstable interchange mode of the system: $\sqrt{X} = H(4Y)$ (with H, X, Y defined in Appendix C) which may be expanded

into the form:

$$\zeta = 1 \pm \left[1 - \left\{A4 + \frac{A3}{A2} H^2(A2[1 + A5(\zeta - A1)^2])\right\}\right]^{1/2} \tag{5}$$

where, using

$$u^i = \frac{1}{\rho}\frac{\mathrm{d}}{\mathrm{d}r}\left(\frac{p_\perp{}^i}{\Omega^i}\right), \qquad \mu = \frac{B_\theta}{r_s B_z}$$

$$\zeta = \frac{\omega_1 r_s}{\frac{1}{2}mu^i}, \qquad \left(\omega_1 = \omega + \frac{mu_\theta}{r_s} + ku_z\right)$$

$$A1 = \frac{u_\theta}{\frac{1}{2}u^i}\left[1 - \frac{\rho k r_s}{mu_\theta}\frac{\mathrm{d}u_z}{\mathrm{d}r}\Big/\frac{\mathrm{d}\rho}{\mathrm{d}r}\right]$$

$$A2 = \frac{\dfrac{-4}{r_s}\left(\dfrac{\mu}{\mathrm{d}\mu/\mathrm{d}r}\right)^2\left[\dfrac{\mathrm{d}}{\mathrm{d}r}\left(\sum_{\text{species}}(p_\parallel - p_\perp) - \dfrac{B_z^2}{\mu_0}\right) - \dfrac{(\rho\,\mathrm{d}u_z/\mathrm{d}r)^2}{\mathrm{d}\rho/\mathrm{d}r}\right]}{\dfrac{B_z^2}{\mu_0} - \sum_{\text{species}}(p_\parallel - p_\perp)}$$

$$A3 = \frac{-16 r_s^3 \mu^2\left[\dfrac{\mathrm{d}}{\mathrm{d}r}\left(\sum_{\text{species}}(p_\parallel - p_\perp) - \dfrac{B_z^2}{\mu_0}\right) - \dfrac{(\rho\,\mathrm{d}u_z/\mathrm{d}r)^2}{\mathrm{d}\rho/\mathrm{d}r}\right]}{(m^2 - 1)\rho(u^i)^2}$$

$$A4 = \frac{1}{\rho\Omega^i{}^2(u^i)^2}\left[\frac{4}{B_z}\frac{\mathrm{d}B_z}{\mathrm{d}r}\left(\frac{1}{2}\frac{\mathrm{d}R^i}{\mathrm{d}r} - \frac{p_\perp{}^i}{\rho}\frac{\mathrm{d}p_\perp}{\mathrm{d}r}\right) + \frac{\left(\dfrac{\mathrm{d}q_z{}^{\perp i}}{\mathrm{d}r} + p_\perp{}^i\dfrac{\mathrm{d}u_z}{\mathrm{d}r} + \dfrac{q_z{}^{\perp i}}{B_z}\dfrac{\mathrm{d}B_z}{\mathrm{d}r}\right)^2}{\left(\dfrac{B_z^2}{\mu_0} - \sum_{\text{species}}(p_\parallel - p_\perp)\right)}\right]$$

$$A5 = \frac{(u^i)^2\dfrac{\mathrm{d}\rho}{\mathrm{d}r}}{4r_s^2\mu^2\left[\dfrac{\mathrm{d}}{\mathrm{d}r}\left(\sum_{\text{species}}(p_\parallel - p_\perp) - \dfrac{B_z^2}{\mu_0}\right) - \dfrac{(\rho\,\mathrm{d}u_z/\mathrm{d}r)^2}{\mathrm{d}\rho/\mathrm{d}r}\right]}$$

The remainder of this section considers: $\mathrm{d}u_z/\mathrm{d}r = 0$.
The constraint $|y| \gg |H(4y)|^2$ may be written

$$|A2(1 + A5(\zeta - A1)^2)| \gg |H(A2(1 + A5(\zeta - A1)^2))|^2$$

Since, by the Schwartz reflection principle $H(z^*) = (H(z))^*$ the two square roots in (5) produce either pairs of real modes or complex conjugate pairs of values of ζ. Thus when calculating ζ, it is sufficient to consider only one of the square roots in the dispersion relation in order to extract the growth rates of the modes. This has been observed in Figs. 2 and 3

The magnitude of u^i describes the degree of FLR introduced into the problem. We observe that $A1$ describes the net plasma rotation velocity at the singular surface. The condition $A2 < 1$ is merely a statement of the Suydam criterion including the effect of anisotropic pressure and hence the possibility of a fire-hose instability.

This can be written as

$$\left(\frac{\mathrm{d}\mu/\mathrm{d}r}{\mu}\right)^2 + \frac{4}{r_s}\frac{\dfrac{\mathrm{d}}{\mathrm{d}r}\left(\sum\limits_{\text{species}}(p_\parallel + p_\perp)\right)}{\dfrac{B_z^2}{\mu_0} - \sum\limits_{\text{species}}(p_\parallel - p_\perp)} > 0$$

Where the equilibrium pressure balance relation

$$\frac{\mathrm{d}}{\mathrm{d}r}\left(\frac{B_z^2}{2\mu_0} + \sum_{\text{species}} p_\perp\right) = 0$$

has been used.

Hence the magnitude of $(A2 - 1)$ describes the degree by which the system is MHD unstable due to adverse pressure gradient. $A3$ is the only parameter in which m explicitly occurs and corresponds to the quantity used by STRINGER (1975) to describe FLR. The first term in $A4$, using a Maxwellian distribution to estimate R, describes the collisionless $\mathbf{B} \times \nabla T_\perp{}^i$ heat flux and hence is likely to be negative $[(\mathrm{d}T_\perp{}^i/\mathrm{d}r) < 0]$. In the absence of a fire-hose effect the second term is positive and destabilizing, but must be restricted in magnitude to remain within the limits of this local expansion (using $C5$). Parameter $A5$ describes the effect of density gradient at the resonant surface and from the dispersion relation we see that its magnitude describes the influence that rotation may potentially have.

Inspection of the dispersion relation (5) yields two immediate results.

(i) We may expect $A4 > 0$ (due to the dominance of its second term) to destabilize and $A4 < 0$ (due to the $\mathbf{B} \times \nabla T_\perp{}^i$ heat flux of the first term) to have a stabilizing influence.

(ii) The case $A5 = 0$ yields marginal stability when $\zeta = 1$ as solved by STRINGER (1975). For $A5 \neq 0$, $A1 = 1$ this situation remains. $A1 = 1$ implies

$$\frac{E_r}{B_z} = \frac{1}{2}\left(\frac{1}{\rho\Omega^i}\frac{\mathrm{d}p_\perp{}^i}{\mathrm{d}r} + \frac{p_\perp{}^i}{2\rho\Omega^i B_z{}^2}\frac{\mathrm{d}}{\mathrm{d}r}(B_z^2)\right)$$

i.e. the centre of mass rotation equals half the diamagnetic rotation. Note that $\zeta = 1$ at marginal stability $(Im(\omega) = 0)$ in the case $A1 = 1$ corresponds to $Re(\omega) = 0$. This special case of rotation has been discussed by ROSENBLUTH and SIMON (1965).

By differentiating (5) with respect to $A2$ (the Suydam parameter) we see that real ζ implies real $\partial\zeta/\partial(A2)$. Thus for a range of values of $A2$ to exist for which ζ is complex, $\partial\zeta/\partial(A2) \to \infty$ at marginal stability. Thus for $A1 \neq 1$, $A5 > 0$ the value of $A2$ for which $\zeta = 1$ is less than $A2_{\text{crit}}$ (the value of $A2$ at marginal stability). Hence a sufficient criterion for stability to localized modes is that $A2 \leqslant A2_{\zeta=1}$. Values of $A2_{\zeta=1}$ calculated by hand iteration using a plot of H on the real axis, are plotted against $1/A3$ in Fig. 1 for various values of $\delta = 1 + A5\,(1 - A1)^2$. $\delta = 1$ corresponds to STRINGER (1975) and is seen to be the most stable case. (Note that when $\delta = 1$, $A2_{\text{crit}} = A2_{\zeta=1}$.)

Using a Newton–Raphson iteration, the behaviour of ζ as a function of the five parameters has been determined using the explicit case $A5 = 0$ to initiate the procedure.

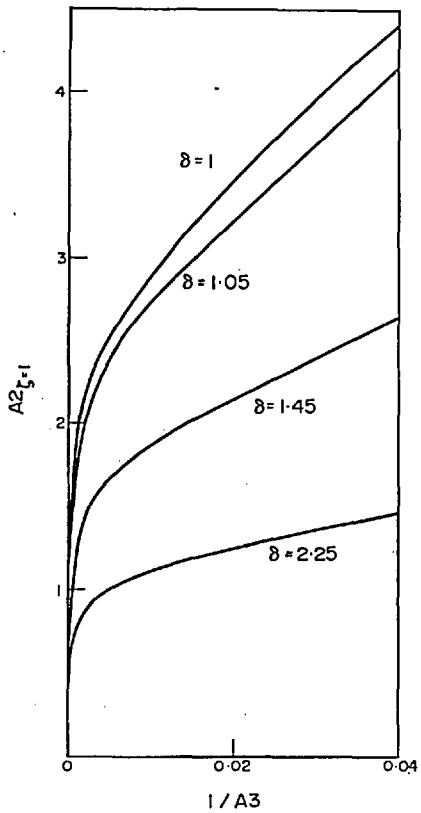

FIG. 1.—The sufficient condition for the stability of Suydam modes for four values of $\delta = 1 + A5(1 - A1)^2$ with $A4 = 0$ and $A5 = 0{\cdot}05$.

Figures 2 and 3 plot the complex frequency as a function of $A2$ for rotations $A1 = -2$ and $+2$ respectively. Observe that although modes become unstable in order of increasing m, modes of higher m number dominate where the Suydam parameter substantially exceeds marginal stability. Such behaviour is a characteristic of finite density gradient ($A5 > 0$) and is evident in the most stable case of rotation ($A1 = 1$) which has the same marginal stability characteristics as $A5 = 0$. Note that the real parts of the Doppler shifted frequency are no longer constant (as in $A5 = 0$ and $A1 = 1$) at finite growth rate, but increase for $A1 > 1$ and decrease for $A1 < 1$ as a function of increasing $A2$.

The dependence of growth rate upon rotation ($A1$) is illustrated in Fig. 4. Observe that $A1 = 1$ is the most stable rotation possible. For comparison with Fig. 1, Fig. 5 plots marginal stability ($A2_{crit}$) against $1/A3$ for various rotations. The special case $A1 = 1$ corresponds, on these diagrams, to $A5 = 0$ and is the most stable. Collisionless heat flux is considered in Fig. 6 by computing with $A4 = -1$. Observe that the larger values of $A2_{crit}$ imply stabilization by this phenomenon. However the increase in $(A2_{crit} - 1)$ due to this effect is small compared to that due to $1/A3$, the dominant FLR term.

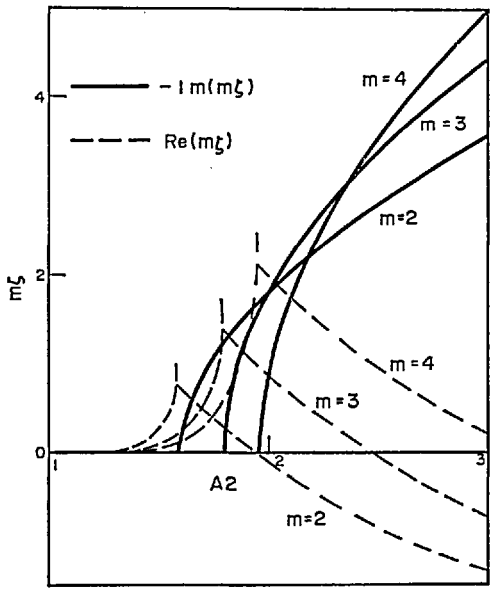

FIG. 2.—Real and imaginary parts of the normalized complex frequency $m\zeta$ plotted against the Suydam parameter $A2$ for $A5 = 0{\cdot}05$, $A1 = -2$, $A4 = 0$, $A3 = 1600/(m^2 - 1)$. Note that the second stable solution has been omitted below marginal stability.

5. NUMERICAL SOLUTION

For the purposes of numerical solution of (4) (on a CDC 6400) we identify a set of scale frequencies:

$$WA^2 = \frac{B_{z0}^2}{\rho_0 \mu_0 r_x^2}; \qquad WE = \frac{E_{rx}}{r_x B_{z0}}; \qquad WF = \frac{KT_{\perp 0}^i}{eB_{z0} r_x^2}$$

$$WZ = \frac{u_{z0}}{r_x}; \qquad (WQZ)^2 = \frac{q_{z0}^{\perp i}}{\Omega_0^i r_x^3 \rho_0}$$

$$(WM)^2 = \frac{K \sum_{\text{species}} (T_\parallel - T_\perp)_0}{M^i r_x^2}.$$

Three further parameters are required

m — azimuthal mode number

$\frac{kr_x}{m}$ — pitch of mode

$$\beta = \frac{n_0 K \sum_{\text{species}} T_{\perp 0}}{B_{z0}^2/2\mu_0} \quad \text{plasma beta}$$

Subscript $_0$ refers to a value on axis.
Subscript $_x$ refers to a value at the wall.

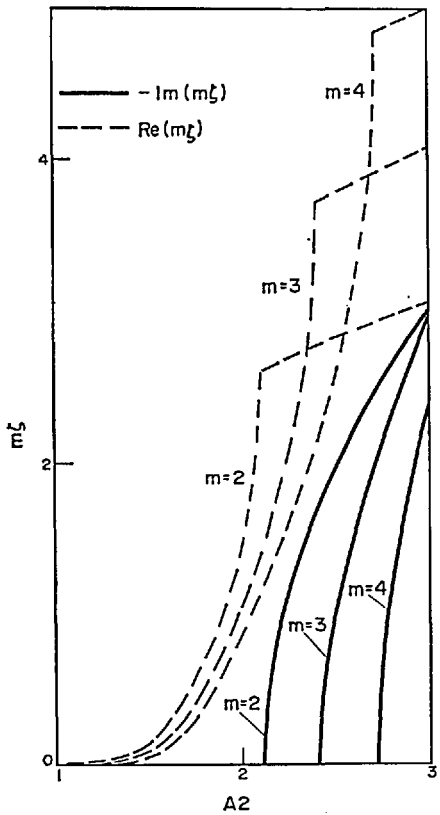

FIG. 3.—Real and imaginary parts of the normalized complex frequency $m\zeta$ plotted against the Suydam parameter $A2$ for $A5 = 0{\cdot}05$, $A1 = 2$, $A4 = 0$, $A3 = 1600/(m^2 - 1)$. Note that the second stable solution has been omitted below marginal stability.

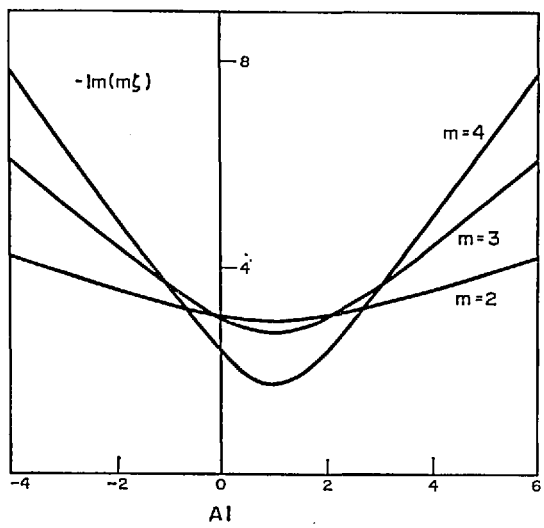

FIG. 4.—The variation of the normalized growth rate with rotation parameter $A1$ for $A4 = 0$, $A2 = 3$, $A5 = 0{\cdot}05$, $A3 = 1600/(m^2 - 1)$.

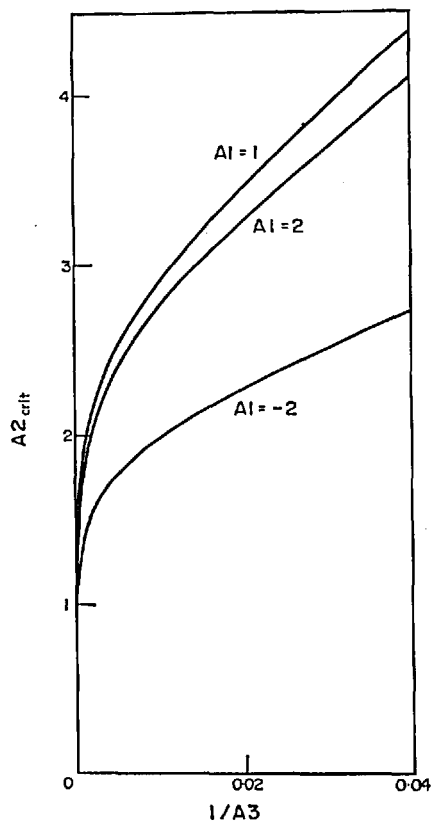

FIG. 5.—Marginal stability values of the Suydam parameter $A2$ vs. dominant FLR term ($1/A3$) for different values of rotation ($A1$) with $A4 = 0$, $A5 = 0{\cdot}05$.

The equilibrium is described by normalized profiles of number density n,

$$\frac{E_r}{rB_z}, \qquad T_\perp^i, \qquad \sum_{\text{species}} T_\perp, \qquad \sum_{\text{species}} (T_\parallel - T_\perp)$$

$$\mu = \frac{r_w B_\theta}{rB_z}, \qquad q_z^{\perp^i}, \qquad u_z.$$

Unless otherwise stated, temperature profiles were taken as constant following BOWERS and HAINES (1971), number density Gaussian and magnetic field pitch Lorentzian. The latter was chosen to approximate the pitch produced by current concentrated in a central channel.

By approximating the differential dispersion equation to a set of difference equations on a discrete mesh, the eigenvalue problem was reduced to finding the roots of a function expressed as a tri-diagonal determinant each element of which is quadratic in ω. After computing all such roots on a mesh of about 20 points, the accuracy of the most unstable root was asserted by searching for it on as large a mesh as required. Muller's method of quadratic interpolation (see e.g. TRAUB (1964)) was used to

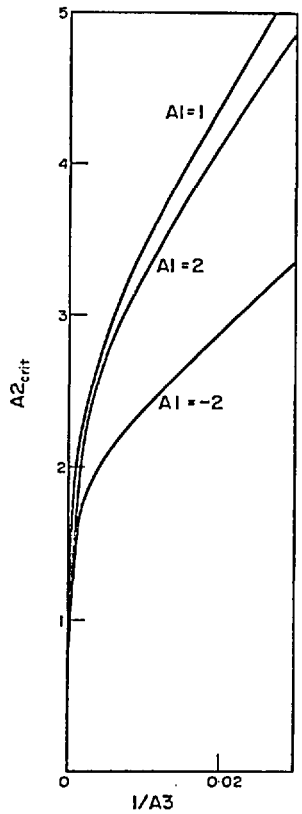

FIG. 6.—Marginal stability values of the Suydam parameter $A2$ vs. the dominant FLR term $(1/A3)$ for different values of rotation $(A1)$ with $A5 = 0{\cdot}05$, $A4 = -1$.

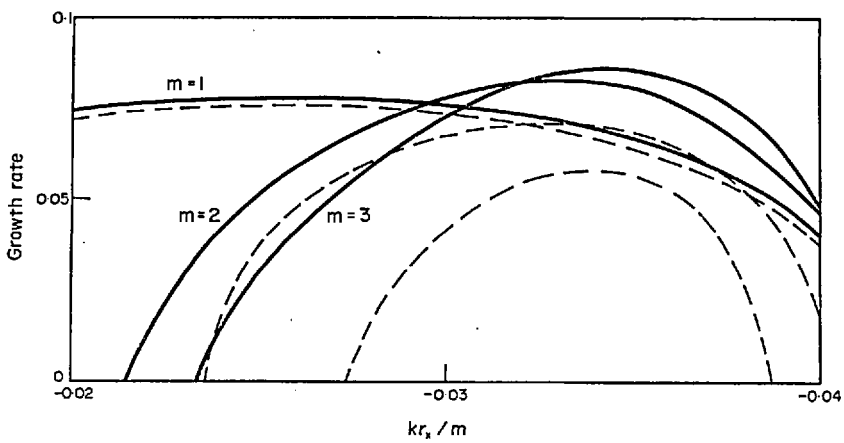

FIG. 7.—The variation of the growth rate of Suydam modes with normalized axial wavenumber for different azimuthal wavenumbers with $\beta = 0{\cdot}5$, $WA = 10$, $n = \exp(-0{\cdot}5(r/0{\cdot}3r_x)^2)$, $\mu = 0{\cdot}01/(0{\cdot}25 + (r/r_x)^2)$. $WF = 0$ on solid lines, $WF = 0{\cdot}0035$ on broken lines.

determine the required roots. Parameter perturbation was sometimes used to follow a mode as a function of the variables used.

(i) *Suydam modes*

Figure 7 (solid lines) illustrate the variation of growth rate of Suydam modes with axial wavenumber in the absence of FLR. The waves are extrapolated below $\gamma = 0{\cdot}02$ since, as MHD marginal stability is approached, the modes become too singular to be resolved on a discrete mesh. It may be established, however, that cut-off of $m = 2$ and $m = 3$ modes occurs approximately where the Suydam stability cirterion is violated but the $m = 1$ mode is unstable far beyond this limit and requires a wall for stabilization. Since increasing $|kr_a/m|$ moves the singular surface towards the origin, cut-off at larger $|kr_a/m|$ occurs soon after $r_s((\mathbf{k} \cdot \mathbf{B})_{r=r_s} = 0)$ passes through zero. In the centre of the kr_a/m spectrum, higher m number modes dominate, whereas, as in Section 4, modes become unstable in order of increasing m as more unstable k values are considered. The peaks of the curves shown occur when r_s lies in the region of greatest pressure gradient.

Figure 8 illustrates the effect of increasing FLR(WF) for a fixed k. Observe the marked lack of influence of gyro radius effects upon $m = 1$ modes in comparison with higher m instabilities, FLR increasing in effectiveness as m number increases. The broken lines of Fig. 7 indicate the k spectrum of the instabilities when FLR is included. Note that the region of sharply varying modes that could not be previously resolved is completely stabilized and that the peaks of the separate spectra now occur in reverse order of m number. Since FLR produces diamagnetic rotation of the plasma

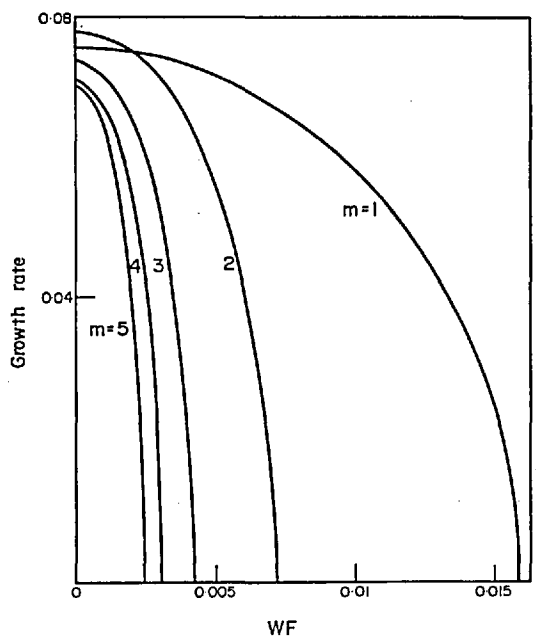

FIG. 8. The stabilization of Suydam modes by FLR effects, with $WA = 10$, $\beta = 0{\cdot}5$, $kr_a/m = -0{\cdot}03$, $n = \exp(-0{\cdot}5(r/0{\cdot}3r_a)^2)$ $\mu = 0{\cdot}01(0{\cdot}25 + (r/r_a)^2)$.

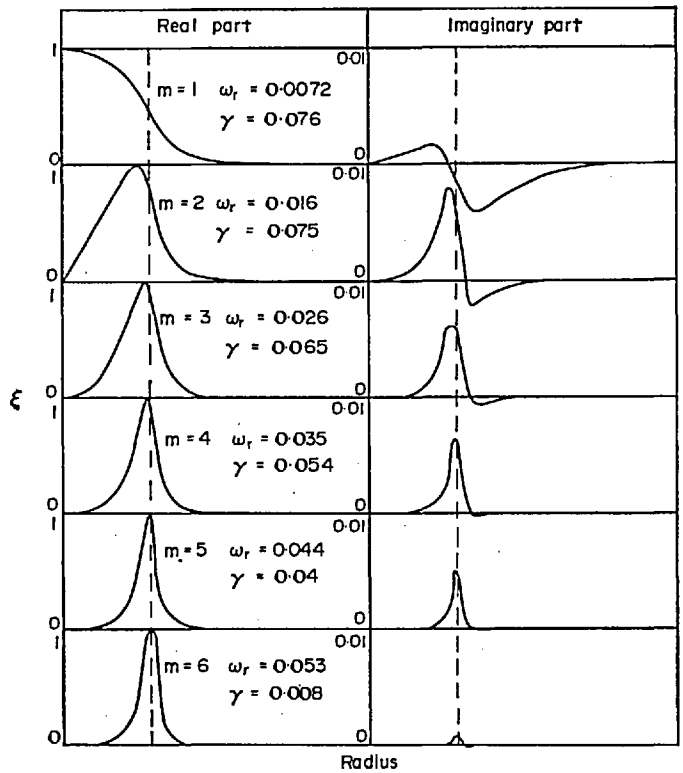

FIG. 9.—Radial dependence of the complex eigenfunctions of Fig. 8 with $WF = 0{\cdot}002$.

(in the absence of electric field), the real part of the frequency increases from zero as WF rises. The eigenfunction itself becomes complex, an imaginary part being generated with increased ion temperature. This signifies the superposition of a small amplitude radial travelling wave component upon the MHD radially standing wave. Figure 9 illustrates the radial plasma perturbations of several modes when FLR is included (Note the expanded scale on the imaginary parts). Mode localization increases markedly as m number increases, such that at $m \geqslant 5$, they appear symmetric about the singular surface and show little of the curvature produced distortion of the lower m modes. The mode structure varies little as FLR increases to sufficient magnitude to quench the instability (except for the introduction of the imaginary part). Recall, however, that very narrow MHD modes are stabilized by very little FLR. As may be expected, the introduction of a steeper profile of μ produces narrower modes and reduced growth rates. It is clear that the analytical expansion of Section 4 is most appropriate for the high m number modes where the numerical approach is limited by the resolution of the finite mesh. To this extent, the two approaches are complimentary and 30% agreement is the position of the cut-off is found for $m = 2$.

In Fig. 10 we investigate the influence of the $q_\theta{}^{\perp i}$ term in the equation. For this purpose, the fourth moment, R, is estimated from a double Maxwellian distribution so that $q_\theta{}^{\perp i}$ is reduced to the $\mathbf{B} \times \nabla T_\perp{}^i$ heat flux (Righi–Leduc effect). A profile of

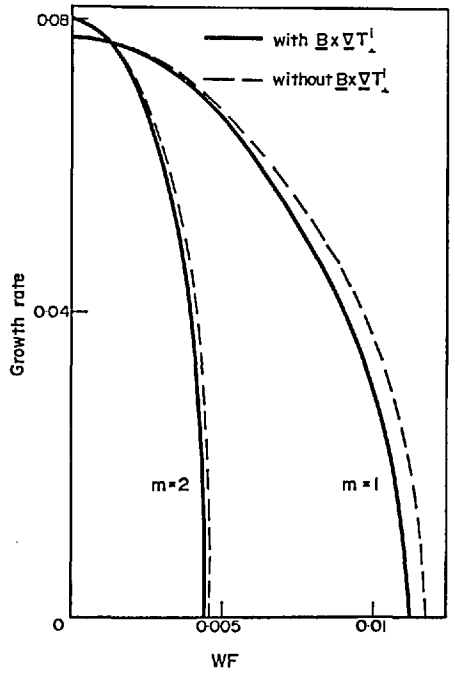

FIG. 10.—FLR stabilization of Suydam modes illustrating the effect of the Righi–Leduc heat flow.
$WA = 10$, $\beta = 0{\cdot}5$, $kr_a/m = -0{\cdot}03$, $\mu = 0{\cdot}01/(0{\cdot}25 + (r/r_a)^2)$,
$n = \exp(-0{\cdot}5(r/0{\cdot}3r_a)^2)$, $T^i \propto \exp(-50(r/r_a)^4)$.

$T_\perp{}^i$ with a steep gradient was employed ($\exp(-50(r/r_a)^4)$), but in spite of this, the stabilizing effect, indicated by the difference of the two sets of curves of Fig. 10, is small.

The choice of a profile of μ having a maximum at $r \neq 0$ enabled the study of modes associated with two resonant surfaces (see NEWCOMB, 1960) within the plasma. The growth rate spectrum in this $WF = 0$ case is portrayed in Fig. 11 (solid lines) and some of the characteristic modes in Fig. 12. With $kr_a/m \sim -0{\cdot}035$, all modes show structure associated with each singular surface. $d\xi/dr$ is greater at the outermost one since the plasma density is less in this region. Since the two singular surfaces coalesce at $-kr_a/m = 0{\cdot}04$, all mode spectra show a peak at this wavenumber followed by an abrupt cut-off at larger values of $-k$ as resonant surfaces are eliminated from the plasma. At small k number, $m > 1$ modes become localized near the origin and cut off as $-kr_a/m$ falls below the value of μ at $r = 0$ (0·025). These modes show very small amplitude features at the outer resonant surface. The $m = 1$ mode persists to smaller k, cutting off abruptly as this outer surface passes through the wall. This eigenfunction approximates a step function more closely as the outer surface occurs in regions of lower and lower plasma density. Effects due to the outer resonant surface are shear stabilized for $m > 1$ modes.

Figure 11 (broken lines) illustrates that the introduction of FLR has a relatively small effect on the $m = 1$ mode, but decreases the growth rates of $m > 1$ modes,

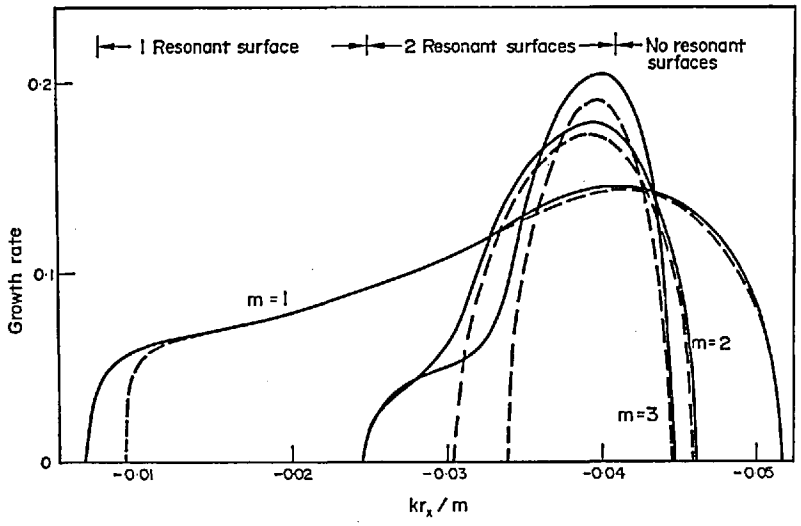

FIG. 11.—The variation of the growth rate of Suydam modes with normalized axial wavenumber with $\beta = 0{\cdot}5$, $WA = 10$, $n = \exp(-0{\cdot}5(r/0{\cdot}3r_a)^2)$, $\mu = 0{\cdot}003\{1/[0{\cdot}08 + (r/r_a - 0{\cdot}4)^2] + 1/[0{\cdot}08 + (r/r_a + 0{\cdot}4)^2]\}$ $WF = 0$ on solid lines, $WF = 0{\cdot}005$ on broken lines.

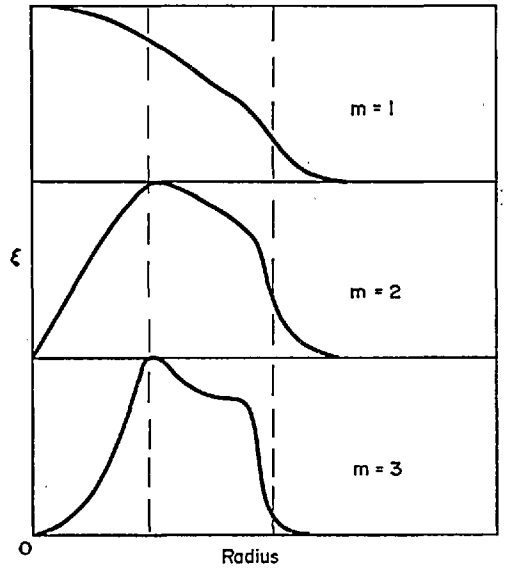

FIG. 12.—Radial dependence of the complex eigenfunctions of Fig. 11 with $WF = 0$, $kr_a/m = -0{\cdot}035$.

higher m number modes being most affected. The most noticeable effect is the stabilization of the low k end of the spectrum (where the modes without FLR approach singular behaviour).

The introduction of radial electric field ($WE \neq 0$) into the equilibrium is illustrated in Fig. 13 for E_r/rB_z independent of r. These diagrams may be explained by

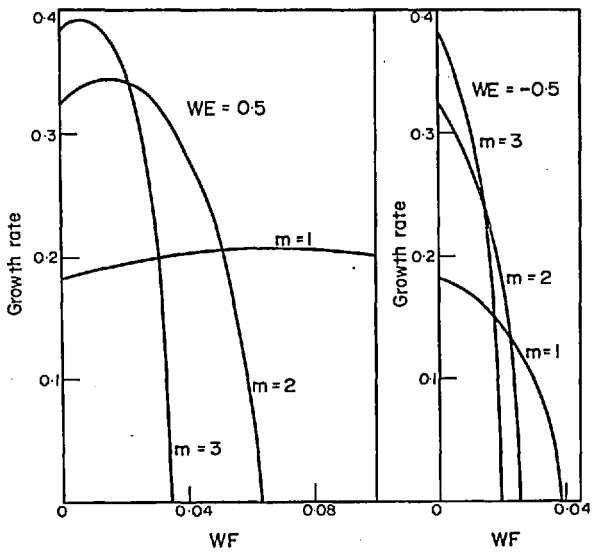

FIG. 13.—FLR stabilization when slight E × B rotation is included with $\beta = 0{\cdot}5$, $WA = 10$, $\mu = 0{\cdot}01/(0{\cdot}25 + (r/r_x)^2)$, $kr_x/m = -0{\cdot}028$, $n = \exp(-0{\cdot}5(r/0{\cdot}3r_x)^2)$.

considering the effect of diamagnetic rotation, introduced as WF increases, on the net plasma rotation (equation A-7). Positive E_r causes an E/B drift that is augmented by diamagnetism and vice-versa. Thus, the peak that occurs with $E_r > 0$ may be explained by the introduction of finite ion temperature initially destabilizing by increasing rotation and finally reducing the growth rate as gyro-viscous effects dominate. The converse initial effect is illustrated by negative E_r.

(ii) *Rotationally driven modes*

The pressure gradient effects of the first term of G in (4) produce Suydam modes, whereas the preceding term induces rotationally driven modes. These were the subject of study by BOWERS and HAINES (1971) in the case $B_\theta = 0$. The present work allows the introduction of B_θ into the theory and a more complete discussion of the eigenfunctions. (Note the difference in normalizing radius between BOWERS and HAINES and this work.)

BOWERS and HAINES (1971) found that the growth rates of the rotational modes as a function of axial wavenumber k showed a peak at $k = 0$. The introduction of constant μ merely shifts this peak to finite kr_x/m and occurs at the resonant wavenumber given by $kr_x/m + \mu = 0$. When μ is prescribed as a Lorentzian function, again all modes show maximum growth rate at similar values of $-kr_x/m$. This value is smaller than for the peak of the Suydam spectrum indicating that the most dangerous resonant surfaces occur in less dense plasma than in the pressure-gradient driven case, due, no doubt, to the radial dependence of centrifugal destabilizing forces. Thus as rotation is increased from zero, the most unstable axial wavenumber moves to progressively smaller values of $-kr_x/m$, the corresponding resonant surface moving out towards the wall. Since stability is enhanced by the absence of singular surfaces in the plasma, cut-off of the instabilities occurs at $-kr_x/m$ values just below that at the

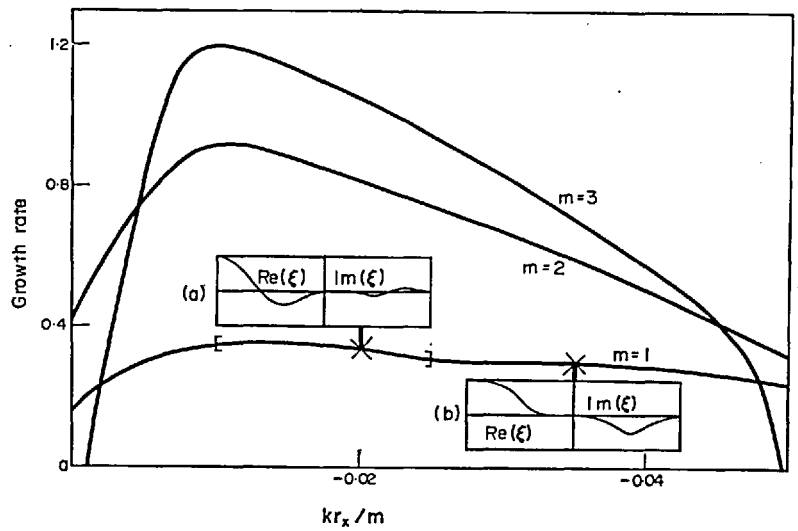

FIG. 14.—The variation of the growth rate of rotationally dominated modes with normalized axial wavenumber with $\beta = 0{\cdot}5$, $WE = 1$, $WF = 0$, $\mu = 0{\cdot}01/(0{\cdot}25 + (r/r_w)^2)$, $n = \exp(-0{\cdot}5(r/0{\cdot}3r_w)^2)$.

cylinder wall. Thus, in many cases, growth rate is a very rapidly increasing function of $-kr_w/m$ for values of this parameter in the neighbourhood of μ_{wall}. A typical case is portrayed in Fig. 14. The sharpness of the low k cut-off is increased still further as WE is reduced.

The $m = 1$ mode merits further discussion. Referring to Fig. 14 we find that the dominant mode within the central region indicated has a radial node [see insert (a)], whereas elsewhere a node-free mode [see insert (b)] predominates. Completely different oscillating parts of the frequency are associated with each type of mode. This effect is present in BOWERS and HAINES (1971) where the region is centred on $k = 0$. Generalization of the theory has thus indicated that the type (a) mode is a feature of the peak region of the spectrum rather than specifically of $k = 0$.

When a radial node is present there is clearly no need for a change in position of the centre of mass for $k = 0$, $m = 1$ and indeed a net electromagnetic force can only cause such an interaction with the conducting wall if an equilibrium B_θ is present. Thus type (b) mode structure which necessarily involves an acceleration of the centre of mass cannot occur in a theta pinch unless the plasma pressure is non-zero at the wall. By varying β we find that the stabilizing effect of finite plasma pressure on $m > 1$ rotational modes is greater towards the cut-off of the growth rate spectra. The $m = 1$ type (b) mode (without a radial node) is found conversely to be destabilized by increased β thus constricting the region of dominance of type (a). The influence of FLR upon strongly rotationally unstable modes is slight and its effect may be viewed as in the context of Suydam modes. Its chief effect is to stabilize the $m = 1$ type (a) mode possessing a radial node in preference to the more common variety type (b), thus narrowing the window of dominance of the former.

As the electric field is reduced, so the rotational modes change continuously into the Suydam spectrum. In this limit the dominant $m = 1$ mode is type (b) i.e. without a radial node so that, as WE becomes smaller, the range of kr_w/m values for which the

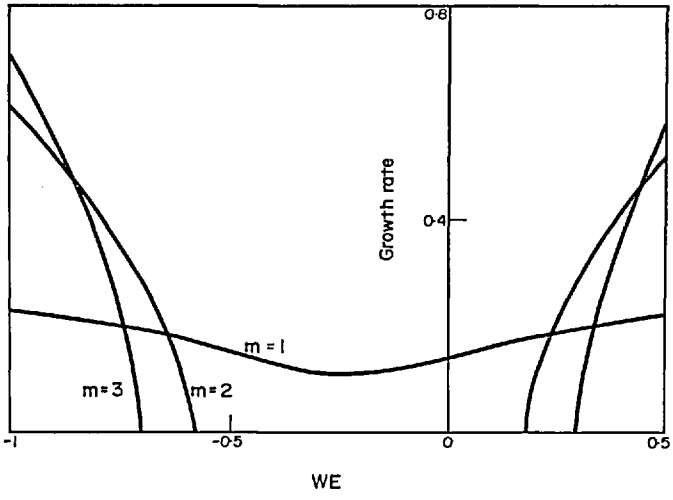

FIG. 15.—The dependence of growth rate upon E × B rotation when FLR is included. $WA = 10, \beta = 0{\cdot}5, WF = 0{\cdot}01, kr_x/m = -0{\cdot}03, n = \exp(-0{\cdot}5(r/0{\cdot}14r_x)^2), \mu = 0{\cdot}01/(0{\cdot}25 + (r/r_x)^2)$.

type (a) mode dominates becomes smaller. Figure 15 illustrates the variation of growth rate with electric field when FLR is included. Note the symmetry of the plot about $WE = -0{\cdot}2$. We calculate that this value of WE corresponds to a total rotation frequency of $+0{\cdot}21$ when diamagnetic effects are included in agreement with the results of Section 4 that $A1 = 1$ produces a minimum growth rate.

(iii) *Heat flux modes*

In order to investigate the influence of the second term of $A4$ in Section 4 that could not be adequately described by the localized theory, we considered the effect of varying the parameter WQZ for both positive and negative directions of $q_z{}^{\perp'}$. The main effect of this is to allow F of equation (4) to vanish for complex ω (negative ω^2 in the $WF = 0$ limit). Thus a continuum of *unstable* modes (with finite growth rate) defined by $F(r) = 0$ at $0 < r < r_x$ is introduced into the eigenvalue equation. Since $F = 0$ defines a singular point of the equation at which the ordering approximations on the scale length of the perturbation break down, the physical reality of such solutions is doubtful. The importance of calculating the eigenfunctions themselves is emphasized by a situation of this sort wherein the growth rates are independent of changes in mesh size, but the modes appear unphysical.

As WQZ is raised from zero, the first effect is a perturbation on the Suydam modes which shifts the peak of the eigenfunction in the direction indicated by relation $C1$ and increases the growth rate as would be expected from the previous localized mode theory. Larger heat fluxes, however, produce the singular modes mentioned above and the growth rates of these dominate the system as seen in Fig. 16. Since the Gaussian density profiles and Lorentzian μ profiles produce the largest growth rate of the continuum with the singularity near the origin, computations were performed using a density profile much flatter near $r = 0$. In this case the eigenfunctions moved and became progressively steeper as the heat flux was increased until they became discontinuous modes of the continuum. Figure 16 illustrates that, beyond stabilizing

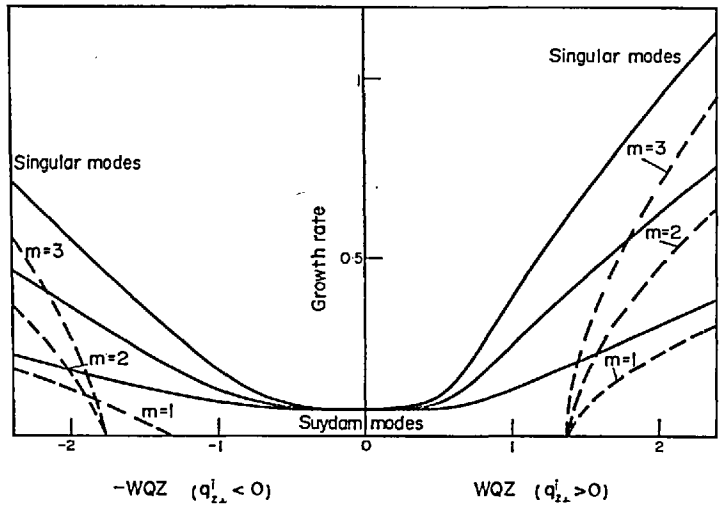

FIG. 16.—The dependence of growth rate upon the axial flux of the ion energy associated with thermal velocity perpendicular to the magnetic field. The right hand half concerns $q_z\perp^t$ parallel to B_z and the left half $q_z\perp^t$ anti-parallel to B_z. Solid lines concern $WF = 0$ (no FLR), broken lines have $WF = 0{\cdot}03$. [$\beta = 0{\cdot}5$, $WA = 10$, $kr_a/m = -0{\cdot}03$, $n = \exp(-0{\cdot}5(r/0{\cdot}3r_a)^2$, $\mu = 0{\cdot}01/(0{\cdot}25 + (r/r_a)^2)$.]

the Suydam modes of the system, the effect of increasing FLR may be entirely accounted for by the $F = 0$ dispersion relation when the ion temperature term is included in F.

(iv) *Temperature anisotropy (Firehose) instability*

As the temperature anisotropy parameter WM is increased from zero, the effective Alfvén speed

$$\left[\frac{B_z^2/\mu_0 - \sum(p_{\|} - p_{\perp})}{\rho}\right]^{1/2}$$

falls to zero and then becomes imaginary so that growth rates increase. The modes spread out over the entire plasma radius, but remain peaked near the resonant surface. Figure 17 shows growth rate of these instabilities as a function of axial wavenumber. Note that the curve is of the same general shape as that for Suydam modes (Fig. 7), but the growth rates are greater throughout, being increasing functions of WM. Superposed on Fig. 17 we see the stabilizing effect of FLR. This increases rapidly with m number, but only has significant effect on modes with small growth rate ($\leqslant 0{\cdot}02\ WA$) where the temperature anisotropy is not dominant.

6. SUMMARY

Using a standard FLR expansion of the collisonless Vlasov equation, we have produced an eigenvalue equation describing an equilibrium containing $B_\theta \ll B_z$ and many other physical quantities. First, following STRINGER (1975) and secondly by direct computation, we have analysed the equation for the effect of the plethora of physical parameters upon the growth rates of firstly the localized Suydam modes and secondly delocalized modes generated by heat flux and anisotropic temperature.

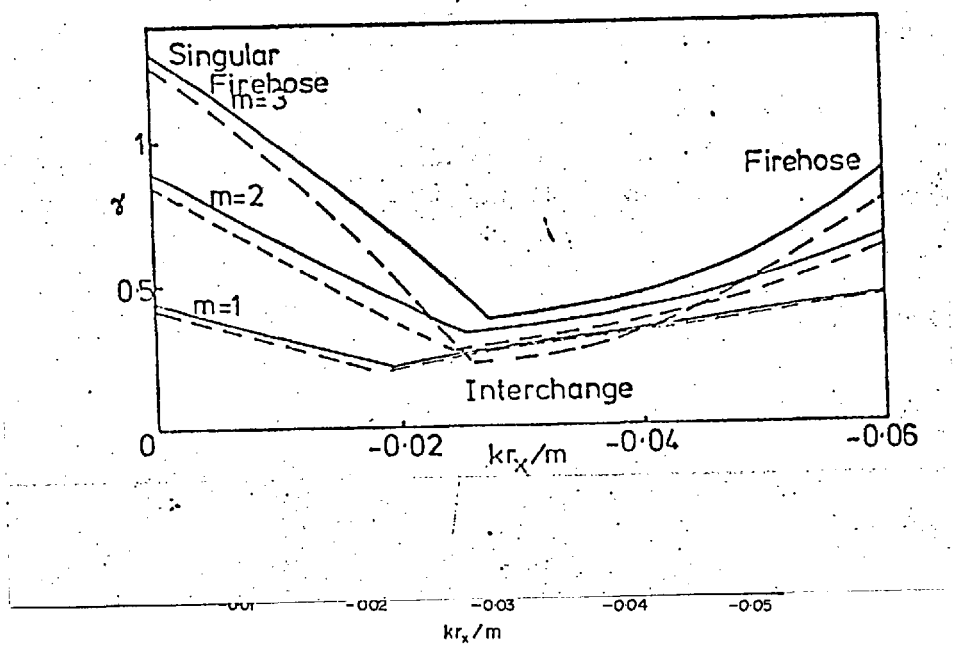

FIG. 17.—Growth rate vs. normalized axial wavenumber with dominant temperature anisotropy. Solid lines have $WF = 0$, (no FLR), broken lines have $WF = 0{\cdot}03$. [$\beta = 0{\cdot}5$, $WM = 15$, $WA = 10$, $n = \exp(-0{\cdot}5(r/0{\cdot}3r_w)^2)$, $\mu = 0{\cdot}01(0{\cdot}25 + (r/r_w)^2)$.]

The manner in which the localized modes blend into the delocalized variety as various driving forces increase has been described in all cases. In particular, the effect of axial heat flux in moving the dominant region of the modes, eventually producing unphysically singular perturbations has been illustrated. Large anisotropic temperature destabilizes and reduces localization. Of primary interest is the interaction of rotational influences with interchange modes. The $m = 1$ mode is shown to be dominated by its second radial harmonic under certain rotational circumstances, rotation being, due to centrifugal effects, a destabilizing influence in most (but not all) circumstances. The special rotational case of ROSENBLUTH and SIMON (1965) has been extended into the realm of localized modes and the interesting result that, when FLR is included, the plasma is most stable with a specific non-zero rotation, has been firmly established. In particular, for maximum stability, the centre of mass rotation should equal half the diamagnetic rotation. Even within the constraints of the assumed ordering scheme it is found that the finite ion Larmor radius effect is only of importance in those equilibria which are very close to marginal stability in all cases.

REFERENCES

BOWERS E. C. (1971) *J. Plasma Phys.* **6**, 80.
BOWERS E. C. (1969) Ph.D Thesis, University of London.
BOWERS E. C. and HAINES M. G. (1971) *Physics Fluids* **14**, 165.
CONNOR J. W. and HASTIE R. J. (1975) *Plasma Phys.* **17**, 97.
COPPI B. (1964) *Physics Fluids* **1**, 1501.
KENNEL C. F. and GREENE J. M. (1966) *Ann. Phys.* **38**, 63.
KULSRUD R. M. (1963) *Physics Fluids* **6**, 904.
LEHNERT B. (1967) *Plasma Phys.* **9**, 301.
NEWCOMB W. A. (1960) *Ann. Phys.* **10**, 232.
ROSENBLUTH M. and SIMON A. (1965) *Physics Fluids* **8**, 1300.
STRINGER T. E. (1975) *Nucl. Fusion* **15**, 125.
TRAUB (1964) *Iterative Methods for the Solution of Equations*, Prentice Hall.

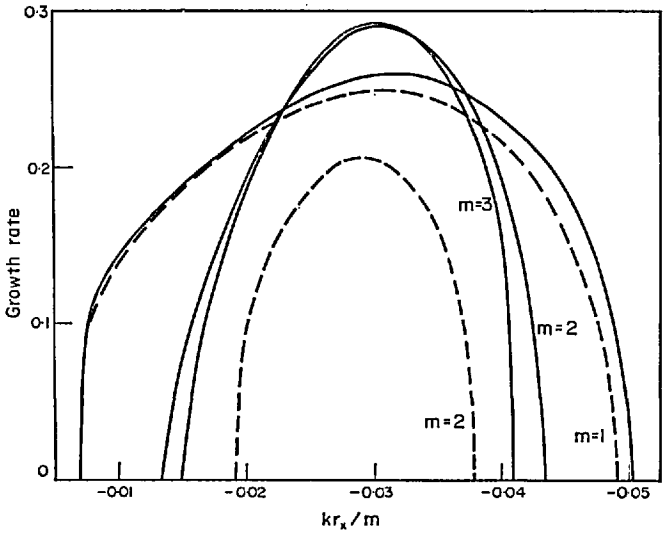

FIG. 17.—Growth rate vs. normalized axial wavenumber with dominant temperature anisotropy. Solid lines have $WF = 0$, (no FLR), broken lines have $WF = 0{\cdot}03$ [$\beta = 0{\cdot}5$, $WM = 15$, $WA = 10$, $n = \exp(-0{\cdot}5(r/0{\cdot}3r_a)^2)$, $\mu = 0{\cdot}01(0{\cdot}25 + (r/r_a)^2)$.]

The manner in which the localized modes blend into the delocalized variety as various driving forces increase has been described in all cases. In particular, the effect of axial heat flux in moving the dominant region of the modes, eventually producing unphysically singular perturbations has been illustrated. Large anisotropic temperature destabilizes and reduces localization. Of primary interest is the interaction of rotational influences with interchange modes. The $m = 1$ mode is shown to be dominated by its second radial harmonic under certain rotational circumstances, rotation being, due to centrifugal effects, a destabilizing influence in most (but not all) circumstances. The special rotational case of ROSENBLUTH and SIMON (1965) has been extended into the realm of localized modes and the interesting result that, when FLR is included, the plasma is most stable with a specific non-zero rotation, has been firmly established. In particular, for maximum stability, the centre of mass rotation should equal half the diamagnetic rotation. Even within the constraints of the assumed ordering scheme it is found that the finite ion Larmor radius effect is only of importance in those equilibria which are very close to marginal stability in all cases.

REFERENCES

BOWERS E. C. (1971) *J. Plasma Phys.* **6**, 80.
BOWERS E. C. (1969) Ph.D Thesis, University of London.
BOWERS E. C. and HAINES M. G. (1971) *Physics Fluids* **14**, 165.
CONNOR J. W. and HASTIE R. J. (1975) *Plasma Phys.* **17**, 97.
COPPI B. (1964) *Physics Fluids* **1**, 1501.
KENNEL C. F. and GREENE J. M. (1966) *Ann. Phys.* **38**, 63.
KULSRUD R. M. (1963) *Physics Fluids* **6**, 904.
LEHNERT B. (1967) *Plasma Phys.* **9**, 301.
NEWCOMB W. A. (1960) *Ann. Phys.* **10**, 232.
ROSENBLUTH M. and SIMON A. (1965) *Physics Fluids* **8**, 1300.
STRINGER T. E. (1975) *Nucl. Fusion* **15**, 125.
TRAUB (1964) *Iterative Methods for the Solution of Equations*, Prentice Hall.

APPENDIX A

The distribution function is expanded in ε and evaluated order by order by a standard method (BOWERS, 1969). Zero order:

$$\frac{\partial f_0}{\partial \alpha} = 0 \quad \text{where, in phase space} \quad v_r = v_\perp \cos\alpha, \qquad v_\theta = v_\perp \sin\alpha$$
$$v_z = v_z$$

1st order:

$$f_1 = f_{10} + 2f_{11}^R \cos\alpha - 2f_{11}^I \sin\alpha$$

$$2f_{11}^R = -\left[\frac{v_\perp}{r\Omega^i}\frac{\partial f_0}{\partial \theta} + \frac{E_{\theta_1}}{B_{z_0}}\frac{\partial f_0}{\partial v_\perp} + \frac{B_{r_1}}{B_{z_0}}\left(v_z\frac{\partial f_0}{\partial v_\perp} - v_\perp\frac{\partial f_0}{\partial v_z}\right)\right] \tag{A1}$$

$$2f_{11}^I = -\left[\frac{v_\perp}{\Omega^i}\frac{\partial f_0}{\partial r} + \frac{E_{r_1}}{B_{z_0}}\frac{\partial f_0}{\partial v_\perp} - \frac{B_{\theta_1}}{B_{z_0}}\left(v_z\frac{\partial f_0}{\partial v_\perp} - v_\perp\frac{\partial f_0}{\partial v_z}\right)\right] \tag{A2}$$

2nd order:

$$f_2 = f_{20} + 2f_{21}^R \cos\alpha - 2f_{21}^I \sin\alpha + 2f_{22}^R \cos 2\alpha - 2f_{22}^I \sin 2\alpha$$

$$\frac{\partial f_0}{\partial t} + v_z\frac{\partial f_0}{\partial z} + \left[v_\perp\left(\frac{\partial}{\partial r} + \frac{1}{r}\right) + \frac{\Omega^i E_{r_1}}{B_{z_0}}\left(\frac{\partial}{\partial v_\perp} + \frac{1}{v_\perp}\right) + \frac{\Omega^i B_{\theta_1}}{B_{z_0}}\left(v_\perp\frac{\partial}{\partial v_z} - v_z\left(\frac{\partial}{\partial v_\perp} + \frac{1}{v_\perp}\right)\right)\right] f_{11}^R$$
$$- \left[\frac{v_\perp}{r}\frac{\partial}{\partial \theta} + \frac{\Omega^i E_{\theta_1}}{B_{z_0}}\left(\frac{\partial}{\partial v_\perp} + \frac{1}{v_\perp}\right) - \frac{\Omega^i B_{r_1}}{B_{z_0}}\left(v_\perp\frac{\partial}{\partial v_z} - v_z\left(\frac{\partial}{\partial v_\perp} + \frac{1}{v_\perp}\right)\right)\right] f_{11}^I$$
$$+ \frac{\Omega^i E_{z_1}}{B_{z_0}}\frac{\partial f_0}{\partial v_z} = 0. \tag{A3}$$

$$4f_{22}^R = \left[\frac{v_\perp}{\Omega^i}\left(\frac{\partial}{\partial r} - \frac{1}{r}\right) + \frac{E_{r_1}}{B_{z_0}}\left(\frac{\partial}{\partial v_\perp} - \frac{1}{v_\perp}\right) + \frac{B_{\theta_1}}{B_{z_0}}\left(v_\perp\frac{\partial}{\partial v_z} - v_z\left(\frac{\partial}{\partial v_\perp} - \frac{1}{v_\perp}\right)\right)\right] f_{11}^I$$
$$- \left[\frac{v_\perp}{r\Omega^i}\frac{\partial}{\partial \theta} + \frac{E_{\theta_1}}{B_{z_0}}\left(\frac{\partial}{\partial v_\perp} - \frac{1}{v_\perp}\right) - \frac{B_{r_1}}{B_{z_0}}\left(v_\perp\frac{\partial}{\partial v_z} - v_z\left(\frac{\partial}{\partial v_\perp} - \frac{1}{v_\perp}\right)\right)\right] f_{11}^R \tag{A4}$$

$$4f_{22}^I = -\left[\frac{v_\perp}{\Omega^i}\left(\frac{\partial}{\partial r} - \frac{1}{r}\right) + \frac{E_{r_1}}{B_{z_0}}\left(\frac{\partial}{\partial v_\perp} - \frac{1}{v_\perp}\right) + \frac{B_{\theta_1}}{B_{z_0}}\left(v_\perp\frac{\partial}{\partial v_z} - v_z\left(\frac{\partial}{\partial v_\perp} - \frac{1}{v_\perp}\right)\right)\right] f_{11}^R$$
$$- \left[\frac{v_\perp}{r}\frac{\partial}{\partial \theta} + \frac{E_{\theta_1}}{B_{z_0}}\left(\frac{\partial}{\partial v_\perp} - \frac{1}{v_\perp}\right) - \frac{B_{r_1}}{B_{z_0}}\left(v_\perp\frac{\partial}{\partial v_z} - v_z\left(\frac{\partial}{\partial v_\perp} - \frac{1}{v_\perp}\right)\right)\right] f_{11}^I \tag{A5}$$

By taking appropriate moments of $f_{21}^R, f_{21}^I, f_{22}^R, f_{22}^I$ we obtain expressions for u_r, u_θ (i.e. $\perp$ components of Ohm's law), the relevant components of the ion stress tensor and for the flux energy of gyration $q_r{}^\perp$, $q_\theta{}^\perp$.

$$u_{r_1} = -\frac{1}{\rho_0\Omega r}\frac{\partial p_{\perp_0}}{\partial \theta} + \frac{E_{\theta_1}}{B_{z_0}} + \frac{B_{r_1}u_{z_0}}{B_{z_0}} \tag{A6}$$

$$u_{\theta_1} = \frac{1}{\Omega\rho_0}\frac{\partial p_{\perp_0}}{\partial r} - \frac{E_{r_1}}{B_{z_0}} + \frac{B_{\theta_1}u_{z_0}}{B_{z_0}} \tag{A7}$$

$$\left.\begin{aligned} q_{\theta_1}{}^\perp &= \frac{1}{\Omega}\frac{\partial R_{\perp_0}}{\partial r} - \frac{2p_{\perp_0}}{\Omega\rho_0}\frac{\partial p_{\perp_0}}{\partial r} + \frac{2B_{\theta_1}}{B_{z_0}}q_{z_0}{}^\perp \\ q_{r_1}{}^\perp &= -\frac{1}{r\Omega}\frac{\partial R_{\perp_0}}{\partial \theta} + \frac{2p_{\perp_0}}{\Omega\rho_0 r}\frac{\partial p_{\perp_0}}{\partial \theta} + \frac{2B_{r_1}}{B_{z_0}}q_{z_0}{}^\perp \end{aligned}\right\} \tag{A8}$$

$$R_{\perp_0} = \frac{\pi M}{2}\int\int v_\perp{}^5 f_0 \, dv_\perp \, dv_z \tag{A9}$$

To obtain a reasonable estimate of $R_{\perp 0}$, write f_0 as a double Maxwellian distribution

$$\rightarrow q_{\theta 1}{}^{\perp} = \frac{2p_{\perp 0}}{\Omega}\frac{\partial}{\partial r}\left(\frac{p_{\perp 0}}{\rho_0}\right) + \frac{2B_{\theta 1}}{B_{z0}}q_{z0}{}^{\perp} \tag{A10}$$

$$q_{r_1}{}^{\perp} = -\frac{2p_{\perp 0}}{\Omega r}\frac{\partial}{\partial \theta}\left(\frac{p_{\perp 0}}{\rho_0}\right) + \frac{2B_{r_1}}{B_{z0}}q_{z0}{}^{\perp} \tag{A11}$$

Traceless Stress Tensor:

$$\tau_{rr_2} = \frac{1}{4\Omega}\left(\frac{q_{\theta 1}{}^{\perp}}{r} - \frac{\partial q_{\theta 1}{}^{\perp}}{\partial r} - \frac{1}{r}\frac{\partial}{\partial \theta}q_{r_1}{}^{\perp}\right) + \frac{p_{\perp 0}}{2\Omega}\left(\frac{u_{\theta 1}}{r} - \frac{\partial u_{\theta 1}}{\partial r} - \frac{1}{r}\frac{\partial}{\partial \theta}u_{r_1}\right) + \frac{B_{r_1}}{2B_{z0}}\tau_{rz1} - \frac{B_{\theta 1}}{2B_{z0}}\tau_{\theta z1} \tag{A12}$$

$$\tau_{\theta\theta 2} = -\tau_{rr_2} \tag{A13}$$

$$\tau_{r\theta 2} = \frac{1}{4\Omega}\left(\frac{\partial q_{r_1}{}^{\perp}}{\partial r} - \frac{q_{r_1}{}^{\perp}}{r} - \frac{1}{r}\frac{\partial q_{\theta 1}{}^{\perp}}{\partial \theta}\right) + \frac{p_{\perp 0}}{2\Omega}\left(\frac{\partial u_{r_1}}{\partial r} - \frac{u_{r_1}}{r} - \frac{1}{r}\frac{\partial u_{\theta_1}}{\partial \theta}\right) + \frac{B_{\theta 1}}{2B_{z0}}\tau_{rz1} + \frac{B_{r_1}}{2B_{z0}}\tau_{\theta z1} \tag{A14}$$

$$\tau_{rz1} = -\frac{1}{\Omega r}\frac{\partial}{\partial \theta}q_{z0}{}^{\perp} - \frac{p_{\perp 0}}{\Omega r}\frac{\partial u_{z0}}{\partial \theta} + \frac{B_{r_1}}{B_{z0}}(p_{\|0} - p_{\perp 0}) \tag{A15}$$

$$\tau_{\theta z1} = \frac{1}{\Omega}\frac{\partial}{\partial r}q_{z0}{}^{\perp} + \frac{p_{\perp 0}}{\Omega}\frac{\partial u_{z0}}{\partial r} + \frac{B_{\theta 1}}{B_{z0}}(p_{\|0} - p_{\perp 0}) \tag{A16}$$

APPENDIX B

Consider perturbations of the lowest order part of the distribution function of form

$$f_0' = f_0'(r)\exp\left[i(\omega t + m\theta + kz)\right]. \tag{B1}$$

Substitute B1, A1 and A2 into A3 and obtain after rearrangement:

$$f_0' = \frac{B_{z0}'}{\mathrm{d}B_{z0}/\mathrm{d}r}\frac{\partial f_0}{\partial r} - \frac{i\Omega r}{mB_{z0}}\frac{\partial f_0}{\partial v_z}\left(B_{r_1}' + \frac{i\bar{k}B_{z0}B_{z0}'}{\mathrm{d}B_{z0}/\mathrm{d}r}\right) + i\left[v_z\left(B_{r_1}' + \frac{i\bar{k}B_{z0}B_{z0}'}{\mathrm{d}B_{z0}/\mathrm{d}r}\right) + \frac{i\bar{\omega}B_{z0}B_{z0}'}{\mathrm{d}B_{z0}/\mathrm{d}r} + E_{0_1}'\right]\cdot\left[\frac{1}{B_{z0}}\frac{\partial f_0}{\partial r} + \frac{1}{2B_{z0}{}^2}\frac{dB_{z0}}{\mathrm{d}r}v_{\perp}\frac{\partial f_0}{\partial v_{\perp}} + \frac{\bar{k}r}{m}\frac{\Omega}{B_{z0}}\frac{\partial f_0}{\partial v_z}\right]}{\bar{k}v_z + \bar{\omega} + \frac{mv_{\perp}{}^2}{2\Omega r B_{z0}}\frac{\mathrm{d}B_{z0}}{\mathrm{d}r}} \tag{B2}$$

where

$$\bar{k} = k + \frac{mB_0}{rB_{z0}}; \quad \bar{\omega} = \omega - \frac{mEr_1}{rB_{z0}} \tag{B3}$$

In lowest order we now apply the charge neutrality condition. Furthermore since as in BOWERS and HAINES (1971) the lowest order non zero axial current is of the order of $\varepsilon^2 nev_r{}^i/\sqrt{\beta}$ we take

$j_{z_0}' = 0$ by taking appropriate moments of f_0'. Charge

$$\sigma_0' = 0 = \left(B_{r_1}' + \frac{i\bar{k}B_{z0}B_{z0}'}{\mathrm{d}B_{z0}/\mathrm{d}r}\right) I_1 + \left(\frac{i\bar{\omega}B_{z0}B_{z0}'}{\mathrm{d}B_{z0}/\mathrm{d}r} + E_\theta'\right) I_2$$

current

$$j_{z0}' = 0 = \left(B_{r_1}' + \frac{i\bar{k}B_{z0}B_{z0}'}{\mathrm{d}B_{z0}/\mathrm{d}r}\right) I_3 + \left(\frac{i\bar{\omega}B_{z0}B_{z0}'}{\mathrm{d}B_{z0}/\mathrm{d}r} + E_\theta'\right) I_1$$

where I_1, I_2, I_3 are integrals involving the resonant denominator of the above expression for f_0', together with suitable summing over particle species.

Resonant microscopic modes are described by the dispersion relation

$$I_1^2 = I_2 I_3$$

whereas the macroscopic modes considered in this work are produced by the solution:

$$B_{r_1}' + \frac{i\bar{k}B_{z0}B_{z0}'}{\mathrm{d}B_{z0}/\mathrm{d}r} = 0 \tag{B4}$$

$$E_{\theta_1}' + \frac{i\bar{\omega}B_{z0}B_{z0}'}{\mathrm{d}B_{z0}/\mathrm{d}r} = 0 \tag{B5}$$

Rearrangement yields

$$\bar{\omega}B_{r_1}' - \bar{k}E_{\theta_1}' = 0 \tag{B6}$$

$$B_{z0}' = \frac{iB_{r_1}'}{\bar{k}}\frac{\mathrm{d}B_{z0}}{\mathrm{d}r} \tag{B7}$$

expanding B6 using B3 and the induction equation:

$$-\omega B_{r_1}' = \frac{m}{r}E_{z2}' - kE_{\theta_1}'$$

yields

$$E_{z2}'B_{z0} + E_{r_1}B_{r_1}' + B_{\theta_1}E_{\theta_1}' = 0$$

or

$$(\mathbf{E}\cdot\mathbf{B})' = 0 \tag{B8}$$

a familiar result of collisionless theory.

Substituting B4 and B5 into B2 yields

$$f_0' = \frac{iB_{r_1}'}{\bar{k}}\frac{\partial f_0}{\partial r}$$

APPENDIX C

Consider an interchange mode localized near $\bar{k}_{r=r_s} = 0$ and expand $\bar{k} = \alpha x$ where $x = r - r_s$,

$$\alpha = \frac{\mathrm{d}\bar{k}}{\mathrm{d}r}\bigg|_{r-r_s}$$

Write

$$\gamma_1 = r_s^3\alpha^2\left(\sum_{\text{species}}(p_\parallel - p_\perp) - \frac{B_{z0}^2}{\mu_0}\right)$$

$$\gamma_2 = \frac{m\alpha r_s^2}{2\Omega}\left(p_\perp\frac{\mathrm{d}u_z}{\mathrm{d}r} + \frac{\mathrm{d}q_{z\perp}}{\mathrm{d}r} + \frac{q_{z\perp}}{B_z}\frac{\mathrm{d}B_z}{\mathrm{d}r}\right)$$

$$\gamma_3 = \rho r_s^3\omega_1^2 - m\omega_1 r_s^2\frac{\mathrm{d}}{\mathrm{d}r}\left(\frac{p_\perp}{\Omega}\right) + \frac{m^2 r}{\Omega^2 B_z}\frac{\mathrm{d}B_z}{\mathrm{d}r}\left(\frac{1}{2}\frac{\mathrm{d}R_\perp}{\mathrm{d}r} - \frac{p_\perp}{\rho}\frac{\mathrm{d}p}{\mathrm{d}r}\right)$$

where all equilibrium quantities are evaluated at $r = r_s$. Transform from x to w:

$$w = \frac{x\gamma_1 + \gamma_2}{(\gamma_3\gamma_1 - \gamma_2^2)^{1/2}} \tag{C1}$$

put

$$X = \frac{\left(\frac{m^2-1}{r_s^2}\right)(\gamma_3\gamma_1 - \gamma_2^2)}{\gamma_1^2} \tag{C2}$$

$$Y = \frac{r_s^2 \frac{\mathrm{d}}{\mathrm{d}r}\left[p\left(\omega_1 - \frac{mu_\theta}{r}\right)^2\right] + k^2 r_s^2 \frac{\mathrm{d}}{\mathrm{d}r}\left(\Sigma(p_\parallel - p_\perp) - \frac{B_z^2}{\mu_0}\right)}{r_s^3\alpha^2\left(\Sigma(p_\parallel - p_\perp) - \frac{B_z^2}{\mu_0}\right)}. \tag{C3}$$

Equation (4) then becomes

$$(w^2+1)\frac{\mathrm{d}^2\xi}{\mathrm{d}w^2} + 2w\frac{\mathrm{d}\xi}{\mathrm{d}w} + [-(w^2+1)X + Y]\xi = 0. \tag{C4}$$

Observe that C4 is symmetric about $w = 0$ and hence we may expect the mode to be localized at this point. Since, originally, localization about $x = 0$ was assumed, we must apply the constraint:

$$\left(\frac{m^2-1}{r^2}\right)^{1/2}\frac{\gamma_2}{\gamma_1} \ll 1 \tag{C5}$$

in order that $k = \alpha x$ is still valid.

Consider the case $|Y| \ll |X|$ required for localization and expand in two regions:

(i) $w \ll \sqrt{Y/X}$ inner region → Legendre's equation.
(ii) $w \gg 1$ outer region → Bessel's equation.
Apply boundary conditions

$$\xi \to 0 \quad \text{as} \quad |w| \to \infty$$

The symmetry of the equations and homogeneity of the boundary conditions imply that at $w = 0$, either (a) $\xi = 0$ or (b) $\mathrm{d}\xi/\mathrm{d}w = 0$.

In region (ii) the solution is

$$\xi \propto K_\eta(w\sqrt{X}) \tag{C6}$$

where $\eta = \frac{1}{2}i(4Y-1)^{1/2}$ which decays exponentially to zero as $w \to \infty$.

Note that since $X = 0$ for $m = 1$ this solution does not exist in this case and localization by the Legendre functions alone which spatially decay as $w^{-1/2}$ is insufficient for the theory to apply.

In region (i) the two cases are:

$$\text{(a)} \quad \xi \propto \frac{\pi}{2}\left(i - \cot\frac{\pi\nu}{2}\right)P_\nu(iw) + Q_\nu(iw) \qquad w > 0$$

$$\text{(b)} \quad \xi \propto \frac{\pi}{2}\left(i + \tan\frac{\pi\nu}{2}\right)P_\nu(iw) + Q_\nu(iw) \qquad w > 0 \tag{C7}$$

where $\nu = -\frac{1}{2} + \frac{1}{2}i(4Y-1)^{1/2}$

Matching the expansion of C6 about $w = 0$ with the asymptotic expansion of C7 about $w \to \infty$ in the region

$$1 < w < \sqrt{\frac{Y}{X}}$$

yields a phase matching condition (STRINGER, 1975), KULSRUD (1963)

$$H_n(4Y) = \sqrt{X}$$

where

$$H_{n_{a)}}^{b)}(4Y) = 16\exp\left[\frac{2}{u}\left(-3i\ln\left\{\Gamma\left(i+\frac{iu}{2}\right)\left(\frac{\sinh\left(\frac{\pi u}{2}\right)}{\pi u/2}\right)^{1/2}\right\}\right.\right.$$
$$\left.\left.+\,i\ln\left\{\Gamma(i+iu)\left(\frac{\sinh\pi u}{\pi u}\right)^{1/2}\right\}\pm\left(\tan^{-1}\left[\exp\left(-\frac{\pi u}{2}\right)\right]-\frac{\pi}{4}\right)-n\pi\right)\right]$$

where n is an integer and $u = (4Y-1)^{1/2}$
(u is *complex* here)

The upper sign is for case (*b*) (odd symmetry modes)

The lower sign is for case (*a*) (even symmetry modes)

The value of n is chosen such that $H \to 0$ as $4Y \to 1$ in order that the Suydam criterion results in this limit.

Thus $n = 1, 2, 3, \ldots, \infty$.

Maximizing H maximizes the growth rate and thus $n = 1$ produces the most unstable modes.

Since

$$\tan^{-1}\left[\exp\left(-\frac{\pi u}{2}\right)\right]-\frac{\pi}{4} \leqslant 0 \quad \text{for} \quad 0 < u < \infty$$

the choice of even symmetry modes maximizes the value of $H_1(4Y)$ and it is thus these modes that will be discussed as the most unstable.

The constraint $|Y| \gg |X|$ of this localized theory may be written in terms of Y alone as

$$|Y| \gg |H_n(4Y)|^2.$$

Acknowledgements.

This work was supported by a bursary supplied by Culham Laboratory. (AGMT/CUL/901).

My supervisor was Professor M.G. Haines who provided my introduction to this field of research.